Investigation of Energy Efficient Magnetic Switching in Novel Materials and Device Structures for Spintronics Application

Jason Cheng-Hsiang Hsu
Sayeef Salahuddin, Ed.
Eli Yablonovitch, Ed.
James Analytis, Ed.
Frances Hellman, Ed.

Electrical Engineering and Computer Sciences
University of California, Berkeley

Technical Report No. UCB/EECS-2024-199
http://www2.eecs.berkeley.edu/Pubs/TechRpts/2024/EECS-2024-199.html

December 1, 2024

Investigation of Energy Efficient Magnetic Switching in Novel Materials and Device Structures for Spintronics Application

by

Cheng-Hsiang Hsu

A dissertation submitted in partial satisfaction of the

requirements for the degree of

Doctor of Philosophy

in

Engineering - Electrical Engineering and Computer Sciences

in the

Graduate Division

of the

University of California, Berkeley

Committee in charge:

Professor Sayeef Salahuddin, Chair
Professor James Analytis
Professor Frances Hellman
Professor Eli Yablonovitch

Summer 2023

Investigation of Energy Efficient Magnetic Switching in Novel Materials and Device Structures for Spintronics Application

Abstract

Investigation of Energy Efficient Magnetic Switching in Novel Materials and Device Structures for Spintronics Application

by

Cheng-Hsiang Hsu

Doctor of Philosophy in Engineering - Electrical Engineering and Computer Sciences

University of California, Berkeley

Professor Sayeef Salahuddin, Chair

Amidst the digital transformation era, data-intensive computing applications such as artificial intelligence and big data analytics are rapidly evolving. As a result, computing hardware development is under pressure to deliver higher performance while minimizing energy consumption. This presents a significant opportunity for hardware research, moving alongside and beyond traditional CMOS technology. Spintronic devices have emerged as a promising candidate to address the gaps in the computing memory hierarchy and serve as an emerging device for beyond von Neumann computing schemes. In the core of a spintronic device, the spin-charge conversion phenomenon plays a crucial role in determining its performance and energy efficiency. Spin-charge conversion enables the generation of a spin current, which can be utilized to manipulate magnetization and magnetic textures - spin-orbit torque. However, several significant challenges hinder the widespread adoption of spintronic devices in future computing hardware. These challenges encompass high operating power in comparison to traditional silicon counterparts, ensuring material compatibility with the silicon CMOS platform, developing highly scalable solutions for future process nodes, and addressing specific fundamental design hurdles. In this dissertation, my primary objective is to tackle various challenges by innovatively designing materials, fabrication processes, and device structures. Firstly, I discover significant spin-charge conversion efficiency in commercially available silicides, which exhibit a scalable underlying mechanism that could offer new insights into spin physics. Leveraging these silicides, I achieve highly energy-efficient magnetic switching, outperforming state-of-the-art heavy metal systems for magnetic memory applications. Moreover, I tackle the fundamental design challenge of achieving field-free spin-orbit torque switching by engineering a device fabrication process that allows for easy tunability of magnetic anisotropy. Lastly, I propose and experimentally explore a potential pathway towards the long-awaited pure voltage-driven magnetic bi-directional switching in commercially available magnetic tunnel junction devices.

To my family,
Jessica, and my dog Bonbon.

Contents

List of Figures

List of Tables

Acknowledgments

This dissertation will not be possible without the immense support from many people. First and foremost, I would like to show my utmost appreciation to my PhD advisor, professor Sayeef Salahuddin. Sayeef has supported me strongly throughout my PhD in many aspects and I am deeply indebted to all the opportunities and personal growth he has brought upon me. I enjoyed many intellectual discussions ranging from fundamental condensed matters physics to technology trends and implementations which shaped my dissertation research and long-term research goals. Secondly, I would like to acknowledge my collaborator and mentor, professor Frances Hellman. The fruitful discussions with her during our biweekly NEMM program meeting have helped shape my dissertation research in significant ways. Also, the continuous support from her in many occasions are truly appreciated. Next, I would like to show my appreciation toward senior lecturer Julie Karel who has been an awesome collaborator since the early days of my PhD studies to a mentor figure in my later years. Julie is a great scientist to work with and a great friend, supporting me throughout my PhD.

I would not have been even doing a PhD if it is not for professor Irena Knezevic at the University of Wisconsin-Madison. Irena has provided me the opportunity and guidance to become interested in the realm of condensed matters physics, material science and solid state device research. I would also like to thank professor Jeffrey Bokor for mentorship and fruitful discussions on spintronics and teaching over the years. I want to also acknowledge the rest of my dissertation committee members professor James Analytis and professor Eli Yablonovitch for their support on the formulation of my dissertation research. I would also like to acknowledge the rest of the NEMM program members including Dr. Peter Fisher, Dr. Sinéad Griffin, Dr. Sujoy Roy, Dr. Stephen Kevan, and Dr. Lin-Wang Wang.

My PhD journey would not be complete without my peers and undergraduate researchers I've had great honor to mentor. Mentoring undergraduate students at Berkeley has been one of the greatest moments in my PhD. Seeing them grow over time and evolve into independent thinkers and researchers brings great sense of accomplishment to me. I am so lucky to have met these undergraduate students which have all been great friends even after being graduates. These undergraduate students are (in chronological order) Jonathan Jeffrey, Megumi Tanaka, Miela Gross, Hannah Kleidermacher, Emma Blenkinsop, Jonathon Webster, Ian Hoffmann, Tarik Fawal and Jennifer Toy. I would like to thank my friends and colleagues at Berkeley and the Bay Area: Steve Volkman, Shehrin Sayed, Adi Jung, Saavan Patel, Niklas Roschewsky, Praveen Gowtham, Dominic Labanowski, Yen-Kai Lin, Li-Chen Wang, Jong-Ho Bae, Daewoong Kwon, Jiuren Zhou, Korok Chatterjee, Ava Tan, Yu-Hung Liao, Ming-Yen Kao, Urmita Sikder, Lars Tatum, Dasom Lee, Pratik Brahma, Jongho Park, Namho Jeon, Meshal Alawein, Michael Oduoza, Hanuman Singh, Jyotirmoy Chatterjee, Sucheta Mondal, Amal El-Ghazaly, Akshay Pattabi, Zafer Mutlu, Debanjan Polly, Hyejin Jang, Maite Goiriena, Niharika Gupta, Der-Hsien Lien, Lucas Caretta, Chien-Ting Tung, Xiaoer Hu, Dwi Patnaik, Alvin C.C Li, Nishita Deka, Allen Yu-Lun Liang, Jeff Lin, Ramo Tsai, Nai-Wen Hu, Chien-Shen Wu, and Emily Beeman.

There will never be enough appreciation to be expressed toward my family: my parents and my brother Vincent. Their care and support since the day I was born is unmatched. I would like to thank my brother Vincent for taking care of me since the day I came to the US for college. He took care of me from time to time during my PhD and sharing conversations on each of our work is very therapeutic. At last and definitely not the least, I will dedicate my utmost appreciation to Jessica Ho, my partner. Coming to Berkeley for my PhD is one of the best decisions I have made because of Jessica. Jessica has been with me since the second year of my PhD and has seen it all in terms of my highs and lows. It is as if we did my PhD together. I wholeheartedly thank her dedication to our relationship and our goals. This PhD will not be possible without her by my side every single day. The addition of our dog, Bonbon, to our family toward the end of my PhD is a blessing.

Chapter 1

Introduction

1.1 Current outlook of computing hardware research

Brief history of technology advancement

Technology advancement in the recent two decades has skyrocketed in multiple facets. The main drivers include the rise of mobile computing devices such as smartphones and tablets since 2007, rapid growth in cloud computing and internet of things (IoT), and faster 5G cellular connectivity. These technology development dramatically reshaped both our daily lives and the technology industry. A few examples include booming of e-commerce, streaming of entertainment content, commercial services conducted directly from smartphones, widespread social media access, increased remote/online working/learning, the adoption of fintech and more advanced electrical appliances. At the heart and soul of all the technological advancement mentioned above is the continuous improvement of computing power enabled by the cutting edge individual devices at the fundamental level. The movement, processing, and creation of data all rely on different designs of circuits that are built from these individual devices such as transistors, diodes, capacitors, resistors and interconnects.

Keeping Moore's Law alive

Gordon Moore passed away but Moore's Law is well alive and the outlook is promising and exciting.[1] Moore's Law was proposed by Gordon Moore in 1965 that the number of transistors on an integrated circuit will double every two years - a prediction that stood the test of time and led the entire semiconductor industry even to this day. Geometric scaling of transistor and interconnect dimensions has long ended in the early 2000s where feature sizes reached below 100 nm [163]. Since then, effective scaling with the FinFET, strained silicon and high-k metal gate technologies has been the main technology scaling approach for higher power efficiency and performance. As we approach the physical limit of the material

[1] Gordon Moore passed away on March 24, 2023 at the age of 94. He is the co-founder of Intel alongside with Robert Noyce.[158]

dimension, news about Moore's Law is dying is circulating and people are wondering what will be the next technological advancement or guiding principal. However, Moore's Law is not simply a geometric scaling principle, it is truly a performance-based scaling principle at the fundamental level. Moore's Law will sustain and the semiconductor industry is on pace to develop device and chip performance improvements that follows the Moore's Law for the next decade.

Current status of technology development

Among the various electronic components and devices, transistor is at the heart of every computing hardware in the modern era. The current most advanced logic transistor is based on the so called FinFET which the silicon channel is formed in a raised 3D fin structure with the high-k dielectric and metal gate formed around the three sides. This is the foundation of modern transistor technology in the 2010s with Intel debuted in its 22 nm process node [136], followed by TSMC in its 16 nm technology node [1] and Samsung in its 14 nm technology node [138]. With FinFET lasting us 10+ years of successful transistor technology scaling, its structure is no longer sustainable for future scaling of power efficiency and performance. This welcomes the beginning of a new era with gate-all-around (GAA) FETs with nanosheet of silicon channel completely surrounded by the high-k dielectric and metal gate which provides even better gate control and off-state-leakage. This transition started with Samsung in 2019 announcing the adoption of GAA technology in its 3 nm technology node [166] which later in 2022 started initial production. TSMC also announced their adoption of GAA structure in 2022 [2] which will begin production by 2025. Unfortunately, as the cutting-edge transistor technology node becomes more sophisticated, not every semiconductor foundry is able to sustain this technology competition at the cutting-edge due to economical challenges. Global Foundries stopped its further development of 7 nm FinFET technology [49] and intel announced it will outsource its latest CPUs to be manufactured by TSMC's 3 nm/5 nm nodes, indicating a sluggish development of its leading-edge foundry technology nodes [137].

One of the most important technologies enabling this continuous scaling of transistor technology in the last decaded is the successful deployment of the extreme ultraviolet (EUV) lithography system [8]. It is no coincidence that the early deployment of the EUV lithography system and integration to its fabrication process in TSMC [3] and Samsung [134] in 2019, led them to be the two only-standing semiconductor foundry business to continue developing the leading-edge technology today. Intel received its first deployment of EUV system in late 2022 hoping to catch up to the two leading-edge leaders in its Intel 4 technology node development [135].

One strong drive for more cutting-edge hardware is the rise of a new era of generative AI applications and tools such as ChatGPT, Bard and deepfakes. These computation intensive applications continues to drive further development of new hardware at the device, circuit and system architectural level. Concepts such as in-memory and near-memory computing especially for cloud computing and edge-AI applications have been intensively researched and developed. The wide-spread of AI applications and tools also drove graphic processing unit

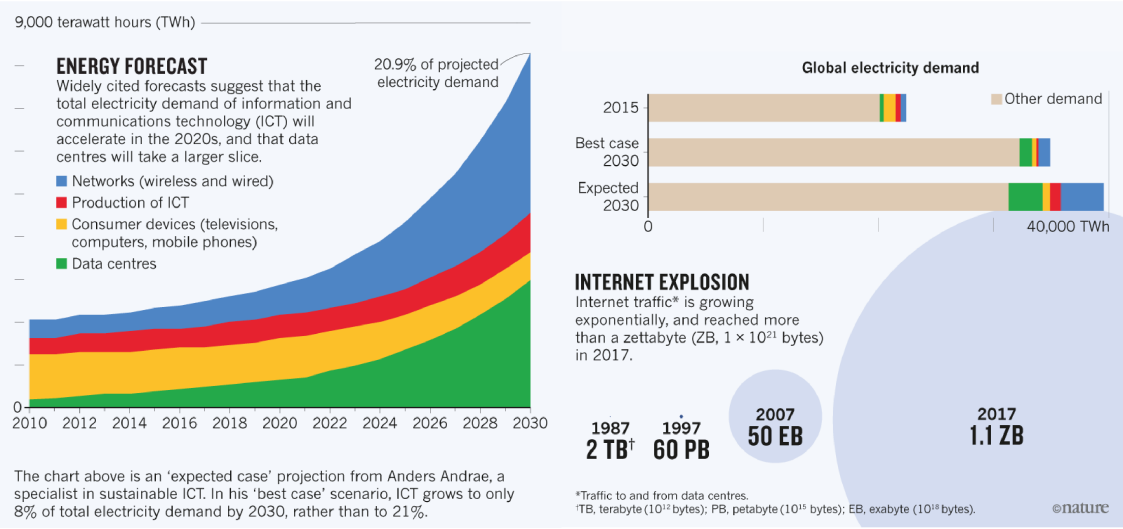

Figure 1.1: Energy forecast of information and communications technology (ICT) compared to the global energy consumption. Global electricity demand forcast by 2030. Figure adapted from *Nature* [83].

(GPU) chip design companies such as NVIDIA and AMD to a new height among the fabless semiconductor companies. However, implementing computation-intensive AI algorithms and models on GPU hardware is not a sustainable solution in terms of performance and power efficiency in the long term.

To address this, emerging memory technologies that provide various attractive properties such as non-volatility and analog computing that are more challenging to implement on traditional silicon CMOS are being heavily and actively studied. In addition, computing schemes that emulate our biological brain such as neuromorphic computing requires devices and hardware architectures that closely resemble the biological neural networks. To this end, emerging memory technologies such as phase-change memory, resistive memory, ferroelecrtic memory and magnetic memory all possess different properties that can suit this need. This dissertation focuses on addressing the fundamental challenges in magnetic memory research and development for spintronics applications and beyond.

Global challenges in computing and information technology

At the global scale, energy consumption for the computing and information technology sector is projected to take up 21% of the global energy consumption by 2030 (see Figure 1.1). This is a very pressing issue adding on to the ongoing annual increase of the total electricity consumption from the ICT sector. The most effective solution to such global energy crisis is to address the source - fundamental building block of electronic circuits: transistors and

memory devices. The creation, movement and processing of data all consumes energy. By reducing the consumption of individual circuit components and devices, there is a hope to at least slow down the increase of the total energy consumption in the ICT sector. As a result, research and development of efficient and task-specific devices for future computing scheme is of utmost importance and urgency.

1.2 Overview of memory technology

Memory hierarchy in computing

The traditional memory hierarchy for a von Neumann computer architecture is depicted in Figure 1.2. In a typical von Neumann computer architecture, running programs are allocated in the main memory with frequently accessed data stored in the cache level memory according to the locality of reference. The higher in the hierarchy pyramid the faster and smaller capacity of the memory devices. Registers are for storing the data and instruction used in carrying out operations in the arithmetic/logic unit (ALU). The lower the pyramid the less frequent the stored information is accessed as well as serving as a non-volatile storage for data, operating system, and program installations. Logic and arithmetic operations are only done in the center processing unit (CPU) with data written, accessed, erased in the main memory. While leading-edge device nodes are often developed for faster and higher performance logic transistor and SRAMs, the DRAM space has been targeting higher density and lower cost per bit a priority. This causes a gap in performance between logic processor and DRAM known as a *Memory Wall* [163]. To combat this growing gap between main memory and the logic processor, innovative solutions at the system architecture level such as multi-threading, increase of embedded SRAM cells and advanced system on chip packaging solutions [163] has been quite successful but not sustainable for the long term and future high performance computing demand. To address this, emerging memory technologies that are based off of different physical phenomena provide not only intrinsically task-specific advantages but also different electrical performance and packaging designs for faster overall system speed and power efficiency.

Emerging memory technologies

Traditional CMOS memory modules throughout the entire memory hierarchy are based off of transistors and/or capacitors wired into specific circuitry for different specifications except hard disk drives which mainly stores information in magnetic disks composed of small magnetic domains. For example, NAND and NOR flash memory devices are floating gate transistors that wire in the architecture that resembles a NAND and NOR gate respectively. On the other hand, dynamic random-access memory (DRAM) cell is a volatile memory component consists of one transistor and one capacitor that serves as the main memory modules in modern computers. Due to this memory hierarchy that is designed for separate

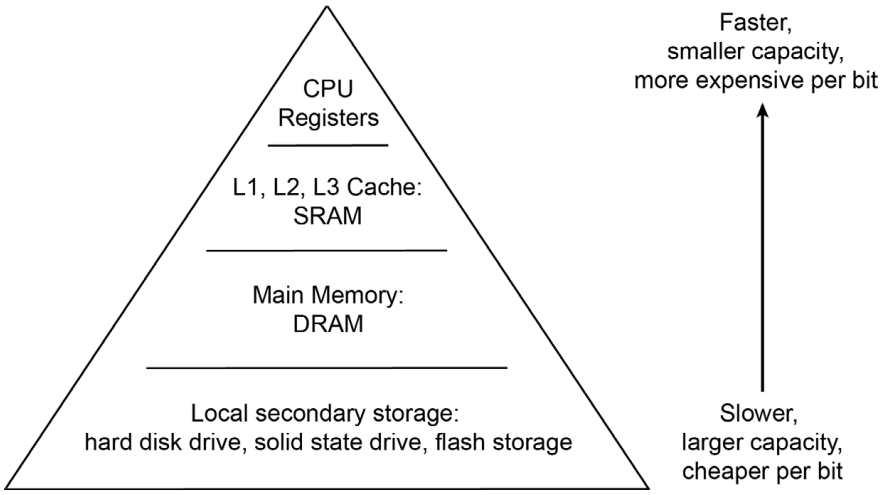

Figure 1.2: Generic memory hierarchy for a classic von Neumann computing architecture.

modules to be assembled on a motherboard, it is quite challenging to simply embed different memory modules on to logic chips and expect this to work flawlessly. Stringent electrical, speed and power specification on-chip makes embedding memory devices directly on or close to the logic unit very difficult. As a result, different memory devices that live in spaces between each level of the memory hierarchy is necessary for faster and more power efficient computing systems.

For the past few decades, there are a variety of emerging non-volatile memory (NVM) technologies in research and development including phase-change memory, resistive memory, ferroelectric memory and magnetic memory (Table 1.1). The common characteristic is non-volatility and the ability to embed with current CMOS technology. While most of the stand alone application of these emerging memory technologies have been commercialized already, the embedded application in large foundries remain to be widely deployed. The reason being the challenge for these emerging memory technologies to perfectly replace or add on to existing technologies without giving up on trade-offs. For example, in table 1.1 we can see that STT-MRAM actually possess characteristics that are either close to or out-perform the embedded SRAM (eSRAM) in terms of speed, cell size, standby power and endurance. However, SRAM design rules are among the most stringent given the closest distance in terms of data transfer to the logic unit. The few nanoseconds slower in speed, slightly lower endurance and the maturity of the CMOS SRAM technology makes CMOS SRAM still the best choice when competing with other emerging memory technologies at this moment.

However, this is not the end of the story as there is great room for improvement on all of the emerging memory technologies listed above. For example, spin-orbit torque (SOT) is a great candidate for next-generation magnetic memory technology due to the separate read/write path, potentially faster writing speed and lower switching power [117]. This

	eSRAM	eDRAM	eFLASH	STT-MRAM	FeRAM	FeFET	PCRAM	RRAM	Vertical RRAM	Crossbar RRAM
	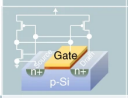	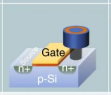	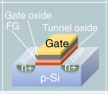		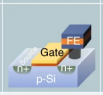	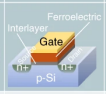	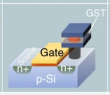	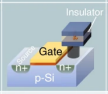	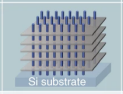	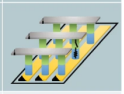
Cell size	120–150 F^2	10–30 F^2	10–30 F^2	10–30 F^2	10–30 F^2	10–30 F^2	10–30 F^2	10–30 F^2	4 F^2/N	4 F^2/N
Cell structure	6T	1T–1C	1T	1T–1MTJ	1T–1C	1T	1T–1PCM	1T–1R	1S–1R	1S–1R
Non-volatility	No	No	Yes	Yes	Yes	Yes	Yes	Yes	Yes	Yes
Write voltage	<1 V	<1 V	~10 V	<1.5 V	<3 V	<4 V	<3 V	<3 V	<4 V	<3 V
Write energy	~fJ	~10 fJ	~100 pJ	~1 pJ	~0.1 pJ	~0.1 pJ	~10 pJ	~1 pJ	~10 pJ	~1 pJ
Standby power	High	Medium	Low	Low	Low	Low	Low	Low	Low	Low
Write speed	~1 ns	~10 ns	0.1–1 ms	~5 ns	~10 ns	~10 ns	~10 ns	~10 ns	~100 ns	~50 ns
Read speed	~1 ns	~3 ns	~10 ns	~5 ns	~10 ns	~10 ns	~10 ns	~10 ns	~1 µs	~50 ns
Endurance	10^{16}	10^{16}	10^4–10^6	10^{15}	10^{14}	>10^5	>10^{12}	>10^7	>10^7	>10^8

Table 1.1: Different memory candidates for embedded applications including emerging memory devices. FG, floating gate; FE, ferroelectric; GST, GeSbTe; F, feature size; N, number of stacked layers. Table adapted from *Nature Electronics* [163].

makes SOT-MRAM a candidate to improve upon STT-MRAM and eventually serve as an alternative eSRAM candidate. Compared to the other emerging non-volatile memory solutions, spintronics-based memory technology is the most mature and possess advantages over the rest in the most specifications. In addition, spintronics devices serve as powerful probes to study spin-based physics and other quantum phenomena. This dissertation investigates in-depth into spintronics at both the fundamental level and application level.

1.3 Spintronics and MRAM

What is spintronics?

Spintronics are electronic devices that leverage the spin degree of freedom in electrons (Figure 1.3) to build components for computing hardware. The term *spintronics* originated from a program of the Defense Advanced Research Projects Agency (DARPA) in 1993 under program manager Stuart Wolf [38]. It was the first program to systematically study and explore magnetic-based quantum microelectronics that contributed to the development of magnetoresistive random-access memory (MRAM). However, the development of spin-based physics started much earlier than 1993 starting from the discovery of magnetic materials among many people around the world including the Romans, Greeks and Chinese [116] to the more recent spin-transport phenomena such as the giant magnetoresistance (GMR) effect in the 1980s which led to the Noble prize award in physics of 2007 [153]. The discovery

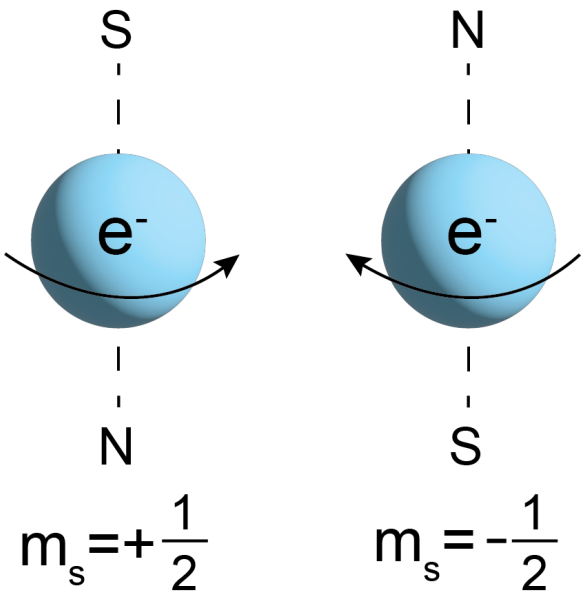

Figure 1.3: Electron spin and its local magnetic field with the respective spin quantum number.

of GMR opened up a brand new avenue for studying spin-transport physics and engineering of spintronics devices such as the spin valve [79]. The spin valve structure consists of two ferromagnetic layers sandwiching a metallic spacer. Electric current can be applied in-plane to the structure or vertical to the structure. As the magnetic moments of the two ferromagnetic layers align in parallel or anti-parallel, the resistance of the spin valve changes (Figure 1.4a). Spin valve drove many subsequent fields of spintronics including the improvement of magnetic read/write head in magnetic hard drives, magnetic sensors and development of the initial versions of MRAM [25]. Modern spintronics development began with the discovery of GMR effect.

Magnetic memory

Since the discovery of GMR, the field of spintronics advanced significantly over the last 30 years. The discovery of tunneling magnetoresistance (TMR) around the 1990s in Fe / Al_2O_3 / Fe with 18% TMR ratio [127], CoFe / Al_2O_3 / Co with 11.8 % [128], and 200 % in Fe / crystalline MgO / Fe [151, 210] further extended the magnetoresistance effect with larger resistance change by replacing the metallic spacer with a insulating tunneling barrier layer sandwiched between two ferromagnetic layers (Figure 1.4b). Similar to the GMR effect, but instead of having a non-magnetic metallic spacer layer where the spin polarization of the polarized current passes through without losing the spin information, a very thin tunneling barrier is in place for the spin-polarized current to tunnel through and

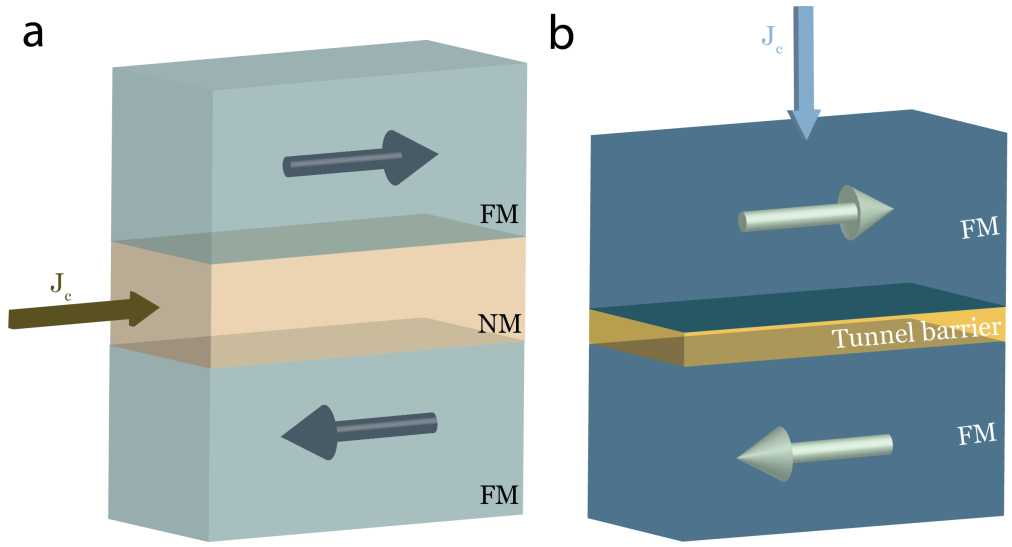

Figure 1.4: Schematic of a: giant magnetoresistance (GMR) and b: tunneling magnetoresistance (TMR). NM is non-magnetic conducting spacer layer and FM is ferromagnetic layer.

reach the other ferromagnetic layer. As the relative orientation of the moments in the two magnetic layer switches between parallel and anti-parallel configuration, the resistance value changes respectively but a higher resistance ratio can be achieved when compared to the GMR effect.

The magnetoresistance effect due to the different configurations of the magnetization in the two ferromagnetic layers can be explained from the perspective of spin-dependent density of states (Figure 1.5). In Figure 1.5, when the magnetic configuration is in the parallel state, equal amount of majority and minority energy states are available on both sides. As a result, majority up spins (in this illustration) can tunnel from the left magnetic layer to the right magnetic layer easily resulting in a low resistance value. In the case of anti-parallel state, majority up spins in the left magnetic layer can not fully tunnel to the right minority up spin states since there are not enough spin up states in the right ferromegnet to tunnel to. Same goes with the minority down spin states in the left ferromagnet. As a result, a higher resistance value is obtained. It is assumed that spin information is preserved during tunneling.

Another important factor for obtaining high TMR ratio is the symmetry consideration in the ferromagnet / tunnel barrier / ferromagnet structure (Fig. 1.4b) [25, 151]. Since the TMR effect is due to the spin-carrying tunneling electrons between the two ferromagnetic electrodes, a higher tunneling rate will result in a higher TMR ratio. To maximize the tunneling rate, matching spin-dependent density of states and tunneling matrix elements of the barrier near the Fermi level is important. When the symmetries of the ferromagnet electrodes and the tunneling barrier are matched, coherent tunneling can happen across the

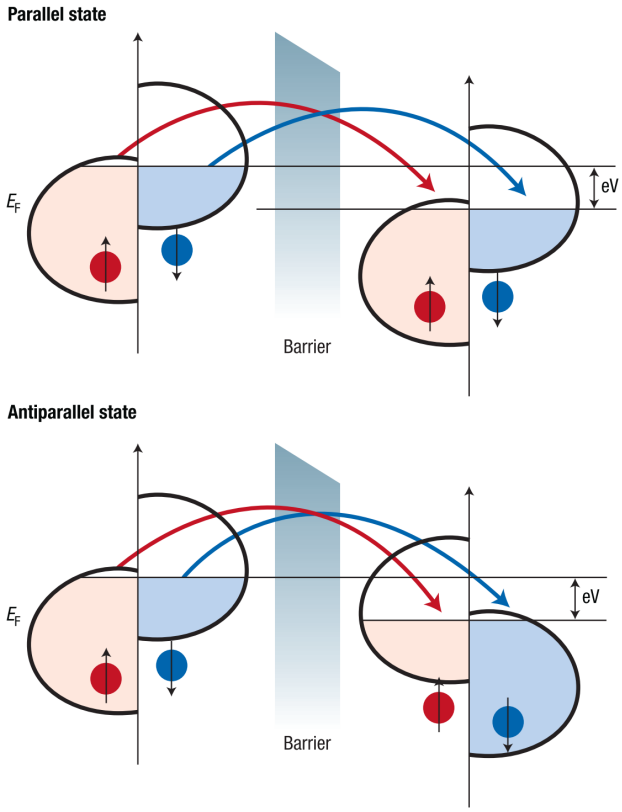

Figure 1.5: Physical origin of tunneling magnetoresistance from a spin-dependent density of states perspective with two-current model. Graph adapted from *Nature Materials* [25].

TMR structure resulting in a higher transmission ratio due to the slower decaying evanescent wave with similar symmetry across the structure [25, 210]. As a result, epitaxial single crystalline Fe (001) / MgO (001) / Fe (001) structure gives a much higher ($\sim$ 200 %) TMR ratio under room temperature when compared to tunnel barrier with amorphous alumina ($\sim$ 70 %) [151, 210]. The discovery of TMR effect pushed the spintronic development further with improved magnetic read/write head in hard disk drives for higher capacity, more sensitive TMR-based magnetic sensors and the development of magnetic tunnel junction (MTJ) for MRAM application. MTJ became the most crucial and widely adopted magnetic device for spintronics applications.

Up to this point, the main focus of spintronic phenomena presented in this chapter has been on the passive behavior of spin-dependent transport or physical mechanisms for magnetic states readouts. Another seminal development in spintronics was the spin-transfer torque (STT). STT allows manipulation of magnetic moments with spin-polarized currents via angular momentum transfer, which was theoretically proposed by John Slonczewski in 1996 [174]. Any finite magnetic moment has a finite angular momentum associated with

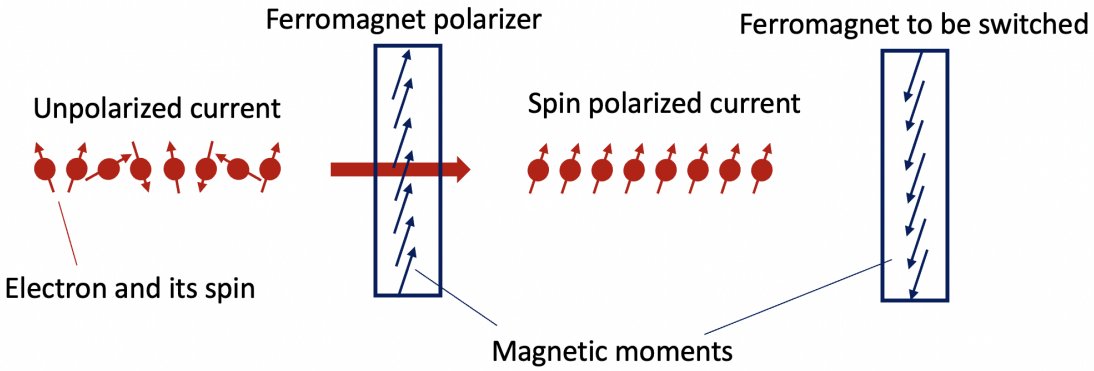

Figure 1.6: Illustration of the physical phenomenon of spin-transfer torque in a magnetic tunnel junction or ferromagnet / tunnel barrier / ferromagnet structure.

it via the gryomagnetic ratio. Through spin-polarizing the electronic charge current, the spin-polarized current can tunnel through the barrier and arrive at the other ferromagnet. The spin-polarized current will carry a non-zero angular momentum that can be transferred to the magnetic moments in the receiving ferromagnetic layer or the so-called free layer (Fig. 1.6). The first ferromagnetic layer in a MTJ thus acts as a spin polarizer. In a practical MTJ, the polarizer is the fixed layer with pinned magnetic orientation via exchange bias from an adjacent synthetic antiferromagnet stack. To write the magnetic state in the free layer back to its original state, a charge current can be injected in the opposite direction [25, 174] (Fig. 1.7b and 1.7c). As a result, simply inject the current in opposite directions with respect to the MTJ vertical transport direction, the magnetic moment in the free layer can be toggled thus creating two different magnetic configurations (parallel/anti-parallel) of the MTJ for TMR readout.

By combining the two effects, TMR can serve as the mechanism for readout of the MTJ and STT can serve as the mechanism for writing information to the MTJ. If we further connect the MTJ to an access transistor, the STT-MRAM cell is born with the transistor supplying a large current to write the information or a small current to read the information in the MTJ. However, MRAM was actually first developed before TMR and STT was discovered. The initial version of MRAM was designed with the Oersted field serving as the mechanism to switch magnetic moments in a spin valve via bit and word line current application. The GMR effect in the spin valve serves as the readout mechanism (Fig. 1.7a). This is a very inefficient way to writing magnetic information since the Oersted field is not only nonuniform but also control of very small and local magnetic layer within a much larger array structure was difficult. With the development of STT, control of local magnetization in a MTJ is much more energy efficient and provides significantly better control of local magnetization (Fig. b and c).

While STT-MRAM is a very promising emerging NVM solution, it still possess some

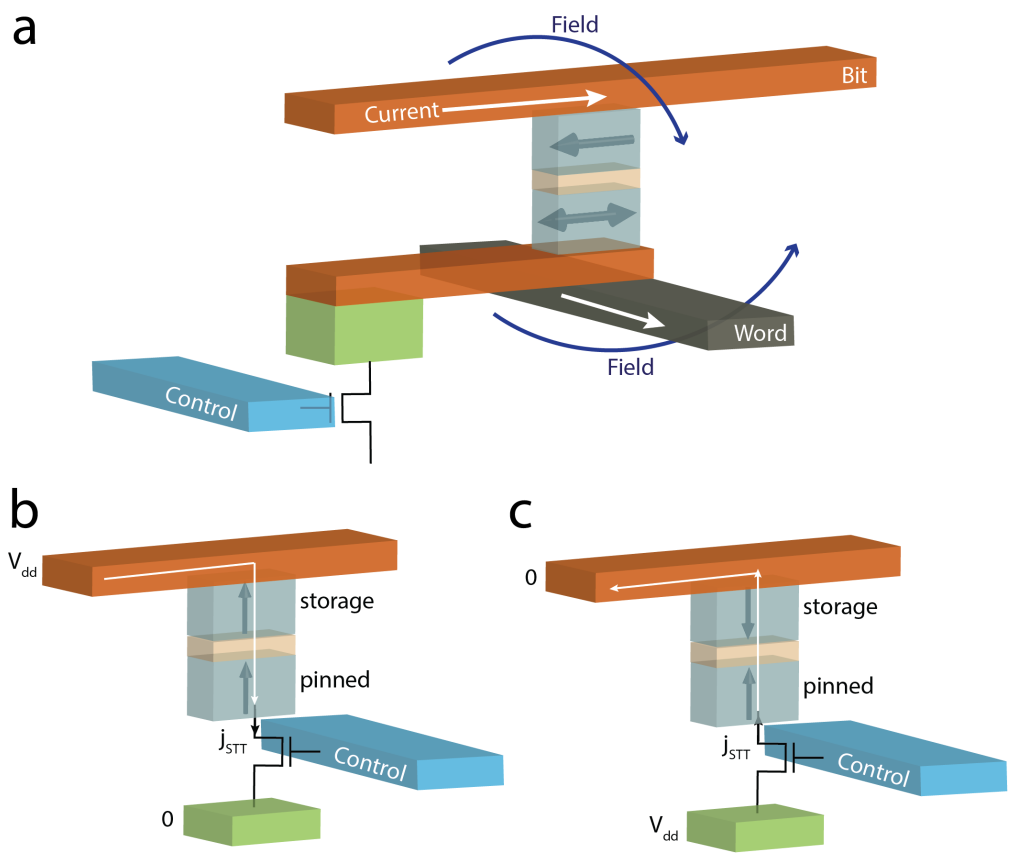

Figure 1.7: Schematic of a, the initial version of MRAM via spin valve and Oersted field writing mechanism, b and c, the individual MRAM cell based off of STT for writing and TMR for reading which includes one magnetic tunnel junction and an access transistor.

challenges or drawbacks including endurance and reliability issues of the tunnel barrier, limited material choice for efficient spin-polarization, and high switching current density. This leads to the research and development of spin-orbit torque as the next generation MRAM technology which will be introduced with great detail in chapter 2.

1.4 Dissertation objectives

The main goal of this dissertation is to explore and investigate novel materials and device structures for efficient manipulation of magnetic states and textures for spintronics application in near future computing schemes. The design principles for the materials and device structures are not only geared toward higher performance and better energy efficiency but also in materials and device structures that are either available in the current silicon platform

or not too drastically different from the existing device or material systems in industry.

In Chapter 2, the fundamentals and history of spin-orbit torque will be introduced. Various techniques to characterize spin-orbit torque and the applications of spin-orbit torque will be presented. The chapter will end with an outlook for the spin-orbit torque MRAM development and how this dissertation contributes to this goal.

In Chapter 3, I present how amorphous iron silicide (a-Fe_xSi_{100-x}) can be a very suitable material for efficient spin current generation in magnetic memory applications. a-Fe_xSi_{100-x} is not expected to have a strong spin-orbit torque according to the conventional understanding of spin current generation, however, a strong spin-orbit torque is discovered. In addition, intriguing scaling trend between the spin-orbit torque efficiency and the resistivity was found in a-Fe_xSi_{100-x} which shows increasing spin-orbit torque efficiency as the resistivity decreases. This trend is opposite to the conventional scaling trend. On the fundamental level, strong spin current generation in a fully amorphous low-Z material system is out of expectation and sheds light on to the possibility of new mechanisms and understandings in spin current generation.

In Chapter 4, I switch gears into presenting cobalt silicide as an successor to iron silicide which extends the scaling trend further toward the ideal direction where high spin-torque efficiency and low resistivity is coupled. A record-high spin Hall conductivity (an important metric when screening materials for magnetic switching) was found in cobalt silicide that beats the heavy metal systems which currently is adopted in the state-of-the-art spin-orbit torque MRAM among the semiconductor foundries and research laboratories worldwide. on the fundamental level, cobalt silicide also exhibits a interesting concentration dependence where the peak of the spin-torque efficiency coincides with the transition of the ferromagnetic phase of it. The underlying physics of spin current generation is similar to the case of iron silicide, however, due to the different electronic property of cobalt silicide, the spin-orbit torque possess a slightly different concentration dependence.

In Chapter 5, I present a way to induce field-free spin-orbit torque switching by engineering the canting angle of the magnetic anisotropy in ferrimagnetic GdCo alloy. The canting can be easily tuned by oxygen plasma treatment after the devices have been fabricated. This is a very easy way of inducing canting of the magnetic anisotropy in GdCo. In addition, interesting magnetic transport signatures such as multistate switching, ratchet effect, and memristor effect were discovered which are all tunable through the different canting angle. This work presents a way to easily and effectively fine tune the magnetic texture in ferrimagnetic GdCo.

In Chapter 6, I present a way to achieve pure voltage-controlled magnetic switching in a device structure similar to a standard magnetic tunnel junction with two additional few-angstrom thick layers. This device utilizes two physical phenomena: resonant tunneling and interlayer exchange coupling to control the configuration between two ferromagnetic layer separated by a quantum well. Theoretical understanding and discussion is presented. Memory cell level simulation results are also briefly mentioned. At last, I will show some initial results toward the demonstration of this engineering design through tunneling I-V measurements and voltage-pulse/TMR readout measurements. This is an ongoing research

project.

In Chapter 7, I will conclude by summarizing the major findings toward addressing the different research questions proposed in this dissertation. I will also provide the potential implication of this dissertation in a more big picture fashion and point to some future directions for continuing study on these materials systems, device structures or concepts.

Chapter 2

Spin-orbit torque: theory, experiments, materials and devices

2.1 Theory

Foreword

Spin-orbit torque (SOT) can be introduced through two different perspectives: technological and fundamental. From the technological perspective, spin-orbit torque is a way to write information into a magnetic bit by switching the magnetic moments via an electrically (current) generated torque. The process of switching the magnetic moments is exactly the same as spin-transfer torque (STT) which angular momentum is transferred from the spin current to the magnetic moments. The main difference is the symmetry/geometry of the spin polarization in SOT which can be very different depending on how the spin current is generated whereas in STT, the spin polarization of the spin current is almost collinear due to the mechanism of spin current generation in STT devices.

From the fundamental perspectives, spin-orbit torque is a probe for studying spin-dependent physics such as spin-charge conversion, spin current generation, spin injection, spin transport and manipulation of complex magnetic textures [61]. The main difference of SOT from STT is the way spin current is generated for SOT. In SOT, spin currents can be generated through many different mechanisms such as topological spin-momentum locking surface states, spin Hall effect, Rashba-interfaces, bulk Rashba effect, and in general non-zero Berry curvature. These effects can be found and engineered in many families of materials. Prior to the discovery of SOT, spintronics research has been mainly focused on magnetic materials and thanks to SOT, materials research in spintronics has expanded to cover a wide range of materials. As a result, SOT is not only attractive for technological reasons but also as a useful probe to study spin physics in many material systems.

Spin-torque driven magnetization dynamics and torque symmetry

Magnetization dynamics can be described by the Landau-Lifsiftz-Gilbert (LLG) equation with the addition of spin-transfer torque by Slonczewski in 1996 [174]. If we consider the dynamics of a normalized ($\mathbf{M}/\mathbf{M}_s$) magnetization $\boldsymbol{m}$ in the macrospin picture (the magnetization is uniform under the external perturbations) under an effective magnetic field $\mathbf{H}_{eff}$ that includes contribution from applied field, magnetocrystalline anisotopry field, and demagnetization field), the LLG equation with contribution from field-like (FL) and damping-like (DL) torque can be written as [139, 117, 174]:

$$\frac{d\mathbf{m}}{dt} = -\gamma\mathbf{m}\times\mathbf{H}_{eff} + \alpha\mathbf{m}\times\frac{d\mathbf{m}}{dt} - |\tau_{FL}|\mathbf{m}\times\hat{\sigma} - |\tau_{DL}|\mathbf{m}\times(\mathbf{m}\times\hat{\sigma}) \tag{2.1}$$

where γ is the gyromagnetic ratio and α is the Gilbert damping constant. In equation 2.1 above, the first term describes the precession of the magnetization $\boldsymbol{m}$ about $\mathbf{H}_{eff}$. The second term accounts for the damping action of the magnetization $\boldsymbol{m}$ that relaxes back to its equilibrium position. The last two terms account for the DL torque and FL torque contribution induced by a spin current with spin polarization direction $\hat{\sigma}$. Since the magnetization $\boldsymbol{m}$ is a unit vector in the LLG equation, the unit of the two torques (τ_{FL} and τ_{DL}) are Hz or 1/s. The unit of $\mathbf{H}_{eff}$ is Tesla (T).

While the LLG (with spin-torque contribution) equation is a very convenient model for studying the magnetization dynamics theoretically, we often measure torques in terms of their effective fields. In this case, the FL torque effective field $\mathbf{H}_{FL}$ is

$$\mathbf{H}_{FL} = \frac{1}{\gamma}|\tau_{FL}|\hat{\sigma} \tag{2.2}$$

and the DL torque effective field $\mathbf{H}_{DL}$ is

$$\mathbf{H}_{DL} = \frac{1}{\gamma}|\tau_{DL}|(\mathbf{m}\times\hat{\sigma}) \tag{2.3}$$

where both $\mathbf{H}_{FL}$ and $\mathbf{H}_{DL}$ have unit of T. These two terms are often used when describing the measured torque strength and also shows up in torque analysis of different techniques such as harmonic Hall measurement and spin-torque ferromagnetic resonance.

In figure 2.1, the schematic of the torque symmetry resulting from the spin current with spin polarization $\hat{\sigma} = \hat{y}$ is shown. This is a simplified picture with only considering the simplified anisotopry coefficients which is sufficient to explain most of the spin-orbit torque phenomena. For a much sophisticated and general treatment of the spin-orbit torque symmetries, Garello *et al.* [55] has done a great work. In short, damping-like torque effective field is an odd function of $\mathbf{m}$ where as the field-like torque effective field is an even function of $\mathbf{m}$ regardless of which plane the magnetization $\mathbf{m}$ is in.

Although a rigorous and more general treatment of spin-orbit torque symmetry is crucial to fully understand and consider the different torque symmetry configurations, the actual switching scenario can be simplified into three: x-type, y-type and z-type. The difference

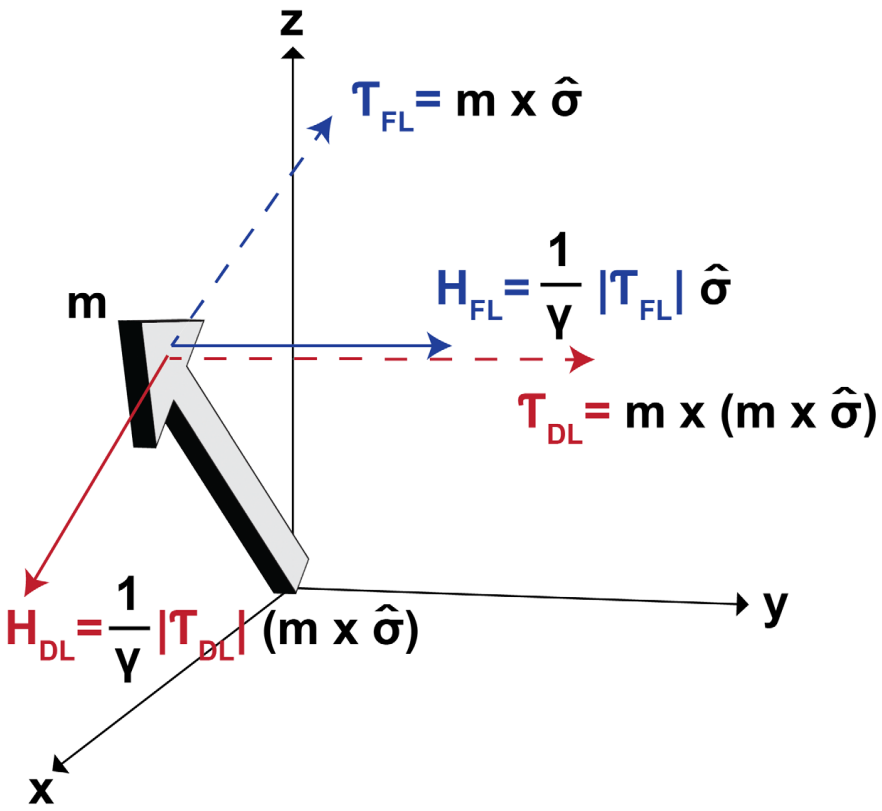

Figure 2.1: Symmetry of damping-like torque and field-like torque on a magnetization unit vector due to a spin current with spin polarization $\hat{\sigma}$. Here, the spin polarization $\hat{\sigma}$ is taken to be $\hat{\mathbf{y}}$.

among the three is the geometry between the spin polarization $\hat{\sigma}$ and the equilibrium magnetization $\mathbf{m}$ direction [52]. In figure 2.2, the three-different type of SOT switching are shown. The most common and well-studied scenario is the type-z where the magnetization with out-of-plane anisotropy is switched by the in-plane $\hat{y}$ spin polarization with a small symmetry breaking field in the $\hat{x}$-direction. The second commonly studies scheme is the type-y since this is the configuration for SOT switching of in-plane MTJs. This is similar to the case of STT switching in a perpendicularly magnetized MTJ since the spin polarization and the magnetic anisotopry shares the same axis. As a result, there is an initial incubation process (Fig. 2.1b lower subplot) where thermal fluctuation is necessary for the full magnetic switching. With these few common SOT switching scenarios, we can focus on torque symmetries with magnetization in the xz plane for type-x and magnetization in xy plane for type-y during the initial switching period of the full switching process. This simplifies ones consideration on the critical SOT torque symmetries.

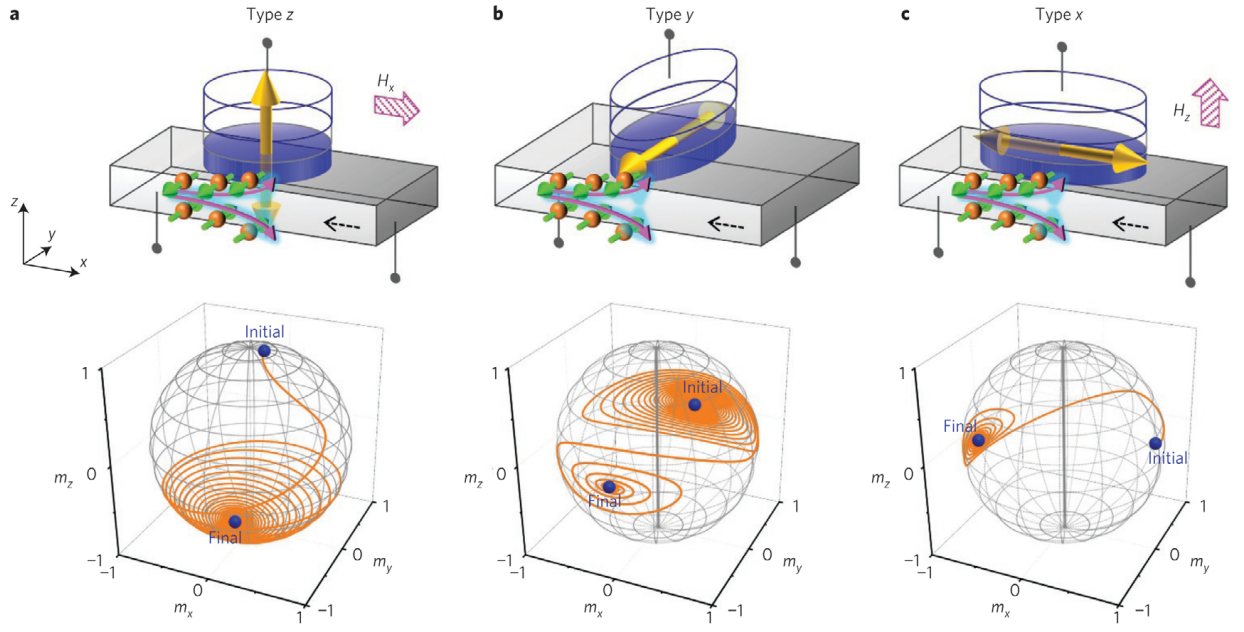

Figure 2.2: Three different type of SOT switching scenario driven by the spin current in the $\hat{z}$ direction with fixed $\hat{y}$ spin polarization. Graph adapted from *Nature Nanotechnology* [52].

Spin diffusion, injection and interface transparency

In the previous subsection, I described how the different torque geometries arise under the presence of a non-zero spin current with spin polarization $\hat{\sigma}$. The torque geometries primarily describe how the magnetization is modulated by the spin current and the resulting magnetization dynamics can be modeled by the LLG equation. Here in this subsection, I briefly discuss how spin current travels from the source and diffuses across a finite distance and arrives at the magnet to be switched or acting as the torque sensing layer. This process is called the spin diffusion and is usually discussed in the sub-100 nm length scale for spin-orbit torque devices and spin-orbit torque measurements.

In a typical nonmagnetic metal / ferromagnet bilayer system, the spin current arises due to spin Hall effect in the bulk of the nonmagnetic (or paramagnetic) metal layer such as Pt[111, 126] W[147], Ta[112]. The spin current diffuses across the Pt layer in the transverse direction and injects into the ferromagnet. Once the spin current enters the ferromagnet, it dephases in a few angstroms as the angular momentum transfers to the magnetization and the spin current should vanish. As a result, there should be a finite spin diffusion length associated with the material to describe this decaying spin current and spin relaxation. On the other hand, while spin-orbit coupling (SOC) is crucial for spin Hall effect, anomalous Hall effect and other spin current generating effects, SOC is also a crucial factor in spin relaxation or spin-dependent scattering events. As a result, to fully capture the spin-orbit torque

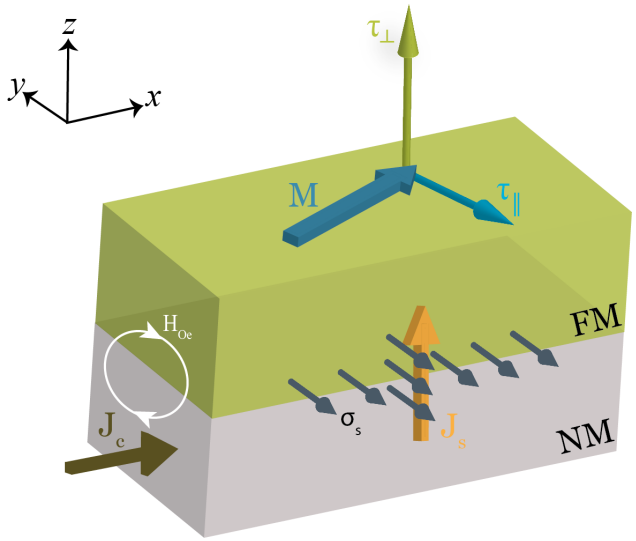

Figure 2.3: Schematic of a typical bilayer structure for studying spin-orbit torque of different materials. The NM (non-magnetic) layer is the material of interest for spin current/spin accumulation generation and the FM (ferromagnetic) layer is the spin detection layer or the magnetic layer to be modulated by spin-orbit torque. For some studies, there will be an insertion layer between the FM and NM layers for enhancing the spin transparency or due to other mechanisms.

generation and detection in different materials and devices, spin diffusion is an important component to be addressed.

A general rule when thinking about spin diffusion from a material perspective is that the greater the spin-orbit coupling the faster the spin current decays. As a result, heavy metals such as Pt, Pd, Ta are good sources for generating spin current but not for spin diffusion. On the other hand, lighter metals such as Al, and Cu [190, 123] are a better spin carrying material with spin diffusion length on the order of a few hundred nm. As a result, a very useful and important experiment to studying new spin-orbit torque material is the thickness dependence experiment.

In a thickness dependence experiment, the thickness of the spin current generating material (SCG) is varied with the ferromagnet thickness being fixed. The ferromagnet is in direct contact with the spin current generating material in a bi-layer structure. As the SCG layer varies, the amount of spin current that arrives at the FM varies due to spin diffusion length [110]. By following the drift-diffusion model [191, 111, 196, 62], the thickness dependence of the measured spin-torque efficiency can be described by,

$$\xi_{ST} = \xi_{ST,\infty}(1 - sech(t_{NM}/\lambda_s)) + C \tag{2.4}$$

where ξ_{ST} is the spin-torque efficiency, $\xi_{ST,\infty}$ is the spin-torque efficiency assuming an ideal

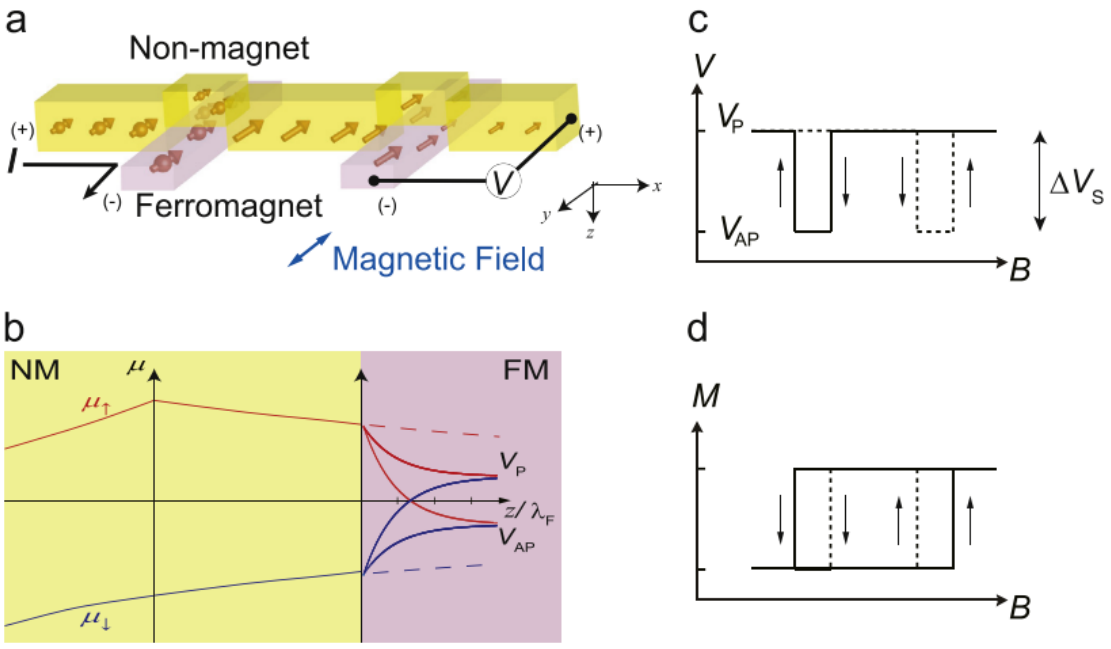

Figure 2.4: Schematic of a non-local spin injection via a non-local spin valve structure. Graph adapted from [80].

spin transparent NM/FM interface and infinite diffusion length, t_{NM} is the thickness of the SCG layer, λ_s is the spin diffusion length of the SCG layer/material and C is the contribution from the interfacial mechanisms such as interfacial Rashba. Although this is a very common theory on spin diffusion and spin-torque generation in materials as a function of thickness, the true manifestation of different contributions such as bulk versus interfacial remains unclear as there is no experimental method that can cleanly discern the two contributions. In other words, having a good functional fit to equation 2.4 does not guarantee a strong bulk origin and a large C value does not guarantee a large interfacial origin. The debate and challenge to discern interfacial and bulk contributions in spin-orbit torque studies remain a difficult challenge. Equation 2.4 serves as a guide to quickly evaluate the thickness dependence of the SOT and the extracted values such as λ_s and C should be taken with cautious or with a further check via other techniques such as spin-pumping.

Here, I will briefly mention two methods for experimentally studying spin diffusion length. The first method is the non-local spin injection through a non-local spin valve structure (figure 2.4) [80]. The first ferromagnet serve as a spin injector and the spins accumulate and diffuse across the non-magnetic metal and arrive at the second ferromagnet serving as the spin detector. By switching the magnetic field to change the magnetization configuration between the injector and detector ferromagnetic layer, a difference in voltage (spin voltage) can be measured due to the GMR effect. From the spin voltage difference, the spin diffusion length

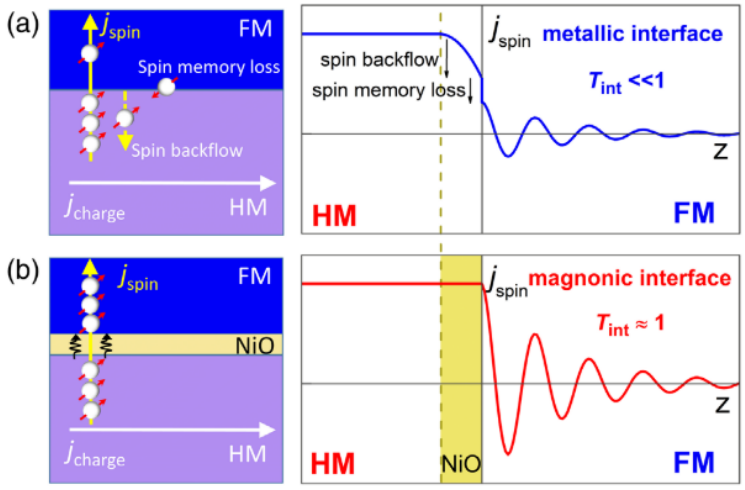

Figure 2.5: Spin transmission across the (a) NM/FM interface and (b) NM/NiO/FM interface. Graph adapted from *Physical Review Letters* [225].

can be extracted. The second method is through spin-pumping [85, 188]. In spin-pumping, a bi-layer of NM/FM is utilized as the spin-orbit torque measurements. By driving the FM layer into ferromagnetic resonance via microwave magnetic field, coherent precession of the magnetization can pump pure spin current into the adjacent non-magnetic layer. Through inverse spin Hall effect, the injected spin current can be converted into electrical voltage and be detected easily. As a result, heavy metals such as platinum is a common detection material for studying spin diffusion of other materials. By varying the non-magnetic layer thickness, we can extract the spin diffusion length.

At last, I will briefly introduce the concept of spin transparency and its importance in studying spin-orbit torque. In a NM/FM bilayer, spin current/accumulation is generated either in the bulk, interface or both. As the spin diffuses and inject into the FM layer, not all spins can be transmitted through the interface. There exist a few mechanisms that can hamper the efficiency of spin transmission across the NM/FM interface including spin-memory loss (SML) and spin back flow (SBF) [145, 225]. The spin back flow can be understood with the effective spin-mixing conductance of the interface $G_{eff}^{\uparrow\downarrow}$ [220]:

$$G_{eff}^{\uparrow\downarrow} = \frac{G_{NM/FM}^{\uparrow\downarrow}}{1 + 2G_{NM-FM}^{\uparrow\downarrow}/G_{NM}} \tag{2.5}$$

where $G_{NM/FM}^{\uparrow\downarrow}$ is the bare interfacial spin-mixing conductance, $G_{NM} = 1/\lambda_s \rho_{xx}$, λ_s is the spin-diffusion length of the NM, ρ_s is the longitudinal resistivity of NM. According to the

drift-diffusion analysis [33, 220], the spin transmission coefficient can be written as:

$$T = \frac{2G_{eff}^{\uparrow\downarrow}}{G_{NM}} \tag{2.6}$$

only at the condition that the thickness of the NM (t_{NM}) is much larger than the spin diffusion length λ_s and the interfacial spin-orbit coupling is negligiable [220].

As one can see, to determine the spin transmission coefficient (T), it is crucial to determine the effective spin-mixing conductance ($G_{eff}^{\uparrow\downarrow}$. To determine $G_{eff}^{\uparrow\downarrow}$), a common experimental method is to measure the effective damping constant of the system under study. For example, if the system under study is Pt/Co, the whole stack will be the system for its damping constant to be measured. The measured damping constant can be written as[220, 11]:

$$\alpha = \alpha_{int} + G_{eff}^{\uparrow\downarrow}\frac{g\mu_B h}{4\pi M_s e^2 t_{FM}} \tag{2.7}$$

where g is the gyromagnetic ratio, μ_B is the Bohr magnetron, M_s is the saturation magnetization of the FM layer, α_{int} is the intrinsic damping constant of the FM, and h is the Planck's constant. This model (equation 2.7) works well with most of the magnetic heterostructures. However, Zhu *et al.* [220, 226] argues that two-magnon scattering is also an important contribution to the measured effective damping constant when: 1) rough NM/FM interface or 2) strong interfacial spin-orbit coupling (such as strong perpendicular magnetic anisotropy at the Pt/Co interface). In this case, the measured effective damping constant will be,

$$\alpha = \alpha_{int} + G_{eff}^{\uparrow\downarrow}\frac{\gamma\hbar^2}{(2M_s t_{FM} e^2)} + \frac{\beta_{TMS}}{t_{FM}^2} \tag{2.8}$$

where β_{TMS} is the two-magnon scattering coefficient.

In figure 2.5, a paramagnetic NiO layer is inserted between Pt and Co which boosted the interface spin transparency to nearly unity [225]. As a result, a large spin-torque efficiency is measured which is very close to the theoretical intrinsic spin Hall angle of Pt [225]. Boosting spin transparency for stronger spin-orbit torque is an active field of research within the spintronics community.

2.2 Material systems and mechanisms

Heavy metals and spin Hall effect

Heavy metals were the first material system to show strong spin-orbit torque especially in Pt [126, 111], Ta [112] and W [147]. The first demonstrated full magnetic switching via spin-orbit torque was done in Pt/Co/AlO_x with perpendicular magnetic anisotropy [126]. Although the paper mainly attributed the origin to the inversion symmetry breaking of the interface and the structure with Rashba effects, others argue that spin Hall effect is a stronger

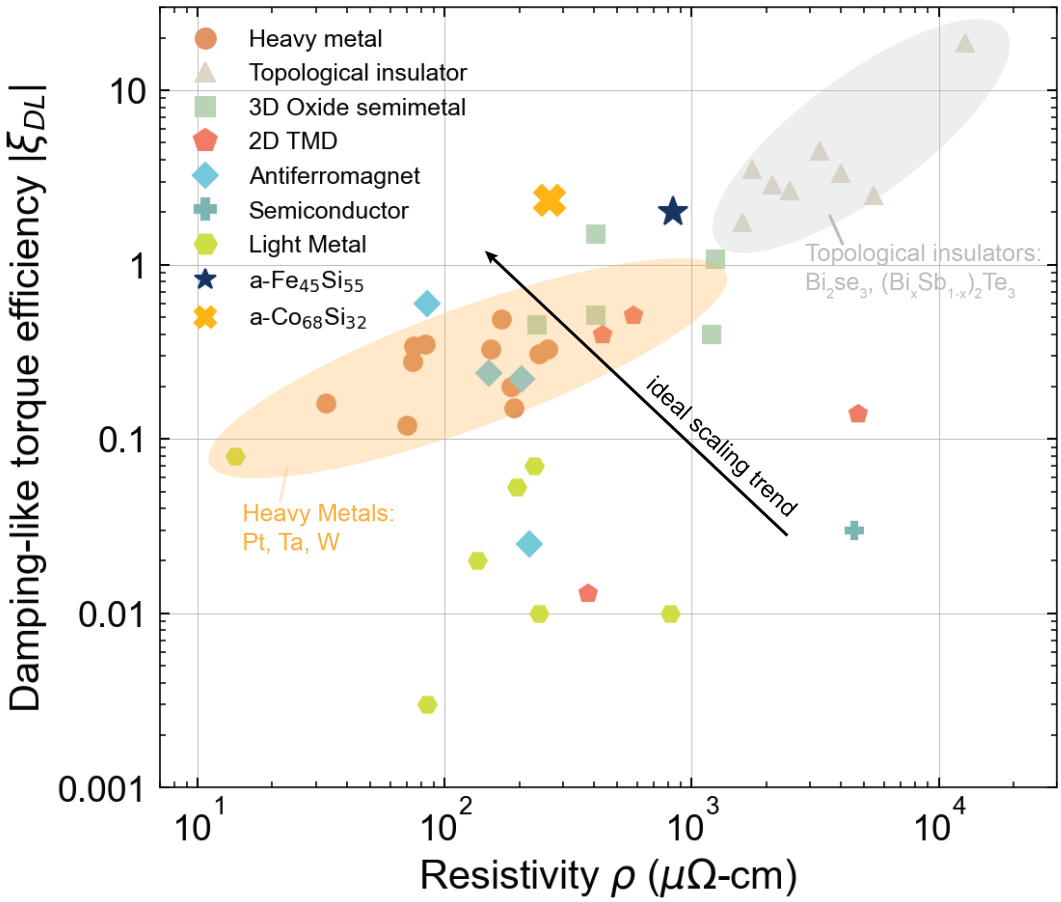

Figure 2.6: Benchmark of spin-torque efficiency ξ_{DL} as a function of resistivity (ρ) in known systems to demonstrate SOT.

contribution to the observed spin-orbit torque and the spin-torque efficiency (then spin Hall angle) is characterized to be around 5∼10 % without further engineering of the interface [111, 112, 110]. Overtime, spin-orbit torque was discovered in Ta (15∼20 %) [112, 95, 55], W (30 ∼ 35 %) [147, 4], Au_xPt_{100-x} [223], rare-earth elements [160], W-Hf alloy [51] and 5d transition metal-Al alloys [194].

Spin Hall effect was attributed as the main mechanism of spin current generation in heavy metals especially in Pt, Ta and W where Pt is widely adopted in many spintronics device research. The phenomenological picture of spin Hall effect is depicted in figure 2.6 where a laterally injected charge current is converted into two spin currents flowing in the transverse opposite directions and each equipped with opposite spin polarization directions that are also transverse to both the charge and spin current direction. Spin Hall effect can be

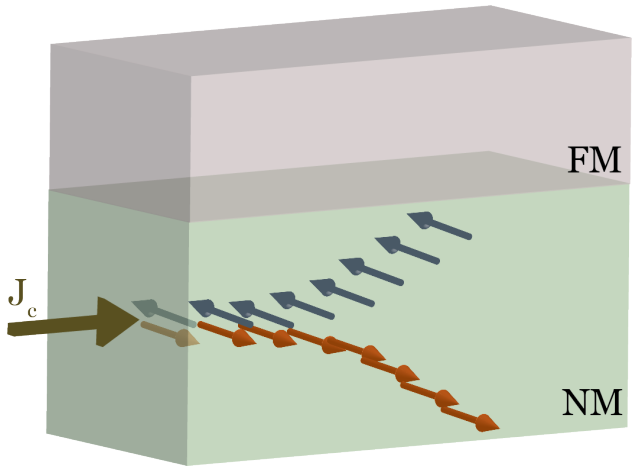

Figure 2.7: Schematic of spin Hall effect. Spin current with opposite spin polarization directions diffuse in the transverse direction to the charge current.

attributed to either the intrinsic origin or extrinsic origins that shares many similarities with anomalous Hall effect in ferromagnets. The intrinsic origin is the non-zero Berry curvature that arise from the bulk band structure of the material [202, 172]. The extrinsic origin includes side-jump and skew-scattering [172, 71]. While most heavy metals are deposited through sputtering which leads to polycrystalline structures, the finite grains structures in single element metallic film possess intrinsic contributions. For studying extrinsic scattering mechanisms, heavy elements embedded in light element metals are the main systems [154, 227].

Rashba-Edelstein effect and Rashba interface

Rashba-Edelstein effect, also known as inverse spin galvanic effect, is an effect based on Rashba spin-orbit coupling (an ubiquitous physics that is not associated with any particular materials system or structure but possess odd-in-p characteristics) [157] which an electron traveling through a constant electric field in the perpendicular direction will experience a Rashba effective field that is perpendicular to both the electric field and electron's moving directions (figure 2.8). This Rashba field can align the electron spin and create a non-zero spin density that can either diffuse into the adjacent ferromagnet or exert a torque on the magnetization via exchange interaction [118]. If we take the electron to be traveling toward the $\hat{x}$-direction and experiencing an electric field in the $\hat{z}$-direction, the Rashba field B_{Ry} will be in the $\hat{y}$-direction and can be written as

$$B_{Ry} = 2\alpha_R k_F / g\mu_B \tag{2.9}$$

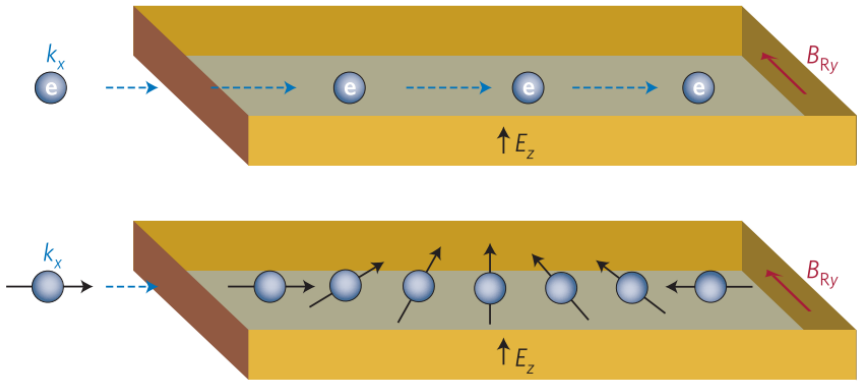

Figure 2.8: Schematic of the Rashba-Edelstein effect and the influence on a traveling electron and its spin. Graph adapted from *Nature Materials* [118].

where α_R is the Rashba parameter, k_F is the wave vector, g is the gyromagnetic ratio, and μ_B is the Bohr magnetron. As the current is applied (e.g. in $\hat{x}$), the Fermi contour of the Rashba interface shifts (in $\hat{x}$) in the direction of the current, resulting in a unbalanced spin population in the transverse direction ($\hat{y}$-spins) (figure 2.9). This spin momentum locking effect is a signature of Rashba spin-orbit coupling effect that requires inversion symmetry breaking and spin-orbit coupling.

This basically shows that at any interface with broken inversion symmetry, a non-zero electric field can generate a net spin density/accumulation or any system with broken inversion symmetry in the bulk lattice can induce a non-zero spin density. Since most material heterostructures in studying spin-orbit torque require at least a bi-layer NM/FM structure, it is challenging to discern the relative strengths of the bulk spin Hall effect and the interfacial Rashba-Edelstein effect.

Semiconductors and bulk Rashba crystals

Rashba spin-orbit coupling does not only apply to broken inversion symmetry at interfaces but actually it applies to any system with broken inversion symmetry of any forms. In semiconductors with non-centrosymmetric structures such as the zinc-blende or wurtzite semiconductors - GaAs, ZnTe, inversion symmetry is broken at the unit cell level inducing a bulk Rashba spin-orbit coupling. Rashba [157] and Dresselhaus [42] were the first to found that in these wurtzite semiconductors with structural inversion asymmetry, bulk spin-orbit coupling is odd in electron momentum p. This odd in p characteristic only survives in system with broken inversion symmetry and is unique on top of the normal spin-orbit coupling as I will show below.

Similar to a traveling electron in a magnetic field will experience a Lorentz force, a

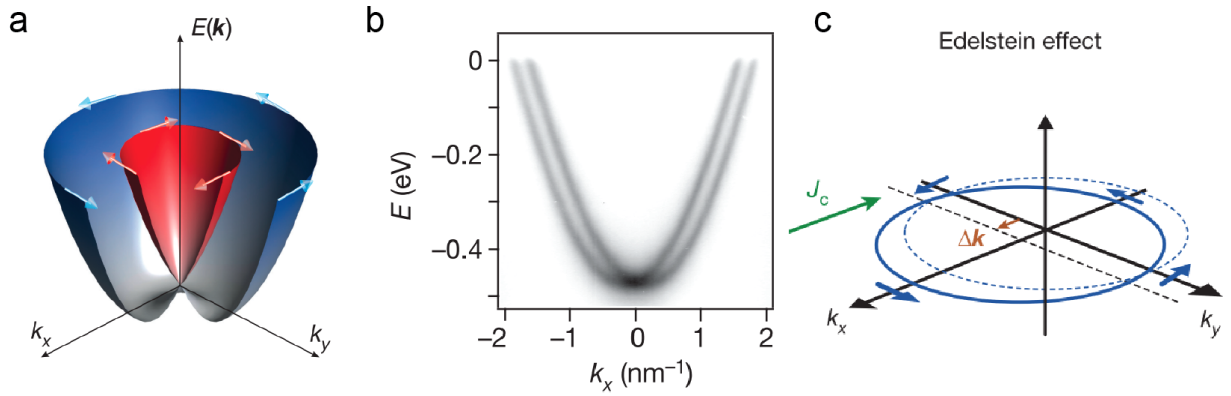

Figure 2.9: Schematic of the spin-momentum locking at a Rashba interface. a, a Rashba band splitting due to inversion symmetry breaking. b, a measured Rashba band at Au (111) surface via angle-resolved photoemission spectroscopy (ARPES). c, the unbalanced population of spins in the Rashba Fermi contour due to the charge current. Graph adapted from *Nature* [178].

traveling electron in an electric field $\boldsymbol{E}$ will experience an effective magnetic field $\boldsymbol{B}$,

$$\boldsymbol{B} \sim \boldsymbol{E} \times p/mc^2 \tag{2.10}$$

where c is the speed of light and m is the electron mass, due to relativistic effects. This field due to the spin-orbit coupling also introduces a energy associated with the momentum of the electron that takes the form of a Zeeman energy Hamiltonian

$$\hat{H}_{SO} \sim \mu_B(\boldsymbol{E} \times p) \cdot \frac{\sigma}{mc^2} \tag{2.11}$$

where σ is the Pauli spin matrices and μ_B is the Bohr magnetron. In crystals, with crystal field $\boldsymbol{E}$=$-\nabla V$, the spin-orbit field becomes

$$\boldsymbol{B}_{SO}(\mathbf{p}) = -\mu_B(\nabla V \times \mathbf{p})/mc^2 \tag{2.12}$$

and since time-reversal symmetry is preserved for spin-orbit coupling,

$$\boldsymbol{B}_{SO}(\mathbf{p}) \cdot \sigma = -\boldsymbol{B}_{SO}(-\mathbf{p}) \cdot \sigma \tag{2.13}$$

, the spin-orbit coupling effective field $\boldsymbol{B}_{SO}$ must be odd in electron momentum p

$$\boldsymbol{B}_{SO}(\mathbf{p}) = -\boldsymbol{B}_{SO}(-\mathbf{p}). \tag{2.14}$$

This snippet of derivation was done with the help of Manchon *et al.* [118].

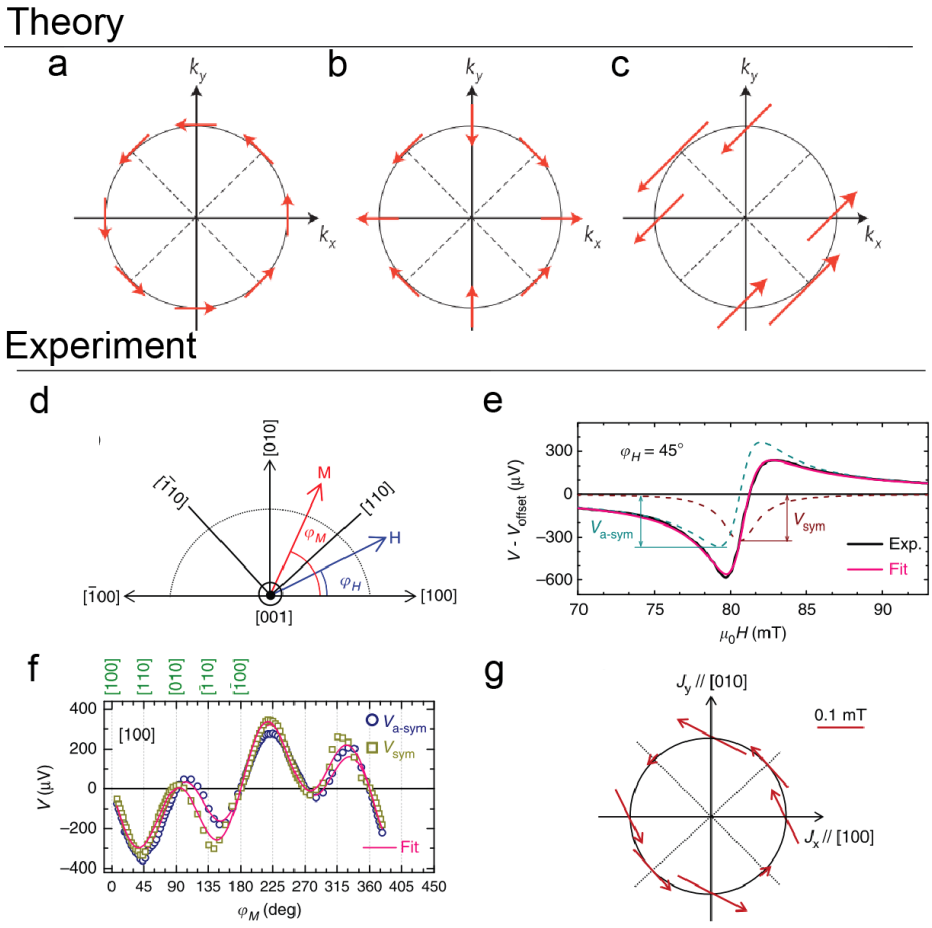

Figure 2.10: (a) Spin-orbit field symmetry from Rashba spin-orbit coupling. (b) Spin-orbit field symmetry from Dresselhaus spin-orbit coupling with strain in the (001) direction (c) the combination of the two types of spin-orbit coupling. (d-f) schematics and representative result of spin-orbit torque characterization with current along the [100] crystal direction and full angle field scan. (g) Experimental result of the measured spin-orbit field symmetry as a function of different current injection direction. Graph adapted from *Nature Materials* [118] and *Nature Communications* [29].

As a result, with inversion symmetry breaking and spin-orbit coupling, odd-in-p spin-orbit coupling field can induce many interesting spin polarization symmetries by injecting current along different symmetry directions in any crystal that lacks bulk inversion symmetry. Here, I will show GaAs as a model system to create spin currents with diverse spin polarization directions [29].

In Chen *et al.*, spin-orbit torque was studied with applying the current along different crystal symmetries that follows the Rashba and Dresselhaus spin-orbit fields. When linear k is small near the Γ point, the Hamiltonian associated with the Rashba spin-orbit coupling [17] can be written as

$$\hat{H}_R = \alpha_R(\sigma_x k_y - \sigma_y k_x) \tag{2.15}$$

where α_R is the Rashba parameter that characterizes the spin-orbit coupling strength. The Hamiltonian associated with the Dresselhaus spin-orbit coupling [42, 118, 29] can be written as

$$\hat{H}_D = \beta_D(\sigma_x k_x - \sigma_y k_y) \tag{2.16}$$

where σ_D is the Dresselhaus parameter that characterizes the spin-orbit coupling strength. The respective resulting spin-orbit field symmetries are shown in figure 2.10a and b. By applying current along the different symmetry directions, the resulting spin-orbit fields manifested as the spin polarization directions of the spin current can be mapped out (Figure 2.10 d-i). We can see that the characterized in-plane spin-orbit field in GaAs/Fe (figure 2.10h) highly resembles the case of the combination of Rashba and Dresselhaus spin-orbit coupling in theory (Figure 2.10c). While the spin symmetry is zinc-blende semiconductor is rich and interesting, the measured spin-orbit torque is not as strong as the heavy metal system with the measured SOT efficiency to be around 3 % [29]. This might due to the semiconducting nature which does not conduct a large amount of current to start with since spin-orbit torque is a current effect.

Topological insulators, spin-momentum locking surface states and Berry Curvature

Topological insulators possess topologically protected spin-momentum locking surface conducting states that can generate efficient spin currents and spin accumulations at the interface. To this date, topological insulator is the material system that exhibits the largest spin-torque efficiency with numbers between 200 % and 1600% [124, 39, 197, 92, 31, 148, 167, 201] depending on the specific topological insulator/ferromagnet heterostructure and the crystallinity of the sample under study.

While the spin-momentum locking surface state is the main factor for such high spin-torque efficiency, this property is very similar to Rashba interfaces and bulk Rashba crystals. In fact, a much general depiction can be adopted to explain the Bandstructure origin in terms of Berry curvature. Berry curvature is the effective field that produces the equivalent Lorentz force on a traveling electron that along with spin-orbit coupling, a transverse spin current

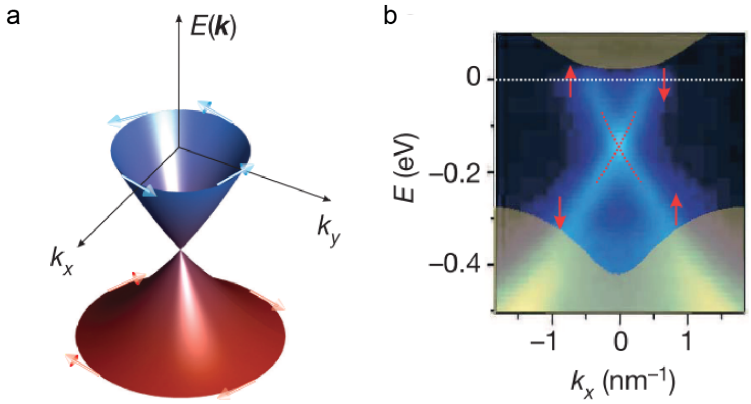

Figure 2.11: (a) Spin-momentum locking surface conducting states with linear band crossing in topological insulators (b) ARPES result on $Bi_{2-x}Ca_xSe_3$. Graph adapted from *Nature* [178].

can be produced. In a crystalline material with a well-defined band structure, we can calculate the spin Hall conductivity (σ^z) through the Kubo formula which the Berry Curvature contributes greatly to the spin Hall conductivity in the k-space[60]. The expressions for the Berry curvature ($\Omega^{\mathbf{k}}$) and the Kubo Formula for spin Hall conductivity (σ^z_{xy}) are [60]:

$$\Omega^z_n(\mathbf{k}) = \sum_{n' \neq n} \frac{2Im[\langle \mathbf{k}n|j^z_x|\mathbf{k}n'\rangle\langle \mathbf{k}n'|v_y|\mathbf{k}n\rangle]}{(\epsilon_{\mathbf{k}n} - \epsilon_{\mathbf{k}n'})^2} \tag{2.17}$$

$$\sigma^z_{xy} = \frac{e}{\hbar}\sum_{\mathbf{k}} \Omega^z(\mathbf{k}) = \frac{e}{\hbar}\sum_{\mathbf{k}}\sum_{n} f_{\mathbf{k}n}\Omega^z_n(\mathbf{k}) \tag{2.18}$$

where $j^z_x = \frac{1}{2}\{s_z, v\}$ is the spin current operator with $s_z = \frac{\hbar}{2}\beta\sum_z$ and $f_{\mathbf{k}n}$ is the Fermi distribution function for the nth band at $\mathbf{k}$. $\Omega^{\mathbf{k}}_n$ is the Berry curvature for the nth band [60]. From expression (1), we can immediately know that a large Berry curvature ($\Omega^{\mathbf{k}}$) can be obtained with near degenerate energy states from the denominator of the expression and large spin-orbit matrix elements in the numerator. In topological insulators, linear band crossing at the Fermi level with spin-orbit coupling is a great representation of near degenerate energy bands and with inversion symmetry breaking providing spin-orbit coupling, a large spin current can be generated.

Although large spin-torque efficiency can be obtained in topological insulators (¿ 200 %), the large resistivity hampers a low critical current density for magnetization switching. This is an issue as more spin-orbit torque materials are discovered. Empirically, high spin-torque efficiency is coupled with high resistivity across the heavy metal, antiferromagnet, and topological insulators (figure 2.6). This is not ideal since achieving low critical switching current density for magnetization switching requires a low resistivity as well. The quest for

higher spin-torque efficiency (ξ_{ST}) is not the only goal but instead achieving high spin-torque efficiency at low resistivity is the desired direction for lowering the critical current density for magnetization switching (figure 2.6 black arrow).

Another very important research field within the topological physics and Berry physics is the origin of such properties and signatures in a fully amorphous material. Led by professor Hellman's group here at Berkeley, topological surface states characterized through ARPES has been observed in a fully amorphous bismuth selenide [37] film and also disorder can drive a topological trivial insulator into a non-trivial topological insulator [36]. In addition, both experimental and theoretical signature of Berry density or Berry curvature have been extensively explored and shown to be appreciable in fully amorphous materials as well [14, 86, 88, 89].

Complex semi-metallic oxides

Following the discussion in the previous subsection, Berry curvature emerges as a design principle for bandstructure engineering of large spin current in crystalline materials. As a result, quantum materials based on complex oxides naturally emerge as a candidate to **1)** engineer large Berry curvature via different oxide crystalline structures, **2)** engineer exotic band symmetries to generate spin current with unconventional spin polarization directions, and **3)** engineer atomically precise defect-free epitaxial interface between the spin current generation layer and the ferromagnet.

The model system for complex oxide was strontium iridate perovskite and pyrochlore where Nan *et al.* [130], Wang *et al.* [193], and Everhardt *et al.* [46] showed a strong torque around 50$\sim$ 100 % SOT efficiency but with sputtered transition metal ferromagnets. Nan *et al.* [130] further showed that the SOT efficiency can be tuned by the orthorombicity of the crystal structure. Shortly after, all-oxide heterostructures that leverage the defect free interface were demonstrated in $SrRuO_3/SrIrO_3$ [109] and $LSMO/SrIrO_3$ [77]. Liu *et al.* [109] showed by controlling the magnetocrystalline anisotopry in $SrRuO_3$, field-free magnetization switching can be achieved in a all-oxide device. Huang *et al.* [77] further demonstrated that a defect-free epitaxial interface between $LSMO/SrIrO_3$ can generate a very large torque over 100 % efficiency. At last, Bose *et al.* [13] showed that following the design principle of Berry curvature through bandstructure engineering in nodal line semimetallic IrO_2, one can tune both the relative strength between FL-torque and DL-torque as well as the strength of the spin-orbit torque and conductivity.

Overall, complex semi-metallic oxides provides a strong torque efficiency in the range of 50% to 110 % with a resistivity value below 1000 $\mu\Omega$-cm. This can provide a well-balanced SOT efficiency and resistivity but more or less still falls on the conventional trend empirically driven by heavy metal and topological insulators (figure 2.6). As a result, a material system that exhibits a drastically different SOT efficiency and resistivity away from the conventional trend is necessary. However, there are still many complex oxides to be explored especially the potential to exhibit z-spin polarization spin current and large torque

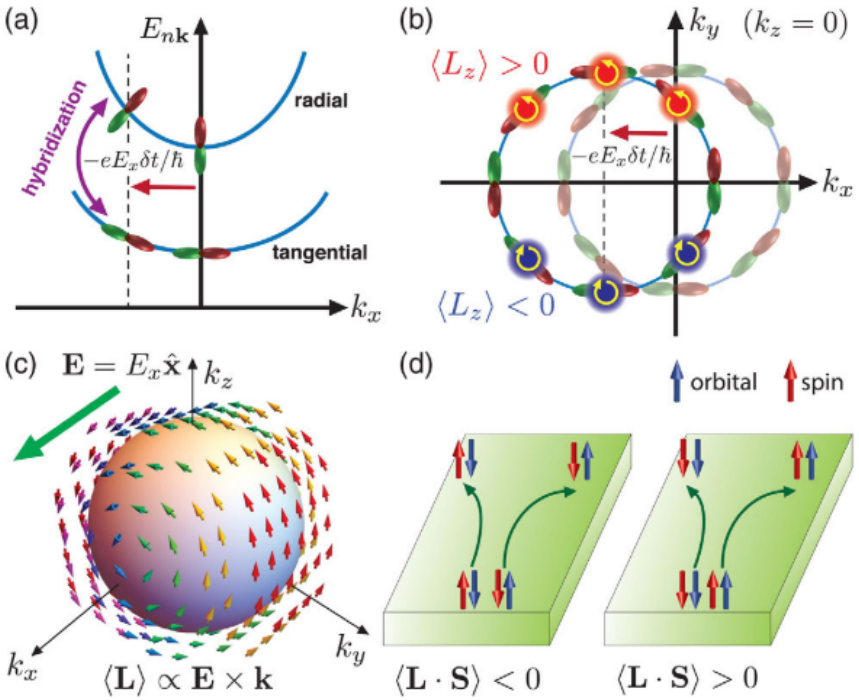

Figure 2.12: (a)(b) Schematic of intrinsic orbital Hall effect from orbital texture. (c) Orbital angular momentum **L** is induced in the E x k direction. (d) With spin-orbit coupling, the geometry of spin Hall effect and orbital Hall effect may be the same or opposite depending on the correlation $\langle \mathbf{L} \cdot \mathbf{S} \rangle$ between **L** (orbital angular momentum) and **S** (spin angular momentum) Graph adapted from *Physical Review Letters* [57].

efficiency by engineering the symmetries in the band structure via strain, crystal structures and different all-oxide heterostructures.

Light elements and orbital effects

According to the conventional wisdom, light elements are not expected to exhibit any spin-orbit torque as the atomistic spin-orbit coupling is weak. Nevertheless, a variety of light element materials have exhibit measureable spin-orbit torque albeit weak ($\xi_{SOT} < 10\%$). While the SOT efficiency is weak, magnetization switching driven by SOT is still achievable [30, 217, 35]. In addition, an emerging theory of understanding spin current generation in light element or light element interface is actively developing - orbital contributions to induce torques on magnetization [57, 56, 103, 64, 34]. The light element materials include Ti (1∼2 %) [45, 64, 34] , Cr (1∼8 %) [199, 35], Zr (∼ 3 %) [217], V (∼ 7 %) [195], Cu (∼ 1 %) [5], Mo (0.3 %) [30], Al_2O_3 interface [96] and more.

The theoretical idea of orbital torque on magnetization was pioneered by Go *et al.* [56], with the origin from the orbital Hall effect [99, 183]. The phenomenological description of orbital Hall effect is the generation of orbital angular momentum in the electrons in response to a transverse charge current or electric field (figure 2.12). It is the analog version of spin Hall effect but instead the electron's orbital moments/angular momentum is polarized rather than its spin. This is more prominent in light element materials or materials with strong orbital hybridization among the p-orbitals [57]. In earlier literature, it was predicted that strong orbital Hall effect originates from the amount of orbital Aharonov–Bohm (AB) phase factor the d-electron acquires as it moves from one orbital to the next (s-d hybridization)[100]. It was also predicted that spin Hall conductivity is approximately the product of orbital Hall conductivity and spin-orbit polarization due to spin-orbit coupling. As a result, Go *et al.* [57, 56] showed that for orbital torque to arise, orbital current can be converted into spin current via spin-orbit coupling in the ferromagnet or at the interface of NM/FM and exert a torque on the magnetization. While there are many theoretical work done recently toward the orbital contribution to spin-orbital torque, the experimental technique remains unclear to cleanly discern orbital torque from spin torque. Another aspect worth mentioning is that torque efficiency arising from orbital contributions remains weak (10∼15 %) [96] as compared to spin-torque in topological insulators > 200%.

Antiferromagnet and the effect of antiferromagnetic ordering

Antiferromagnets (AFM) have several advantages when it comes to spintronics application including lack of stray fields, high magnetic resonance frequency (THz range), versatile manipulation and coupling to rich magnetic ordering. Antiferromagnet has not been an active component in spintronics until the discovery of spin current generation in AFM/FM bilayers that kicked off the research in manipulating magnetic texture through antiferromagnets especially the Cu-Au-I type AFM such as $X_{50}Mn_{50}$ (X=Pt, Ir, Fe, Pd) [215, 214, 53, 144].

The Cu-Au-I type AFM exhibits a spin-torque efficiency in the range of 8 % ∼ 24 %[189, 214, 144] for polycrystalline samples and up to 60 % in epitaxial IrMn [219]. The origin of spin current generation in AFM can be attributed to two main categories: **1)** spin-orbit coupling driven effects or **2)** antiferromagnetic ordering. From this experimental results, it seems like both categories contributed to the spin current generation with spin-orbit coupling driven effects being the dominant one and the AFM ordering at the interface enhanced the SOT efficiency by a constant amount across all the different Mn-based AFM alloys. From multiple studies [215, 214, 144] the strength of spin current generation and spin-torque efficiency characterized through both spin-pumping and spin-torque ferromagnetic resonance shows such order PtMn > IrMn > PdMn > FeMn. This matches the order of spin-torque efficiency in the heavy metal systems: Pt > Ir > Pd. The much larger SOT efficiency in these AFM shows the enhancement due to the AFM ordering on top the varying spin Hall effect contributed by the heavy element. Another Cu insertion experiment done by Tshitoyan *et al.* [189] shows that in IrMn/Cu/FM exhibits a SOT efficiency of 5.6 % while IrMn/FM exhibits 22 %. This further indicates that the AFM/FM ordering at the surface is crucial to

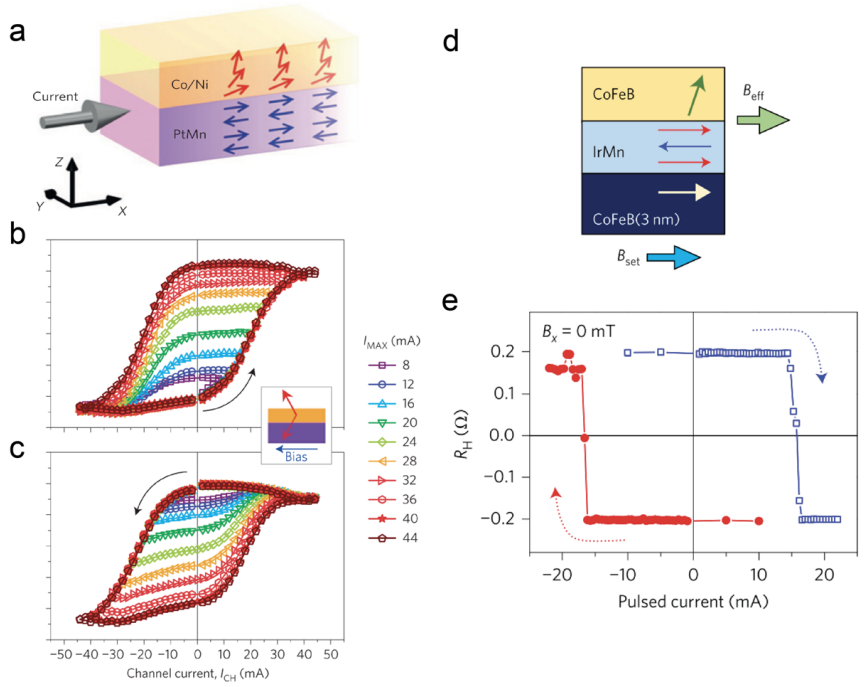

Figure 2.13: (a) Schematic of exchange bias in PtMn/[Co/Ni]. (b)(c) Field-free SOT switching and memristor effect. (d) Stack design for field-free SOT switching in IrMn/CoFeB. (e) Field-free switching in IrMn/CoFeB. Graph adapted from *Nature Materials* [53] and *Nature Nanotechnology* [141].

enhance the overall SOT efficiency and spin Hall effect survives even with a thin $1 \sim 2$ nm insertion.

In addition to the enhancement of SOT efficiency due to the interface AFM/FM ordering effects, exchange bias effect due to the pinned interfacial moments is useful in achieving field-free spin-orbit torque deterministic switching (figure 2.13) [53, 141]. Exchange bias effect exists in system where AFM is in direct contact with FM. At the AFM/FM interface, individual AFM moments try to align with the FM moments while balancing the AFM coupling with the moments underneath the interface, resulting in a thin pinned layer of AFM moments. These pinned moments can act as a in-plane field during magnetization reversal of the FM moments thus a symmetry breaking field is no longer required during SOT switching.

At last, another class of AFM that possess non-collinear AFM ordering can go one step further in providing strong AFM ordering-dependent SOT that shows rich torque symmetry [216, 131]. Noncollinear AFM has exhibit strong anomalous Hall effect due to the large momentum-dependant spin-splitting driven by the non-collinear magnetic ordering [98]. This is similar to the bulk Rashba type spin-orbit coupling but instead of dominantly driven by

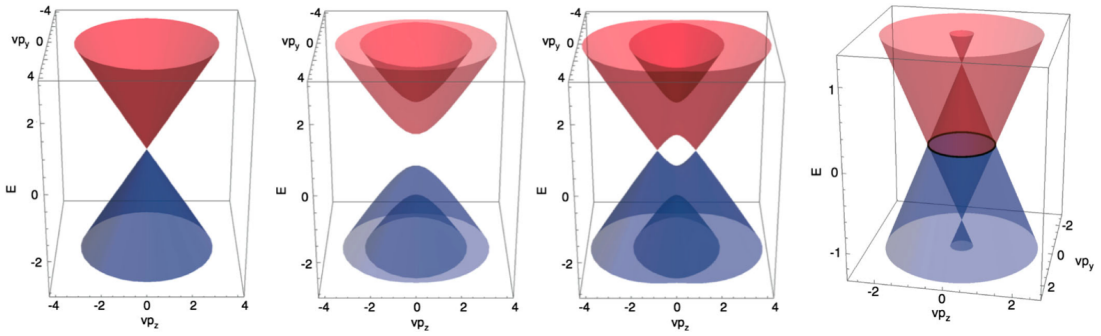

Figure 2.14: Different bandstructure topologies with left to right being: Dirac semimetal, magnetic semiconductor, Weyl semimetal and line node semimetal. Graph adapted from *Reviews of Modern Physics* [7].

crystal field, here, it is driven by the noncollinear magnetic ordering resulting in a non-zero polarizing field. Evidence of AFM ordering driven mechanism include the crystal symmetry dependent SOT strength in $IrMn_3$[216] and Mn_3GaN [131]. In Mn_3GaN, appreciable damping-like torques in $\hat{x}$-direction and $\hat{z}$-direction were observed. This indicates a different way of engineering unconventional spin-orbit torque symmetries through noncollinear AFM ordering and inducing field-free SOT switching through $\hat{z}$-spins instead of the exchange bias effect.

Overall, AFM is a very versatile and strong spin current generating material with a relatively low resistivity. In epitaxial IrMn [219], the large SOT efficiency (60 %) couple with low resistivity ($< 100\mu\Omega - cm$) is one of the highest spin Hall conductivity (σ_s) materials beating Pt (figure 2.15).

Two-dimensional materials and low-symmetry crystalline effects

Two-dimensional materials span across a wide range of rich physical properties including topological semi-metallic physics, and low-symmetry crystalline structure that can exhibit exotic torque symmetries. Along with the rise of two-dimensional (anti)ferromagnets and Moire superlattice-based physics, abundant phenomena and physical properties can be explored in 2D material spintronics.

The emphasis of 2D material in the context of spin-orbit torque research has been the transitional metal dichalcogenide (TMD) especially the Weyl semimetal WTe_2 [169, 106, 115]. Other TMDs such as MoS_2 shows a weak spin-torque efficiency of 2 % [168] and the origin of such SOT is attributed to intarfacial Rashba-Edelstein effect. On the other hand, strong SOT efficiency was found in thick WTe_2 [169] with values up to 51 % with a strong bulk contribution and long spin diffusion length, which exhibits signatures of bulk band topology. Weyl and Dirac semimetal possess a bulk band gap in its bandstructure

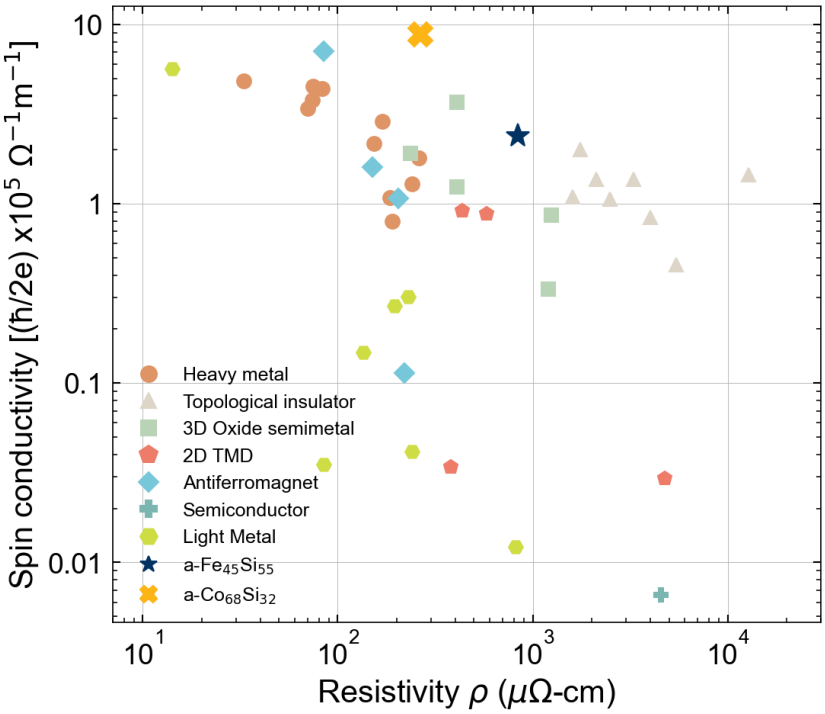

Figure 2.15: Benchmark of the spin-Hall conductivity ($\sigma_s = \xi_{DL,SOT}\sigma_c$) among the well-studied materials including best results of cobalt and iron silciides from this dissertation.

due to spin-orbit coupling except certain points where isolated linear band crossing exist [204]. The linear band crossings arise from the topological surface states due to the bulk band topology similar to the topological insulators. In Dirac semimetals, the bands are doubly-degenerate whereas the degeneracy is lifted in Weyl semimetals creating a pair of Weyl nodes with opposite chirality resulting in opposite spin polarization directions similar to spin-momentum locking[82].

In addition to the large SOT efficiency, non-trivial torque symmetry can arise due to the low crystal symmetry leveraging the atomically thin two-dimension nature can [115]. MacNeil *et al.* showed that z-spin polarized spin currents can be generated in single to few-layers WTe_2. At last, with the discovery of two-dimensional ferromagnet such as $Cr_2Ge_2Te_6$ [59], CrI_3 [75] and twisted bi-layer graphene (Moire crystals) [28], building van der Waals heterostructures for efficient spin current generation, complex magnetic texture manipulation, and studying new quantum and topological physical phenomena.

2.3 Brief introduction on experimental measurement techniques

In this section, I will present a brief introduction of several common experimental techniques for characterizing spin-orbit torque at the materials level, device level, and memory cell level.

Materials level characterization

The material design space for generating spin-orbit torque is very wide and diverse. The abundance in materials for spin current generation can be seen in the previous section of this chapter. At the materials level, the focus is on characterizing material properties at a macro scale without other significant considerations beyond the spin current generating **(SCG)** material such as optimizing the magnetic properties of the spin detection ferromagnetic layer or effect of device dimensions. At the materials level, the common device structure as a vehicle to characterize spin-orbit torque is the SCG layer / ferromagnet detection layer structure similar to the NM/FM bi-layer in figure 2.3. A few other variant structures include the insertion of a thin paramagnetic or antiferromagnetic oxide layer between the SCG layer and the ferromagnet, and the insertion of a metallic spacer layer for diffusion of spin current but separating the SCG layer and the ferromagnet to eliminate interface effects. Aside from extracting the individual damping-like and field-like torque strength (per unit charge current density), the three metrics that are the most crucial for designing SOT-devices are **spin-torque efficiency** $\xi_{DL,FL}$, **resistivity** ρ_c and **interfacial spin transparency** T_{int}. For spin-torque efficiency, damping-like torque efficiency ξ_{DL} is more often the focus since it directly relates to the SOT switching of magnetization. In the recent years, research on enhancing spin transparency at the SCG / FM interface has become very active.

Harmonic Hall measurement

Harmonic Hall measurement is a transport technique that utilizes the Hall signal from the ferromagnet that is modulated by the spin-torque [65, 55, 9]. The amount of modulation is small and only pulls the magnetization away from equilibrium (held by an external field in the in-plane geometry or by magnetic anisotropy in the out-of-plane geometry) by no more than $1\sim 2$ degrees. By injecting an a.c. current into the Hall bar device, Hall voltages at the first and second harmonic of the injected a.c. current frequency are recorded. In the first harmonic, planar (or anomalous for out-of-plane geometry) Hall effect voltage of the ferromagnet is present which includes information such as magnetic anisotropy geometry and quality of the ferromagnet. The second harmonic Hall signal is produced due to the magnetization being modulated by spin-torque. Planar Hall effect (or anomalous for out-of-plane geometry) signal in the first harmonic shows a linear response to the injected a.c. current thus when a spin-torque that follows the a.c. current frequency acts upon a magnetization, which its transport readout is also oscillating at the a.c. current frequency, a second harmonic voltage arises and contains information regarding the spin-torque acting

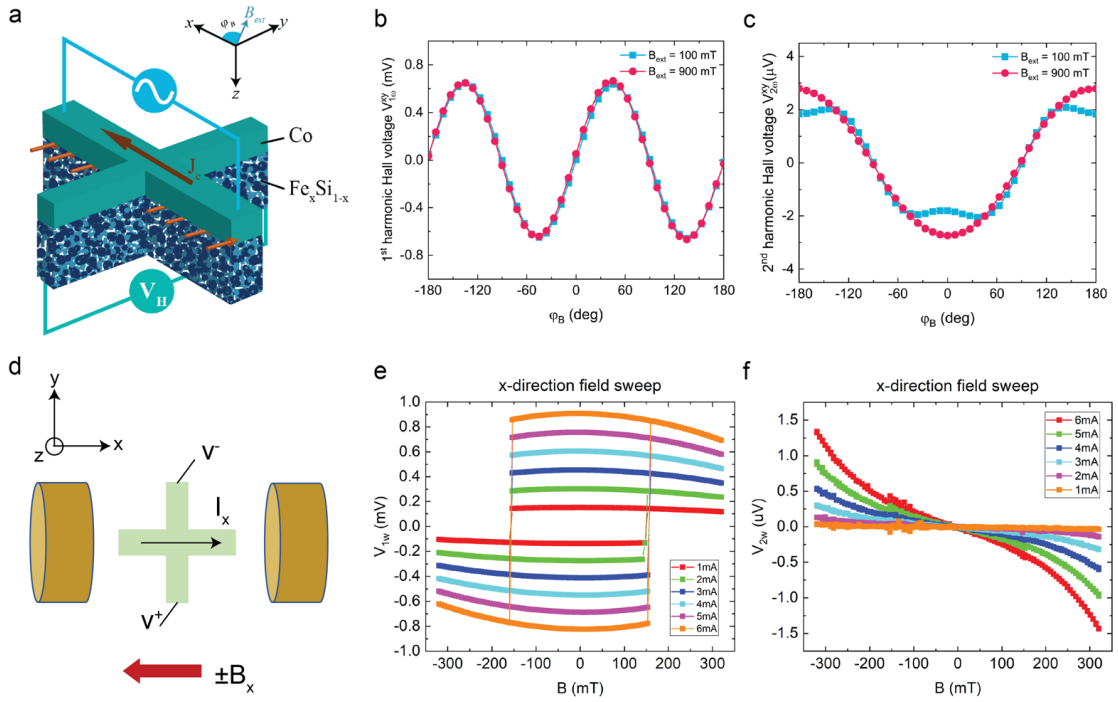

Figure 2.16: a, schematic of in-plane harmonic Hall measurement. b, first harmonic Hall signal of the in-plane geometry. c, second harmonic Hall signal of the in-plane geometry d, schematic of out-of-plane harmonic Hall measurement. e, first harmonic Hall signal of the out-of-plane geometry. f, second harmonic Hall signal of the out-of-plane geometry

on the magnetization. In addition, thermoelectric effects in the the second harmonic signal is present because the SCG material/ferromagnet bi-layer or tri-layer structure is composed of materials with different resistivity values, a temperature gradient in the stacking direction will be present due to Joule heating [9, 162]. From the first and second harmonic Hall signals, damping-like and effective fields can be extracted. Further, the spin-torque efficiency ($\xi_{DL,FL}$) can be extracted by

$$\xi_{DL,FL} = \frac{2e}{\hbar} M_s t_{FM} \frac{\Delta B_{DL,FL}}{j_{SCG-layer}} \tag{2.19}$$

where M_s is the saturation magnetization, t_{FM} is the thickness of the ferromagnet spin detection layer, $\Delta B_{DL,FL}$ is the damping-like or field-like torque effective fields, and $j_{SCG-layer}$ is the current density in the spin current generating layer during the experiment.

Depending on the geometry of the measurement, the requirements on the scanning parameters and magnetic properties will be different. For in-plane harmonic Hall measurements, the ferromagnet will have in-plane magnetic anisotropy (IMA) with as minimal uniaxial anisotropy as possible and a full angle 360° scan is required. In order to separate the

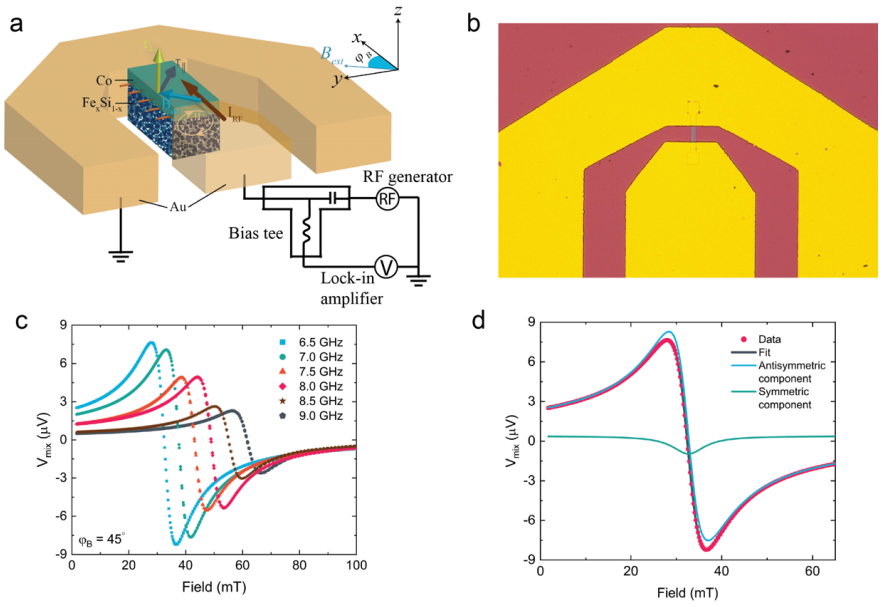

Figure 2.17: a, schematic of spin-torque ferromagnetic resonance (STFMR) measurement. b, Optical microscope image of a STFMR device. c, STFMR lineshape with different microwave frequency. d, Fitting of symmetric and antisymmetric Lorentzian to the lineshape.

thermoelectric effects from the spin-orbit torque effects in the second harmonic signal, a field-sweep starting from a few hundreds of Oe higher than the IP coercive field up to a large field value ($\sim$ 1 T) is crucial to ensure the ferromagnet is pinned by the external field during the measurement and minimize the effect of magnetic domain pinning. For out-of-plane harmonic Hall measurements, the ferromagnet will have a strong perpendicular magnetic anisotropy (PMA) with nearly no IMA and a bipolar hysteric field scan is required. The magnetization will be pinned in the out-of-plane direction and the field will be applied in the in-plane direction to slightly bring the magnetization equilibrium direction away from the $\hat{z}$-axis. Modulation of the spin-torque will be present as small angle dynamic deviation from the equilibrium direction similar to the in-plane harmonic geometry. One field sweep measurement will be done in the $\hat{x}$-direction and $\hat{y}$-direction. Certain corrections may be necessary to account for finite amount of IMA in the sample under study [65, 161].

Spin-torque ferromagnetic resonance measurement

Spin-torque (ST) ferromagnetic resonance (FMR) measurement is a microwave frequency transport measurement that relies on driving the ferromagnet into resonance and modulating the damping of the resonating magnetization via spin-torque. In ST-FMR measurement, the device structure contains a co-planar waveguide contacted microstrip fabricated from the SCG layer/ferromagnet bi-layer. A single-port microwave current is injected into the

microstrip and the mix-down DC voltage (V_{mix}) is measured across the microstrip. As the in-plane field is applied, the magnetization is brought into resonance and out of resonance as the field continues to increase away from the resonance field. The field-dependent V_{mix} contains two separate lineshapes: symmetric Lorentzian representing the damping-like torque and the antisymmetric Lorentzian representing the field-like torque. If we conduct a microwave frequency dependent sweep, the linewidth (ΔB) of the Lorentzian should increase according to

$$\alpha = \frac{\gamma}{2\pi f}\Delta B, \tag{2.20}$$

where α is the damping constant, γ is the gyromagnetic ratio, f is the frequency of the microwave current. The presence of the symmetric Lorentzian component and the direct modulation of ΔB as a function of microwave frequency are signatures of spin-orbit torque modulating the resonating magnetization. To extract the spin-torque efficiency, one need to be careful on what assumptions can be made to simplify the analysis. For a more generic case, one would need to calibrate the amount of current running through the SCG layer with a vector network analyzer and some calculations. Once that is done, the expression for symmetric Lorentzian component [115, 124, 197]

$$V_s = -\frac{I_{rf}\gamma cos(\theta_H)}{4}\left(\frac{dR}{d\theta_H}\right)\tau_{ip}\left(\frac{1}{\Delta H}\right)F_s(H_{ext}) \tag{2.21}$$

where $\frac{dR}{d\theta_H}$ is the anisotropic magnetoresistance, τ_{ip} is the damping-like torque strength in the unit of Oe or T, ΔH is the linewidth, and $F_s(H_{ext})$ is the symmetric Lorentzian function. Afterwards, the spin-torque efficiency can be extracted with the expression

$$\xi_{DL} = \frac{\sigma_s}{\sigma_c}\left(\frac{2e}{\hbar}\right) = \frac{\tau_{ip}M_s t_{FM}}{\sigma_c E cos(\phi)}\left(\frac{2e}{\hbar}\right) \tag{2.22}$$

where E is the electric field across the microstrip, M_s is the saturation magnetization and t_{FM} is the thickness of the ferromagnet. The above treatment is a more generic case. When the field-like torque is purely due to Oersted field arising from the current in the SCG layer, a much simple analysis can be implemented with expression

$$\xi_{DL} = \frac{J_s}{J_c} = \frac{V_s}{V_a}\left(\frac{2e}{\hbar}\right)\mu_0 M_s t_{FM} d_{SCG}\sqrt{1+\frac{4\pi M_{eff}}{H_{res}}} \tag{2.23}$$

where d_{SCG} is the SCG layer thickness, V_s is voltage of the symmetric Lorentzian component, V_a is voltage of the antisymmetric Lorentzian component, $4\pi M_{eff}$ is the demagnetization field and H_{res} is the resonant field.

STFMR is also a useful method to characterize the damping constant of the ferromagnet for ultimately characterizing the interfacial spin transparency. On page 20-21 of this dissertation, I briefly introduced the extraction of the spin transmission coefficient through spin-mixing conductance and the magnetic damping constant. Here, I will extend that introduction to include

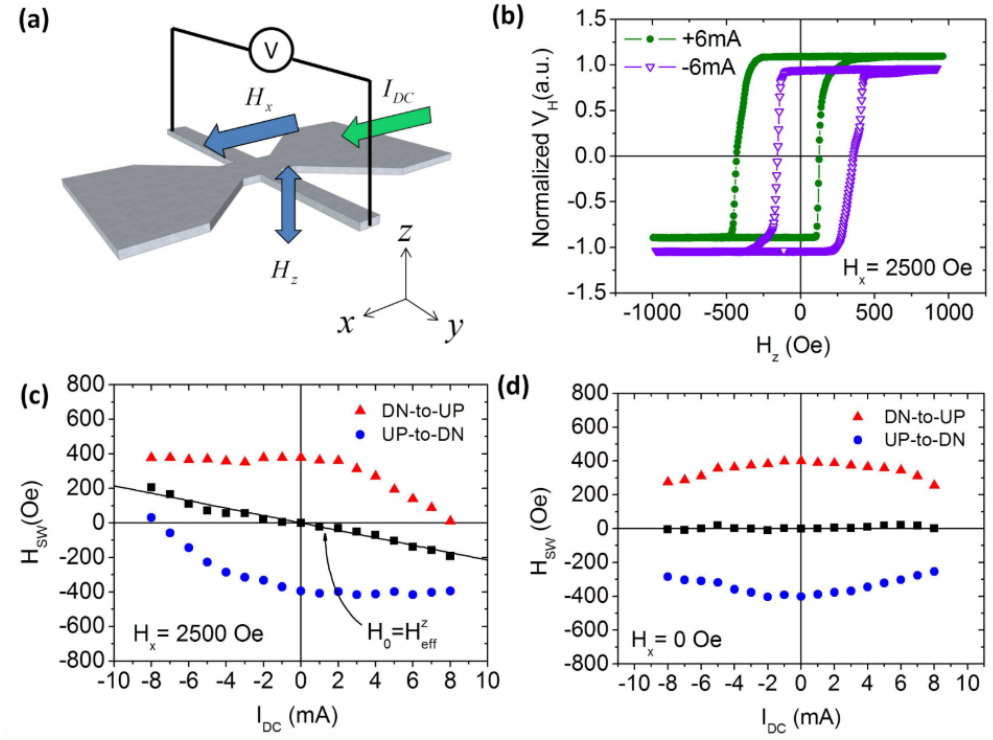

Figure 2.18: a, schematic of magnetic loop shift measurement. b, Anomalous Hall effect (AHE) voltage field loops with opposite DC current and fixed in-plane field. c, the measured coercive field and amount of field shift as a function of current. d, same as *c* but without in-plane field to compensate the DMI. Graph adapted from *Physical Review B* [146].

Magnetic loop shift measurement

The magnetic loop shift measurement takes into account of the DMI interaction and the magnetic textures in the ferromagnet that serves as the spin-torque detection layer. This method allows the extraction of damping-like spin-orbit torque efficiency and DMI field strength simultaneously.

This technique is pioneered by Pai *et al.* [146] which an in-plane H_x is fixed during the measurement to reorient the domain wall moments that have been pinned by the DMI and sweep the out-of-plane field to switch the PMA magnet while measuring the anomalous Hall effect voltage (figure 2.18). The amount of the loop shift magnetic field is proportional to the damping-like torque effective field by a factor of $(2/\pi)$ -

$$\Delta H_{DL} = \left(\frac{2}{\pi}\right) H^z_{shift,eff}. \tag{2.24}$$

Once the damping-like torque effective field is obtained, one can use expression 2.19 to extract the damping-like torque efficiency. While this technique is simple in terms of not

requiring an a.c. current injection or any lock-in detection and the analysis is relatively simple compared to the three previous methods, there are few drawbacks. The drawback are the lack of field-like torque characterization, requirement of a strong PMA magnet on top of the SCG material and the accuracy of field geometry between the fixed in-plane field and sweeping out-of-plane field.

Spin pumping

Spin pumping method utilizes the inverse of charge-to-spin conversion process in the SCG material and readout the induced voltage due to inverse spin Hall effect (iSHE) or spin galvanic effect (inverse Rashba-Edelstein effect). By placing a electrically connected SCG/FM bi-layer or tri-layer device on top of a microwave transmission line or microwave cavity that generates a microwave magnetic field, the magnetization is driven into resonance and begin to inject spins into the SCG layer. Through spin-to-charge conversion processes mentioned above, a non-zero voltage can be measured. By fitting to the iSHE voltage expression in [188, 6], the spin-charge conversion efficiency can be extracted. This method has become less common among the spin-orbit torque community as it is highly sensitive to the placement of the sample in the microwave field and due to the inverse effect of spin-orbit torque. As a result, the efficiency values extracted via spin pumping has become less reliable and recognized among the spin-orbit torque community.

Device level characterization

At the device level, emphasis is shifted to achieving efficient magnetization switching thus material properties of the ferromagnet are now a crucial design parameter. Magnetic properties such as thermal stability, saturation magnetization, magnetic anisotropies and other coupling effects with the SCG layer become important. The common device structure as the testing vehicle is still the SCG / FM bi-layer but the ferromagnetic layer now possess perpendicular magnetic anisotropy (PMA) since magnetic tunnel junction (MTJ) with PMA provides a higher device density thus more memory capacity. The important metrics at the device level are **Critical switching current density $\mathbf{J}_c$**, **thermal stability of the ferromagnet to be switched Δ**, and **switching efficiency $\mathbf{J}_c/\Delta$**. A much more rigorous testing vehicle structure is the nanopillar consists of the ferromagnet with PMA located on top of the cross-point of a Hall bar made up of the SCG material. This testing vehicle is more involved in terms of fabrication but is closely resembling the actual MTJ device in cross-bar memory arrays and a device dimension/geometry-dependent switching experiment can be systemically designed.

SOT-induced magnetic switching measurement

SOT-induced magnetic switching measurement is the most direct experiment to probe the effectiveness of SOT magnetic switching [126]. The experimental setup is quite simple and the

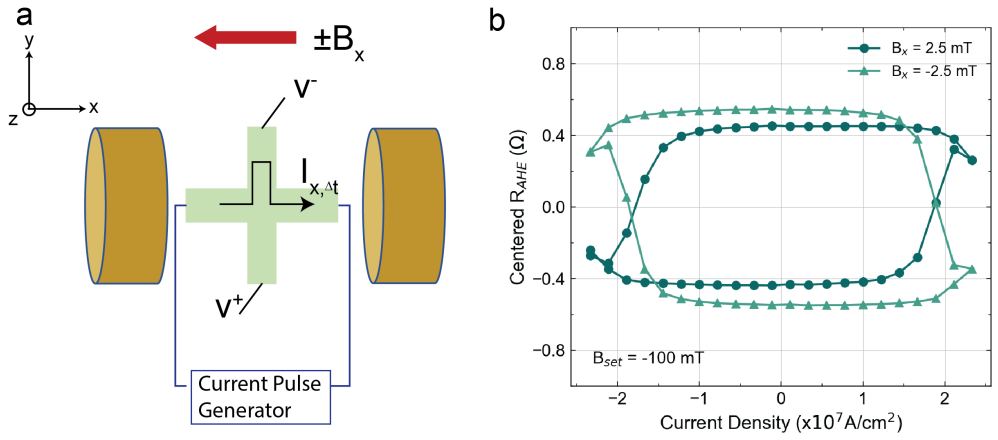

Figure 2.19: a, schematic of SOT-driven magnetic switching experiment. b, SOT switching loops of Ta/GdCo/Pt with PMA of opposite symmetry breaking field sign.

data does not require any sophisticated post-processing. One will need a current pulse generator and a nanovoltmeter or any sourcemeter that has such capability. During switching, a non-zero in-plane symmetry breaking field is necessary for deterministic switching, unless there are field-free mechanisms designed or built-in to the material stack or device structure. By conducting a current pulse amplitude sweep in a hysteric manner, the critical current density (j_c)can be found at the current density where the magnetization switch from down to up state and from up to down state. The readout of the magnetization state is through anomalous Hall effect voltage. One can either program a synchronized pulse-I-measure-V with a small delay during the pulse or a pulse train that alternates between write current pulse and read (small) current pulse. In figure 2.19, a schematic of the SOT switching setup and measurement geometry is shown and a very clean SOT switching loop of Ta/GdCo/Pt is shown.

Thermal stability measurement

The thermal stability of a ferromagnet characterizes how stable the ferromagnet retains its magnetization along the magnetized direction from existing thermal energy in the ambient environment. The thermal stability measurement is based on the fact that field switching of the magnetization is a thermal activation process. Due to the time-dependent nature of such thermal activation process, the coercive field at which magnetization switching occurs is a function of the magnetic field ramp rate [69, 161]. The relation between thermal stability factor (Δ), coercive field (H_c) and ramp rate (r) is [161]:

$$H_c = H_k \left(1 - \sqrt{\frac{1}{\Delta} ln \left(\frac{f_0 H_k}{2\Delta} \frac{1}{r}\right)}\right) \tag{2.25}$$

By fitting this expression to the coercive field as a function of ramp rate, we were able to extract the thermal stability factor (Δ) and the anisotropy field (H_k) in the easy-axis (out-of-plane) direction. f_0 is the attempt frequency and it is often assumed to be a few to tens of GHz in the fitting. The thermal stability in the unit of energy can be calculated by multiplying Δ by $k_B T$ where k_B is the Boltzmann constant and T is the temperature.

Switching efficiency

Once we obtain both j_c and Δ, we can easily calculate the switching efficiency with

$$\frac{j_c}{\Delta}. \tag{2.26}$$

In reality, the same type of PMA magnet deposits/grows differently on the different SCG materials and some type of PMA magnet are even very difficult to be deposited on certain SCG materials. As a result, it is crucial to have a metric that allows researchers to compare SOT switching efficiency that is not affected by the different properties across a diverse range of materials. This metric characterizes how much current density is required to switch the magnetization per unit amount of thermal stability. Instead of comparing solely on critical switching current density, this metric provides a much more fair comparison between different SCG materials and magnetic heterostructures.

Memory Cell level characterization

At the cell level, there are a few important metrics as design principals for SOT-MRAM. This subsection is intended to be kept short since this is not the main focus of the dissertation. At the cell level, a full MTJ is connected with an access transistor in both stand alone and embedded applications. The state-of-the-art MTJ design usually follows a structure such as: underlayer or seed layer/free magnetic layer/tunnel barrier/reference magnetic layer/synthetic antiferromagnetic layer/capping layer. The MTJ is built on a SOT line that's made of the SCG material of choice. In a cross-bar array structure, the top and bottom electrodes of the MTJ are sandwiched between word lines and bit lines similar to figure 1.7. A few important metrics at the memory cell level include the **tunneling magnetoresistance (TMR) ratio**, **critical switching current I_c**, **tunneling resistance times the cross-sectional area of the MTJ - RA**, **thermal stability of the MTJ Δ** which is associated with reliability, and **access speed**. Most of these metrics are coupled with each other, consequently, it is quite challenging to optimize the design trade-off in a SOT-MRAM. I will go over more on how a purely voltage-driven memory cell can overcome many of these design trade-offs that provide a scalable MRAM solution.

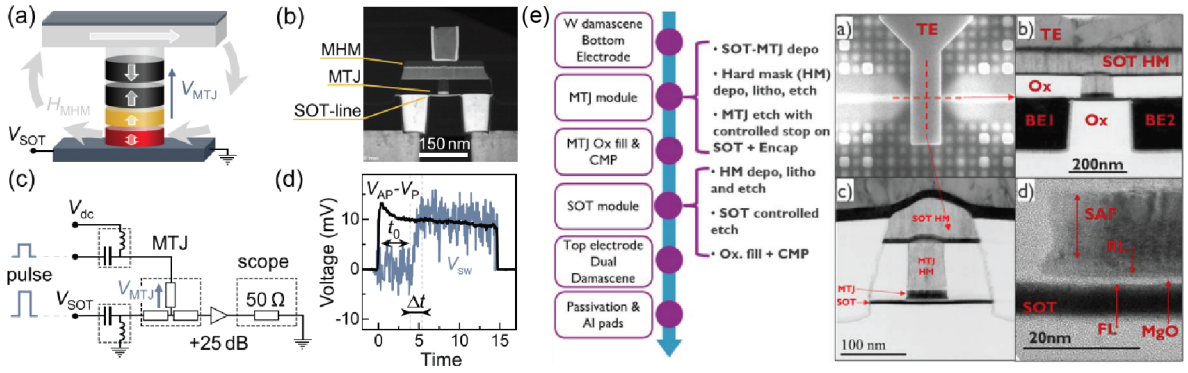

Figure 2.20: a, schematic of field-free SOT-MRAM cell design. b, Cross-sectional TEM of the MRAM cell. c, the MRAM characterization scheme. d, time-dependent switching experiment. e, fabrication process of the SOT-MRAM cell at IMEC's CMOS line and cross-sectional TEM image of the fabricated cell.

2.4 Spin-orbit torque device applications

SOT-MRAM: Developments and Challenges

STT-MRAM research has been ongoing for more than a decade with most leading semiconductor foundries and a few MRAM start-up/spun-off companies such as EverSpin, Avalanche Technology and Grandis. However, public knowledge of SOT-MRAM development and research in industry is not revealed until 2018 by IMEC (Interuniversity Microelectronics Centre) [54]. Since then, leading foundries began releasing the news of developing SOT-based MRAM products and presented progress and findings at the annual MRAM forum at IEDM (International Electron Device Meeting) [175]. Although SOT-MRAM products remains primitive compared to STT-MRAM as STT-MRAM is still continuously scaling, increasing number of research institutes have announced the integration of SOT-MRAM to 12 inch silicon CMOS platform [54, 72].

SOT-MRAM cell design includes material choice in MTJ stack and SOT line, etching optimization, and field-free engineeing. The material choice for the SOT line is ubiquitously tungsten especially in its β-phase. This is because tungsten has the highest spin-torque efficiency among the single element heavy metals and tungsten is a common refractory metal for transistor gate metal and contact metal in most CMOS fabrication lines. The MTJ stack design is very similar to STT-MRAM since the readout of a SOT-MRAM is still via tunneling magnetoresistance (TMR). Etching the nanopillar of the MTJ has been a challenging task not only in SOT-MRAM but also STT-MRAM since the magnetic property of the MTJ is very sensitive to side-wall redeposition and side-wall damage. For SOT-MRAM, the etching parameters are even more stringent as the MTJ pillar need to be precisely fabricated on top of the SOT line, thus, precise etch stop on the SOT line is required for optimal SOT performance

and device-to-device variability. At last, for SOT-MRAM to switch deterministically via spins generated by tungstern, field-free switching design need to be incorporated into the SOT-MRAM cell. For the work done at IMEC [54, 101], a magnetic heavy metal line is incorporated on top of the full MTJ stack to create a stray field as symmetry breaking field. For the work done at Tohoku University, a canting angle of the magnetic free layer in the MTJ was made but the magnetic anisotropy direction is in-plane thus not the industry standard perpendicular MTJs [72]. Nevertheless, the ability to integrate a canting design into the current CMOS 12 inch line is a valuable demonstration and a further step toward SOT-MRAM commercialization.

Other useful SOT applications

While the SOT-MRAM is the main application this dissertation addresses, there are an abundant of spintronics device applications that SOT can provide. This include spintronic oscillators, and spin logic devices. These applications all leverages the efficient manipulation of the magnetic textures via electric current that SOT provides. In spintronic oscillators, devices such as spin-torque nano-oscillators that requires a RF spin-torque to drive the magnetization oscillating in the RF frequency. Other applications of spintronics oscillation includes DC-to-RF for RF generation and RF-to-DC for RF detection. These could have impact in the field of communication and mix-signal circuits [41]. As for logic devices, a few proposals such as using domain wall as logic components [114], MESO (magnetoelectric spin-orbit) devices [119], and other proposals [10, 50] have been proposed or demonstrated in the past decade.

Chapter 3

Large spin-orbit torque in amorphous iron silicide

This chapter is based on a paper submitted for publication that I am the lead author of and I have obtained the permission from my co-authors to use the data for this dissertation.

3.1 Foreword and motivation

SOT induced magnetization switching has shown great potential for next-generation magnetic memory technology beyond conventional spin-transfer torque in terms of faster switching, separate read/write current path and broader material design space [105, 163, 41]. Beyond its application as a magnetic memory, SOT is also an effective probe to study rich spin-dependent transport physics [61] such as the spin Hall effect[111, 43, 70, 91], the Rashba-Edelstein effect [126, 44, 67, 118] and spin-momentum locking surface states in topological materials [73, 124, 197, 178]. These mechanisms have been studied in many material systems including heavy metals [111, 112, 147, 126], topological insulators [124, 39, 92, 162], transition metal chalcogenides [168, 169], antiferromagnets [144, 219, 131], light metals [102, 195, 217], oxide semi-metals [130, 13], semiconductors [173], two-dimensional electron gas [205] and all-oxide epitaxial systems [77].

According to the conventional wisdom of SOT generation, an amorphous material, which has no bulk bandstructure defined, and without any heavy element is unlikely to exhibit a large spin current [172, 111, 124]. In fact, low-Z materials such as Si ($\xi \sim 0.01$)[6], V ($\xi \sim 0.07$) [195] and Zr ($\xi \sim 0.02$) [217] usually do not exhibit a strong spin current due to the weak atomistic spin-orbit coupling [102, 195, 217, 6]. Although large spin-orbit coupling is not required for spin current generation via spin-momentum locking surface states in topologically non-trivial materials [47, 142], whether this persists in a fully amorphous low-Z system is the question to be addressed. Here, the amorphous phase is very distinct compared to nanocrystalline phases in sputtered topological insulators or transition metal alloys where a finite size grain exists [39]. However, in the last few years, anomalous Hall Effect (AHE)

has been observed in amorphous materials such as amorphous Fe_xSi_{100-x}[87, 89, 86, 14]. Theoretically, it was shown that, even in the amorphous phase, a Berry density can be defined and calculated [14], which in turn, allows the calculation of an AHE conductivity. This shows that spin related phenomena in amorphous materials carry an intrinsic contribution. Indeed, the Berry density shows well-defined functional dependence as a function of energy. Similar effects have been observed in amorphous CoFeB [76] and intrinsic contributions to AHE has been discussed in amorphous systems [89, 86, 14]. To this aspect, we closely collaborated with Professor Frances Hellman's group where tremendous effort has been put in to study spin polarization effects in fully amorphous ferromagnetic iron silicide and iron germanide. This brings up an intriguing possibility – in a structure with a broken symmetry at the interface, an amorphous material should be able to generate spin current and potentially torque a magnet. In fact, strong spin Hall effect has been found in amorphous-like ferromagnetic heavy metal alloys [224, 113]. In this work, we examine this possibility in fully amorphous Fe_xSi_{100-x} (a-Fe_xSi_{100-x}), an amorphous material with only light elements, where conventionally, one would not expect a spin current. Remarkably, we find that, spin-torque efficiency higher than 2.0 can be achieved. In addition, the spin-torque efficiency shows a clear functional dependence on the Fe concentration, indicating a direct correlation to the density of states of the material. This strong Fe concentration dependence with the peak near 45 % Fe points to a potential topological origin in a fully amorphous material analogous to the crystalline bandstructure topology of FeSi and other topological insulators with finite grain sizes.

From a technological standpoint, it is crucial to have a new material system readily integrable into the silicon CMOS line, outperforming tungsten ($\xi_{DL} = 32 \sim 37\%$, $\rho_c \sim 330\mu\Omega - cm$)[54, 147, 72]. Additionally, this system should possess a scalable mechanism, offering high spin-torque efficiency and low resistivity with tunable knobs, to accelerate the deployment of SOT-MRAM.

3.2 Sample design and deposition

For our experiments, I collaborated with professor Julie Karel and professor Frances Hellman on the materials deposition in the early phases of this study. Eventually, I developed my own sample deposition process and have deposited a-Fe_xSi_{100-x} with x varying from 24% to 60%. In this study, samples deposited by me and Karel are all well-studied. Co is used as the ferromagnet to study the spin-orbit torque. I note here that metal-Si junctions are often plagued by interface states originating from uncompensated bonds which leads to the pinning of the Fermi level, as is well-known in semiconductor literature[74]. The interface of Si and Co is very likely to suffer from such pinning, making it impossible to study any density-dependent phenomena. One way to remove the pinning is to introduce an oxide layer in between the two materials, so that each can form its own oxide and reduce the amount of uncompensated bonds (figure 3.1a). Accordingly, I developed a process to insert a ∼1 nm oxide in between a-Fe_xSi_{100-x} and Co.

There are two main thin film stack designs in this study: Si substrate / a-Fe_xSi_{100-x} /

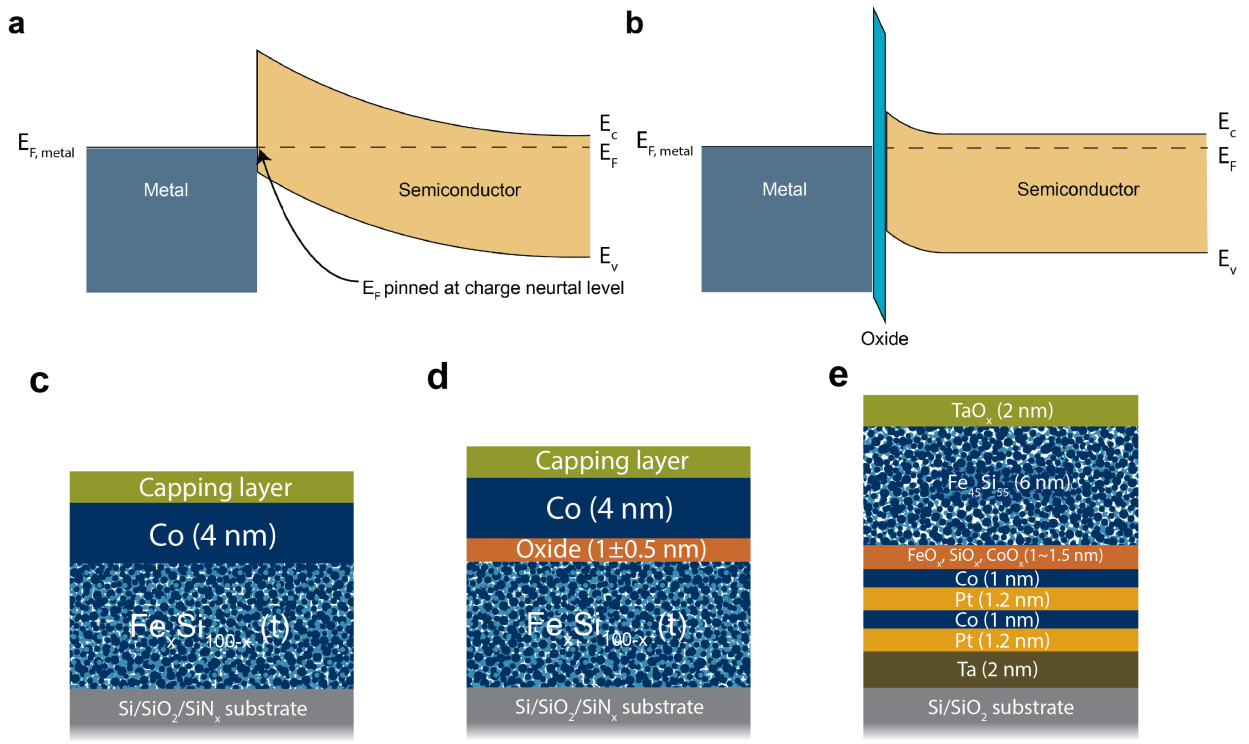

Figure 3.1: a,b, schematic of Fermi-level pinning and alleviation via oxide insertion. c, *a*-Fe_xSi_{100-x}/Co bi-layer d, *a*-Fe_xSi_{100-x}/oxide/Co tri-layer. e, *a*-Fe_xSi_{100-x} / oxide / $[Pt/Co]_2$ with PMA.

oxide / ferromagnet with in-plane magnetic anisotropy (IMA) and Si substrate / ferromagnet / oxide / *a*-$Fe_{45}Si_{55}$ with perpendicular magnetic anisotopry (PMA). For the IMA stack, *a*-Fe_xSi_{100-x} thin films (5.5±0.5 nm) with composition ranging from x = 24 to 60 were deposited at room temperature on amorphous SiN_x on Si substrates by co-sputtering of iron and silicon elemental targets and electron beam co-evaporation from elemental iron and silicon sources in an ultra high vacuum system (base pressure for this work 1e-9 Torr). 4 nm of ferromagnet Co is subsequently sputtered on top of *a*-Fe_xSi_{100-x} more precisely, onto a thin oxide that is approximately 1∼1.5 nm thick formed on top of *a*-Fe_xSi_{100-x}. All heterostructures are capped with sputtered silicon oxide. The thin oxide insertion was done by wet chemical treatment. First, single layer *a*-Fe_xSi_{100-x} capped with aluminum oxide was deposited. Next, the aluminum oxide layer is washed away by wet-etching with MEGAPOSIT MF-26A photoresist developer, a 2.0-2.5 % tetramethylammonium hydroxide (TMAH) based developer. After aluminum oxide wet-etching, de-ionized water was used to rinse off the developer and blow dried with N2. The uncapped *a*-Fe_xSi_{100-x} is immediately transferred into the sputtering chamber (base pressure below 1e-8 Torr) with a load-lock. Prior to sputter deposition of cobalt, low power RF back-sputter of the sample was done

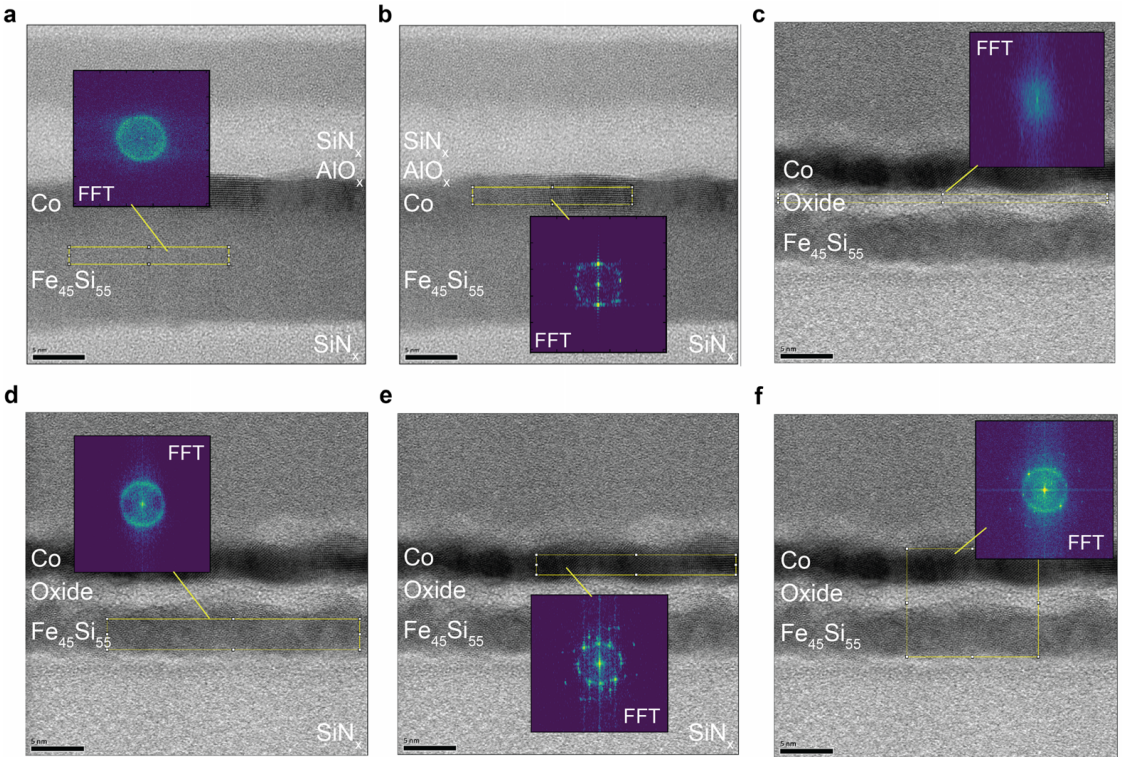

Figure 3.2: a,b, TEM of a-$Fe_{45}Si_{55}$ / Co and the local FFT of $Fe_{45}Si_{55}$ and Co region respectively. c,d,e, TEM of a-$Fe_{45}Si_{55}$ / oxide / Co and the local FFT of oxide, $Fe_{45}Si_{55}$ and Co region respectively. f, TEM of a-$Fe_{45}Si_{55}$ / oxide / Co and the local FFT of entire tri-layer.

to clean off the surface contamination. For the PMA stack, the heterostructure is reversed with the PMA ferromagnet [Pt (1.2 nm)/Co (1 nm)]$_2$ deposited on Ta (2 nm) seed layer on silicon substrate as the first layer. The ferromagnet is than capped with 1$\sim$1.5 nm of a-$Fe_{45}Si_{55}$ and 2 nm of AlOx consecutively. We perform the same aluminum oxide wet-etch as mentioned above and this process oxidizes the thin layer of a-$Fe_{45}Si_{55}$. Afterwards, 6 nm of a-$Fe_{45}Si_{55}$ is deposited with 2 nm Ta capping layer to be oxidized in air.

Sputtering deposition is done in an ATC 2200 UHV 8-gun sputtering chamber at room temperature with base pressure below 1.5e-8 Torr. Evaporation is done in an ATC 1800-HY Hybrid ion mill/electron beam evaporator chamber.

3.3 Structural and magnetic properties

Structural characterization

The amorphous structure of a-Fe_xSi_{100-x} is studied through high-resolution cross-sectional transmission electron microscopy (TEM) (Fig. 3.2) and synchrotron X-ray diffraction (Fig. 3.3). In figure 3.2, no local nanocrystal formation or lattice fringes are observable across the entire a-$Fe_{45}Si_{55}$ layer in both the a-$Fe_{45}Si_{55}$/Co bi-layer and a-$Fe_{45}Si_{55}$/oxide/Co tri-layer. Further analysis of the TEM image with local fast Fourier transform (FFT) also confirms the amorphous phase of a-$Fe_{45}Si_{55}$ without any distinct reciprocal space peaks (Insets of figure 3.2a, 3.2d). As a quick comparison, the 4nm Co layer has visible grains in the cross-sectional TEM. This is visible in both the bi-layer and the tri-layer heterostructure. The reciprocal space FFT also exhibit distinct reciprocal space peaks in the Co layer of the two stacks. Distinct grains in a 4 nm Co layer serves as a clear comparison to the fully amorphous structure in a-$Fe_{45}Si_{55}$ layers where no local order can be found at the single atomic length scale.

To further confirm the amorphous phase, I did synchrotron grazing incidence diffraction at Stanford Synchrotron Radiation Lightsource (SSRL) in SLAC National Accelerator Laboratory. Synchrotron diffraction was carried out at beamline 11-2 with a high-flux X-ray source generated by a 26 pole, 2 Tesla wiggler insertion device. Grazing incidence X-ray diffraction (GI-XRD) measurements are carried out to characterize the film structure of a-Fe_xSi_{100-x} at an incident angle of 0.25 degree and the 2D X-ray pole figures were measured via a two-dimensional 100-pixel monolithic solid state Ge detector array at room temperature. The X-ray 2D pole figure (figure 3.3a) shows the diffraction pattern of a 10 nm a-$Fe_{40}Si_{60}$ film, where a diffused pattern is observed and the only observable peaks connected by Kikuchi lines are associated with the single crystal silicon substrate (figure 3.3a). The absence of a diffraction signal from the a-$Fe_{40}Si_{60}$ layer confirms the lack of long-range ordering or textured nanocrystals in the a-$Fe_{40}Si_{60}$ thin film. For a-$Fe_{40}Si_{60}$ (10 nm) / Co (4 nm) bi-layer, the additional peaks are associated with the polycrystalline 4 nm Co layer. The observation is similar in 10 nm a-$Fe_{45}Si_{55}$ blanket film and a-$Fe_{45}Si_{55}$/Co bi-layer where no long-range ordering is observed. To check whether GiXRD at a synchrotron facility is capable of resolving small grains on the order of 4 nm or even smaller, I tested a control sample Pt (6nm) / Co (2.5 nm). In the 2D pole figure (figure 3.3e), clear polycrystalline rings from Pt and Co are observable and the textured Co peaks are also observable which is similar to the Co signal in a-$Fe_{40}Si_{60}$/Co and a-$Fe_{45}Si_{55}$/Co. This shows that synchrotron GiXRD can easily resolve grain size < 2.5 nm with mid-level atomic weight of Fe and Co. The confirmation on the lack of both short-range and long-range ordering well agrees with the great amount of structural characterization Professor Karel and Professor Hellmsn's group has done in such Fe-based amorphous thin films [90, 87, 89, 88, 14].

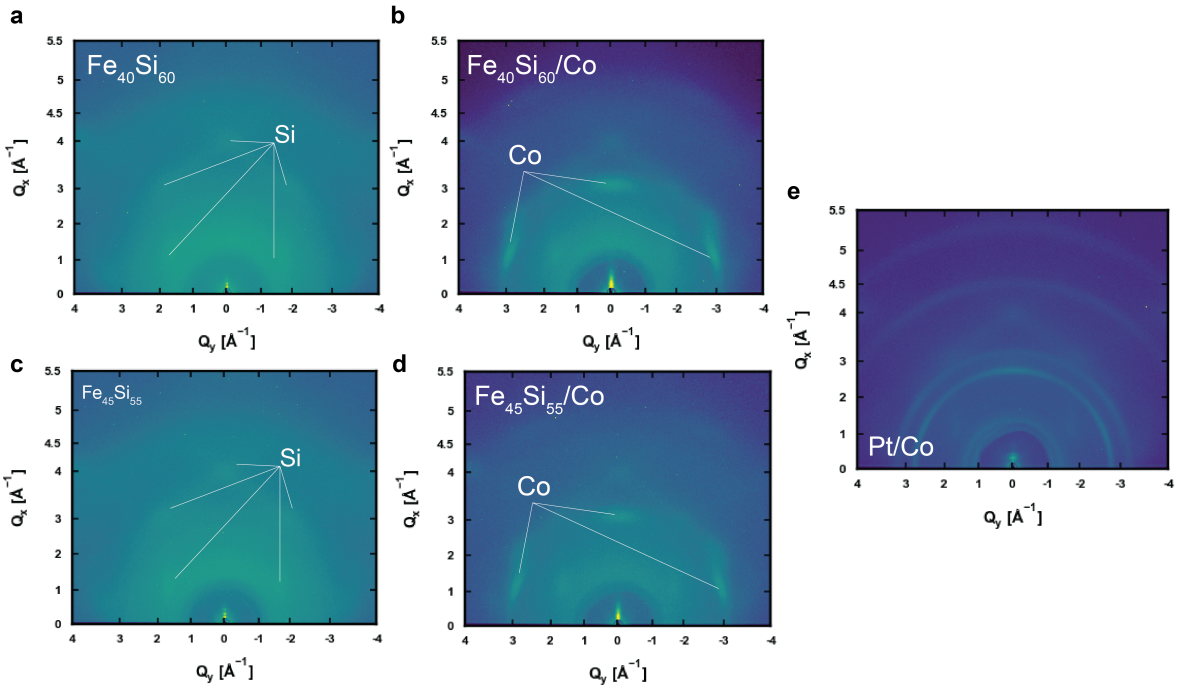

Figure 3.3: All grazing incidence XRD (GiXRD) are done at 0.25 degree angle to minimize substrate signals. a, 2D GiXRD of a-$Fe_{40}Si_{60}$ (8 nm). b, 2D GiXRD of a-$Fe_{40}Si_{60}$(8 nm)/Co(4 nm). c, 2D GiXRD of a-$Fe_{45}Si_{55}$(8 nm). d, 2D GiXRD of a-$Fe_{45}Si_{55}$(8 nm)/Co(4 nm). e, 2D GiXRD of Pt(6 nm)/Co(2.5 nm).

Magnetic Characterization

Magnetic characterization on the a-Fe_xSi_{100-x} magnetic heterostructures include vibrating sample magnetometry and X-Ray magnetic circular dichroism (XMCD). Vibrating sample magnetometer (VSM) measurements are done in-house with a Lakeshore VSM 7400 series at room temperature with sample rotating capability and fields up to 1.75 Tesla. We conducted VSM measurements on blanket a-Fe_xSi_{100-x} thin films in the in-plane geometry. From vibrating sample magnetometry measurements, a-Fe_xSi_{100-x} shows no appreciable ferromagnetism (from the negligible saturation magnetization and zero remanence) for Fe concentrations below x = 50 at room temperature. For $50 < x < 60$, a-Fe_xSi_{100-x} transitions away from the non-ferromagnetic phase characterized by the increased saturation magnetization from nearly zero to 50 emu/cc and 80 emu/cc respectively (figure 3.4), which is consistent with previous literature by professor Hellman's group [87].

I further characterize these a-Fe_xSi_{100-x} films through XMCD. XMCD is a powerful experimental technique used to study the magnetic properties of materials at the atomic

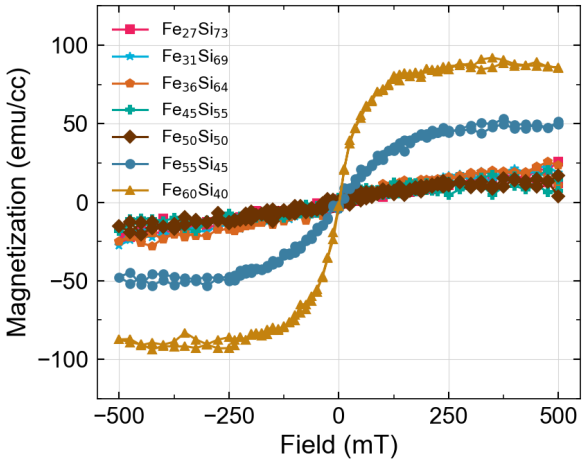

Figure 3.4: Magnetization versus in-plane external field of a-Fe_xSi_{100-x} blanket films with x = 27 $\sim$ 60 via vibrating sample magnetometer (VSM).

level. In XMCD, circularly polarized X-rays with a very specific energy (associated with the specific electronic energy transition) are shined onto a sample and measuring the difference in absorption between left and right circularly polarized light. If the element associated with the energy transition of the material under study is magnetic, the difference will be non-zero. As a result, XMCD is a very sensitive probe for studying elemental magnetism. In my measurements, I primarily check magnetism arising from Fe in a-Fe_xSi_{100-x}. As we can see in figure 3.5a, the XMCD (difference) is increasing with increasing Fe content. This is expected as higher Fe concentration means more likely to develop exchange-coupled magnetic moments. The curve is skewed due to the drift in energy of the beam at the time of the measurement. It can be filtered out by a background subtraction. In figure 3.5b, a typical x-ray absorption spectroscopy data is shown with the two circular polarization of the beam. A difference in the XAS signal at L_3 and L_2 edge is visible exhibiting a clear dichrosim. One additional feature in the XAS spectroscopy data (figure 3.5b) is the post-edge bump feature. This is associated with the oxidized Fe in the 2+ oxidation state[22]. In figure 3.5c, a strong XMCD in the Co L-edge is observed representing the strong ferromagnetism in elemental Co layer of a-$Fe_{45}Si_{55}$/oxide/Co.

3.4 Electronic and charge transport properties

Within the Fe concentration range of a-Fe_xSi_{100-x} in this study, the electronic property is close to a semimetal and close to a small gap semiconductor only when the Fe concentration very low (<15%) [87, 107]. The resistivity of the a-Fe_xSi_{100-x} layer was determined by

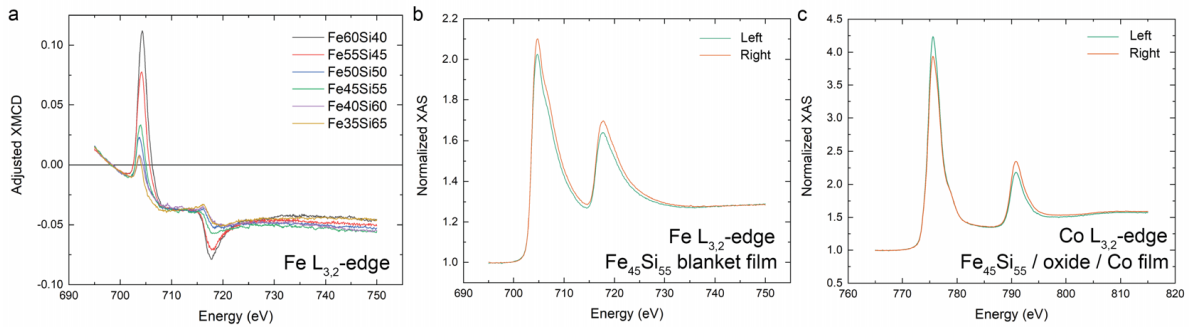

Figure 3.5: X-ray magnetic circular dichroism (XMCD) on a) a-Fe_xSi_{100-x} blanket films. b) Circular polarization dependent X-ray absorption spectroscopy at Fe - $L_{3,2}$ edge on a-$Fe_{45}Si_{55}$ blanket films. c) Circular polarization dependent X-ray absorption spectroscopy at Co - $L_{3,2}$ edge on a-$Fe_{45}Si_{55}$/Co bi-layer.

conducting a four-point resistance measurement on double Hall bar devices fabricated from a blanket film. We characterize the resistivity through two different double Hall bar dimensions (figure 3.6a, b). For the smaller double Hall bar, the current lead in the double Hall bar for resistivity measurements is 6 micron in width and 40 micron in length, and the Hall voltage leads are 2.5 micron in width and 14 micron in length. For the larger double Hall bar, the current lead in the double Hall bar for resistivity measurements is 12 micron in width and 40 micron in length, and the Hall voltage leads are 5 micron in width and 14 micron in length. The resistivity values of Fe_xSi_{100-x} (x = 25 to 60) are shown in figure 3.6. The resistivity values are reasonably close to the previous work done by Karel and Hellman on much thicker films ($\sim$ 100 nm).

3.5 Large spin-orbit torque efficiency

Measurement of large SOT in a-$Fe_{45}Si_{55}$/oxide/Co

The harmonic Hall measurement is conducted to characterize the effective field strength due to current-induced spin-orbit torque that modulates the ferromagnetic thin film adjacent to a-Fe_xSi_{100-x}. It is capable of differentiating different components of the spin-orbit torque and obtaining the spin-orbit torque efficiency. The harmonic Hall measurement was conducted on a home-built setup composed of a 1 Tesla electromagnet with a Lakeshore HMMT-6J04-VR Hall probe/475 Gaussmeter for field precision control, a Signal Recovery 7270 dual harmonic lock-in amplifier, a Keithley 6221 AC/DC current source, a sample rotation stepping motor and a home built coaxial cable connection network to the devices under test. The single Hall bar and double Hall bar devices are wirebonded to non-magnetic chip carriers. Chip carriers

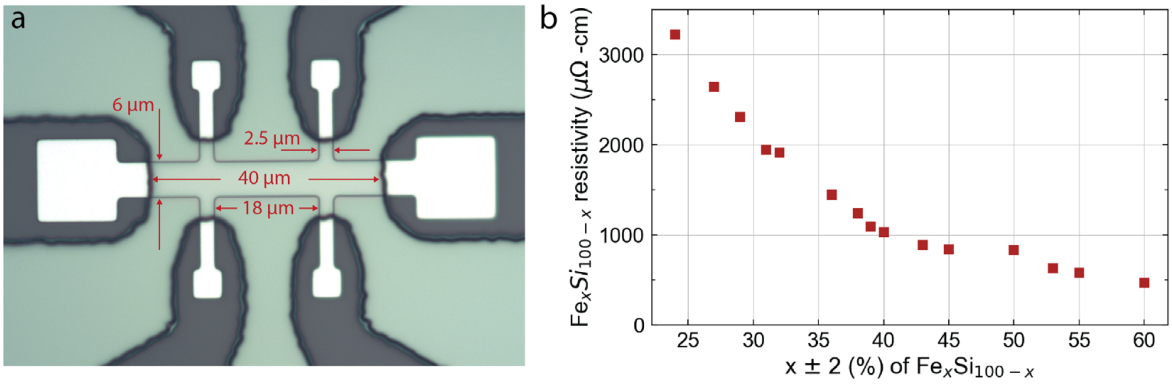

Figure 3.6: a) Optical microscope image of a small double Hall bar. b) Resistivity of *a*-Fe_xSi_{100-x}as a function of Fe concentration x.

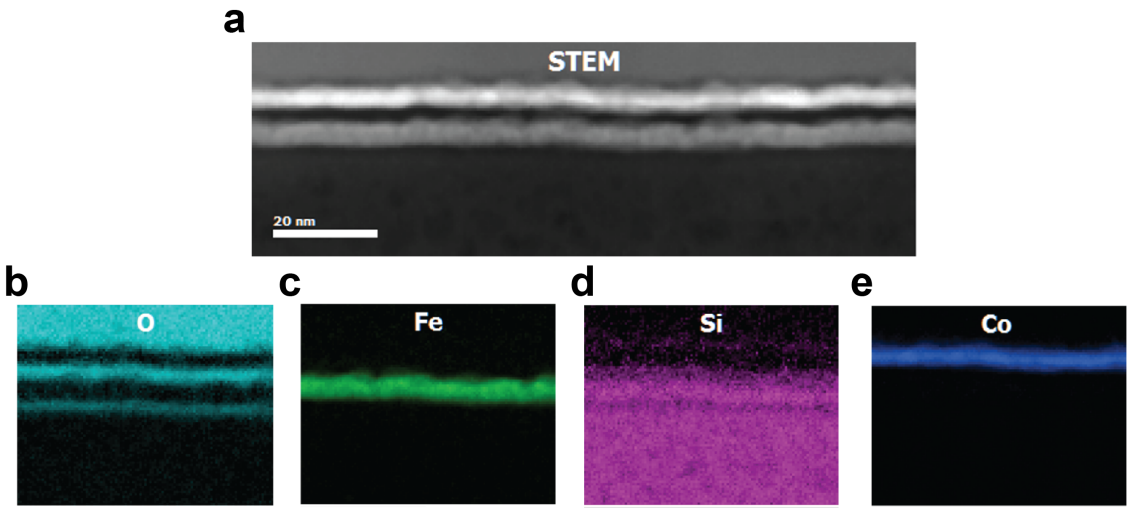

Figure 3.7: a, TEM imaging in STEM mode. b,c,d,e, EELS elemental mapping with different colors.

are then mounted onto the sample rotation stepping motor with a socket connected to the home-built connection network. AC current at low frequency (< 1500 Hz) is injected with a Keithley 6221 AC/DC current source, and both first and second harmonic Hall voltages were detected through Signal Recovery 7270 dual harmonic lock-in amplifier. This measurement is carried out as a function of three parameters including the angle between current and external magnetic field, magnetic field strength and current amplitude. We measured at least three different devices on each a-Fe_xSi_{100-x} sample, and we repeat this through 4 different batches of depositions. In other words, we repeat the deposition of concentration series of a-Fe_xSi_{100-x} at least 4 times, fabricated devices out of all the samples and measured at least three different devices on each sample via the full current, field, angle dependence harmonic Hall measurements.

To characterize spin-orbit torque in a-Fe_xSi_{100-x}, we first patterned the stacks into Hall bar structures (Fig. 3.a, inset) with optical lithography and Ar ion-milling (Appendix C). We measured both double Hall bars mentioned above in section 3.4 and different single Hall bars for the harmonic Hall measurement. The single Hall bars have current lead of 5 (12) micron in width and 30 (30) micron in length and Hall voltage leads that are 3 (5) micron in width and 30 (30) micron in length. Next, we carried out harmonic Hall measurements [9, 162] on a concentration series of a-Fe_xSi_{100-x} (5.5 ± 0.5 nm) / oxide (1 ± 0.5 nm) / Co (4 nm) tri-layer at room temperature. The insulator is formed by a chemical wet-etch treatment that constructs an oxide composed of iron oxide, silicon oxide and cobalt oxide characterized through electron energy loss spectroscopy (EELS) (Fig. 3.7, Appendix C). The structure of the oxide is characterized through high-resolution TEM and local FFT to be amorphous (Fig. 3.2c). In Fig. 3.8, we show a full set of measured signal and extracted parameters from a single device (current line width 12 micron) from a-$Fe_{45}Si_{55}$ (5.5 nm) / oxide (1 ± 0.5 nm) / Co (4 nm). For the harmonic Hall measurement, an oscillating a.c. current is injected, and transverse voltages at both its first (Fig. 3.8b) and second harmonic (Fig. 3.8c) are measured. We conduct this measurement as a function of in-plane angle, current magnitude and external field strength. A clean planar Hall signal is observed in a-$Fe_{45}Si_{55}$ (Fig. 3.8b) as well as all other a-Fe_xSi_{100-x} concentrations with no appreciable in-plane uniaxial anisotropy. In addition to the SOT signals including the field-like (FL) torque (Figure 3.8) and the damping-like (DL) torque, thermoelectric effects, such as anomalous Nernst effect (ANE) and ordinary Nernst effect (ONE) that can lead to spurious results have been carefully considered [9, 162] (Fig. 3.8d, h). By doing a full field angle (φ_B) and magnitude (B_{ext}) sweep, each individual contribution in the second harmonic signal can be differentiated (Fig. 3.8d, 3.8h). After separating out the thermoelectric contribution and field-like torque in the second harmonic signal (Fig. 3.8e), we obtain the effective field strength due to the damping-like spin-orbit torque $\Delta B_{DL,SOT}$ at different injected current densities in the a-Fe_xSi_{100-x} layer (Fig. 3.8f). One important quantity required in the extraction of $\Delta B_{DL,SOT}$ from the second harmonic voltage is the anomalous Hall voltage V_{AHE} (or resistance R_{AHE}). For my samples, I saturate the magnetization of the magnetic stacks understudy in the out-of-plane direction to obtain this quantity (Fig. 3.9). This has to be done on every sample since slight variation exists across different device dimension and

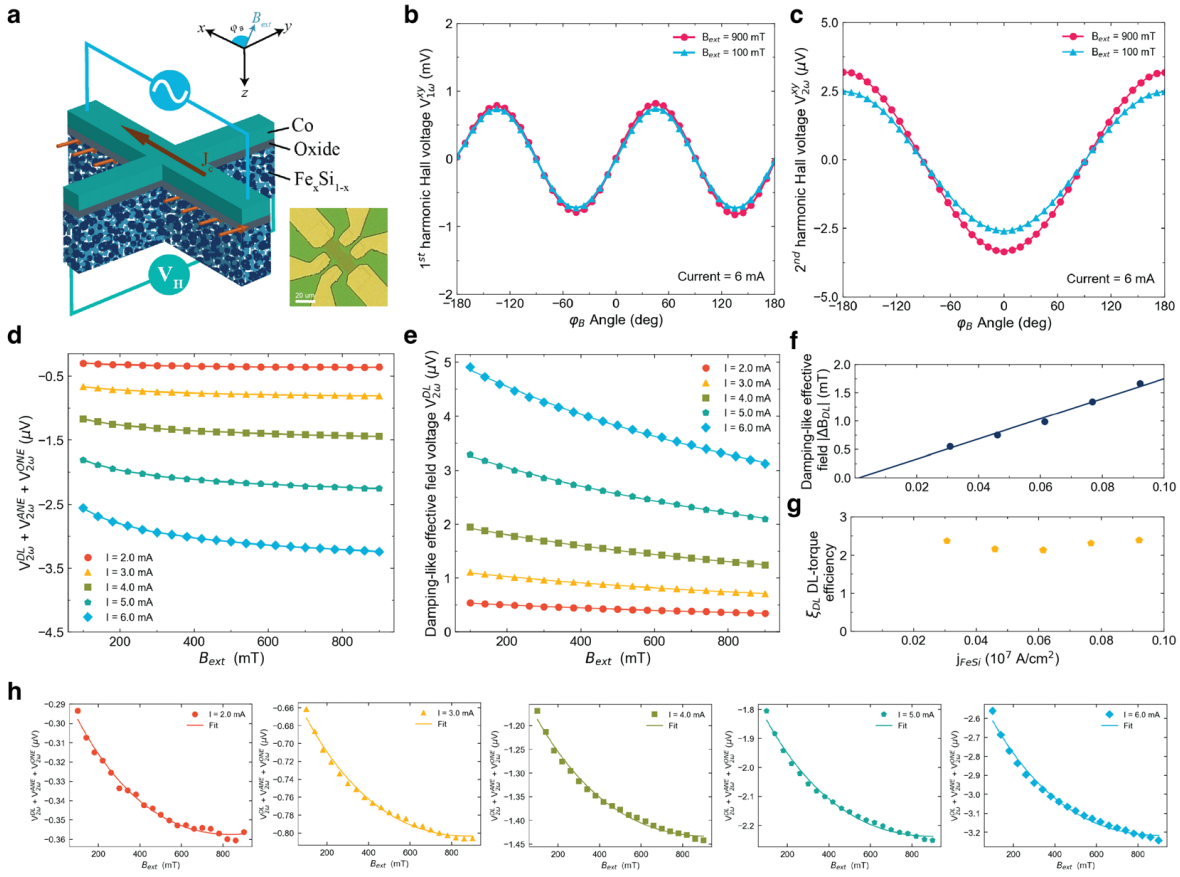

Figure 3.8: a, Schematic of patterned Hall bar on a-$Fe_{45}Si_{55}$ (5.5 nm) / oxide (1∼1.5 nm) / Co (4 nm) and measurement scheme. Inset, optical microscope image of the double Hall bar device structure patterned for harmonic Hall measurement. b, First harmonic voltage of the a-$Fe_{45}Si_{55}$ (5.5 nm) / oxide (1∼1.5 nm) / Co (4 nm) heterostructure. c, Second harmonic voltage. d, The DL torque effective field and thermoelectric contribution as a function of external field obtained from angle fit to $\cos(\varphi_B)$. e, The DL torque effective field signal after eliminating the thermoelectric effects including anomalous Nernst effect and ordinary Nernst effect. The clear $1/(B_{ext}+B_{anisotropy})$ dependence shows a strong signature of DL spin-orbit torque. f, DL torque effective field as a function of injected current density in the a-$Fe_{45}Si_{55}$ layer. g, SOT efficiency (ξ_{DL}) extracted to be an average of 2.13 across five different current values. The consistency across different current values confirms the clear signal of SOT. h, Individual plots (varying a.c. current amplitude) of the field-dependent fit to the $\cos(\phi_B)$ component of the second harmonic signal.

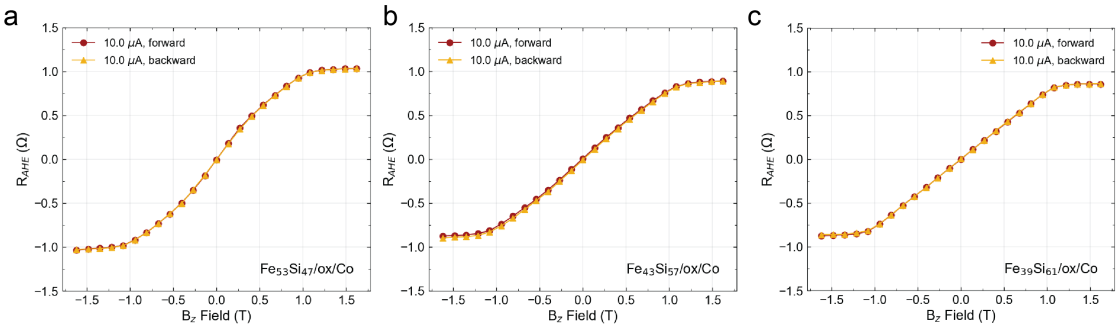

Figure 3.9: Anomalous Hall resistance (R_{AHE}) as a function of magnetic field in the out-of-plane direction (z-direction) on several devices of different Fe concentration.

sample-to-sample variability (Fig. 3.9).

Detail analysis of in-plane harmonic Hall measurement data

From the harmonic Hall measurement, a set of first and second harmonic voltages as a function of current, magnetic field and angle between field and current is obtained (Fig. 3.8b and 3.8c, Fig. 3.10b and 3.10c, Fig. 3.12a, 3.12b). First, we carry out an angle fit with

$$V_{1\omega}^{xy} = V_{PHE} \times sin(2\varphi_B) \tag{3.1}$$

to the first harmonic Hall voltage for each set of current and field combinations to extract out V_{PHE} (Fig. 3.8b, Fig. 3.10b). Next, we carry out an angle fit of

$$V_{DL+ONE+ANE} \times cos(\varphi_B) + V_{FL} \times cos(\varphi_B)cos(2\varphi_B) \tag{3.2}$$

to the second harmonic Hall voltage for each set of current and field combinations. At this point, $V_{DL+ONE+ANE}$ as a function of current and field (Fig. 3.8d) and V_{FL} as a function of current and field (Fig. 3.10i) are obtained. From V_{FL}, we carry out a field-dependence fit with

$$V_{PHE} \times \frac{\Delta B_{FL}}{B_{ext}} \tag{3.3}$$

, to extract the field-like torque effective field ΔB_{FL} as a function of current (Fig. 3.10j). Since the field-like torque effective field ($\Delta B_{FL} = \Delta B_{FL,SOT} + B_{Oe}$) contains both the Oersted field B_{Oe} and field-like spin-orbit torque effective field $\Delta B_{FL,SOT}$, by subtracting out the Oersted field contribution from the total field-like torque effective field, the effective field due to field-like spin-orbit torque $\Delta B_{FL,SOT}$ is obtained (Fig. 3.10j). The Oersted field is calculated from

$$H_{Oe} = j_{FeSi} \times \frac{t_{FeSi}}{2} \tag{3.4}$$

and is found to have the same direction as the field-like spin-orbit torque effective field $\Delta B_{FL,SOT}$ and minimal in samples with insulator insertion. Next, to extract the damping-like torque effective field, we conduct a field-dependence fit to $V_{DL+ONE+ANE}$ with expression

$$\frac{V_{AHE}}{2}\frac{\Delta B_{DL}}{B_{ext}+\mu_0 M_{eff}}+\alpha\nabla T+\beta\nabla T B_{ext} \tag{3.5}$$

to separate thermal contributions (Fig. 3.8d and 3.8e, Fig. 3.10d) and extract ΔB_{DL} (Fig. 3.8f, Fig. 3.10k) as a function of current density. To quantify the spin-charge conversion efficiency, the often-used figure of merit is the so called SOT efficiency ξ_{SOT}. From the harmonic Hall measurement, the effective SOT efficiency due to the damping-like torque is given by[9, 161]

$$\xi_{DL}=\frac{2e}{\hbar}M_s t_{FM}\frac{\mu_0 H_{DL}}{J_{NM}}, \tag{3.6}$$

where M_s is the saturation magnetization of the ferromagnet, t_{FM} is the thickness of the ferromagnet, $\mu_0 H_{DL}$ is the damping-like torque effective field strength and J_{NM} is the current density flowing through the a-Fe_xSi_{100-x} layer. This expression captures the amount of spin current generated per charge current injected in the a-Fe_xSi_{100-x} layer. With ΔB_{DL}, we can calculate the SOT efficiency for each injected current value or current density in the underlayer (Fig. 2g, Fig. 3.10l).

Discussion on large damping-like SOT efficiency (ξ_{DL})

From this analysis, the SOT efficiency is found to be around 2.13 for a single device over five different current densities on a-$Fe_{45}Si_{55}$ (5.5 nm) / oxide (1∼1.5 nm) / Co (4 nm) (Fig.3.8g). The large SOT efficiency found in a-$Fe_{45}Si_{55}$ (5.5 nm) / oxide (1∼1.5 nm) / Co (4 nm) ($\xi_{DL}\sim$ 2.0) has the same order of magnitude as that in topological insulators ($\xi_{DL}>2.0$) [124, 39, 92], which has the highest SOT efficiency ever observed. For the sample without the oxide insertion (Fig. 3.10), the SOT efficiency is about two orders of magnitude smaller ($\xi_{DL}\sim$ 0.04) but observable. For both samples, SOT is clean and observable from a few signatures: 1. the clear $1/(B_{ext}+B_{demagnitizing})$ dependence in the second harmonic Hall signal, 2., the linear increase in ΔB_{DL}, and 3, the near constant SOT efficiency across different current density. While there is a small amount of field-like SOT in the sample without the oxide insertion, there is no appreciable field-like SOT in the sample with oxide insertion (figure 3.8, 3.10). To even further confirm the large SOT efficiency measured in a-$Fe_{45}Si_{55}$/oxide/Co, I benchmarked my measurement with a commonly studies SOT system - Pt/Co (figure 3.11) where the SOT efficiency should be between $5\sim20\%$ [111, 222] and a simple control sample with only Co layer grown on SiN_x substrate. From my measurement on Pt(6 nm)/Co (2.5 nm) and Co (4)-only samples, the SOT efficiency is 0.2 for Pt(6 nm)/Co (2.5 nm) (figure 3.11) and negligible in Co (4 nm)-only (figure 3.12).

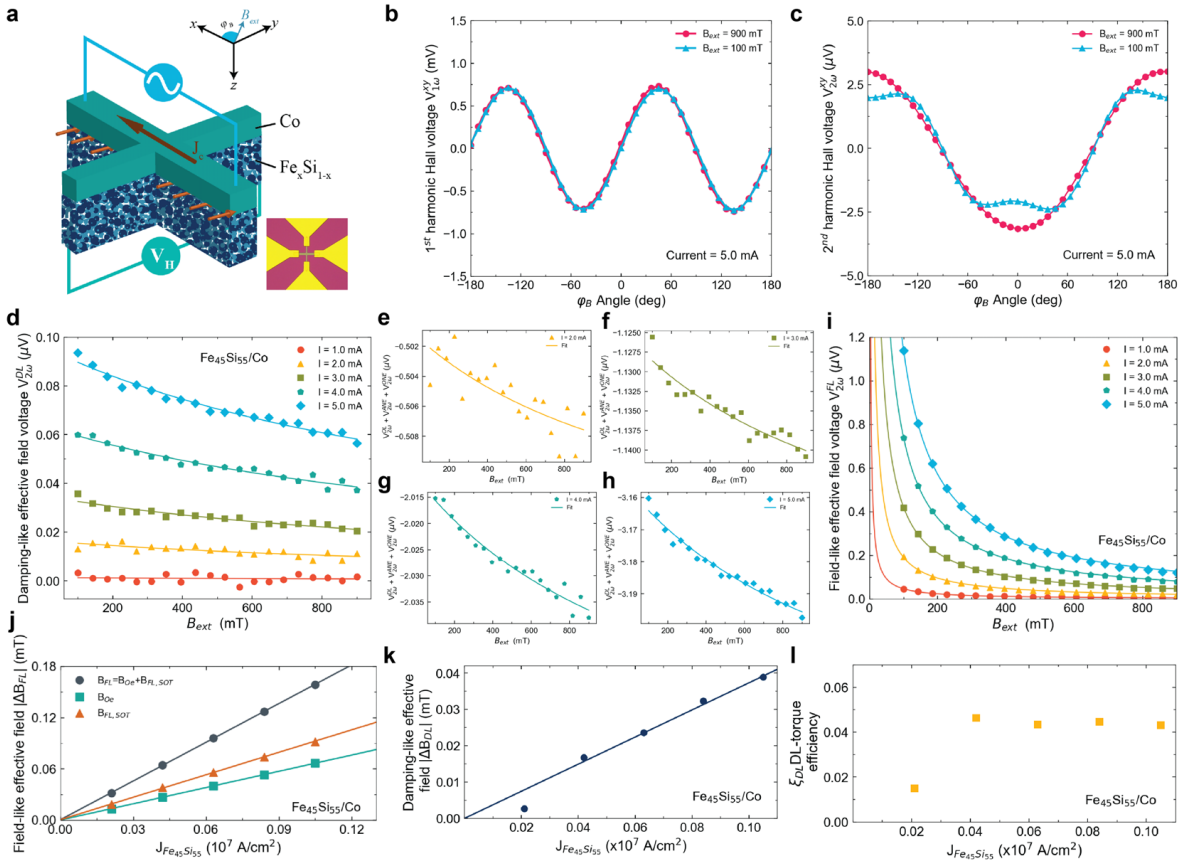

Figure 3.10: Spin-orbit torque characterization of a-$Fe_{45}Si_{55}$ (8±0.5 nm) / Co (4 nm) by harmonic Hall measurements. a, Schematic of the harmonic Hall measurement setup. Inset: Optical microscope image of the fabricated single Hall bar device. The device shown here has a current line of 5 micron in width and a voltage line of 3 micron in width. Both lines are 30 micron in length. b, First harmonic voltage of the a-$Fe_{45}Si_{55}$ (8±0.5 nm) / Co (4 nm) heterostructure. c, Second harmonic voltage of the a-$Fe_{45}Si_{55}$ (8±0.5 nm) / Co (4 nm) heterostructure. d, The DL torque effective field signal after eliminating the thermoelectric effects including anomalous Nernst effect and ordinary Nernst effect. e-h, Detail individual plots and fitting of the field dependent $\cos(\phi_B)$ component from four different current amplitudes. i, Extracted FL torque effective field voltage in the second harmonic signal. j, Extracted FL torque effective field. Here, field-like torque includes the contribution not only from FL SOT but also from the Oersted field contribution. In a-$Fe_{45}Si_{55}$ / oxide / Co, no appreciable FL SOT signal is observed. k, DL torque effective field as a function of injected current density in the a-$Fe_{45}Si_{55}$ layer. l, SOT efficiency (ξ_{DL}) extracted to be an average of 0.04 across five different current values.

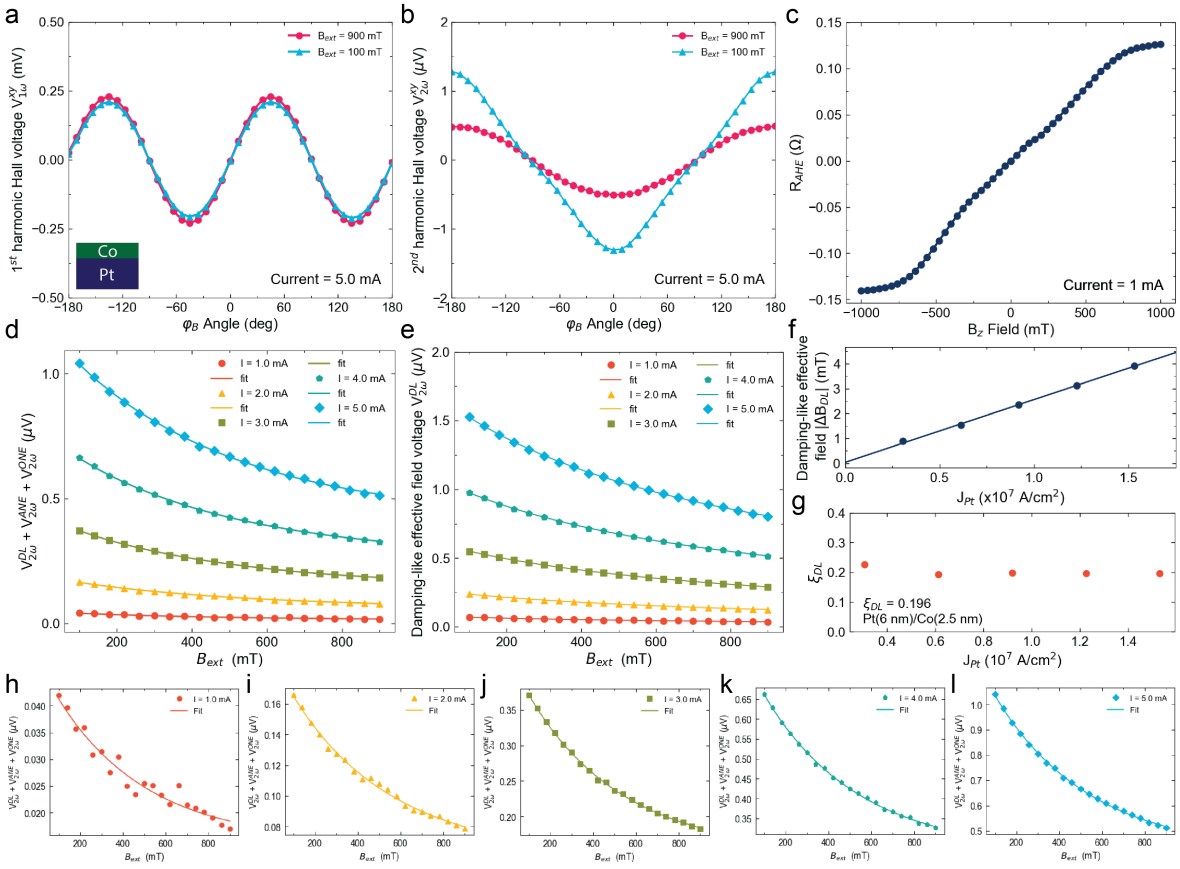

Figure 3.11: Harmonic Hall measurement on benchmark sample Pt (6 nm) / Co (2.5 nm). a, First harmonic Hall voltage of Pt (6 nm) / Co (2.5 nm). Inset, schematic of the stack under study. b, Second harmonic Hall voltage of Pt (6 nm) / Co (2.5 nm). c, Anomalous Hall effect resistance in with the field applied in the z-direction to saturate the in-plane moments out-of-plane. d, The $\cos(\phi_B)$ component from the second harmonic Hall signal which contains information including the damping-like (DL) SOT, anomalous Nernst effect, and ordinary Nernst effect. e, DL-torque component of second harmonic voltage. f, Extracted DL-torque effective fields as a function of current density in Pt. g, Extracted DL-SOT efficiency in Pt (6 nm) / Co (2.5 nm) is around 0.2. This value is close to the reported value of slightly higher resistivity Pt or when the Pt/Co interface exists a very thin Pt-Co alloy[222]. h, Individual plots and fitting of the field dependent $\cos(\phi_B)$ component from five different current amplitudes.

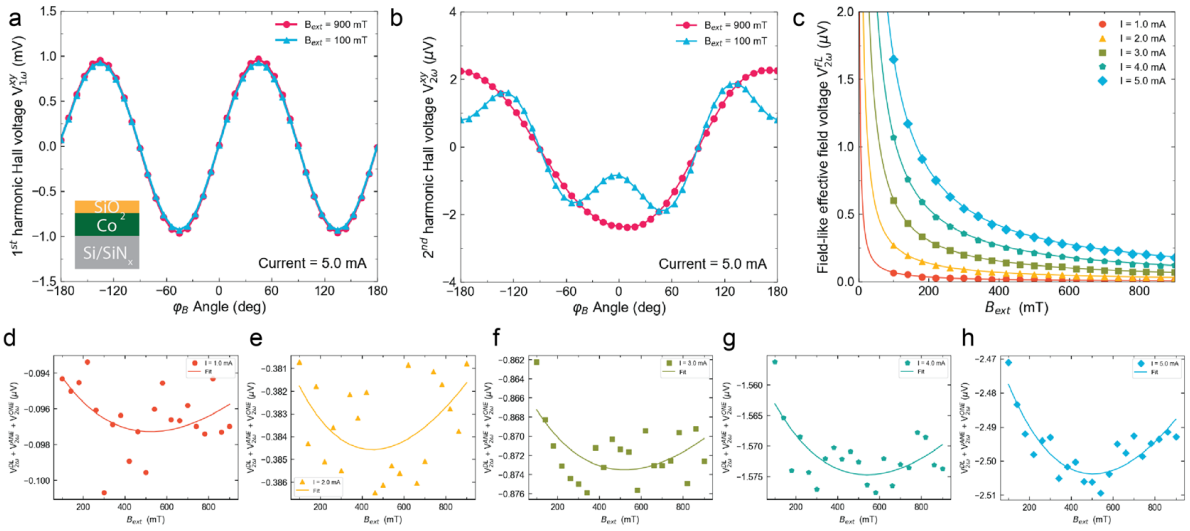

Figure 3.12: Harmonic Hall measurement on control sample Si / SiN_x substrate / Co (4 nm) / SiO_2 (3 nm). This control sample is to check any SOT generation due to strain effect of the 280 nm silicon nitride underlayer or SiO_2 capping. a, First harmonic voltage of Si / SiN_x / Co (4 nm). Inset shows the detail of the stack. b, Second harmonic voltage. c, Extracted field-like torque effective field voltage in the second harmonic signal. The strong field-like torque signal here is due to the Oersted field generated from the contact Ti / Au layer or current distribution imbalance in the Co layer. d-h, Detail individual plots and fitting of the field dependent $\cos(\phi_B)$ component from five different current amplitudes. No clear dependence of the $1/(B_{ext}+B_{demagnitizing})$ in the fitting indicates no SOT generated in this stack, which is expected. Without any spin source such as Pt or a-Fe_xSi_{100-x}, no damping-like SOT can be observed. This also shows that no torque arises from the SiO_2 capping layer.

a-$Fe_{45}Si_{55}$ thickness dependence of SOT

Thickness dependence of SOT efficiency is carried out from 2.5 to 8.5±0.5 nm at the concentration close to 45% Fe. The resistivity values of a-$Fe_{45}Si_{55}$ across all thicknesses are within ± 25 of 900 $\mu\Omega$-cm. This indicates that the Fe concentration does not deviate from 45% significantly. In Fig. 3.13a, we observe a steady increase in SOT efficiency as the a-$Fe_{45}Si_{55}$ thickness increases. While the SOT efficiency (ξ_{DL}) reaches 2.706 at 8.5±0.5 nm, for 4.5 and 6.5±0.5 nm the ξ_{DL} are 1.883 and 1.964 respectively which agrees well with the peak ξ_{DL} (1.99) of a-$Fe_{45}Si_{55}$ (5.5±0.5 nm) in Fig. 3.13a. If we fit the thickness dependence result to the diffusion theory [213, 155] with the assumption of perfect spin transparency across the oxide, the SOT efficiency can expressed as

$$\xi_{DL} = \theta_{SH}\left[1 - sech\left(\frac{t_{Fe_{45}Si_{55}}}{\lambda_s}\right)\right] + C \tag{3.7}$$

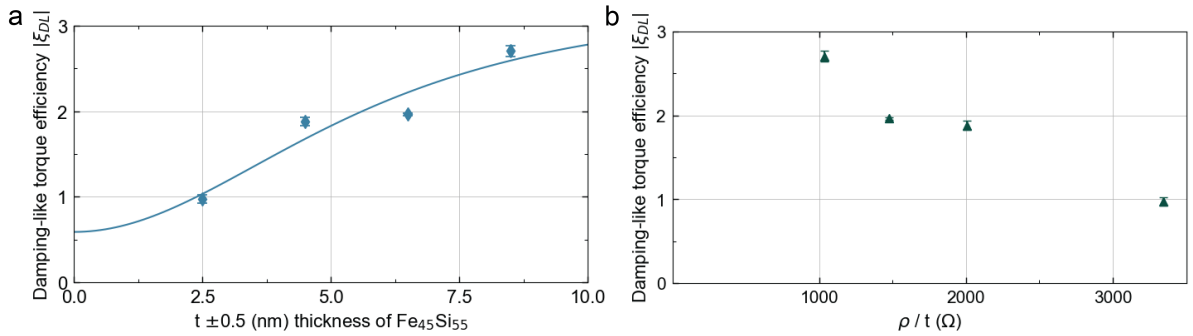

Figure 3.13: a, Thickness dependence of damping-like SOT efficiency in a-$Fe_{45}Si_{55}$ (t) / oxide (1±0.5 nm) / Co (4 nm) tri-layer. The SOT efficiency increases as the a-$Fe_{45}Si_{55}$ thickness increases. To extract parameters such as intrinsic spin Hall angle (θ_{SH}) and spin diffusion length (λ_s) we fit the thickness dependence SOT efficiency according to the diffusion theory[213, 155]. b, Damping-like SOT efficiency as a function of the ratio between the resistivity and thickness. According to the conventional trend, the higher the resistance the larger the spin-torque. Here, we see an opposite trend which the largest SOT efficiency is observed at the lowest resistance.

where λ_s is the spin diffusion length, θ_{SH} is the intrinsic spin Hall angle and C is the constant due to interfacial Rashba contribution. From the fitting, we obtain $\theta_{SH} = 2.605$, λ_s= 3.96 nm and $C = 0.59$.

While SOT materials are often benchmarked with resistivity being the characteristic materials transport property, individual device resistance is another metric to be utilized when comparing absolute quantities. In Fig. 3.13b, we compare the SOT efficiency as a function of resistance (i.e. ρ / $t_{a-Fe_{45}Si_{55}}$). We found that the SOT efficiency decreases as the device resistance increases. This is opposite to the conventional trend where higher resistivity yields higher SOT efficiency. Also, this shows that the SOT may not be an artifact due to heating in a-$Fe_{45}Si_{55}$ / oxide / Co.

3.6 Fe concentration dependence of spin-orbit torque and its potential origin

Fe concentration dependence results

For the Fe concentration study, we repeat this measurement on multiple devices of each sample from the concentration series a-Fe_xSi_{100-x} (5.5±0.5 nm) / oxide (1±0.5 nm) / Co (4 nm). We limited the maximum Fe concentration to be x = 60, since a-Fe_xSi_{100-x} begins to transition away from the non-ferromagnetic phase with onset concentration near x = 50 [87]. For $Fe_{55}Si_{45}$ and $Fe_{60}Si_{40}$ single layer films, we point out that the saturation magnetization

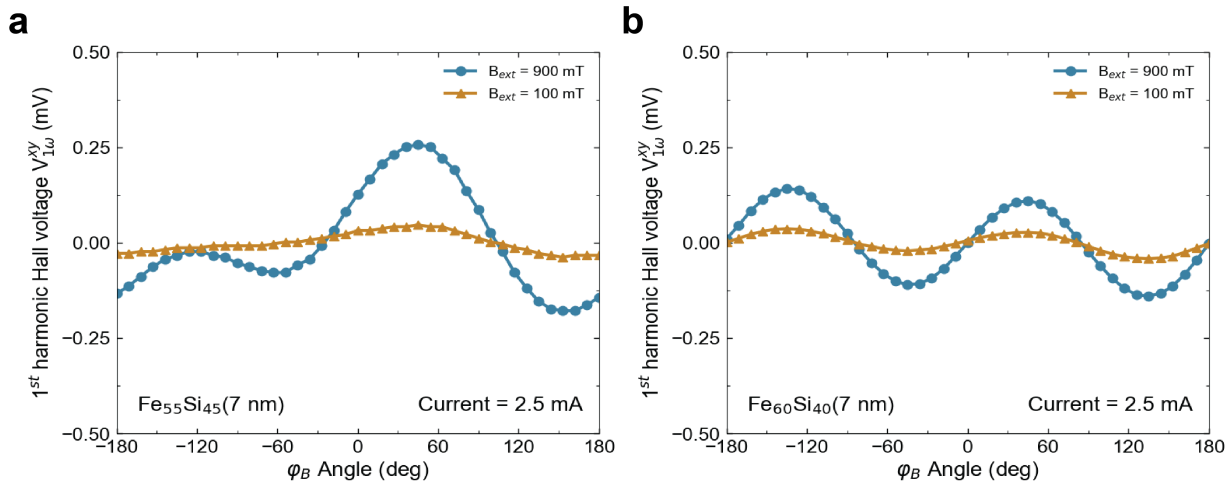

Figure 3.14: a, 1st harmonic Hall signal of $Fe_{55}Si_{45}$ and b, $Fe_{60}Si_{40}$.

values (Fig. 3.4) are increased and a small planar Hall effect voltage can be observed at large magnetic fields (>500 mT) (figure 3.14).

By varying the concentration of Fe we found not only a clear concentration dependence on ξ_{DL} but also an overall enhanced ξ_{DL} (Fig. 3.15a). We observed a maximum ξ_{DL} of 2.0 around x = 45 and the ξ_{DL} decreases as the concentration moves away from x = 45 in both directions (Fig. 3.15a). While the clear Fe concentration dependence is observed in a-Fe_xSi_{100-x} (5.5±0.5 nm) / oxide (1±0.5 nm) / Co (4 nm), no Fe concentration dependence is observed in a-Fe_xSi_{100-x} (8 nm) / Co (4 nm) (Fig. 3.15b). In addition, the overall ξ_{DL} is found to be much smaller ($\sim$ 0.05 across all Fe concentrations) when there is no oxide insertion (Fig. 3.15b). This observation shows the importance of the oxide insertion for unpinning the Fermi level in revealing the intrinsic SOT efficiency which is a function of Fe concentration. This concentration trend agrees with the view of Berry density as a function of energy in typical crystalline materials. Here, the change in reduced density of state region on the energy scale through Fe concentration engineering [87] drives an equivalent effect on the SOT generation, which is similar to the case of intrinsic AHE scaling in ferromagnetic a-Fe_xSi_{100-x}[87, 89]. More detail on the origin of such large torque and the role of oxide insertion is provided in the following paragraph.

Potential origin of large SOT in amorphous a-Fe_xSi_{100-x}

There are a few potential origins that can contribute to such concentration dependence profile including the effect of DOS and onset of the ferromagnetism. We propose that one potential origin of the large SOT in a-Fe_xSi_{100-x} is the reduced density of states (DOS) in the energy scale near the Fermi level [87]. We borrow the concept of Berry Curvature in crystalline

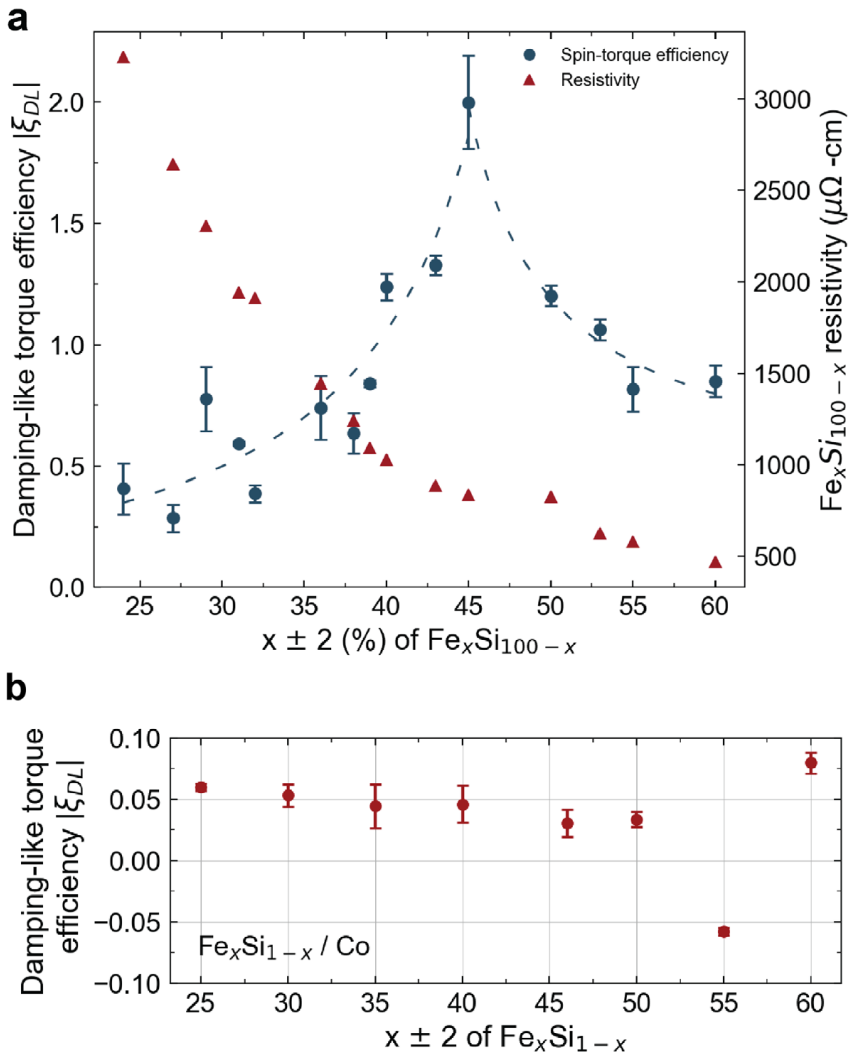

Figure 3.15: a, Fe (x) concentration dependent damping-like SOT efficiency (ξ_{DL}) in a-Fe_xSi_{100-x} (5.5±0.5 nm) / oxide (1±0.5 nm) / Co (4 nm) tri-layer. ξ_{DL} increases and reaches maximum around x = 45 and further decreases as Fe concentration increases above x = 45. Error bars represent one standard deviation uncertainty. The resistivity of a-Fe_xSi_{100-x} as a function of Fe concentration is plotted with the axis on the right as convenient comparison. b, Fe concentration dependence of SOT efficiency in a-Fe_xSi_{100-x} / Co bi-layers. SOT efficiencies are measured to be around 0.05 across all Fe concentrations in a-Fe_xSi_{100-x} / Co except x = 55 and 60, which are potentially due to the weak ferromagnetism in a-Fe_xSi_{100-x} (x = 55 and 60) layer.

materials to explain the spin current generation in amorphous materials. However, instead of utilizing band structure which is well-defined in a crystalline material, we attempt to explain the spin current generation in terms of density of states in a fully amorphous material. In a crystalline material with a well-defined band structure, we can calculate the spin Hall conductivity (σ^z) through the Kubo formula which the Berry Curvature contributes greatly to the spin Hall conductivity in the k-space [60]. The expressions for the Berry curvature ($\Omega^{\mathbf{k}}$) and the Kubo Formula for spin Hall conductivity (σ^z_{xy}) are [60]:

$$\Omega^z_n(\mathbf{k}) = \sum_{n' \neq n} \frac{2Im[\langle \mathbf{k}n|j^z_x|\mathbf{k}n'\rangle\langle \mathbf{k}n'|v_y|\mathbf{k}n\rangle]}{(\epsilon_{\mathbf{k}n} - \epsilon_{\mathbf{k}n'})^2} \tag{3.8}$$

$$\sigma^z_{xy} = \frac{e}{\hbar}\sum_{\mathbf{k}} \Omega^z(\mathbf{k}) = \frac{e}{\hbar}\sum_{\mathbf{k}}\sum_{n} f_{\mathbf{k}n}\Omega^z_n(\mathbf{k}) \tag{3.9}$$

where $j^z_x = \frac{1}{2}\{s_z, v\}$ is the spin current operator with $s_z = \frac{\hbar}{2}\beta\sum_z$ and $f_{\mathbf{k}n}$ is the Fermi distribution function for the nth band at $\mathbf{k}$. $\Omega^{\mathbf{k}}_n$ is the Berry curvature for the nth band[60]. From expression (1), we can immediately know that a large Berry curvature ($\Omega^{\mathbf{k}}$) can be obtained with near degenerate energy states from the denominator of the expression and large spin-orbit matrix elements in the numerator.

B20 phase FeSi is known to be a small gap semiconductor (50∼100 meV) [47, 142, 122] and non-magnetic in its ground state from DFT calculations. However, experimentally, B20 FeSi possess rich signatures of correlated system and topological properties including Kondo insulator [47], conducting surface state [47], ferromagnetic conducting surface state [142] and spin-momentum locking surface state[142]. These properties indicate the potential to generate a large spin-torque. In the terms of Berry curvature, near degenerate states close to the Fermi level in B20 FeSi along with the large spin-orbit coupling near the surface (e.g. Rashba-type spin splitting at the interface in Ohtsuka *et al.* may intrinsically contribute to a large spin Hall conductivity thus a large spin-orbit torque. In Mazurenko *et al.*, the band structure calculation via DFT with varying atomic position parameters indicates: 1. a small gap exists along several k-vectors (Fig. 1 of Mazerenko *et al.*) with different atomic position parameters [u(Si), u(Fe)], 2. by changing the atomic position parameters the relative position of these small gap region to the Fermi level in the energy scale can be tuned. Since tuning the atomic position is nontrivial in a real crystal or thin film epitaxy growth, it may be challenging to observe these effects in single crystals. As a result, we ask the question of whether an amorphous system can also meet these criteria: 1. near degenerate states near the Fermi level 2. large spin-orbit coupling near the surface/interface. If so, we can tune the relative concentration between Fe and Si in a-Fe_xSi_{100-x} to achieve this Fermi level-dependent spin current generation. Since the positioning of the Fermi level near the small gap or reduced density of state (DOS) region in the amorphous material is important, elimination of Fermi level pinning issue is crucial to observe the spin current generation in a-Fe_xSi_{100-x}.

Fermi level pinning is a common issue at Schottky junctions where semiconductor interfaces metal. The free electron wavefunction from the metal penetrates into the first few

angstroms of semiconductor where no electronic states are allowed. As a result, the Fermi level will be pinned at the energy level where charge neutrality is satisfied (Fig. 3.1a,b). Although a-Fe_xSi_{100-x} is a high resistivity metallic-like alloy of silicon and iron, there exists an abundance of Si atoms at the interface between a-Fe_xSi_{100-x} and Co. Locally, Fermi level pinning can still be an issue and plaque the spin current generation. As a result, insertion of a thin oxide that can both alleviate Fermi level pinning and provide spin transmission is essential to the observation of a large spin-orbit torque in a-Fe_xSi_{100-x}.

While the potential origin due to the electronic structure (DOS) is reasonable and matches the Fe concentration dependence, the effect from the onset of ferromagnetism can not be overlooked and remain elusive in a-Fe_xSi_{100-x}. In the next chapter, I will discuss the effect of ferromagnetic transition toward SOT generation in such light element silicide system - amorphous CoSi.

Experimental evidence of weak enhancement in spin transparency to reinforce the role of Fermi level depinning in a-Fe_xSi_{100-x}/oxide/Co

Insertion of a thin nickel oxide in a heavy metal/ferromagnet bi-layer has been shown to be capable of enhancing the interfacial spin transparency to near unity [225] which in turn greatly enhances the measured SOT efficiency. To further study the effect of insulator insertion on the enhancement of SOT efficiency and the spin transparency at the interface, I conducted ferromagnetic resonance (FMR) measurement to compare the interfacial spin-mixing conductance of a-$Fe_{45}Si_{55}$ / oxide / Co and a-$Fe_{45}Si_{55}$ / Co. FMR was conducted through a home-built setup composed of a Model 5403 GMW electromagnet with a Hall probe for field sensing and controlling, an Agilent E4421B RF Generator, a Signal Recovery 7270 lock-in amplifier, a home-built RF network and impedance matched chip holder. The fabricated micron size strip is contacted with a co-planar waveguide and then mounted on a impedance matched chip carrier with wirebonding. An amplitude modulated RF current is injected by the Agilent E4421B through a bias T to the sample, and the DC mix down voltage is measured by the lock-in amplifier locking to the amplitude modulation frequency. As the in-plane magnetic field is swept in magnitude, the ferromagnetic resonance criteria was satisfied thus a resonance linewidth is measured.

Spin-mixing conductance of the ferromagnet adjacent to a-Fe_xSi_{100-x} is extracted through the enhancement of damping constant. This enhancement can be described by the expression[145]

$$\alpha = \alpha_{int} + \frac{G_{eff}^{\uparrow\downarrow}\gamma\hbar^2}{2M_s d_{FM} e^2} \tag{3.10}$$

where α_{int} is the intrinsic damping constant of the ferromagnet, $G_{eff}^{\uparrow\downarrow}$ is the effective spin-mixing conductance, γ is the gyromagnetic ratio, M_s is the saturation magnetization, d_{FM} is the thickness of the ferromagnet, and e is the electron charge. The Gilbert damping

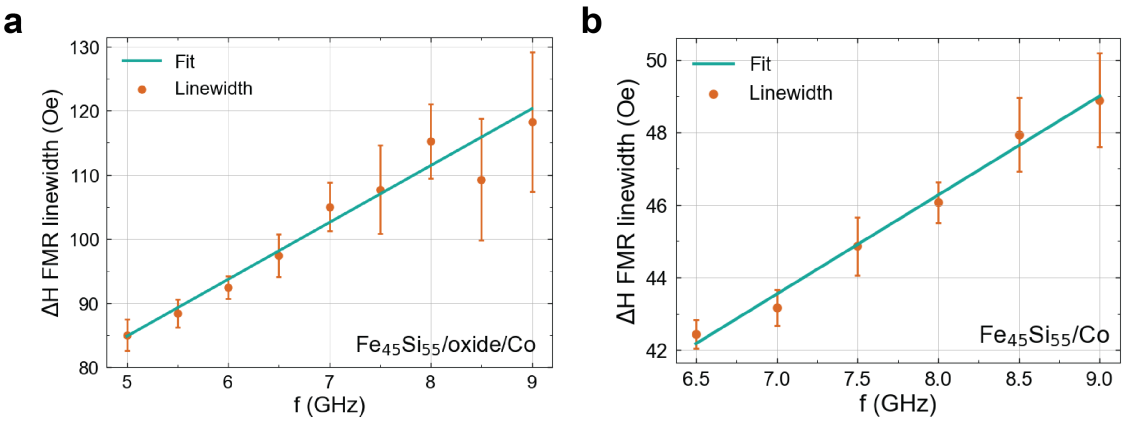

c

	Damping constant α	$\frac{\gamma\hbar^2}{2M_s d_{FM} e^2}$ [Ωm²]
$Fe_{45}Si_{55}$/Co	0.00765	8.775 x 10^{-18}
$Fe_{45}Si_{55}$/oxide/Co	0.02482	9.192 x 10^{-18}

d

$$\alpha = \alpha_{int} + G_{eff}^{\uparrow\downarrow} \frac{\gamma\hbar^2}{2M_s d_{FM} e^2}$$

Figure 3.16: Measurement of effective damping constant for extracting spin-mixing conductance through ferromagnetic resonance (FMR). Linewidth of FMR measurement curve as a function of frequency in **a**, *a*-$Fe_{45}Si_{55}$ / oxide / Co and **b**, *a*-$Fe_{45}Si_{55}$ / Co. Broadening of the linewidth corresponds to the enhancement of the magnetic damping constant due to spin current injection. By fitting the relation $\alpha = (\gamma/2\pi f)\Delta B$ where ΔB is the FMR linewidth and γ is the gyromagnetic ratio, the effective damping constant under the presence of spin current can be obtained. c, d, Spin mixing conductance via FMR measurement of effective magnetic damping constant on *a*-$Fe_{45}Si_{55}$ / Co and *a*-$Fe_{45}Si_{55}$ / oxide / Co for the comparison of spin transparency with the oxide insertion. The spin-mixing conductance in *a*-$Fe_{45}Si_{55}$ / oxide / Co is approximately 3x larger than that in *a*-$Fe_{45}Si_{55}$ / Co.

coefficient can be extracted by fitting the relation

$$\alpha = \frac{\gamma}{2\pi f}\Delta B, \tag{3.11}$$

to the linewidth which is a function of frequency. In this relation, α is the Gilbert damping coefficient, γ is the gyromagnetic ratio, ΔB is the linewidth of the resonance curve (Fig. 3.16). From our measurement, α is measured to be 0.00765 for *a*-$Fe_{45}Si_{55}$ / Co and 0.02482 for *a*-$Fe_{45}Si_{55}$ / oxide / Co (Fig. 3.16c). In the expression [145] (Fig. 3.16d) above, we found the factor $\gamma\hbar^2/(2M_s d_{FM} e^2)$ for *a*-$Fe_{45}Si_{55}$ / oxide / Co and *a*-$Fe_{45}Si_{55}$ / Co are 9.192 x 10^{-18} (Ωm^2) and 8.775 x 10^{-18} (Ωm^2) respectively. Because these both factors are very close and the intrinsic damping constant should be similar (since the same Co magnet is in

both samples), we estimate that $G_{eff}^{\uparrow\downarrow}$ is approximately 3x larger in a-$Fe_{45}Si_{55}$ / oxide / Co than that in a-$Fe_{45}Si_{55}$ / Co. According to spin transparency expression [221]

$$T_{int} = 2\frac{G_{eff}^{\uparrow\downarrow}}{G_{Fe_{45}Si_{55}}} \tag{3.12}$$

where $G_{Fe_{45}Si_{55}} = 1/(\lambda_s \rho_{Fe_{45}Si_{55}})$ and λ_s is the spin diffusion length, a 3x larger $G_{eff}^{\uparrow\downarrow}$ in a-$Fe_{45}Si_{55}$ / oxide / Co yields an approximately 3x larger spin transparency (T_{int}) compared to a-$Fe_{45}Si_{55}$ / Co.

From the FMR measurements (Fig. 3.16), we found that while the enhancement of the spin transparency at the interface due to the oxide insertion is appreciable (3x), it is insufficient to quantitatively explain the overall enhancement (20x to 40x) of the SOT efficiency especially for a-Fe_xSi_{100-x} (x = 40 % to 50 %). The enhancement of SOT efficiency with the insulator insertion is dominated by unpinning of the Fermi level on top of the increase in spin transparency, which unlocks their higher intrinsic spin current generation efficiency. This is distinct compared to the SOT efficiency enhancement due to enhanced interface spin transparency when a thin oxide is inserted between Pt and the ferromagnet [225]. In addition, this reinforces the understanding of reduced DOS as a function of energy for generating spin current in a-Fe_xSi_{100-x} through Fe concentration engineering. To reinforce the main role of the oxide to be Fermi level unpinning, SOT measurements are carried out in a-Fe_xSi_{100-x} / NiO / Co with a different type of oxide insertion - NiO. In a-Fe_xSi_{100-x} / NiO / Co, a large SOT and the Fe concentration dependence are still observable.

3.7 Unconventional scaling trend between resistivity and spin-torque efficiency

Following conventional understanding of SOT generation, the SOT efficiency (ξ_{SOT}) increases as the resistivity (ρ_c) of the spin source material increases [117] since

$$\xi_{SOT} = \frac{\sigma_s}{\sigma_c}\left(\frac{2e}{\hbar}\right) = \sigma_s \rho_c \left(\frac{2e}{\hbar}\right). \tag{3.13}$$

This is observed across commonly studied material systems that exhibits appreciable SOT [143, 223, 194] (Fig. 3.17). However, for an amorphous material, this trend is not expected as the symmetry breaking at the interface plays the dominant role for SOT and hence the bulk resistivity should not matter. Indeed, SOT efficiency in a-Fe_xSi_{100-x} shows an opposite trend where the SOT efficiency increases with decreasing resistivity (Fig. 3b). We note that the the conventional trend of decreasing SOT efficiency with decreasing resistivity presents a trade-off for SOT devices as this means that product of conductivity and SOT efficiency remains somewhat independent; consequently increasing SOT efficiency may not help in reducing the total switching current (flowing through spin Hall material and the magnet). Our results show that a-Fe_xSi_{100-x} shows a completely opposite trend, which otherwise seems

fundamental, while achieving large SOT efficiency (Fig. 3.17). This potentially significant because for the first time, a material system can provide a scalable spin-torque efficiency as a function of resistivity in the ideal direction for lowering the switching power or spin-torque energy cost. Moreover, this is achieved in a material system that is commercially ready similar to tungsten as a refractory metal in CMOS baseline.

A similar trend in terms of anomalous Hall angle as a function of charge conductivity is seen for ferromagnetic amorphous Fe, Co-based silicide and germanide [86] where an increasing conductivity is coupled with an increasing anomalous Hall angle. This shares the same signature as the SOT efficiency we observe in Fig. 3.17. The similarity between Fig. 3.17 and Fig. 5c in Karel *et al.* [86] shows the importance of the fully amorphous structure where the bulk resistivity is decoupled from the spin current generation phenomenon or origin.

3.8 SOT-switching of magnetization with PMA

SOT switching experiment

The most direct experimental method for studying SOT is to demonstrate SOT switching of a PMA magnet. In this section, we explore the possibility of efficient magnetization switching via the large SOT generated by a-Fe_xSi_{100-x}. The pulsed-current switching measurement was done through a home-built setup composed of a Keithley 6221 AC current source, a Keithley 2181A Nanovoltmeter, a Lakeshore 475 Gaussmeter, and a GMW 5403 electromagnet driven by a kepco power supply that can produce a bi-polar magnetic field up to 330 mT. To apply short current pulses and measure the voltage simultaneously, Keithley 6221 and 2181A are connected with RS-232 and trigger link cables in and configured in the pulse-delta mode. Keithley 6221 applies a short current pulse (200μs) with a series of amplitude and the 2181A measures the anomalous Hall voltage to read out the magnetization state. Device is connected in the Hall geometry. During the current pulse train with varying amplitudes and signs, an in-plane field is applied to break the symmetry along the current direction.

To study the switching properties, we integrated a ferromagnet with strong perpendicular magnetic anisotopry (PMA) on the a-$Fe_{45}Si_{55}$ layer with a thin oxide layer in between (Fig. 3.18a inset). From the vibrating sample magnetomery data, we can confirm the strong PMA (Fig. 3.18a). To conduct SOT switching measurements, we fabricated Hall bars from the PMA thin film heterostructure with various device dimensions in the micron size regime. The anomalous Hall resistance as a function of perpendicular field were measured on the device confirming the strong PMA after device fabrication (Fig. 3.18b). In Fig. 3.18c and 3.18d, clear magnetization switching can be observed with the expected chirality reversal upon reversing the in-plane symmetry breaking field sign. We find the critical switching current density (J_c) is as low as 1.3 x 10^6 A/cm^2 through the a-$Fe_{45}Si_{55}$layer for Hall bar device with dimension 6 μm in width and 40 μm in length and approximately 4.0 x 10^6 A/cm^2 for device with dimensions 20 μm in width and 70 μm in length (Fig. 3.18c, 3.18d).

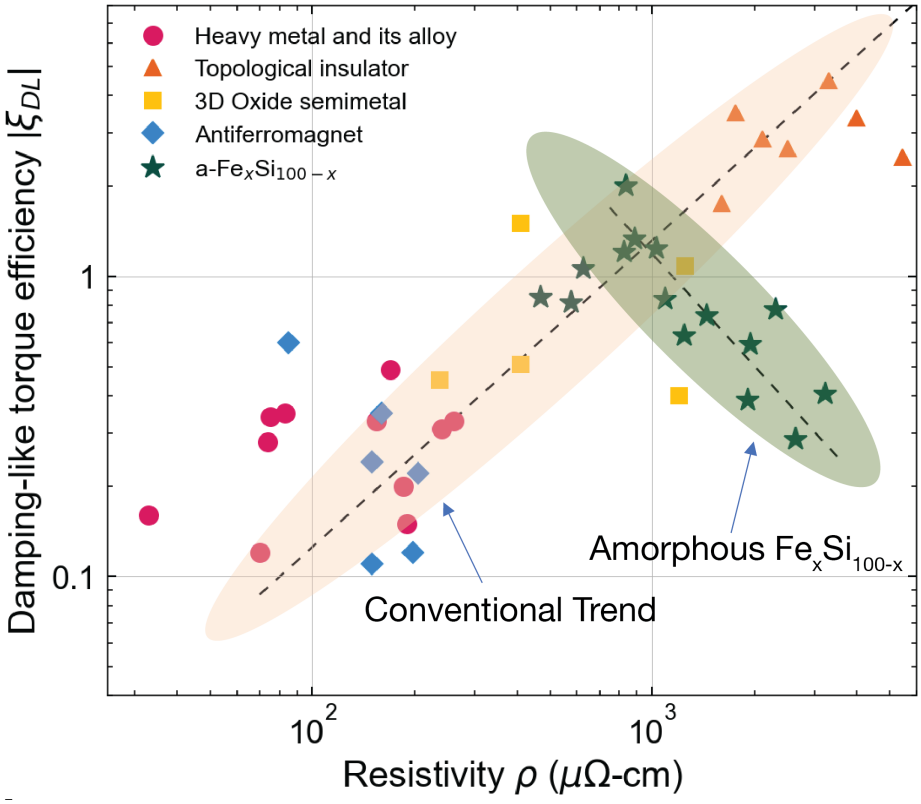

Figure 3.17: Benchmark of SOT efficiency in a-Fe_xSi_{100-x} against materials shown to possess appreciable SOT as a function of resistivity. The conventional trend of the SOT efficiency as a function of resistivity of the spin source material is that as resistivity increases the SOT efficiency increases. Here, the trend in a-Fe_xSi_{100-x} is completely opposite with the SOT efficiency increasing with decreasing resistivity from 25 % Fe to 45 % Fe. References to each data point is included in appendix D.

Thermal Stability of the PMA ferromagnet

If we benchmark the switching performance against different material systems with J_c alone, the legitimacy can be plagued by the different strength and properties of ferromagnet being switched. Thus, a good metric for evaluating switching performance is the switching efficiency (j_c / Δ) where Δ is the thermal stability factor of the ferromagnet being switched. The thermal stability (Δ) measurement was done through a home-built setup composed of a Keithley 6221 AC current source, a Signal Recovery 7270 Lock-in amplifier, a Lakeshore 475 Gaussmeter, and a GMW 5403 electromagnet driven by a kepco power supply that can produce a bi-polar magnetic field up to 330 mT. A small a.c. current (100uA) is applied to a Hall bar device and the transverse voltage is measured with the lock-in amplifier as a function of magnetic field applied in the out-of-plane direction (z-direction) with a hystere-

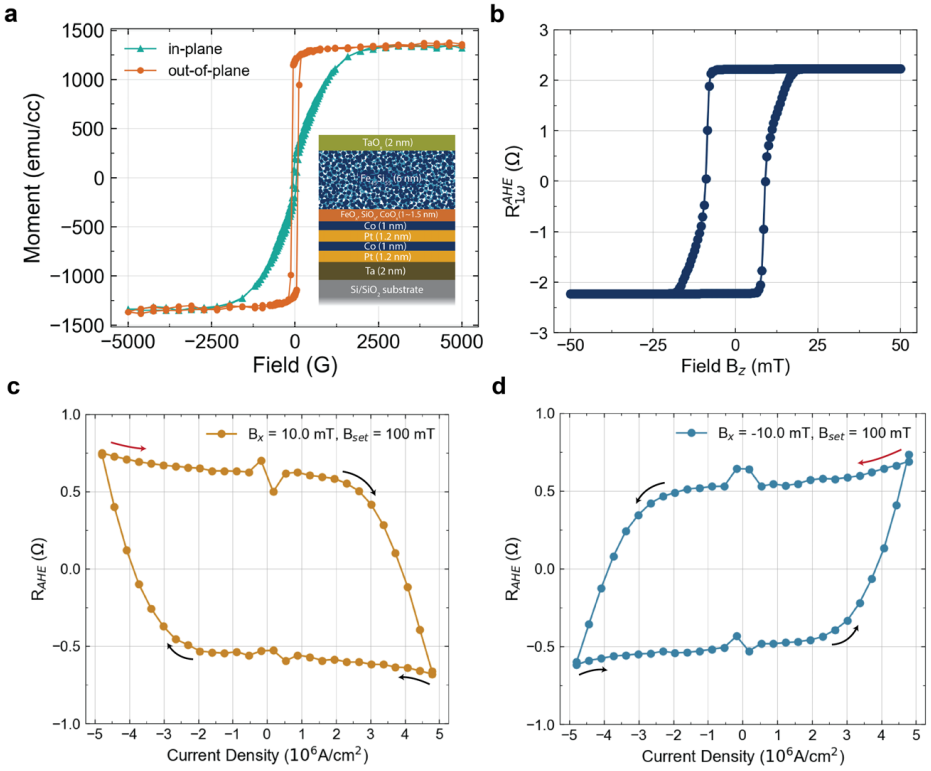

Figure 3.18: a, Magnetometry of blanket film [Pt (1.2 nm)/Co (1 nm)]$_2$ / oxide (1±0.5 nm) / a-$Fe_{45}Si_{55}$ (6 nm) stack showing the strong out-of-plane magnetic anisotropy. b, Anomalous Hall resistance as a function of out-of-plane field (B_z) measured on device fabricated from the PMA heterostructure. Device under test is a Hall bar structure with 20 μm in width and 70 μm in length. c, d, Spin-orbit torque switching curve with a + (-) 10 mT symmetry breaking field in the + (-) x-direction. Clear switching between two states is observed regardless of the symmetry breaking field sign. The opposite chirality between the two curves is due to opposite sign of symmetry breaking field for deterministic SOT switching. The critical current density (J_c) is approximately 3.998 x 10^6 A/cm^2, which is defined when the majority of the magnetization switches to the opposite direction (R_{AHE} crossing zero). Current pulse width is 200 μs.

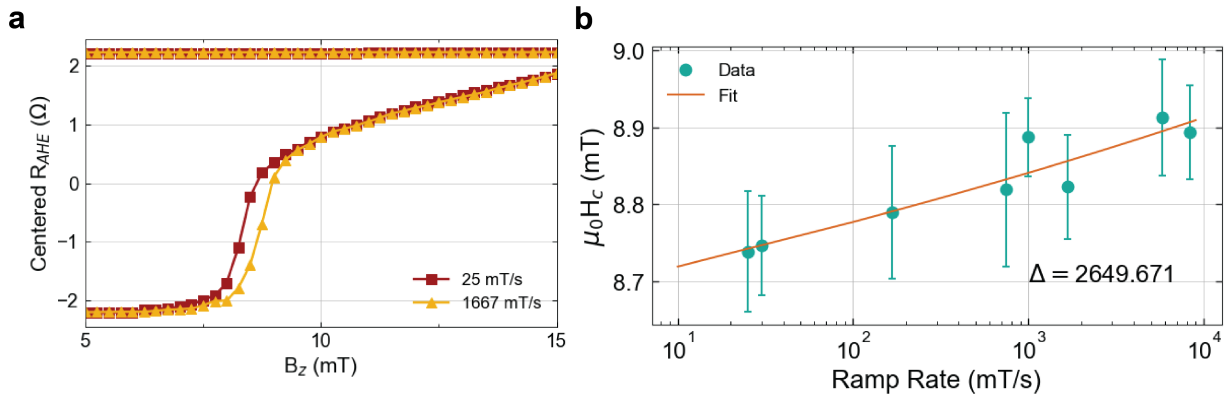

Figure 3.19: a, Measurement of the thermal stability via ramp rate dependent coercive field. This plot shows the typical hysteresis switching due to magnetic field along the easy-axis (z-direction in this case) as a function of ramp rate. b, Since field switching is a thermal process, the coercive field ($\mu_0 H_c$) increases as the ramp rate increases. We repeated the measurement at each ramp rate for at least 15 times to get the average $\mu_0 H_c$. By fitting the results with the model from El-Hilo *et al.*[69], we can extract the thermal stability (Δ) of the PMA magnet in the device. In this device, we find the thermal stability factor (Δ) to be around 2650.

sis profile. The measurement is repeated as a function of magnetic field ramp rate in three different orders of magnitude. At each ramp rate, we repeat the measurement at least 10 times to find the average coercive field.

The thermal stability measurement is based on the fact that field switching of the magnetization is a thermal activation process. Due to the time-dependent nature of such thermal activation process, the coercive field at which magnetization switching occurs is a function of the magnetic field ramp rate[69, 161]. The relation between thermal stability (Δ), coercive field (H_c) and ramp rate (r) is[161]:

$$H_c = H_k \left(1 - \sqrt{\frac{1}{\Delta} ln \left(\frac{f_0 H_k}{2\Delta} \frac{1}{r}\right)}\right). \tag{3.14}$$

By fitting this expression to the coercive field as a function of ramp rate, we were able to extract the thermal stability (Δ) and the anisotropy field (H_k) in the easy-axis (out-of-plane) direction. f_0 is the attempt frequency and we assume it to be 10 GHz in our fitting. We extracted the thermal stability factor of our PMA magnet through the sweep rate dependent coercivity measurement (Fig. 3.19a, 3.19b) and find it to be around 2650 for this device.

We conducted the switching experiment and thermal stability measurement on other device dimensions for repeatability and elimination of size dependence. If we benchmark the average switching efficiency from multiple devices against several well-studied systems

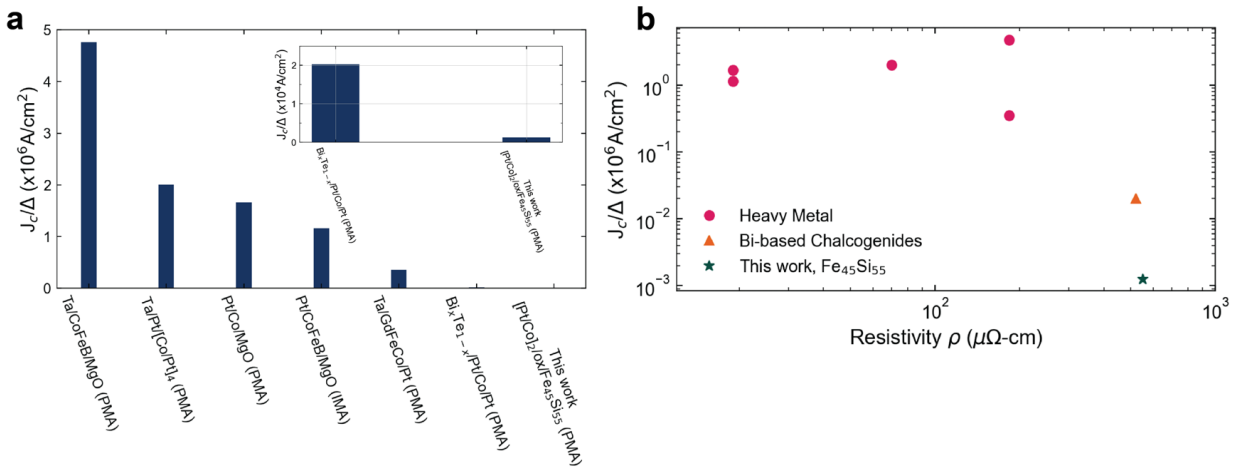

Figure 3.20: a, Benchmark of SOT switching efficiency, which is the ratio of critical switching current density over thermal stability factor (J_c / Δ). Comparing to the well-studied systems (heavy metal and topological insulators/sputtered chalcogenides), iron silicon is approximately 3 orders of magnitude more efficient than heavy metals and 1 order of magnitude more efficient compared to chalcogenides. b, Benchmark of SOT switching efficiency as a function of resistivity.

including heavy metal[53, 81, 104, 125] and chalcogenides or sputtered topological insulators[31], the switching efficiency is at most three orders of magnitude better than the heavy metals and approximately one order better than chalcogenides/sputtered topological insulators (Fig. 3.20a). While the maximum improvement on switching efficiency is three orders of magnitude better than heavy metals, the resistivity is still one order higher than most heavy metals (Fig. 3.20b). This implies that silicides in general can serve as a new platform for further down-scaling of switching efficiency through routes such as resistivity lowering and SOT efficiency increasing. Therefore amorphous silicides present new opportunities for achieving highly efficient SOT devices.

Chapter 4

Efficient spin-orbit torque in amorphous cobalt silicide

4.1 Foreword and motivation

In the previous chapter, large spin-orbit torque has been observed in fully amorphous iron silicide. While the concentration dependence of spin-orbit torque in iron silicide can potentially arise from the change in density of states near the Fermi level, the role of magnetism in magnetic element silicide has not been fully understood. In addition, although iron silicide shows a promising scaling trend between the SOT efficiency and resistivity, its resistivity ($\rho_{a-Fe45Si55} \sim 850$ $\mu\Omega$-cm) is still quite high for lowering the critical switching current density even further. This is apparent in the benchmark of spin Hall conductivity (σ_s)

$$\sigma_s = \frac{\xi_{DL,SOT}}{\rho_c}\left(\frac{2e}{\hbar}\right) \tag{4.1}$$

in Fig. 4.1. Spin Hall conductivity is a very useful metric for capturing the amount of spin current density a material can supply. For topological insulators, the record high SOT efficiency is unfortunately coupled with a very high resistivity (> 1000 $\mu\Omega$-cm). On the other hand, heavy metal systems exhibit SOT efficiency lower than 35 % [111, 112, 155, 147] but the much higher charge conductivity they possess, especially for Pt, lowers the amount of SOT efficiency required to achieve a high spin Hall conductivity thus a low critical switching current density. The highest spin Hall conductivity ever reported was found in epitaxial IrMn with $\xi_{DL} = 0.6$ at $\rho_c = 85$ $\mu\Omega$-cm [219]. Although a-$Fe_{45}Si_{55}$ beats the state-of-the-art SOT line material - β-W, it still falls behind most heavy metal systems and epi-IrMn. As a result, a pathway to continue the opposite scaling trend of increasing SOT efficiency with decreasing resistivity beyond what a-Fe_xSi_{100-x} already provide is necessary for technological advancement in SOT-MRAM.

To address these questions, I turned to a different silicide - cobalt silicide a-Co_xSi_{100-x}. a-$Co_xSi_{100-x}$is another commonly studied silicide for CMOS applications since the 1990s [120, 27] especially $CoSi_2$ and B20-phase CoSi. In addition, elemental Co has been used as

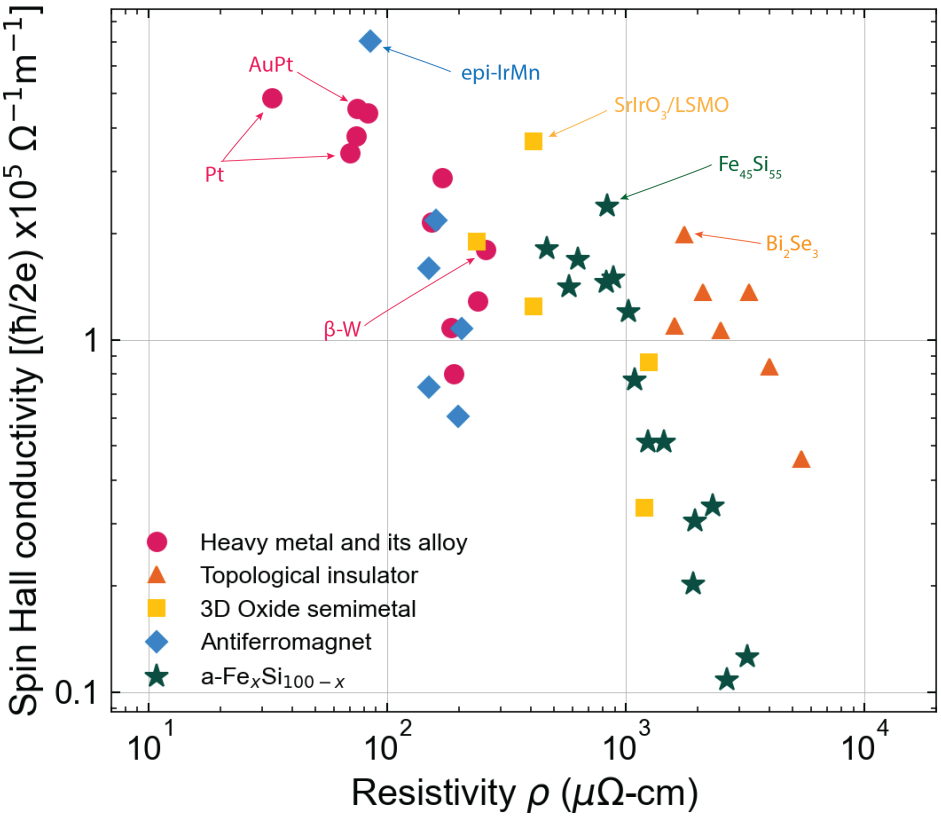

Figure 4.1: Benchmark of spin Hall conductivity on a-Fe_xSi_{100-x} against well-studied SOT materials.

a cap/linear metal for the first few interconnect layers in CMOS back-end of line processing [171]. As a result, cobalt silciide is a material system that with compatibility with the current silicon CMOS platform. From the physics point of view, CoSi has been shown both experimentally[209, 182] and theoretically[186, 23] to possess topologically protected chiral Fermions. Specifically, these chiral topological Fermions such as spin-1 Weyl Fermion and double Weyl Fermion are different from the well-known spin-1/2 Fermion found in many Weyl semimetals[209, 186]. CoSi belongs to the space group 198 $P2_13$ along with other experimentally studied non-symmorphic chiral crystals [165, 23]. These materials possess topologcial features such as non-trivial multi-fold band crossing at the Fermi level, multiple topological chiral nodes near the Fermi level and extensive Fermi arcs[209, 165]. With spin-orbit coupling degeneracy at certain time reversal asymmetry points is lifted, and spin-1 Weyl Fermion becomes a spin-3/2 Rarita-Schwinger-Weyl Fermion with spin degree of freedom and the double Weyl Fermion becomes a double spin-1 Weyl Fermion with spin degree of freedom

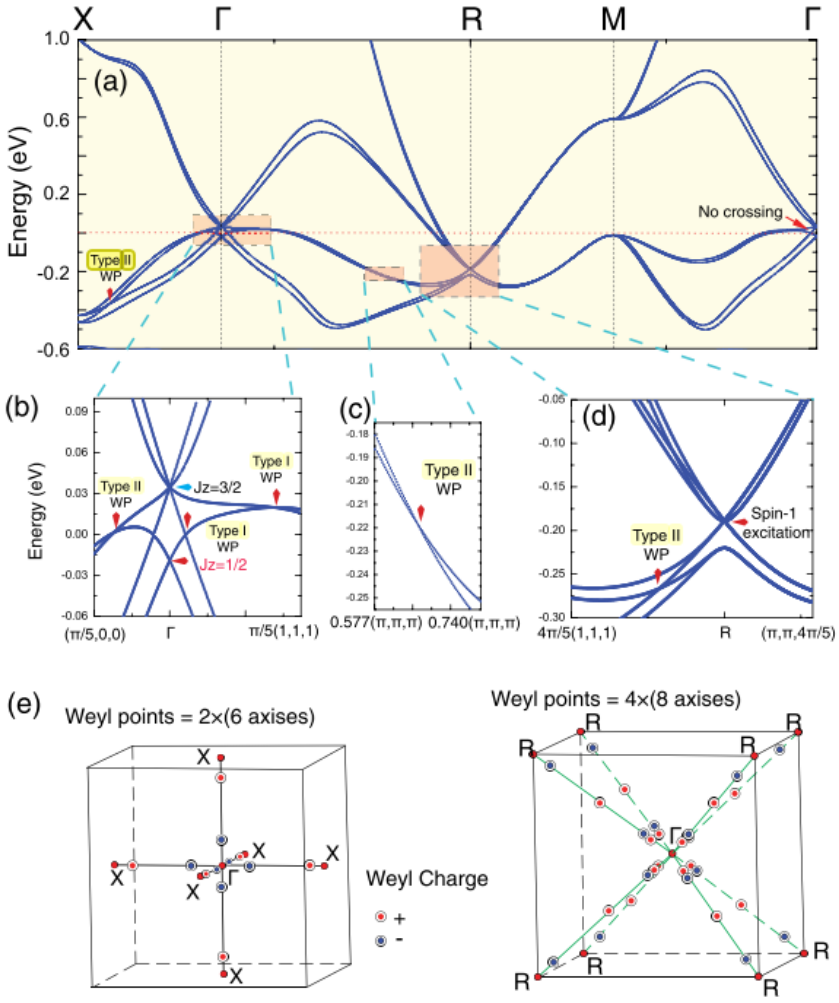

Figure 4.2: Theoretical band structure calculation with spin-orbit coupling in CoSi. a, calculations along high-symmetry directions. b, c, d, detail of region of interest near the band crossing the nodes. Weyl Fermions are indicated by red arrows and Rarita-Schwinger-Weyl Fermions are indicated by blue arrow. e, distribution of the topological fermions. Graph adapted from *Physical Review Letters* [186].

(Fig. 4.2). These non-trivial topological energy states near the Fermi level with spin-orbit coupling are ideal environment for large spin current generations. As a result, topological chiral semimetal CoSi is a great candidate.

In fact, spin-orbit torque and spin Hall effect has been experimentally explored in B20-phase single crystal CoSi [185, 184]. However, the SOT efficiency is found to be around only 10% in CoSi with and without Cu insertion between the CoSi and the ferromagnet. Tang *et*

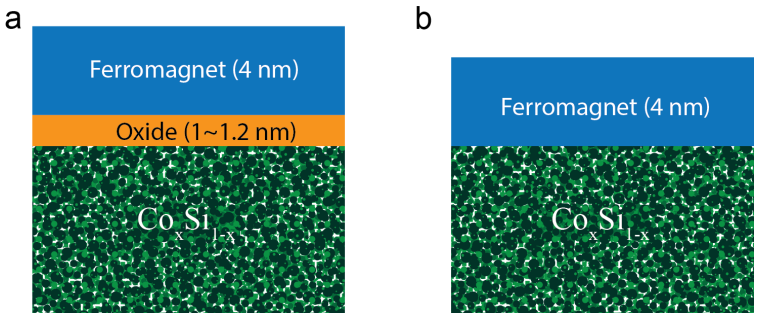

Figure 4.3: a, Tri-layer stack structure with oxide insertion. b, bi-layer stack structure.

al. tried to modulate the Fermi level through substitutional doping with Fe and Ni elements and the SOT efficiency remains below 10 %. The small SOT efficiency is not surprising as the interface states are extremely important and sensitive when it comes to engineering large SOT in SCG/FM bi-layers. To unlock the intrinsic large spin-torque CoSi potentially can produce, ensuring the Fermi level is located close to the non-trivial topological nodes are critical. Since CoSi is a semimetal, the Fermi level in the CoSi when interfaced with a metallic ferromagnet will be strongly affected by the metallic nature of the ferromagnet thus pins the the Fermi level away from the non-trivial topological nodes. It is promising that in Tang *et al.*, the Cu insertion indeed improved the SOT efficiency albeit not by a large amount. This shows that SOT generation is indeed sensitive to interface conditions. However, since Cu is metallic as the transition metal based ferromagnet, the Fermi level is still likely pinned away from the region of the band crossings. To combat this, insertion of a thin insulator while maintaining spin transmission is essential to alleviate this issue similar to the case in a-Fe_xSi_{100-x} from the previous chapter.

Since large SOT is discovered in co-sputtered amorphous a-Fe_xSi_{100-x} I will continue using co-sputtered amorphous a-Co_xSi_{100-x}as the vehicle to investigate whether CoSi can be a possible route to extend the scaling trend for high SOT efficiency and low resistivity. Moreover, co-sputtering allows easy tuning of the relative concentration between Co and Si thus the Fermi level position and the density of states bandwidth near the Fermi level.

4.2 Sample design and deposition

Our sample design consists of two different heterostructures: 1) a-Co_xSi_{100-x} / FM bi-layer and 2) a-Co_xSi_{100-x} / oxide / FM tri-layers (Fig. 4.3. The Co concentration (x) ranges between 35 and 75 % with the a-Co_xSi_{100-x} thickness to be around 5.5±0.5 nm and the ferromagnet thickness is around 4±0.5 nm. All samples are deposited on 300 nm amorphous low-stress LPCVD silicon nitride on silicon substrates by co-sputtering of elemental Co and Si targets. All heterostructures are capped with 2.5 to 3 nm of silicon oxide to prevent

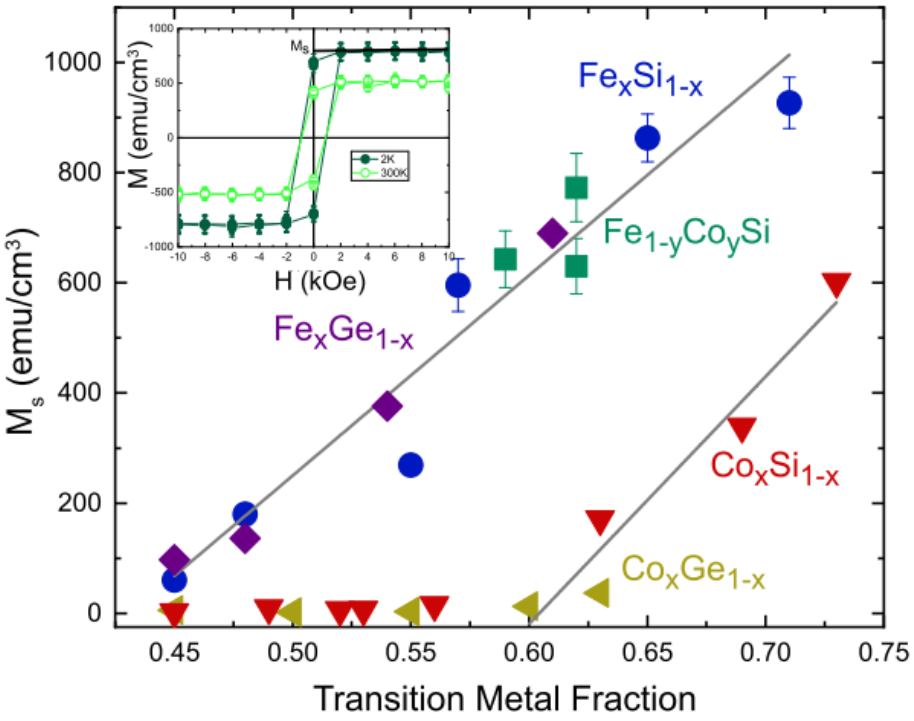

Figure 4.4: Saturation magnetization measured at 2K in various amorphous Fe and Co silicon thin films as a function of transition metal content. Graph adapted from *Physical Review Materials* [86].

oxidizing in ambient. In this study, we inserted a thin oxide layer (1∼1.2 nm) between a-Co_xSi_{100-x} and the ferromagnet via a chemical treatment. The chemical treatment is done in a similar way as in a-Fe_xSi_{100-x}/oxide/FM with MEGAPOSIT MF-26A TMAH based photoresist developer. Sputtering is done in the same sputtering chamber as a-Fe_xSi_{100-x} study with base pressure below 2.0e-8 Torr.

4.3 Structural and magnetic properties

Structural characterization

The structure of a-Co_xSi_{100-x} is mainly characterized through high-resolution cross-sectional TEM. In Fig. 4.5, no nanocrystals or clear lattice fringes can be observed in the a-$Co_{68}Si_{32}$ and a-$Co_{70}Si_{30}$ layers. Local FFT is performed on the respective layers to probe any reciprocal space peaks that may be associated with any appreciable lattice fringes. In both a-Co_xSi_{100-x} layers, the FFT pattern shows an amorphous ring without any peaks. The fully amorphous structure is confirmed previously in a-Co_xSi_{100-x} up to 73 % Co [86]. On

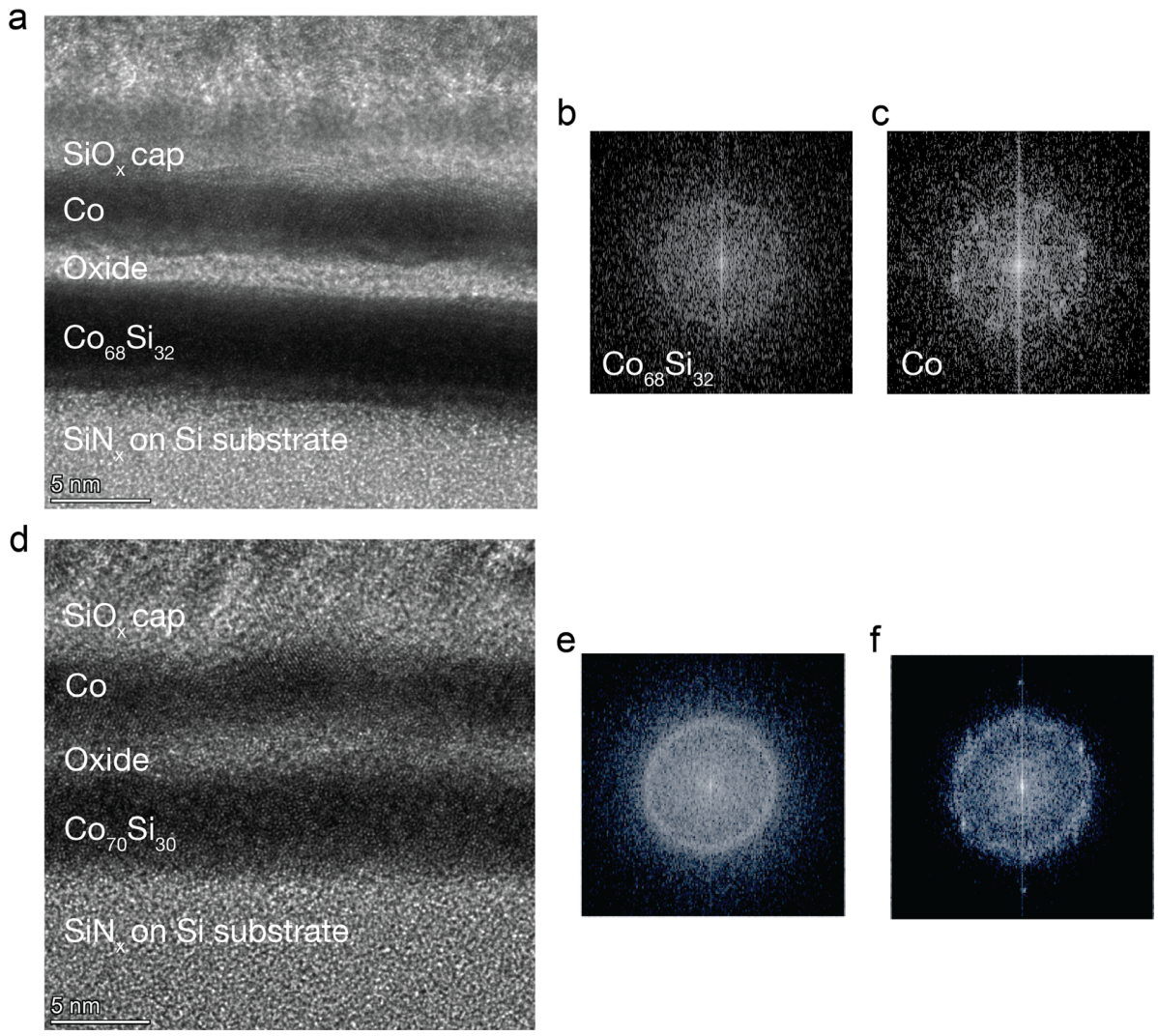

Figure 4.5: a, Cross-sectional TEM image of *a*-$Co_{68}Si_{32}$ / oxide / Co. b, Local FFT of *a*-$Co_{68}Si_{32}$showing an amorphous ring, c, Local FFT of Co layer showing a polycrystalline rings and reciprocal space peaks associated with the grain orientations. d, Cross-sectional TEM image of a-$Co_{70}Si_{30}$ / oxide / Co. e, Local FFT of a-$Co_{70}Si_{30}$. f, Local FFT of Co layer in d.

the other hand, finite size grains are observable in the Co layer for both tri-layer structures and their respective FFT spectrum shows reciprocal space peaks on top of a polycrystalline ring (Fig. 4.5b, 4.5e).

Magnetic characterization

Magnetic characterization is done through two different techniques: 1) Vibrating sample magnetometry (VSM) and 2) X-ray magnetic circular dichroism (XMCD). In Fig. 4.6a, the M-H curves shows a sharp ferromagnetic transition between 65 % and 70 % Co. This is very different from the the case of a-Fe_xSi_{100-x} where the magnetic transition is much gradual as we can see in Fig. 3.4. In the case of a-Fe_xSi_{100-x}, the increase in saturation magnetization is much smaller per unit increase in Fe concentration and also no hysteresis opening is observed before 60 % Fe with a paramagnetic or superparamagnetic lineshape. It is expected if the Fe concentration in a-Fe_xSi_{100-x} increases beyond 60 % at some point the ferromagnetism will arise but in a gradual manner.

In Fig. 4.6b, the increase in XMCD is taken in a tri-layer structure with the inserted oxide separating a-Co_xSi_{100-x} and Fe as the ferromagnet. The measured XMCD amplitude is also very sharp with most a-Co_xSi_{100-x} not exhibiting any appreciable XMCD until 65 % Co. However, in Fig. 4.6c, a much gradual increase in XMCD as the Co concentration increases in a-Co_xSi_{100-x} / Fe bi-layer is observable. This is due to the fact that ferromagnetic Fe magnetizes the Co atoms near the interface via strong exchange coupling. This signature is a great evidence how free electron wavefunction in the metallic ferromagnet can penetrate into the a-Co_xSi_{100-x} layer and affect the energy states near the interface in a-Co_xSi_{100-x}. As a result, in insertion of an oxide between the ferromagnet and a-Co_xSi_{100-x} is essential.

A similar signature in terms of the sharp onset of ferromagnetism is also observed at low temperature 2K for a-Co_xSi_{100-x}(Fig. 4.4 [86]. An interesting observation is that the gradual transition of the ferromagnetic phase in a-Fe_xSi_{100-x} as compared to a-Co_xSi_{100-x} is also prominent at low temperature (Fig. 4.4.

4.4 Electronic and charge transport properties

Single cyrstalline CoSi is a semimetal with band crossing at specific high symmetry points [209, 186] that is different from FeSi which is a small-gap semiconductor with topological surface conducting state [47] and non-trivial surface ferromagnetism [142]. However, this may be very different in the amorphous phase. The resistivity of a-Co_xSi_{100-x} single layer in the sub-10 nm regime is measured through a four-point probe resistance measurement on different double Hall bar devices. The average value of the measured resistivity is presented in Fig, 4.7b, c. a-Co_xSi_{100-x} is a dirty/semi-metal similar to a-Fe_xSi_{100-x} (Fig. 4.7b). The resistivity is high in the low Co regime < 50 % and quickly drops below 500 $\mu\Omega$-cm as Co content increases beyond 60 %. The a-Co_xSi_{100-x} resistivity increases much drastically as the amount of Co concentration decreases below 50 % whereas the resistivity change is much gradual in a-$Fe_xSi_{100-x}$with a plateau in the range of 40$\sim$50 % Fe (Fig. 4.7c). Interestingly, the concentration range between 40 and 50 % Fe is also where the peak of SOT efficiency resides (Fig. 3.15).

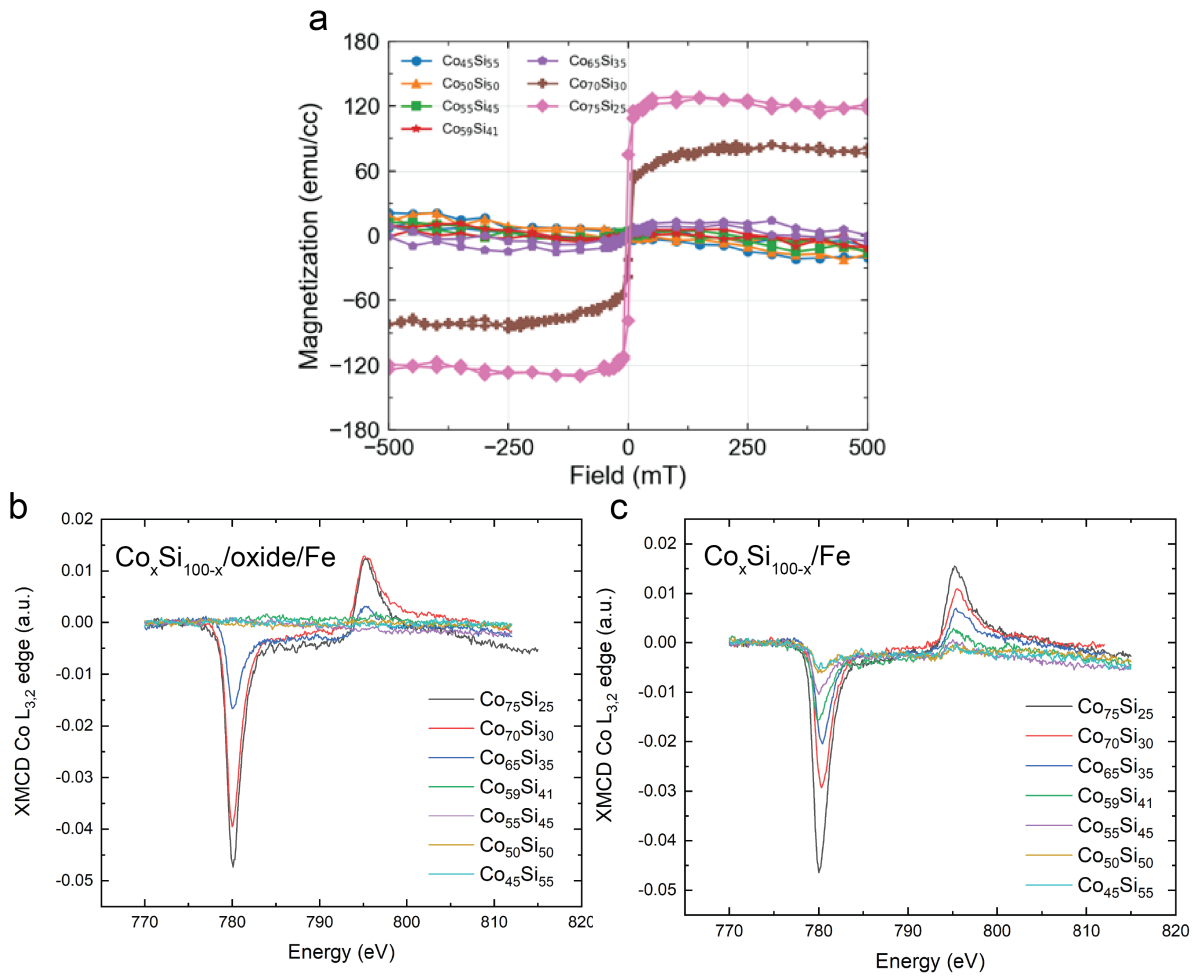

Figure 4.6: a, M-H magnetometry curves as a function of Co concentration via VSM. b, XMCD at Co $L_{3,2}$ edge in a-Co_xSi_{100-x} / oxide /Fe tri-layer. c, XMCD at Co $L_{3,2}$ edge in a-Co_xSi_{100-x} / Fe bi-layer.

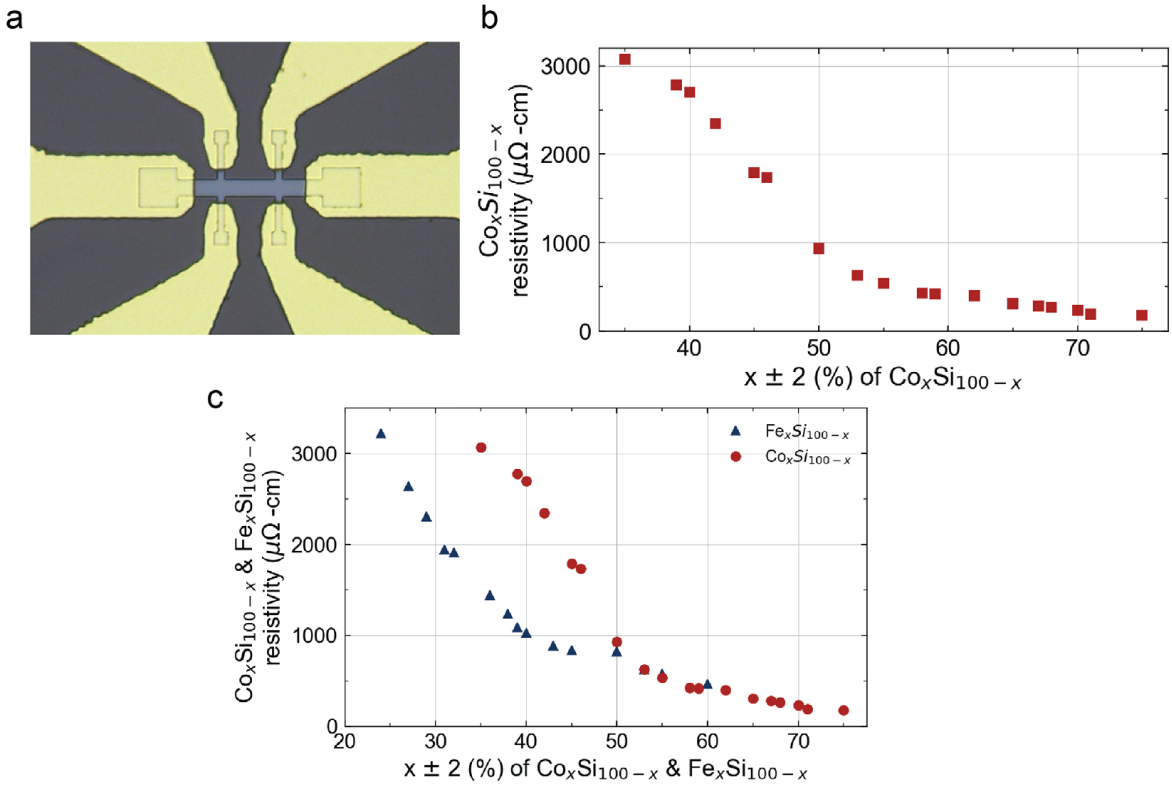

Figure 4.7: a, Optical microscope image of a double Hall bar device used for resistivity measurement. b, Resistivity of a-Co_xSi_{100-x} as a function of Co (x) concentration in atomic percentage.

4.5 Large spin-orbit torque efficiency

In-plane harmonic Hall measurement

To measure the spin-orbit torque in a-Co_xSi_{100-x}, I conducted in-plane harmonic Hall measurements on both a-Co_xSi_{100-x} / oxide / FM and a-Co_xSi_{100-x} / FM heterostructures with varying Co concentration. The ferromagnet is either Co or Py ($Ni_{81}Fe_{19}$) at thicknesses of 4 nm. The experimental setup is the same as described in section 3.5 of chapter 3 and the measurement geometry is shown in Fig. 4.9a. The magnetic heterostructure thin films are patterned into Hall bar device of different dimensions for cross-check. The fabrication process is the same as the devices made for a-Fe_xSi_{100-x} studies (Section 3.5). The details of the dimensions can be found in section 3.4 and 3.5. The oxide insertion is also analyzed through EELS for composition analysis mapping (Fig. 4.8) and the tri-layer structure is distinct with lack of intermixing. From the high-resolution cross-sectional TEM (Fig. 4.5), the oxide insertion can be seen to be amorphous which is similar to the case of a-Fe_xSi_{100-x}

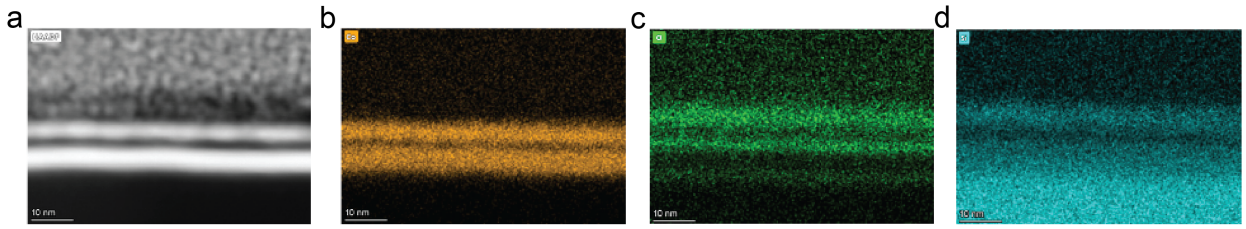

Figure 4.8: a, Cross-sectional TEM image of a-$Co_{68}Si_{32}$ / oxide / Co in STEM mode. b, EELS mapping of Co. c, EELS mapping of oxygen, d, EELS mapping of cobalt.

(Fig. 3.2).

In Fig. 4.9, a complete set of harmonic Hall data is shown. The first harmonic Hall signal shows a nice V_{PHE} $\sin(2\phi_B)$ dependence with no uniaxial in-plane anisotropy (Fig. 4.9b). The second harmonic Hall shows a field dependence which may arise from ordinary Nernst effect or SOT effects (Fig. 4.9c). After analyzing the angle dependence and field dependence data, the extracted $\cos(\phi_B)$ component in the second harmonic signal is shown in Fig. 4.9d. In Fig. 4.9d, anomalous Nernst effect is manifested as a negative constant offset independent of field, the ordinary Nernst effect is a linear increase with field which suppresses the $1/(B_{ext}+B_{anisotropy})$ lineshape of damping-like torque effective field. After eliminating the two Nernst effect, the strong $1/(B_{ext}+B_{anisotropy})$ dependence of the ΔB across 5 different current amplitudes is strong. The damping-like effective field ΔB scales linearly with increasing current amplitude as SOT is driven by current and the ΔB is an absolute quantity. After calibrating the amount of current in the a-$Co_{67}Si_{33}$ layer, the SOT efficiency ξ_{DL} of the damping-like torque can be calculated (Fig. 4.9g), which is around 1.81 (181 %). Individual fitting plots of the $\cos(\phi_B)$ component across five different current values are shown in Fig. 4.9h-g with good matching fits and strong DL-torque signature as comparisons to control samples (Pt/Co and Co only) previously discussed in section 3.5. Since the anomalous Hall resistance directly affects the extraction of ΔB, the R_{AHE} as a function of B_z on selected devices are shown in Fig. 4.10.

4.6 Co concentration dependence of spin-orbit torque

Pronounced Co concentration dependence

Next, extensive spin-orbit torque characterization on the Co concentration series of a-Co_xSi_{100-x} / oxide / FM is done with the in-plane harmonic Hall measurement on multiple devices over 3 different rounds of sample deposition, device fabrication and harmonic Hall measurement to complete the full a-Co_xSi_{100-x} concentration spectrum of SOT efficiency. In Fig. 4.11, the SOT efficiency and the resistivity in a-Co_xSi_{100-x} across the studied concentration range is shown. A clear peak of SOT efficiency can be seen around 68 % Co and

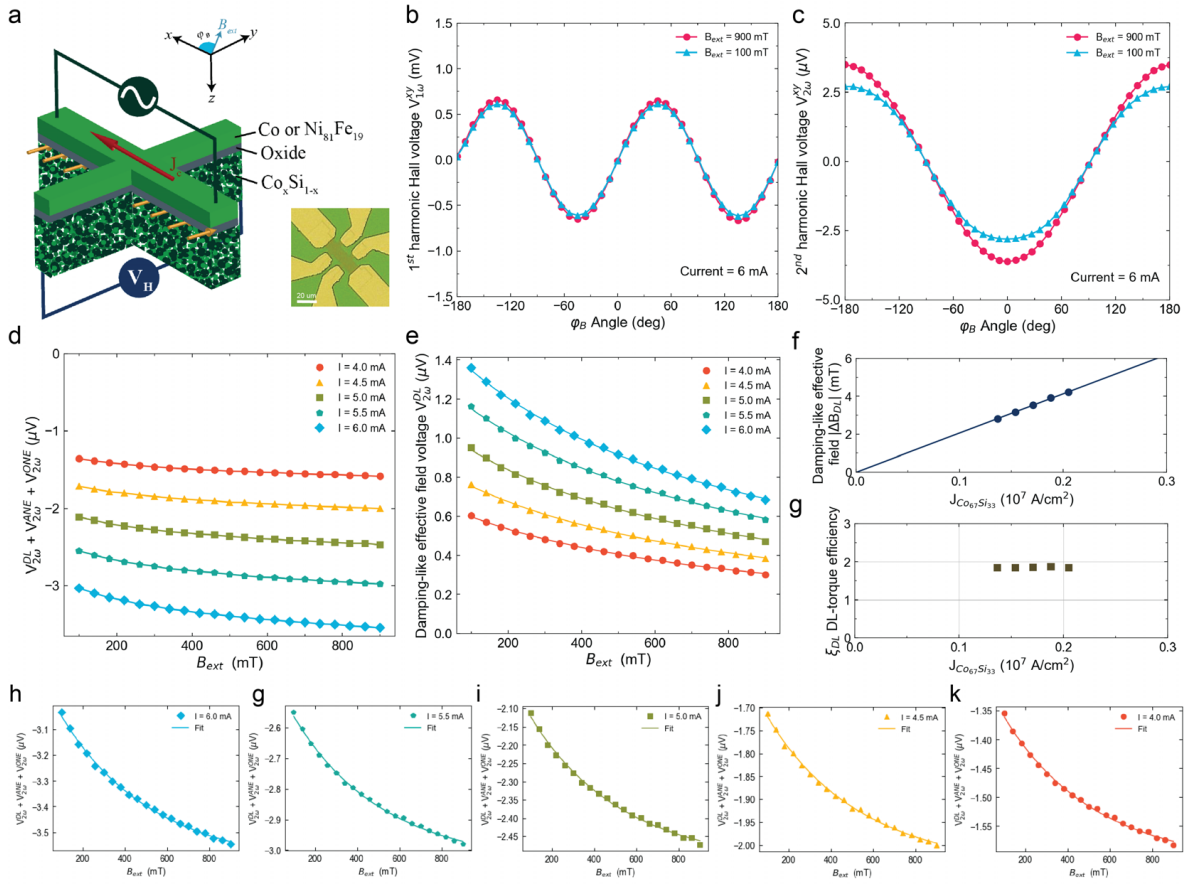

Figure 4.9: a, Schematic of patterned Hall bar on a-$Co_{67}Si_{33}$ (5.5 nm) / oxide (1 nm) / Py (4 nm) and measurement scheme. Inset, optical microscope image of the double Hall bar device structure patterned for harmonic Hall measurement. b, First harmonic voltage of the a-$Co_{67}Si_{33}$ (5.5 nm) / oxide (1 nm) / Py (4 nm) heterostructure. c, second harmonic voltage. d, The DL torque effective field and thermoelectric contribution as a function of external field obtained from angle fit to $\cos(\varphi_B)$. e, The DL torque effective field signal after eliminating the thermoelectric effects including anomalous Nernst effect and ordinary Nernst effect. The clear $1/(B_{ext}+B_{anisotropy})$ dependence shows a strong signature of DL spin-orbit torque. f, DL torque effective field as a function of injected current density in the *a*-$Fe_{45}Si_{55}$ layer. g, SOT efficiency (ξ_{DL}) extracted to be an average of 1.81 across five different current values. The consistency across different current values confirms the clear signal of SOT. h-k, Individual plots (varying a.c. current amplitude) of the field-dependent fit to the $\cos(\phi_B)$ component of the second harmonic signal.

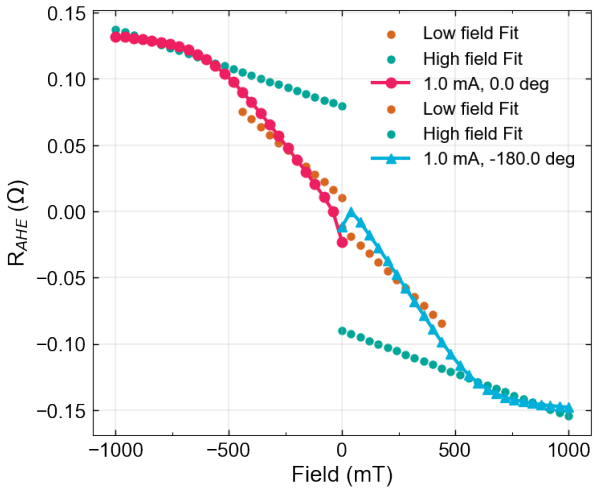

Figure 4.10: R_{AHE} versus B_z in a-Co_xSi_{100-x} / oxide / Co.

a gradual decrease of SOT efficiency extends toward the lower Co concentration region. On the other side of the peak, a sharp drop of SOT efficiency is visible once the Co concentration crosses the 70 % mark. For a-Co_xSi_{100-x} with x $<$ 58 %, the SOT efficiency stays around 25% with a steady but mild increase as Co concentration decreases.

Enhanced SOT efficiency near ferromagnetic phase transition of a-Co_xSi_{100-x}

While there does not seem to have a direct correlation between resistivity and SOT efficiency in Fig. 4.11, the peak of the SOT efficiency nicely coincides with the transition of the ferromagnetic phase in a-Co_xSi_{100-x}. In Fig. 4.12, the XMCD amplitude at the Co L_3-edge is plotted on top of the SOT efficiency as a function of Co concentration. This is first time ever that a material system shows a strong dependence of the magnetic phase in SOT generation. This potentially provides a perspective on tuning the strength of interfacial spin-orbit coupling for optimal SOT generation. As mentioned in chapter 2, spin-orbit coupling is essential for generating spin current but also strong spin-orbit coupling can induce spin dephasing resulting in fast decay of the spin current. Since a-Co_xSi_{100-x} is fully amorphous, the underlying mechanism of spin current generation is dominantly interfacial. As a result, once the a-Co_xSi_{100-x} becomes a ferromagnetic, the spin current generated at the interface can quickly dephase before it injects through the oxide insertion and into the adjacent ferromagnet. This also indicates the importance of interfacial spin-orbit coupling in generating spin current in a-Co_xSi_{100-x} via an intrinc-like origin similar to a-Fe_xSi_{100-x}. Here, a-Co_xSi_{100-x} is also a semimetal with a reduced density state region near the Fermi

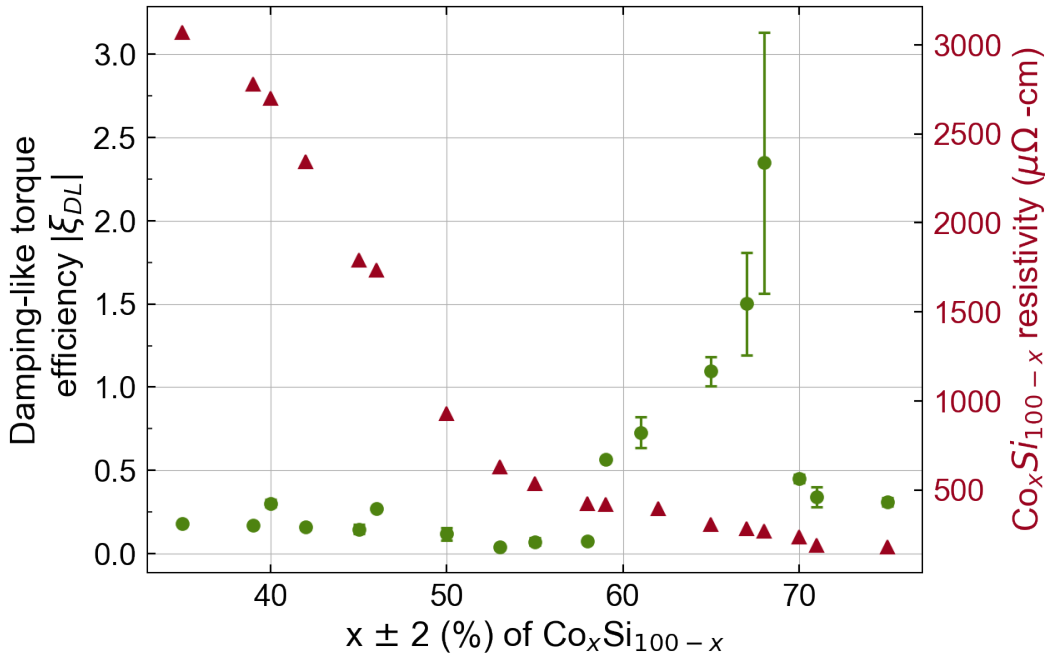

Figure 4.11: Co concentration dependence of damping-like SOT efficiency and charge resistivity in a-Co_xSi_{100-x} / oxide / Co.

level [89, 86] that can be modulated by the Co concentration. However, since its resistivity is much higher when x< 50 % and decreases sharper as compared to a-Fe_xSi_{100-x}, this indicates a much stronger density of states modulation due to the Co concentration.

I would like to point out that onset of ferromagnetism seems to be play a much more important role in a-Co_xSi_{100-x} for spin-current generation. This shares a very similar signature as the anomalous Hall effect in ferromagnetic a-Co_xSi_{100-x} [86]. In Karel *et al.*, the trend of anomalous Hall angle as a function of Co content is the same as the SOT as a function of Co concentration in Fig. 4.12. Also, the sharper peak in transition metal concentration dependence of SOT efficiency as compared to a-Fe_xSi_{100-x} is also simialr to how a-Fe_xSi_{100-x} compares to a-Co_xSi_{100-x} in terms of anomalous Hall angle in Karel *et al.* [86]. This points to the experimental evidence of the importance in magnetic origin of such large SOT and spin polarization phenomena in fully amorphous transition metal silicides.

SOT in a-Co_xSi_{100-x} / FM

In Fig. 4.13, the harmonic Hall measurement result on a-$Co_{65}Si_{35}$ (8 nm)/Fe (4 nm) is shown. Similar to the case of a-Fe_xSi_{100-x} / FM, weaker SOT efficiency and lack of Co concentration dependence is observed when no oxide is inserted between a-Co_xSi_{100-x} and the adjacent ferromagnet (Fig. 4.14. This is due to the Fermi level pinning issue and the

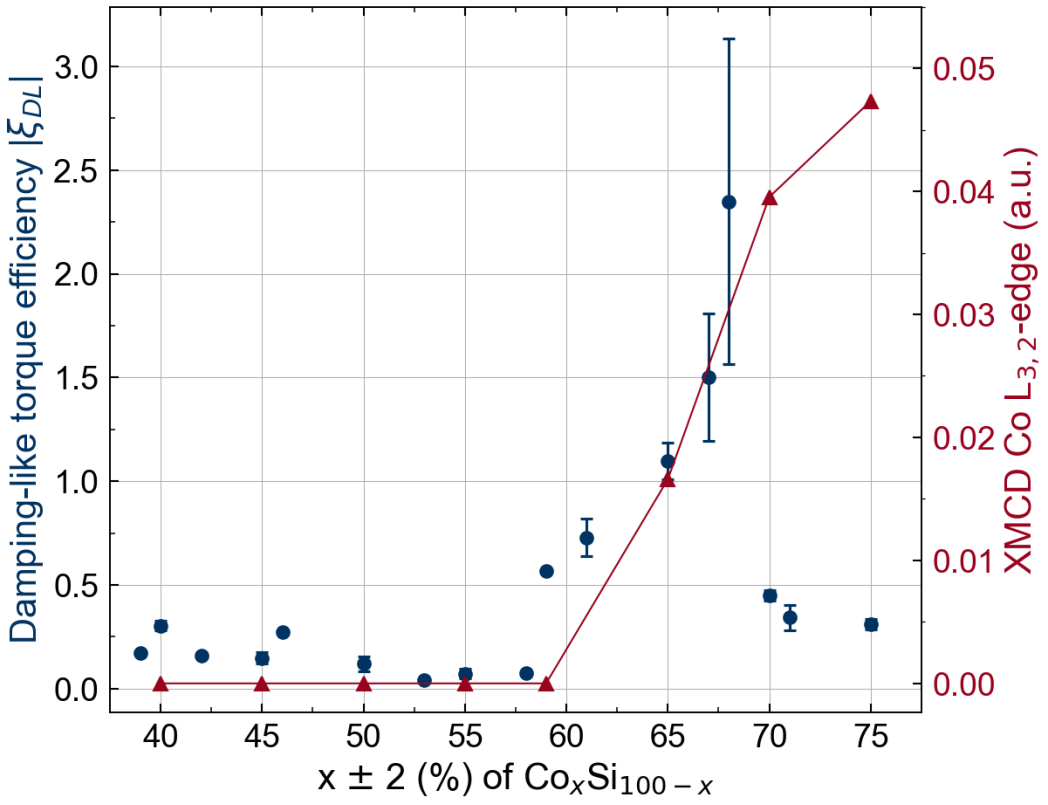

Figure 4.12: Co concentration dependence of damping-like SOT efficiency and XMCD amplitude at the Co L_3-edge in a-Co_xSi_{100-x} / oxide / FM.

strong ferromagnetic order at the interface that eliminates the spin current before it diffuses across the interface. This is apparent in Fig. 4.6c where the XMCD amplitude of Co $L_{3,2}$-edge in a-Co_xSi_{100-x} / Co increases as the Co content increases which is opposite to the case in a-Co_xSi_{100-x} / oxide / Co. Due to the Fermi level pinning at the a-Co_xSi_{100-x} / FM interface, the SOT efficiency is near constant around 10 % between Co concentration range of 35 % and 65%. Similarly, once a-Co_xSi_{100-x} becomes ferromagnetic at 70 % the SOT efficiency drops significantly to close to zero Fig. 4.14.

Non-trivial scaling trend between the SOT efficiency and resistivity

In a-Co_xSi_{100-x}, a novel scaling trend between the SOT efficiency and resistivity is found (Fig. 4.15). Here scaling trend can be categorized into two type: 1) the conventional course where SOT efficiency increases with increasing resistivity and 2) the novel course where SOT efficiency increases with decreasing resistivity. The conventional course can be expected from

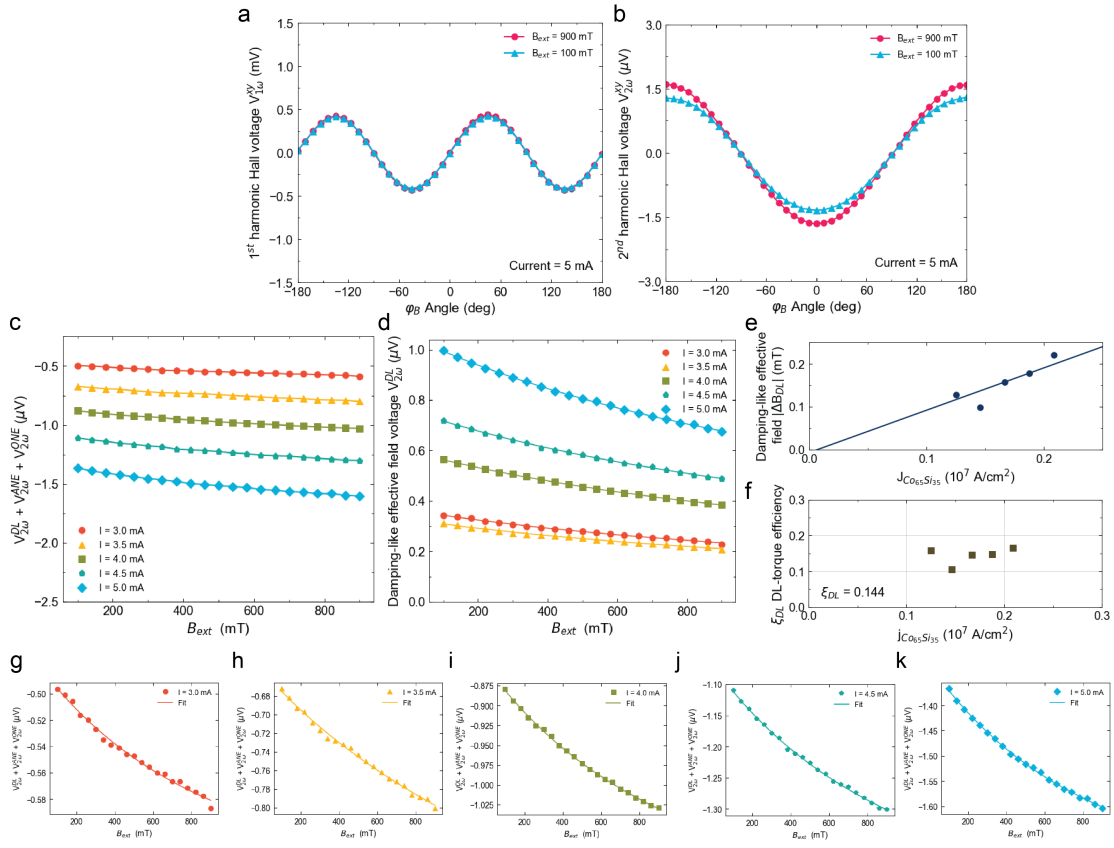

Figure 4.13: Harmonic Hall measurement on a-$Co_{65}Si_{35}$ (8 nm)/Fe (4 nm). a, first harmonic Hall signal. b, second harmonic Hall signal. c, $\cos(\phi_B)$ component of the second harmonic signal. d, damping-like torque signal as a function of external field. e, damping-like torque effective field. f, extracted damping-like SOT efficiency. g-k, individual plots of the field dependence fitting to the $\cos(\phi_B)$ component.

the spin Hall conductivity (σ_{SH}) theory

$$\theta_{SH} = \frac{\sigma_{SH}}{\sigma_c}\left(\frac{2e}{\hbar}\right) = \sigma_{SH} \times \rho_c \left(\frac{2e}{\hbar}\right) \tag{4.2}$$

where θ_{SH} is the intrinsic spin Hall angle (i.e. measured SOT efficiency ξ_{SOT} with 100 % spin transparency), σ_c is the charge conductivity and ρ_c is the resistivity. Since σ_{SH} is associated with the intrinsic mechanism, one can design the sample in a way that preserves the intrinsic mechanism but introduce certain amount of impurities to increase the resistivity such as oxidizing heavy metals [5, 129, 203, 40].

The scaling trend can be divided into two phases based on the resistivity value of around 350 $\mu\Omega$-cm, acting as a threshold (Fig. 4.15). For samples with resistivity greater than 350

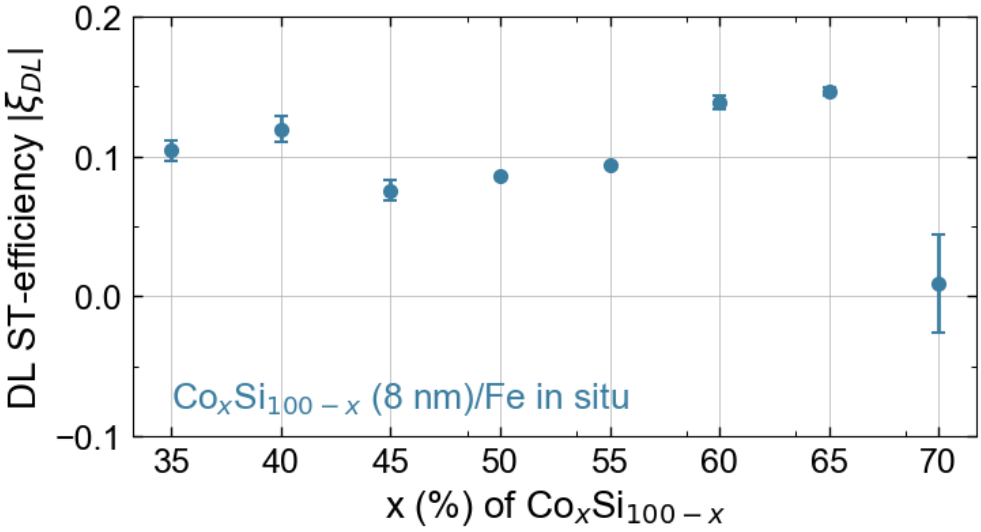

Figure 4.14: Co concentration dependence of damping-like SOT efficiency in a-Co_xSi_{100-x} (8nm) / Fe (4nm).

$\mu\Omega$-cm, the scaling trend follows the conventional course. However, for samples with resistivity below 350 $\mu\Omega$-cm, a remarkably sharp opposite trend is observed before a-Co_xSi_{100-x} becomes ferromagnetic. This is distinct from a-Fe_xSi_{100-x} in two aspects. Firstly, a mild increase is seen for samples with resistivity values above 350 $\mu\Omega$-cm whereas in a-Fe_xSi_{100-x}, the scaling trend is consistently opposite for samples lacking magnetism (< 55 % Fe). Secondly, the scaling trend in a-Co_xSi_{100-x} exhibits a much sharper opposite behavior compared to a more gradual trend in a-Fe_xSi_{100-x}. Based on these observations, it appears that multiple contributions of spin current are either competing or synergistically adding in a-Co_xSi_{100-x}.

4.7 Improving the state-of-the-art spin Hall conductivity

SOT efficiency (ξ_{SOT}) serves as an important metric for studying and comparing spin-charge conversion efficiency in materials. However, in most spintronic applications, the goal is to generate spin currents for manipulating magnetic texture or magnetization switching. Therefore, solely relying on SOT efficiency might not fully capture a material's ability to supply spin current(density) in response to a voltage(electric field). Similar to charge conductivity, which measures the current per unit cross-sectional area (current density) a material can carry in response to an electric field, spin Hall conductivity quantifies the spin current density a material can carry in response to an electric field with spin-charge conversion. The presence of a critical amount of spin current, supplying enough angular momentum, is

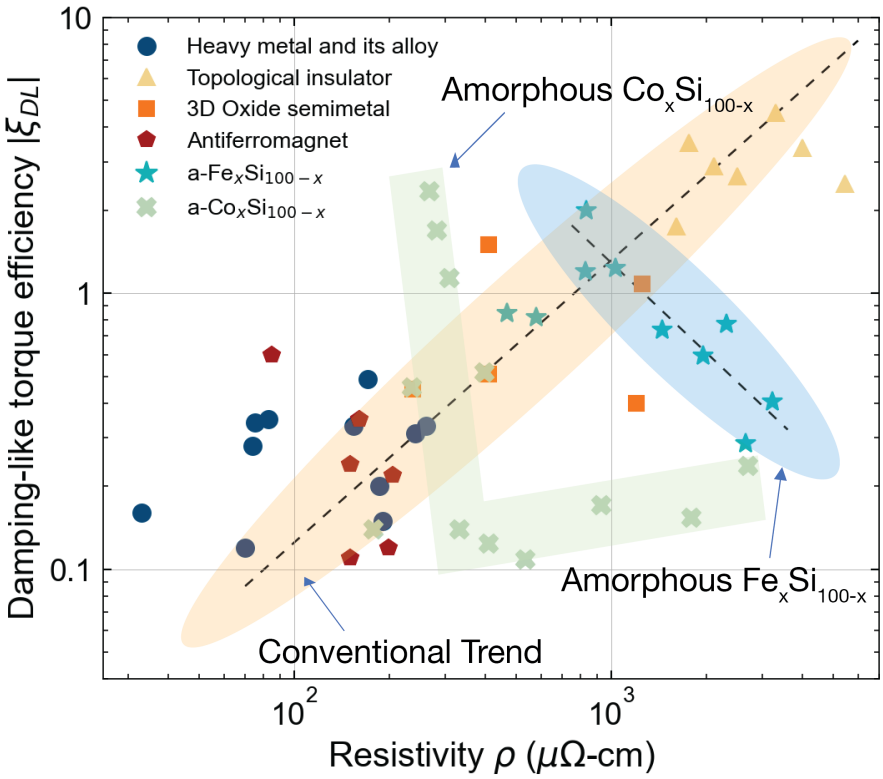

Figure 4.15: Benchmark of SOT efficiency in a-Co_xSi_{100-x} with other well-studied material systems and a-Fe_xSi_{100-x}.

necessary to switch a certain amount of magnetic moments effectively. Thus, spin Hall conductivity not only reflects spin-charge conversion efficiency but also indicates the material's inherent ability to carry charge current. This highlights the reason why high SOT efficiency at low resistivity is desired. In essence, achieving a remarkably high spin-charge conversion efficiency is only half of the requirement for low critical switching current. The material must also be capable of carrying sufficient charge current that are effectively polarized into spin current.

In Fig. 4.16, I show the experimentally measured spin Hall conductivity among the well-studied material systems. Immediately, a strong correlation between σ_{SH} and ρ_c can be observed where the materials with the highest σ_{SH} are the ones with very low resistivity values but $< 50\%$ SOT efficiency such as Pt [227], PtAu alloy [223] and epi-IrMn [219]. Topological insulators with the highest SOT efficiency did not directly translate to high spin Hall conductivity due to their very high resistivity values. For a-Fe_xSi_{100-x}, its spin Hall conductivity is approximately the same as topological insulators with a-$Fe_{45}Si_{55}$ recording a

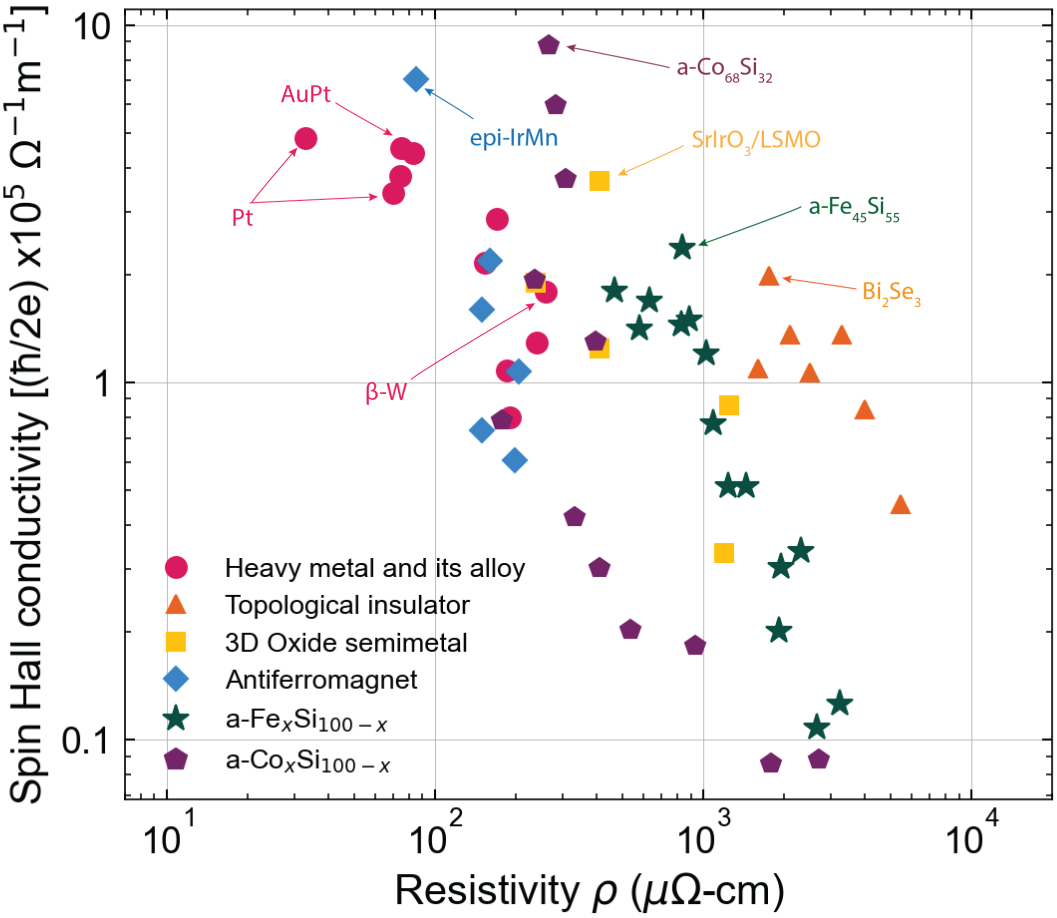

Figure 4.16: Benchmark of spin Hall conductivity σ_{SH} in a-Co_xSi_{100-x} with other well-studied material systems and a-Fe_xSi_{100-x}.

slightly higher spin Hall conductivity than the best performing topological insulator [124]. As a result, while a-Fe_xSi_{100-x} shows a promising trend in terms of SOT efficiency and its resistivity, the best-performing a-$Fe_{45}Si_{55}$ still falls behind most of heavy metal systems and transition metal-based antiferromagnets when it comes to spin Hall conductivity. However, if we were able to hold on to the large SOT efficiency in a-$Fe_{45}Si_{55}$ and lower its resistivity without losing the large SOT efficiency, a much higher spin Hall conductivity can be achieved.

In a-Co_xSi_{100-x}, the highest SOT efficiency appears at 68 % Co (Fig. 4.15 which is much higher in transition metal atomic concentration compared to a-$Fe_{45}Si_{55}$. This also means that the peak of SOT efficiency is now at a much lower resistivity value due to the higher transition metal content. Due to this fact, the entire concentration series of a-Co_xSi_{100-x} spin Hall conductivity values in the benchmark graph (Fig. 4.16) is shifted to the left of a-Fe_xSi_{100-x}. With this discovery of a very large spin-orbit torque efficiency (230 %) at a relatively low resistivity value ($\sim$180 $\mu\Omega$-cm) in a-$Co_{68}Si_{32}$, a record-high spin Hall conductivity beating the state-of-the-art heavy metal-based systems for efficient magnetic switching applications is found. This extends the scaling trend in amorphous iron silicide and pushes the performance closer to ideal with high spin-torque efficiency and low resistivity. One last thing to note is that while a-$Co_{68}Si_{32}$ achieved a very high spin Hall conductivity, its resistivity is the worse among the high spin Hall conductivity materials (Pt, PtAu, epi-IrMn). There is immense opportunity for research to continue lowering the resistivity while holding on to the large SOT efficiency in silciides.

Chapter 5

Spin-orbit torque driven switching phenomena in canted ferrimagnetic alloy $\mathbf{Gd}_x\mathbf{Co}_{100-x}$

5.1 Foreward and motivation

Ferrimagnets (FiM) have been an emerging material system that possess abundant magnetic properties for interesting phenomena and potential spintronics applications [97]. Ferrimagnets are composed of two different magnetic sublattices that are antiferromagnetically coupled which yields a non-zero magnetization [132]. As a result, ferrimagnets combine the unique properties of both ferromagnets (FM) and antiferromagnets (AFM), enabling magnetic properties and phenomena such as bulk perpendicular magnetic anisotropy (PMA) [26], bulk Dzyaloshinskii–Moriya Interaction (DMI) [93], magnetic skyrmion host [18], spin-orbit torque switching [161], and all optical switching [180]. While there exist many different families of ferrimagnets, rare earth (RE) - transition metal (TM) ferrimagnetic alloy stands out for spintronics applications [26, 180, 161, 97] due to its highly tunable magnetic, electronic, thermomagnetic, optical properties and relatively simple thin film deposition method [26, 16, 187, 97].

Among many fascinating properties of RE-TM ferrimagnetic alloys, the bulk perpendicular magnetic anisotropy (PMA) which even persists in thick films in the micro-meter regime [26, 187] is the driving force behind all the fascinating magnetic phenomena. However, switching a PMA magnet with an in-plane polarized spin current requires an in-plane symmetry breaking field to achieve deterministic switching [208, 207, 53]. This is one of the main technological challenges for developing SOT-based magnetic memory. Despite many efforts in studying RE-TM ferrimangetic alloys for spintronics applications [97, 26, 93, 18, 161, 180, 66, 63, 16, 187], it is not until recently that field-free spin-orbit torque switching can be achieved in RE-TM ferrimagnetic systems [94, 159, 200, 218]. It is not surprising that RE-TM ferrimagnets carry the capability of inducing a tilt in its anisotropy since it

possess properties of both FM and AFM. In fact, one of the most common systems designed to induce a tilt in its PMA for field-free SOT switching is the AFM/FM bi-layer where an exchange-bias is present [141, 53].

In AFM/FM bi-layer systems, not only field-free switching [15, 141, 53] can be realized but also many interesting magnetic textures and switching behaviors such as electrical control of antiferromagnetic order [108, 152], multistate switching [53, 211], and memristor behavior [53, 211] can be observed owing to its dynamic and intricate magnetic interaction at the AFM/FM interface [78]. Due to the exchange coupling at the AFM/FM interface, AFM spin configuration at the interface can be controlled via SOT and exhibits an exchange spring effect that manifests in a ratchet behavior of the magnetic states [78] and antiferromagnetic states [32, 58].

Since ferrimagnetism combines both FM and AFM properties, it is possible to observe not only tilting in its magnetic anisotropy but also possibly all the switching behaviors found in AFM/FM systems such as field-free switching, multistate switching, memristor behavior, exchange spring effect and ratchet effect. In RE-TM ferrimagnetic alloys, the parameter space for material design is also much wider with knobs on atomic concentration between RE and TM, thickness scaling (not limited to ultrathin $\sim$1 nm thickness due to interfacial PMA), different RE and TM elements, growth condition, and operating temperature. With this motivation, we explore the possibility of achieving the interesting switching behaviors and phenomena observed in AFM/FM systems in a single layer ferrimagnetic GdCo alloy without any superlattice design that is deposited in a single shot. In this paper we report field-free spin-orbit torque switching of GdCo near its magnetic compensation with canted anisotropy and exchange spring behavior at room temperature via transport and magnetometry measurements. Through angle dependent anomalous Hall resistance field loop measurement, the angle of the canting can be characterized. In addition, multistate switching, memristor behavior and ratchet effect are observed where the multistate and ratchet effect are tunable with the in-plane symmetry breaking field. This demonstrates that single shot RE-TM ferrimagnetic alloys possess similar properties to AFM/FM bi-layers which expands the material design space for spintronics applications.

5.2 Design of canted magnetic anisotropy in ferrimagnetic $\mathbf{Gd_xCo_{100-x}}$

The magnetic structure in Gd_xCo_{100-x} can be very complex. Here I will explain a few competing interactions arising from intrinsic magnetic properties and structural properties. PMA can be induced in RE-TM ferrimagnetic alloys due to antiferromagnetic coupling between the two different atoms and the pair-correlation structure induced during growth via sputtering or evaporation [66, 63]. It was found that during the physical vapor deposition of these two elements, the unlike atom pairing (e.g. RE-TM) tends to align out-of-plane whereas the like atom pairing (e.g. RE-RE or TM-TM) tends to align in-plane. In TbCo,

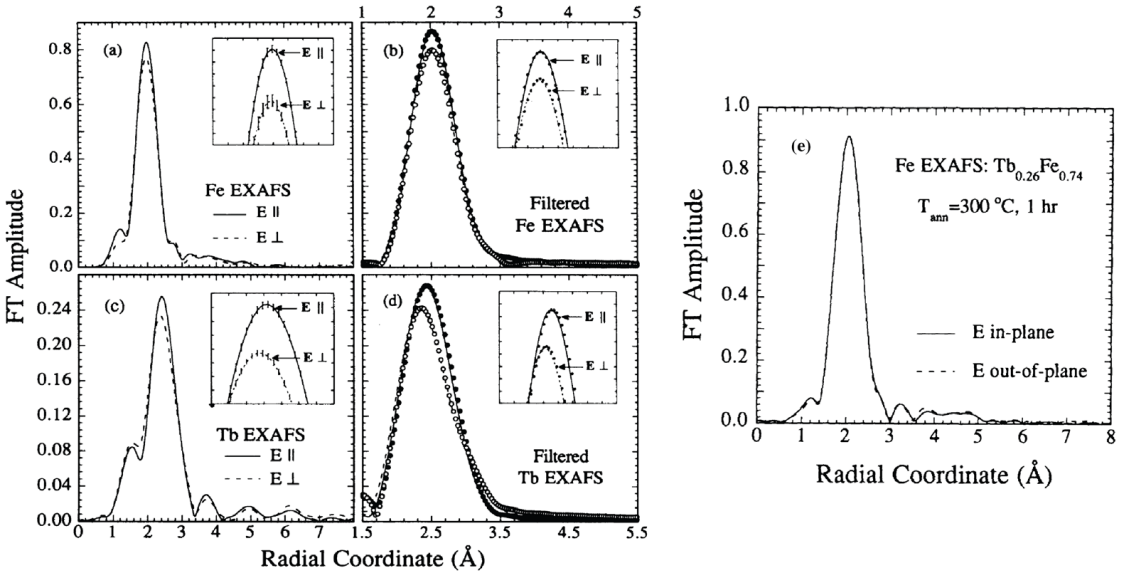

Figure 5.1: Extended X-ray absorption fine structure measurement done on TbFe with perpendicular and in-plane geometry with respect to the film plane. Graph adapted from *Physical Review Letters* [63].

TbFe, structural signatures of such pair-correlation was found [66, 63]. However, this origin is not so apparent and simple in the case of Gd-based FiM as compared to Tb-based FiM [20, 21, 19].

Structural origin of PMA in RE-TM and the exception of Gd-based ferrimagnet

PMA in RE-TM ferrimagnet is mainly due to the pairings of unlike atoms in the out-of-plane direction as compared to the pairings of like atoms in the in-plane direction. As a result, the overlap between the relevant orbitals of the RE atom and TM atoms for ferrimagnetic coupling is very important to induce PMA. In RE-TM ferrimagnetic alloy, the magnetic moment in the RE atom arises from the 4f shell whereas the the magnetic moment in the TM atom arises from the 3d shell. The antiferromagnetic coupling between the two sublattices are through an indirect exchange interaction between the 4f shell of the RE atom and the 3d shell of the TM atom through 5d shell of the RE atom. Since the 4f shell give rise to the magnetism from the RE atom, the filling of the 4f shell may be crucial to the magnetic anisotropy. Combining the orbital picture and the growth-induced mechanism, fully filled 4f shell in Gd does not provide any directionality as compared to the partially filled 4f shell in Tb. Because of this asymmetry in 4f shell filling in Tb, PMA has been shown to be more robust in TbCo as compared to GdCo [21]. This also means that it is more likely for GdCo

to possess canted magnetic anisotropy even though the concentration of GdCo is projected to have PMA.

Consequently, there is an opportunity to tune the PMA and canting of the magnetic anisotropy in Gd_xCo_{100-x} FiM through tuning both its chemical structure and atomic orbital fillings. During my study of Gd_xCo_{100-x} FiM thin films, I found that the magnetic anisotropy of certain Gd_xCo_{100-x} thin films change over time even though with a 2.5 nm of Pt capping layer to prevent oxidation. In some cases, the magnetic anisotropy changes from a canted state (appreciable hysteresis opening and remanence in both in-plane and out-of-plane directions) to fully PMA. In other cases, the PMA films transform into fully in-plane. The time length of such change is around more than 6 months to a few years. This indicates that very slow and trace amount of oxygen can tune the magnetic property especially the magnetic anisotropy direction. A small amount of oxygen incorporation during growth of Gd_xCo_{100-x} can also lead to much stable PMA which has been shown by the Hellman group in the past [20, 21]. I then ask the question: **Can Gd_xCo_{100-x} thin films possess tunable magnetic anisotropy through engineering the oxygen content in a systematic way?**

Sample and device preparation

To study in a systematic way, canted Gd_xCo_{100-x} are deposited via co-sputtering of elemental Gd and Co targets with base pressure around 1e-8 Torr prior to deposition. The canted Gd_xCo_{100-x} thin films are deposited on thermally oxidized silicon substrate with 8 nm Ta as the underlayer and capped with 2$\sim$2.5 nm Pt to prevent fast oxidation (see Fig. 5.2a). In this study, three samples (sample-45, sample-56 and sample-13) with different anisotropy canting angles are obtained with the as-deposited nominal Gd concentrations to be around 24$\sim$25% (see Table 5.1), which is close to the magnetic compensation point[187, 16, 84]. Hall bar devices are patterned onto these thin films through standard lithography and ion-milling technique similar to the two previous chapters (Appendix C).

Thin film magnetometry on canted Gd_xCo_{100-x}

The thin film magnetometry conducted under room temperature on sample-45 reveals an exchange spring behavior and a large canting of magnetic anisotropy (see Fig. 5.2b). The magnetization hysteresis loops taken along the OOP and IP directions show comparable remanent magnetization in both directions indicating a large canting and the total effective anisotopry is close to none. Not only the remanent magnetization is comparable, but also a two-phase switching characterized by a small coercive field and a large coercive field can be observed in both IP and OOP directions. This two-phase switching indicates the Gd_xCo_{100-x} layer is most likely composed of a soft magnetic layer and a hard magnetic layer, which is a signature of exchange-spring behavior [19]. This phenomenon has also been observed in other RE-TM ferrimagnetic systems such as TbCo especially when the thickness is ultrathin ($<$ 10 nm) [19]. In TbCo, the first 2 nm layer is composed of a soft low-density magnetic

Magnetic Property	Sample-45	Sample-56	Sample-13
Atomic Concentration	$Gd_{24.7}Co_{75.3}$	$Gd_{24.7}Co_{75.3}$	$Gd_{24}Co_{76}$
Canting Angle (°)	45	56.25	13.5
Saturation Magnetization M_s (emu/cc)	40	94	111
IP Remanent Magnetization $M_{r,\,IP}$ (emu/cc)	37	44	17
OOP Remanent Magnetization $M_{r,\,OOP}$ (emu/cc)	20	75	102
IP Coercive Field $B_{c,\,IP}$ (G)	180	87	49
OOP Coercive Field $B_{c,\,OOP}$ (G)	41	95	97

Table 5.1: Magnetic properties of canted Gd_xCo_{100-x} moments with different magnetic canting angle in this study.

layer. The sequential layers deposited are much denser and harder magnetic layers. The coexistance of soft and hard magnetic layer in RE-TM ferrimagnetic alloy that are exchange coupled serve as a great exchange spring system to engineer a tunable anisotropy tilting through controlling the concentration, growth condition, underlayer and overlayer [19, 177]. Here, in Gd_xCo_{100-x} this effect can be amplified due to the symmetric filling of the $4f$ shell in Gd compared to Tb mentioned earlier in this section.

Characterization of the magnetic anisotropy direction via angle-dependent anomalous Hall effect transport measurement

In order to quantify the anisotropy canting angle of each sample, we present a new way of characterizing anisotropy canting angle through anomalous Hall effect (AHE) measurements with the field direction to be a function of angle between z-axis and x-axis (see Fig. 5.2c inset). Most often for thin film magnets, the magnetic easy-axis is either strictly in-plane (θ_B = 90°) due to the shape anisotropy or strictly out-of-plane due to strong interfacial or bulk PMA ($\theta_B = 0°$). In our case, due to large canting of the magnetic anisotropy, the easy-axis will be between 0° and 90°. In a typical AHE measurement, when the field is applied in the magnetic easy-axis, the AHE hysteresis will behave as constant resistance values above the two coercive fields (B_c) and the switching between the two constant resistance values occurs upon crossing the coercive fields. In the case of the field being applied in the magnetic hard-axis, the AHE hysteresis curve is a sloped line with minimal hysteresis opening below the anisotropy field before the moments are saturated. This is because there are magnetization

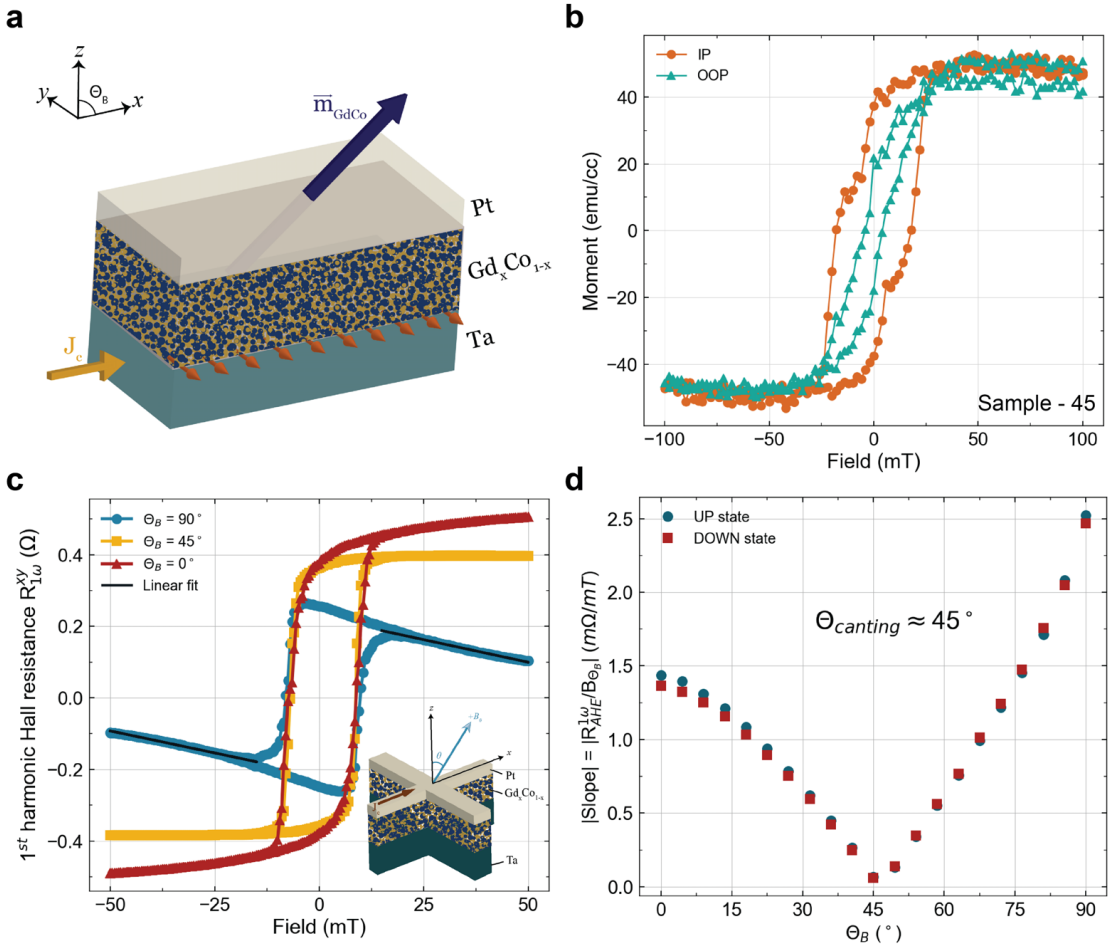

Figure 5.2: a, The magnetic heterostructure under study. Ta (8 nm) bottom layer as spin Hall source for switching experiments, 10 nm Gd_xCo_{100-x} as the ferrimagnet with canted magnetic anisotropy and 2 nm Pt capping. b, Magnetization hysteresis of sample-45 shows that $Gd_{24.7}Co_{75.3}$ is close to magnetic compensation at room temperature characterized by the small saturation magnetization. Exchange spring behavior can be observed in both directions with IP direction being more pronounced. c, Linear fit to the field region above the coercive field to obtain the slope in angle dependent anomalous Hall effect field sweep measurement. For $\theta_B = 45°$, the slope is nearly zero. Inset, angle (θ_B) dependent AHE measurement setup schematics and Hall bar device geometry. θ_B is defined from the z-axis toward the x-axis. d, Slope of the high field region as a function of external field angle from the z-axis. With this technique, the canting angles θ_B are found to be 45 ° for sample-45 where the slope is the minimum.

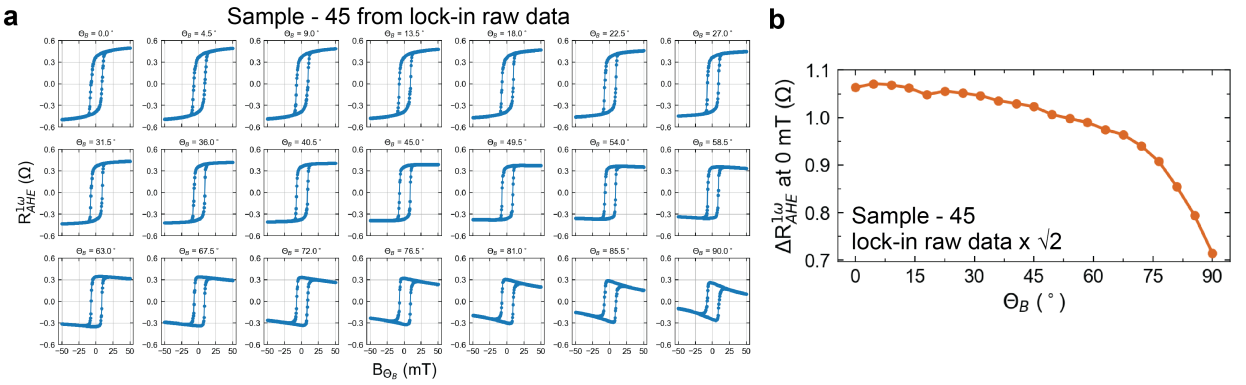

Figure 5.3: a, Full data set of angle dependence anomalous Hall effect field scan from 0°(out-of-plane) to 90° (in-plane) in sample-45. b, ΔR_{AHE} amplitude at zero field in sample-45

which its easy-axis does not align with the field direction thus as the field increases these magnetization are pulled into the field direction and away from their magnetic easy-axis. However, when the external field direction is aligned with the magnetization easy-axis, the slope in the higher field region (above B_c) should be close to zero since all moments are saturated. As a result, when the AHE measurements are done with the field applied in a direction between the easy-axis and the hard-axis, the superposition of the AHE hysteresis from both cases (easy axis and hard axis) occurs and the AHE resistance should be a sloped line in the region above the coercive fields.

We patterned the thin films into Hall bar devices and carried out the angle dependent AHE measurement on sample-45. In Fig. 5.2c and Fig. 5.3a, a series of AHE hysteresis loop measured at different field directions θ_B are shown. In the region above the coercive fields, the slopes of the curve decreases in magnitude as the field direction approaches 45 degrees and once it crosses 45 degrees, the slope magnitudes begin to increase again (see Fig. 5.2d). By fitting a line to the region above the coercive fields (see Fig. 5.2c), we are able to find the angle at which the minimum slope is obtained. In sample-45, the minimum slope is found to be at 45 degrees away from the z-axis (see Fig. 5.2d). This confirms that the magnetic easy-axis in sample-45 is indeed largely canted from the typical IP or OOP directions.

Tuning of magnetic anisotropy through oxygen plasma treatment

As oxygen content can potentially influence magnetic anisotropy, I conducted an experiment involving the gradual treatment of devices patterned on Gd_xCo_{100-x} with a concentration close to compensation. These devices did not exhibit significant magnetic anisotropy canting or perpendicular magnetic anisotropy (PMA); instead, they showed an in-plane anisotropy to start with. To introduce oxygen, a gentle oxygen plasma treatment was employed, considering that oxidation in the ambient environment over extended periods with a 2 nm Pt

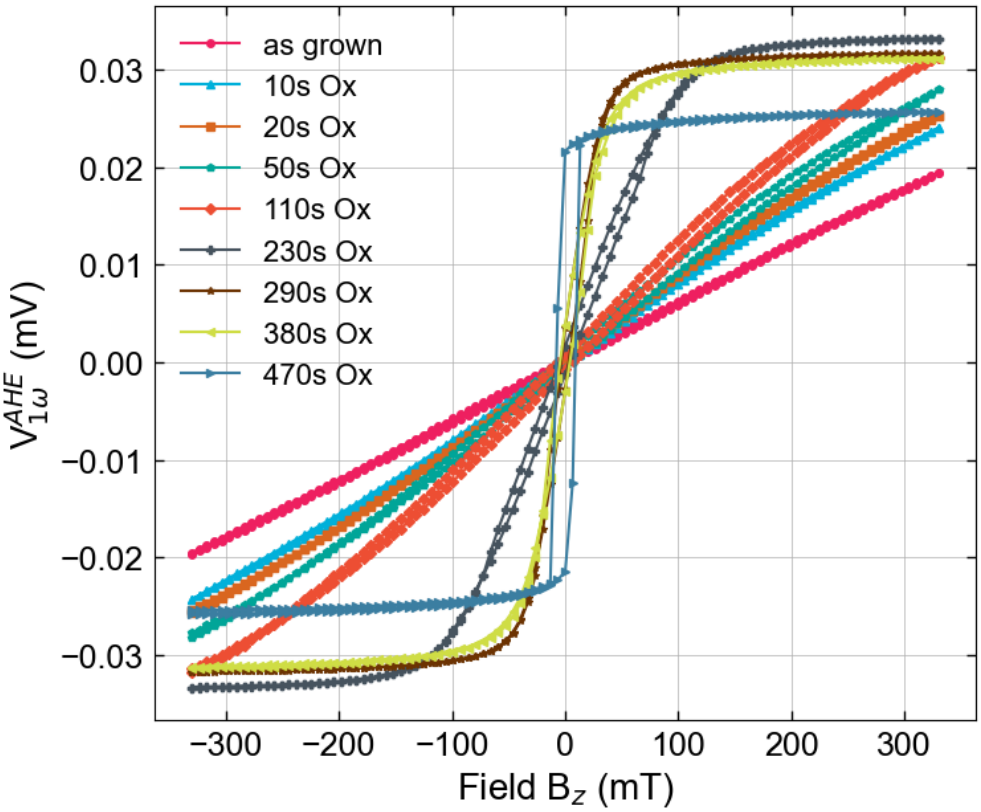

Figure 5.4: Tuning the magnetic anisotropy in Gd_xCo_{100-x} heavy metal heterostructure through oxygen plasma treatment.

capping layer should occur at a slow pace, resulting in only a mild amount of oxygen in the film.

Oxygen plasma is done in a Technics PE II-A plasma etched with oxygen pressure of 180 mTorr and 50W RF power. The chuck is at 50 degrees C. The magnetic anisotropy is characterized by the anomalous Hall effect resistance as a function of the out-of-plane magnetic field B_z. In Fig. 5.4, the device started with a strong in-plane anisotropy characterized by the hard-axis line without any hysteresis opening since AHE is only sensitive to the out-of-plane component of the magnetization. With longer exposure to oxygen, the shape of the AHE curve changes from the hard-axis line to a small opening of the hysteresis (110s) and more pronounced curvatures near the zero field region. Between 380s and 470s of oxygen plasma treatment, the large portion of the magnetization in Gd_xCo_{100-x} transformed into having strong out-of-plane anisotropy. This shows that magnetic anisotropy in Gd_xCo_{100-x} can be easily tuned via low power oxygen plasma treatment.

5.3 Field-free spin-orbit torque switching

With the magnetic anisotropy canting angle quantified, we first performed the spin-orbit torque switching experiments to realize the possibility of SOT switching in the absence of a symmetry breaking field on the canted GdCo samples (experimental method is similar to section 3.8). We performed pulsed current measurements (200 μs) on Hall bar devices (see Fig. 5.5a) with anomalous Hall effect as the voltage readout mechanism to probe the magnetic state of the canted GdCo moments. Before we applied the current pulses, a large set field in the z-direction ($B_{set,z} = \pm 100$ mT) was applied to initialize the magnetic moments to a known state. After the moments are initialized, the large set field is removed. The current pulse amplitude sequence for studying the SOT switching behavior in Fig. 5.5 starts from a large negative current value (-27 mA) above the critical switching threshold and traverses to the positive critical switching current value (+27 mA) and back to the negative critical switching current value with a hysteresis profile.

SOT switching curves from sample-45 without symmetry breaking fields are shown in Fig. 5.5b. Switching between two magnetic states are observable, which confirms the field-free switching behavior in largely canted GdCo moments. In addition to the field-free switching, the ΔR_{AHE} appears to be dependent on the initialization direction with the case of $B_{set,z} =$ +100 mT having a larger ΔR_{AHE} and the switching chirality is independent of the initialization direction. This indicates that the symmetry breaking caused by the canting is fixed in a particular direction but the strength of the canting is dependent on the initialization direction. The difference in ΔR_{AHE} is amplified under certain combination of $B_{set,z}$ and B_x. In Fig. 5.5c and 5.5d, the switching curves were obtained with ± 2.5 mT symmetry breaking fields during the switching experiments and the magnet was initialized with $B_{set,z} = \pm$ 100 mT. From these four switching curves, we can confirm that the effective canting field in Gd_xCo_{100-x} is in the direction of $-x$ since the switching chirality is the same between the case of $B_x = 0$ and the case of B_x = -2.5 mT. By comparing the four curves, the switching chirality is consistent with the symmetry breaking field sign. However, for the case of [$B_{z,set}$, B_x] = [+ 100 mT, + 2.5 mT] (see Fig. 5.5c), the ΔR_{AHE} is highly suppressed compared to the rest of the three switching curves. While it is expected that a positive B_x may partially cancel out the canting since the effective canting field is in the $-x$ direction, it is not immediately clear on the $B_{z,set}$ dependence of ΔR_{AHE} suppression.

5.4 Rich switching phenomena by spin-orbit torque

In-plane symmetry breaking field dependence SOT switching

In order to better understand how the symmetry breaking field (B_x) and the initialization conditions affect the canting of the anisotropy during SOT switching, I repeated the switching experiment over a series of B_x for both initialization cases $B_{set,z} = \pm$ 100 mT (see Fig. 5.6). In Fig. 5.6, all R_{AHE} loops are plotted as they are without any centering or normalization

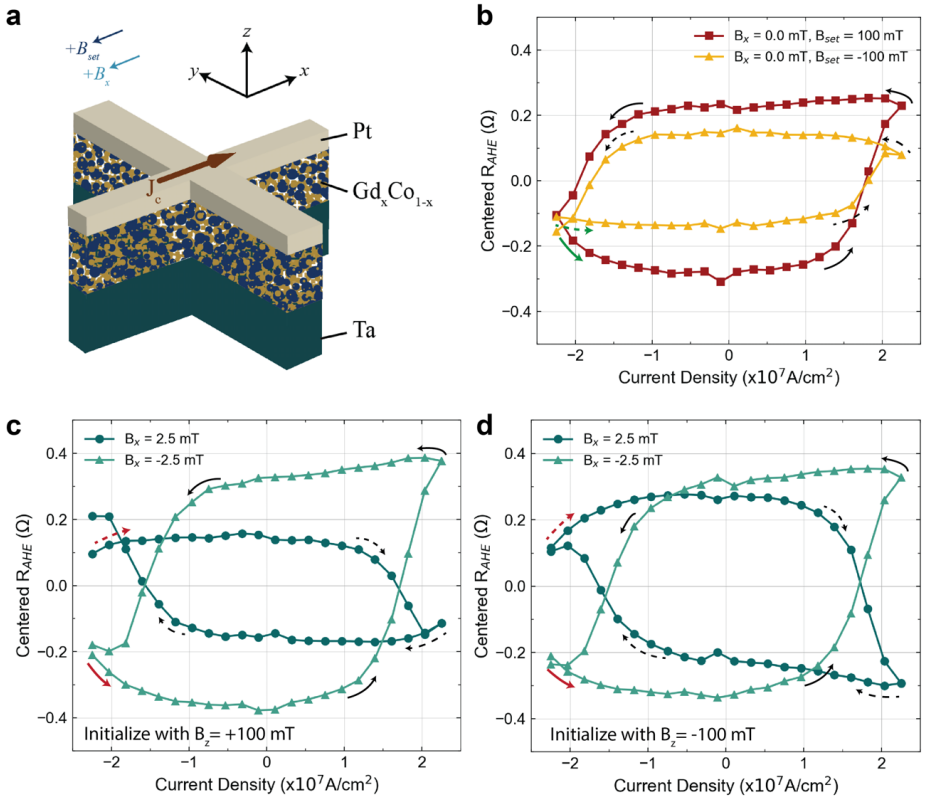

Figure 5.5: a, Schematics for switching experiment configuration on the Hall bar device. b, Spin-orbit torque switching without a symmetry breaking field on sample-45 with anomalous Hall effect resistance (R_{AHE}) as the readout. Clear switching of the canted moments for both initialization conditions $B_{set,z}$ = +100 mT and -100 mT is apparent with the case of $B_{set,z}$ = -100 mT having a smaller ΔR_{AHE}. Start of the current pulse is denoted with a green arrow in both cases (dashed for $B_{set,z}$ = -100 mT). c, d, Spin-orbit torque switching of canted GdCo moment in sample-45 with initialization field of ±100 mT and $B_x = \pm$ 2.5 mT. Start of the current pulse is denoted with a red arrow in both cases (dashed for B_x = +2.5 mT).

since the DC offsets of the R_{AHE} are dependent on B_x. For moments initialized by +100 mT, clear switching due to SOT can be clearly seen in all symmetry breaking fields (see Fig. 5.6a). However, reduced ΔR_{AHE} are present for B_x = 1 mT and 2.5 mT (See Fig. 5.6a and 5.6c), indicating partial switching. This can be due to the canting effective field being cancelled by the externally applied in-plane field (B_x). The effective canting field from Fig. 5.6a is between 1 and 2.5 mT in the direction of $-\hat{x}$. This is further supported by the fact that the switching chirality changed between +1 mT and + 2.5 mT. In a usual SOT switching framework without any canting in the anisotropy[208, 207], switching chirality reverses when the sign of the symmetry breaking field reverses. However, in Fig. 5.6a, the switching chirality did not reverse upon crossing the zero symmetry breaking field, instead, the chirality reversed between +1 and +2.5 mT. As for the moments initialized by -100 mT (see Fig. 5.6b and 5.6d), similar switching behavior is observed as the case of $B_{set,z}$ = +100 mT. However, the field where the switching chirality reverses is reduced to be between 0 and +1 mT with the ΔR_{AHE} to be heavily diminished at B_x = +1 mT.

From the B_x dependent switching experiment (see Fig. 5.6), we found the effective symmetry breaking field due to canting is between 0 and 2.5 mT in the $-\hat{x}$ direction and it is also dependent on the initialization direction ($\pm\hat{z}$) with $B_{set,z}$ = +100 mT yielding a larger canting effective field. This can be self-consistently observed in the amplitude of the ΔR_{AHE} at zero symmetry breaking field. Since the canting is weaker when the magnetic state is set with a - B_z compared to + B_z, this means it is more difficult to achieve deterministic switching in the cases of - B_z. As a result, the ΔR_{AHE} at B_x = 0 will be smaller for the case of $B_{set,z}$ = -100 mT. This also explains the diminished ΔR_{AHE} in Fig. 5.5c for the case of [B_x = 2.5 mT, $B_{set,z}$ = + 100 mT]. Another observation from this experiment is the flatness of the up and down magnetic states in the switching curves as a function of the symmetry breaking field. Regardless of the initialization field direction, the magnetic state that is set by a positive current in both switching chirality is always sloped in the current sweep direction that goes from positive to negative. This is visible in the up state for $B_x \leq -2.5$ mT and the down state for $B_x \geq 2.5$ mT in Fig. 5.6a, 5.6c. This has been observed in the AFM / FM bilayer system with in-plane exchange bias field acting on the FM with PMA in past studies[53]. The fact that this behavior only shows up in one magnetic state rather than both can be due to the exchange spring effect, also the ratchet effect in SOT which is asymmetry in the magnetic state stability[78]. In addition to the observations in Fig. 5.6, we repeated the B_x dependent switching experiment with + 27 mA instead of - 27 mA in both initialization cases ± 100 mT (Fig. 5.7) and found even more distinct features. By starting the current pulse sequence from + 27 mA, we found that for $B_{set,z}$ = 100 mT case, a gap in R_{AHE} exists when the SOT tries to switch the canted moments back to the initial state for $B_x \geq 5$ mT. Similar behavior can be observed in the case of $B_{set,z}$ = -100 mT when $B_x \leq -2.5$ mT while the rest of the switching curves resemble the case in Fig. 5.6 correspondingly. To try to understand such gap in R_{AHE}, we carried out more in-depth switching experiments.

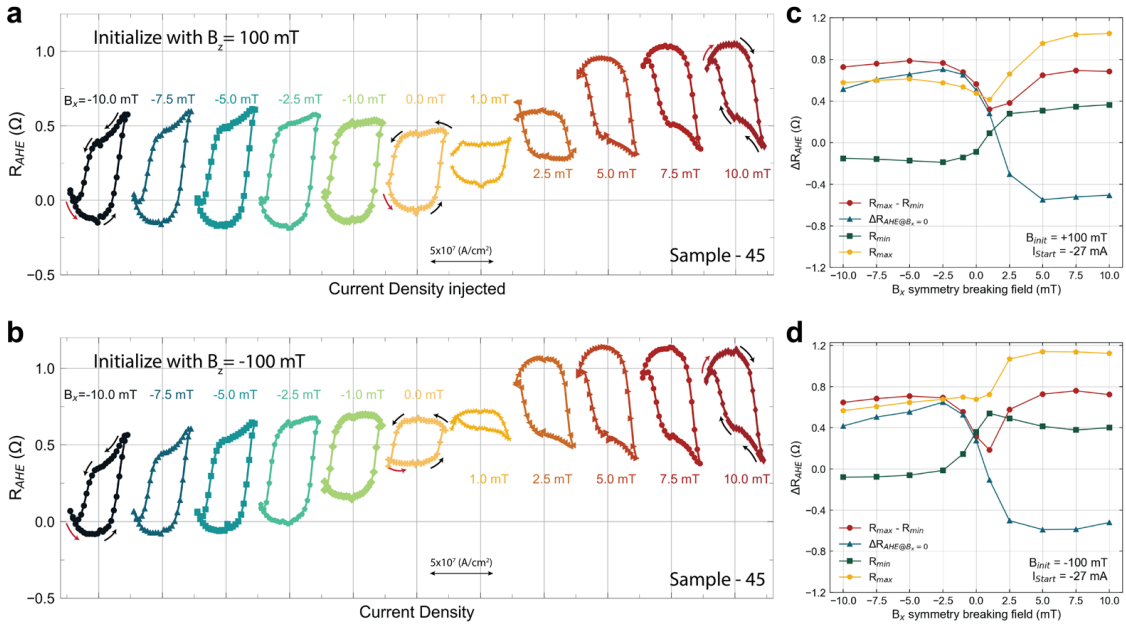

Figure 5.6: In-plane symmetry breaking field (B_x) dependence on SOT switching of GdCo moments with 45° anisotropy canting angle (sample-45). a, b, SOT switching curves with varying symmetry breaking field (B_x) from -10 mT to 10 mT. Before each switching experiment, initialization field ($B_{set,z}$) +100 mT and -100 mT was applied to initialize the moments into a known state, respectively. c, d, Extracted information of each switching curve as as function of symmetry breaking field for the case of $B_{set,z}$ = + 100 mT and - 100 mT respectively. We extracted the ΔR_{AHE} of maximum and minimum R_{AHE} throughout the entire switching curve, the ΔR_{AHE} of R_{AHE} at the zero current crossing, the minimum R_{AHE}, and the maximum R_{AHE}.

Tunable multistate switching and SOT ratchet effect

Ratchet effect in SOT is manifested in the asymmetry of SOT switching via a variety of transport signatures. It is mentioned in the previous section that only one magnetic state is sloped which is always set by the positive current in Fig. 5.6a and 5.6b. Another signature of SOT ratchet effect is the sharpness of the switching between the two magnetic states. This is usually more prominent in system with higher saturation magnetization such as IrMn/CoFeB systems[78], nevertheless, it is still observable here in Gd_xCo_{100-x}. In Fig 5.6a and 5.6b, for switching curves with decent switching amplitude ($|B_x| > 1$ mT), the amount of ΔR_{AHE} per unit current density increase is larger when switching with positive current regardless of the chirality (down to up state for $-B_x$ and up to down state for $+B_x$). In canted Gd_xCo_{100-x}, ratchet effect in SOT can be more complex where exchange spring effect shows up in both in-plane and out-of-plane magnetic component. Since the initialization field direction affects

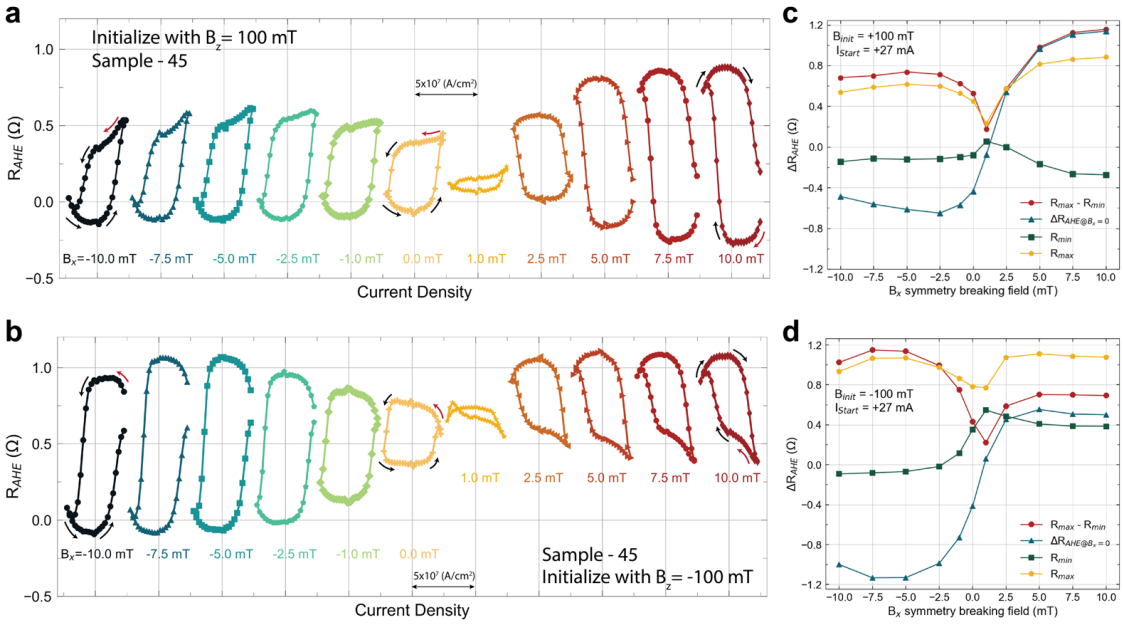

Figure 5.7: In-plane symmetry breaking field (B_x) dependent switching curves with starting current value of + 27mA and initial set field ($B_{set,z}$) of +100 mT and -100 mT in sample-45. a,b, The ΔR_{AHE} for [$B_x = \pm 7.5$ mT, $B_{z,set} = 100$ mT] is 1.124 Ohms, which is very similar to the ΔR_{AHE} value (1.064 Ohms from Fig. 5.3b) from the field sweep AHE hysteresis loop. c, d, Extracted information of each switching curve as as function of symmetry breaking field for the case of $B_{set,z}$ = + 100 mT and - 100 mT respectively. We extracted the ΔR_{AHE} of maximum and minimum R_{AHE} throughout the entire switching curve, the ΔR_{AHE} of R_{AHE} at the zero current crossing, the minimum R_{AHE}, and the maximum R_{AHE}.

the SOT switching behavior including the effective canting field amplitude and the difference in ΔR_{AHE} from the B_x dependent switching experiment, it is important to understand what the magnetic state (R_{AHE}) has been set to by the initialization field ($B_{set,z}$) before applying a large current pulse to switch the magnetic moments. As a result, we performed the B_x dependent switching experiment with a starting current that is small so the SOT is negligible and the initial magnetic state can be probed. Interestingly, the large initial set field $B_{set,z}$ sets the magnetic moments into a state that is not reachable by SOT (see Fig. 5.8) and this initial state is successfully initialized to the same state regardless of the symmetry breaking field applied during the switching experiment. This consistent initial state is quantitatively characterized by the constant R_{AHE} value (R_{min} for $B_{set,z}$ = 100 mT and R_{max} for $B_{set,z}$ = - 100 mT) in Fig. 5.8c and 5.8d. Thus, an additional state is visible and this irreversible behavior manifests a similar SOT ratchet effect in a single layer RE-TM ferrimagnetic alloy as in AFM/FM systems[58, 192, 78].

The multistate and SOT ratchet effect can be observed in certain combinations of $B_{set,z}$

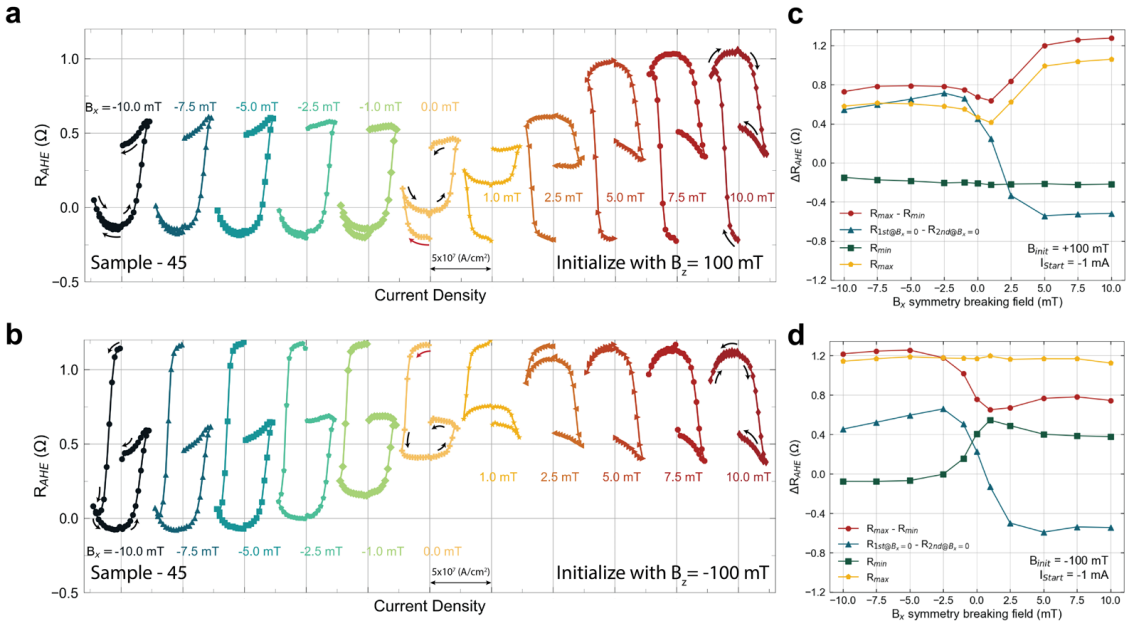

Figure 5.8: Tunable multi-magnetic state switching and SOT ratchet effect as a function of (B_x) and ($B_{set,z}$). a,b, SOT switching curve with varying external symmetry breaking field (B_x) and initialization with $B_{set,z}$ of +100 mT and -100 mT respectively. Current pulse sequence starts from a small negative current (-1 mA) then traverses in the negative direction to the negative critical switching current and back to the positive critical current density then stops at a small positive current (+1 mA). c,d, Extracted information of each switching curve as as function of symmetry breaking field for the case of $B_{set,z}$ = + 100 mT and - 100 mT respectively. We extracted the ΔR_{AHE} of maximum and minimum R_{AHE} throughout the entire switching curve, the ΔR_{AHE} of R_{AHE} at the zero current crossing, the minimum R_{AHE}, and the maximum R_{AHE}.

and B_x in our study. In Fig. 5.8a, the initial magnetic states are consistently set to the lowest R_{AHE} value around -0.25 Ohms by $B_{set,z}$ = + 100 mT across all the different B_x-dependent scans and in Fig. 5.8b, the initial magnetic states are set to the highest R_{AHE} value consistently as well. Here, there are two observations we would like to point out and they are differentiated by the switching chirality. In the first observation, we focus on the switching curves set by $B_x \geq 2.5$ mT with $B_{set,z}$ = 100 mT and $B_x \leq 0$ mT with $B_{set,z}$ = - 100 mT (Fig. 5.8a and 4b). In these cases, the current pulse amplitude increases to the first critical current value where SOT is strong and the magnetic state is switched to the opposite direction away from the initial state. The reverse switching occurred upon reaching the second critical current with opposite sign. However, the canted moments did not switch back to the original R_{AHE} state set by the large initial field for cases of $B_x \geq 2.5$ mT in Fig. 5.8a and $B_x \leq 0$ mT in Fig. 5.8b. Instead, the R_{AHE} state set by the SOT is near the

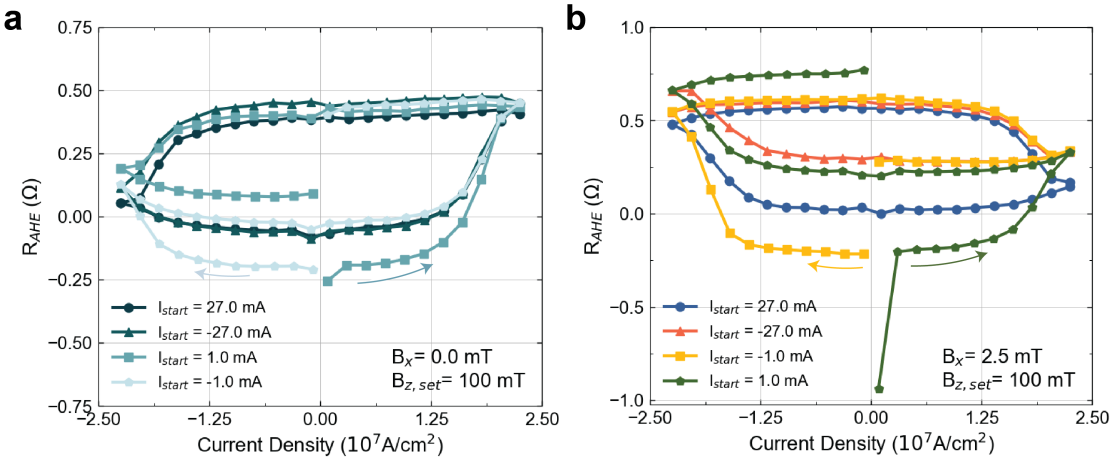

Figure 5.9: Superposition of spin-orbit torque switching curves with varying starting current amplitude of the pulsing sequence. a, Superposition of the switching curves with varying starting current pulse train amplitude obtained with no symmetry breaking field and initialization field of $B_{z,set}$ = + 100 mT. b, with B_x = + 2.5 mT and $B_{z,set}$ = + 100 mT. All curves are plotted as measured without normalization, DC shift or any further processing. Multistate behavior can be observed by starting with a small current pulse amplitude and gradually traverse to large current amplitudes to observe the SOT switching. It is also clear that the large initialization z-field sets the magnetic state to the same state in the curves obtained by starting with a small current amplitude.

mid-point of the full R_{AHE} curve, exhibiting a ratchet behavior.

More interestingly, this ratchet effect exists for both switching chiralities. For the first observation, ratchet switching is defined in the fashion that the first critical current switched the R_{AHE} state away from the initial state to the opposite state and when the current amplitude reaches the second critical current with opposite sign, the R_{AHE} state that is set by the SOT does not return to the initial R_{AHE} state set by the large magnetic field. For the second observation, we focus on the switching curves of $B_x = -2.5 \sim 1$ mT with $B_{set,z}$ = 100 mT and $B_x = 1 \sim 5$ mT with $B_{set,z}$ = - 100 mT. In this case, we still observe the multistate even though the first critical current sign already favors the initial magnetization state direction. Upon reaching the first critical current, the R_{AHE} state is set to a different value from the initial R_{AHE} and once the current reaches the second critical current with opposite sign, the R_{AHE} state is switched to the opposite magnetic state. In fact, as the symmetry breaking field becomes stronger, the middle R_{AHE} state that is set by the first critical current shifts into the R_{AHE} state that is set by the second critical current value and the multistate is absent. This shows that the middle R_{AHE} state can be tuned by the external symmetry breaking field.

If we disregard the initial magnetic state in Fig. 5.8, the middle R_{AHE} is essentially the

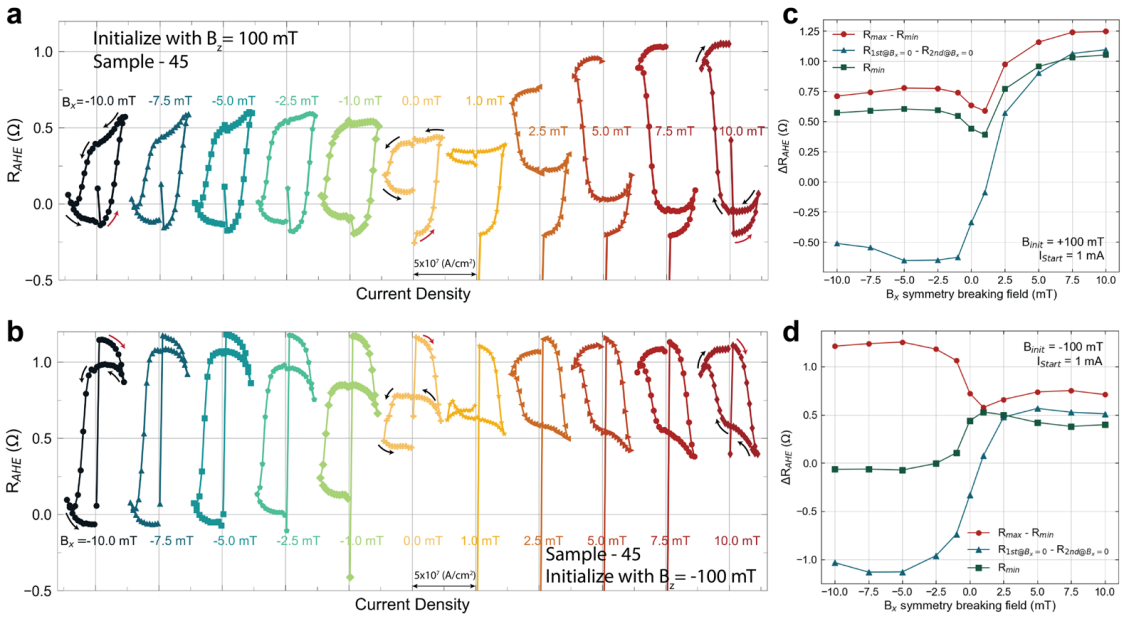

Figure 5.10: In-plane symmetry breaking field (B_x) dependent switching curves with starting current value of + 1mA and initial set field ($B_{set,z}$) of +100 mT and -100 mT that exhibits the three different switching magnetic states in sample-45. a, The ΔR_{AHE} between the top and middle states for [B_x = 7.5 mT, $B_{z,set}$ = 100 mT] is 1.065 Ohms, which is very similar to the ΔR_{AHE} value (1.064 Ohms) from the field sweep AHE hysteresis loop (from Fig. 5.3b). The ΔR_{AHE} between the top and bottom states for B_x = 7.5 mT, $B_{z,set}$ = 100 mT] is 1.241 Ohms, which is slightly above the ΔR_{AHE} value (1.064 Ohms) from the field sweep AHE hysteresis loop. b, The ΔR_{AHE} between the top and middle states for [B_x = - 7.5 mT, $B_{z,set}$ = - 100 mT] is 1.132 Ohms, which is very similar to the ΔR_{AHE} value (1.064 Ohms) from the field sweep AHE hysteresis loop. The ΔR_{AHE} between the top and bottom states for B_x = 7.5 mT, $B_{z,set}$ = 100 mT] is 1.239 Ohms, which is slightly above the ΔR_{AHE} value (1.064 Ohms) from the field sweep AHE hysteresis loop. c, d, Extracted information of each switching curve as as function of symmetry breaking field for the case of $B_{set,z}$ = + 100 mT and - 100 mT respectively. We extracted the ΔR_{AHE} of maximum and minimum R_{AHE} throughout the entire switching curve, the ΔR_{AHE} of R_{AHE} at the zero current crossing, and the minimum R_{AHE}.

bottom (top) state for the case of $B_{set,z}$ = +100 mT (-100 mT) in Fig. 5.6. To facilitate the comparison, the superposition of the switching curves obtained with different starting current values but same symmetry breaking field and initialization field is plotted in Fig. 5.9. The two states achieved by the SOT with a large starting current is exactly overlapping on the part where the middle state and the final state is achieved by the SOT in the curve with the multistate (see Fig. 5.9). By calculating the ΔR_{AHE} for [B_x, $B_{set,z}$] = [7.5 mT, 100 mT] and [−7.5 mT, −100 mT] in Fig. 5.8, we obtain ΔR_{AHE} = 1.26 and 1.25 Ohms respectively (see Fig. 5.8c, and 4d). If we further compare these values to the ΔR_{AHE} at zero field (1.064 Ohms), obtained by multiplying the AHE field sweep hysteresis loop in the z-direction by $\sqrt{2}$ since it is detected by a lock-in amplifier (See Fig. 5.5b and methods), we find very similar values. This indicates that SOT either fully switched or very close to fully switched the canted moments from its initial state set by the large $B_{set,z}$ to the opposite state resulting in a ΔR_{AHE} close to the ΔR_{AHE} obtained by field sweep where the moments are fully saturated in the z-direction. However, only partial switching can be obtained when the moments are switched back resulting in the presence of a middle state in Fig. 5.8 thus the ratchet effect. This phenomenon suggests the presence of fixed effective fields due to canting in both the in-plane and the out-of-plane direction. The change of the R_{AHE} under different [B_x, $B_{set,z}$] condition in Fig. 5.8 is the result of both the in-plane and the out-of-plane components of the canted GdCo moments are being manipulated by the SOT and the switching dynamics of both components are affecting each other, potentially due to the exchange spring effect. For completeness and repeatability, the symmetry breaking field dependence switching curves of conditions [I_{start} = +1mA, $B_{set,z}$ = 100 mT] and [I_{start} = +1mA, $B_{set,z}$ = -100 mT] are shown in Fig. 5.10 and the results are consistent and symmetric to the cases in Fig. 5.8.

5.5 Effect of canting angle on various SOT switching phenomena

From the SOT switching results on sample-45, it is shown that strong magnetic anisotropy canting can lead to different switching phenomena such as ratchet effect, field-free switching, and multistate switching. Here we further explore the effect of canting angle on the various switching phenomena.

Canting closer to in-plane

Two other samples with different canting angles are shown in Fig. 5.11 (56.25°) and Fig. 5.12 (13.5°). Sample-56 has a much larger saturation magnetization (Fig. 5.11a) and the canting angle (56.25°) is closer to in-plane (Fig. 5.11c). For sample-56, the two-phase switching in the magnetometry data is weaker but still observable especially in the OOP direction (Fig. 5.11a). Although the anisotropy is closer to being in-plane thus the smaller squareness (M_r / M_s), the field-sweep AHE curve still exhibits a clear hysteresis (Fig. 5.11b). However, the SOT switching curve does not exhibit a strong two-state switching, instead, a

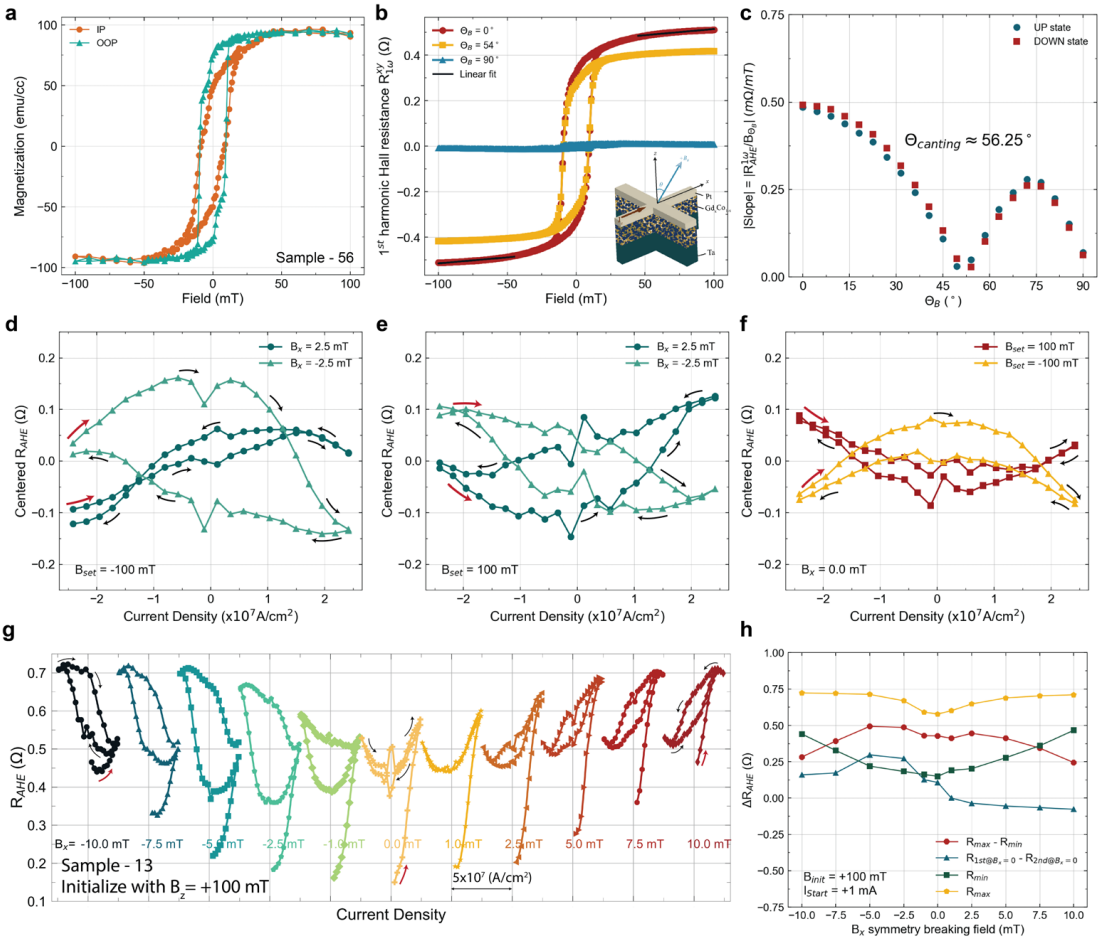

Figure 5.11: SOT switching of canted GdCo moments with magnetic canting angle of 56 degrees (sample-56). a, Thin film magnetometry of sample-56. b, Angle-dependent anomalous Hall effect measurement and the linear fit to data above the coercive field region for obtaining the slope. c, Slope in the field region above the coercive field as a function of field angle. The minimum of the slope resides at 56.25° from the z-axis. d-e, Spin-orbit torque switching curve with starting current value of -27 mA. The four different switching curves are obtained with four different combination of initialization field (± 100 mT) and symmetry breaking field (± 2.5 mT). f, Spin-orbit torque switching curve with starting current vlaue of -27 mA without a symmetry breaking field. The two curves shows the dependence of initialization direction. g, SOT switching curves with varying external symmetry breaking field (B_x) and initialization with $B_{set,z}$ of +100 mT. Current pulse sequence starts from a small positive current (+1 mA, red arrow) then traverses in the positive direction following the rest of the black arrows. h, We extracted the ΔR_{AHE} of maximum and minimum R_{AHE} throughout the entire switching curve, the ΔR_{AHE} of R_{AHE} at the zero current crossing, the minimum R_{AHE}, and the maximum R_{AHE}.

very gradual switching curve as a function of current amplitude is observed (Fig. 5.11d and 5e). This is mostly due to the weak PMA of sample-56 since the readout of the magnetic state is through the anomalous Hall effect. Interestingly, among the two different switching conditions [$B_{z,set}$= - 100 mT, B_x=± 2.5 mT], the ΔR_{AHE} of the case [B_x= + 2.5 mT] is highly suppressed but largely enhanced for the case [B_x= - 2.5 mT] (Fig. 5.11d). This is similar to sample-45 (Fig. 2c) where ΔR_{AHE} is suppressed for the case of [$B_{z,set}$= + 100 mT, B_x= + 2.5 mT] but the discrepancy between the opposite sign of B_x is enhanced with a larger canting angle (sample-56). For the cases of [$B_{z,set}$= + 100 mT, B_x= ± 2.5 mT] in sample-56, the ΔR_{AHE} is comparable regardless of the symmetry breaking field and also the chirality switches accordingly which is the same as the case [$B_{z,set}$= - 100 mT, B_x= ± 2.5 mT] (Fig. 5.5d) in sample-45.

While it is expected that very minimal magnetic switching can be observed in sample-56 without a symmetry breaking field due to the weak PMA, a non-zero hysteresis is still observed at zero symmetry breaking field (Fig. 5.11f). In addition, the switching chirality is fixed regardless of the initialization field (Fig. 5.11f), which is also similar to the zero-field switching result in sample-45 (Fig. 5.5b). The opposite sign of the curvature in the two switching curves (Fig. 5.11f) is most likely due to the IP moments that are initialized by the opposite perpendicular field. Here, we also observed a minimal hysteresis opening at B_x = 1 mT which indicates that the canting effective field is close to 1 mT and also the switching chirality changes upon crossing B_x = 1 mT. Next, we investigate how the canting angle affects the multi-state switching and ratchet effect. Clearly, the ratchet effect persists in all the switching curves with different B_x (Fig. 5.11g) and the main difference from sample-45 is that the initial magnetic state (R_{AHE})is no longer constant (Fig. 5.8) across the different symmetry breaking fields in sample-56. In fact, the initial state R_{min} (Fig. 5.11h) is symmetric against $B_x = 0$. As for the ratchet effect, it is clear that once the SOT switches the moments to the other direction, the opposite SOT sign does not switch the moments back to their initial state R_{min} (Fig. 5.11g). Due to the weak PMA in sample-56, effective canting field is smaller (between $0 \sim 1$ mT) than sample-45 across all the sets ([$B_{z,set}$, B_x]) of switching curves.

Canting closer to out-of-plane

Next, we investigate the effect of a much weaker canting on the switching phenomena. A strong PMA can be obtained with clear exchange spring behavior from the magnetometry measurement in the OOP direction for single-shot co-sputtered GdCo with its composition close to the magnetic compensation - sample-13 (Fig. 5.12a). From the angle-dependent AHE field sweep measurement (Fig. 5.12b, 6c), the canting angle is close to 13°. The discrepancy of ΔR_{AHE} between the two $B_x = \pm$ 2.5 mT switching curves, when the moments are initialized by $B_{z,set}$ = - 100 mT, is observable but much smaller (Fig. 5.12d) compared to sample-45 (Fig. 5.5b) and sample-56 (Fig. 5.11d). As for the other initialization case ($B_{z,set}$ = + 100 mT), the ΔR_{AHE} are the same between the two $B_x = \pm$ 2.5 mT switching curves and their chiralities behave as expected correspondingly (Fig. 5.12e). Due to the weaker

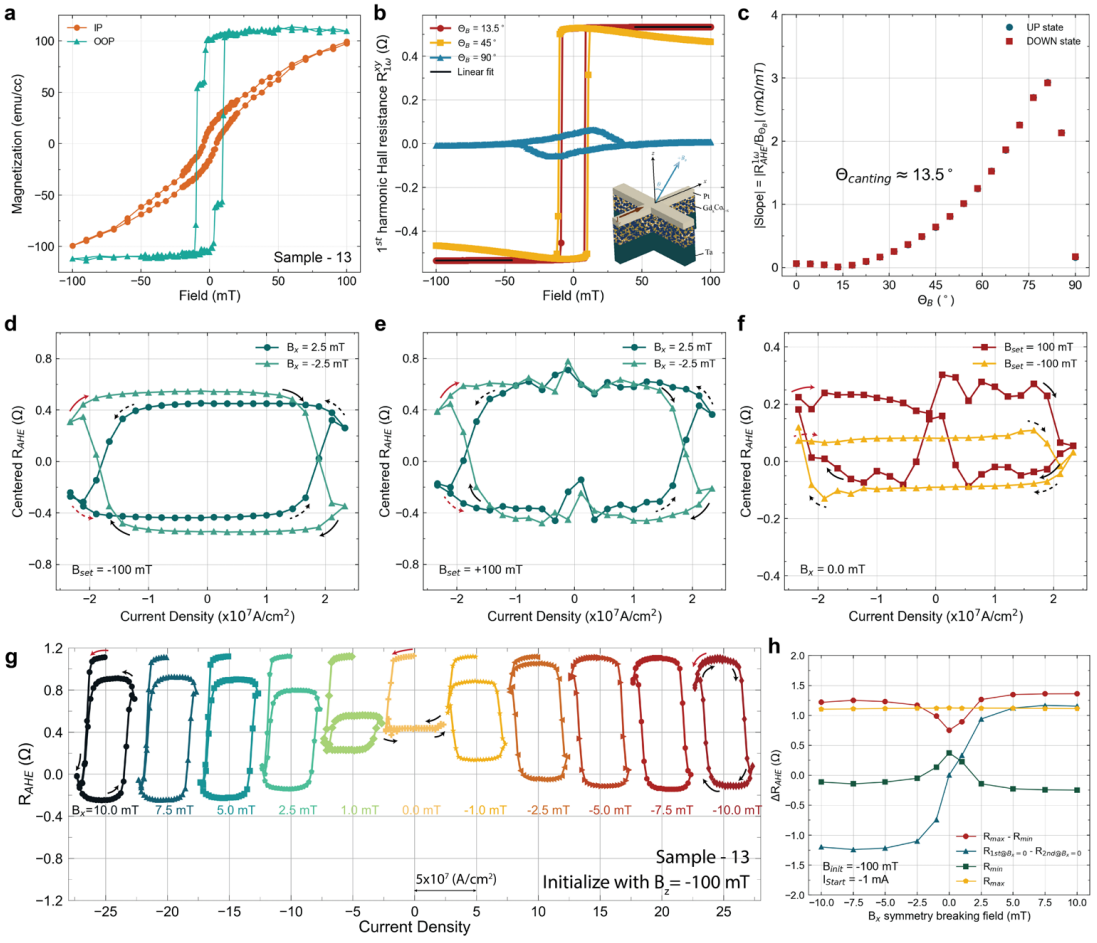

Figure 5.12: SOT switching of canted GdCo moments with magnetic canting angle of 13 degrees (sample-13). a, Thin film magnetometry of sample-13 via vibrating sample magnetometer. b, Angle-dependent anomalous Hall effect measurement and the linear fit to data above the coercive field region. c, Slope in the field region above the coercive field as a function of field angle. The minimum of the slope resides at 13.5° from the z-axis. d-e, Spin-orbit torque switching curve with starting current value of -28 mA. The four different switching curves are obtained with four different combinations of $B_{set,z}$=± 100 mT and B_x=± 2.5 mT). f, SOT switching curve with starting current value of -27 mA without a symmetry breaking field. The two curves shows the dependence of initialization direction. g, SOT switching curves with varying external symmetry breaking field (B_x) and initialization with $B_{set,z}$ of -100 mT. Current pulse sequence starts from a small negative current (-1 mA) then traverses in the negative direction following the black arrows. h, Extracted information of each switching curve as as function of B_x for the case of $B_{set,z}$ = + 100 mT. We extracted the ΔR_{AHE} of maximum and minimum R_{AHE} throughout the entire switching curve, the ΔR_{AHE} of R_{AHE} at the zero current crossing, the minimum R_{AHE}, and the maximum R_{AHE}.

canting and strong PMA, minimal switching is observed at zero symmetry breaking field (Fig. 5.12f) and the switching chirality is again fixed. Although the canting is weak, clear SOT ratchet effect is observable across the different symmetry breaking field switching loops (Fig. 5.12g). However, due to the strong PMA and weak canting, the switching curves and multistate behavior are less tunable across the different in-plane symmetry breaking fields. For example, in sample-45, the switching curves as a function of in-plane field (B_x) resided in the R_{AHE} range of 0 to 0.5 Ω for B_x = -10 mT and as B_x increases, the switching curve moved up in R_{AHE} values and end up in the range of 0.5 to 1.2 Ω for B_x = + 10 mT. This can be characterized by the R_{min} (Fig. 5.6d) and R_{max} (Fig. 5.6d) in Fig. 5.6b. This is not the case for sample-13 where the switching curves do not move up by more than 0.125 Ω from B_x = -10 mT to + 10 mT in Fig. 5.12g and characterized by R_{min} in Fig. 5.12h.

Spin-orbit torque memristor switching

The possibility of the memristor behavior[53, 211] in sample-13 is also studied since the strong PMA can lead to much easily observable SOT switching loops and R_{AHE} value changes. Due to the strong exchange spring effect in the OOP direction and the small canting, GdCo in sample-13 serves as an equivalent system as AFM/FM which possess a small canting from the exchange bias and the exchange spring behavior from the coupling between pinned interface AFM moments and FM moments. Indeed, the memristor behavior can be observed in sample-13 with a small symmetry breaking field to assist full switching (Fig. 5.13). In addition, the spacing between the R_{AHE} states achieved by the different I_{max} values can be tuned by the symmetry breaking field strength.

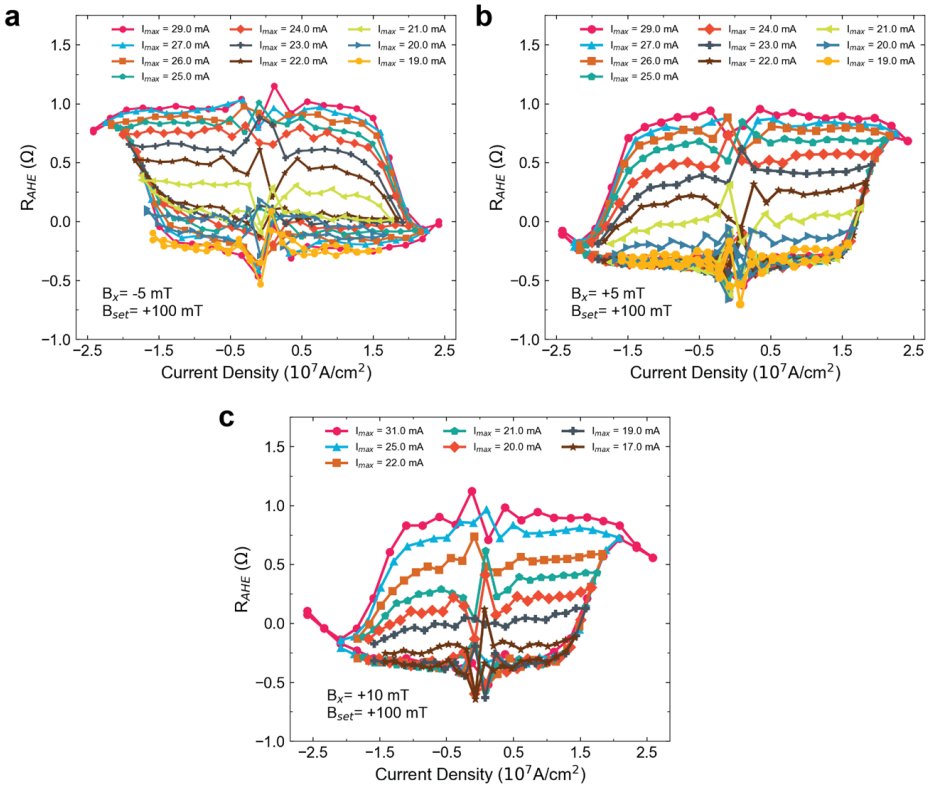

Figure 5.13: Memristor behavior in sample-13 with small magnetic canting and strong perpendicular magnetic anisotropy. Switching curve as a function of maximum current amplitude in the current pulse train with symmetry breaking field of B_x = **(a)** -5 mT, **(b)** +5 mT, and **(c)** +10 mT are shown. As expected, with a smaller symmetry breaking field, the increment of ΔR_{AHE} is smaller per unit increase in I_{max} by comparing Fig. S7b and S7c. Moreover, the onset of nonzero ΔR_{AHE} is lower with higher symmetry breaking field. In Fig. 5.13c, switching hysteresis opens up at 17 mA for B_x = +10 mT as compared to 20 mA for B_x = +5 mT.

Chapter 6

Pure voltage-driven magnetic switching via resonant tunneling interlayer exchange coupling

6.1 Foreword and motivation

Magnetism is inherently a current-driven phenomenon from moving charges creating an Oersted magnetic field to an electron possessing spin angular momentum that carries a finite magnetic moment. Unlike most electronic devices such as transistors, capacitors or diodes where the device operations are governed by the electric field applied to the device, magnetic devices are operated by magnetic fields which naturally arise from a current. From a intrinsic standpoint, electric field does not break time-reversal symmetry. As a result, there is no way for an electric field to change the relative energy barrier between the two stable magnetic field without breaking the time-reversal symmetry. In most experiments that was able to achieve a bi-directional switching via voltage or electric field, a magnetic field is required [170, 206]. Consequently, it has been extremely challenging to achieve bi-directional magnetization switching by only applying an electric field across a ferromagnet thin film, or even a magnetic tunnel junction. However, there is significant progress in understanding how magnetic material and devices respond to an electric field such as voltage-controlled magnetic anisotropy (VCMA) [121, 198], voltage-controlled exchange coupling (VCEC) [212, 228], and multiferroic switching [68].

VCMA is driven by the modulation of carrier densities between majority and minority spins near the surface of ultrathin ferromagnetic films since most transition metal ferromagnets are metallic so the electric field does not penetrate deep [176]. With the occupation of the majority and minority spin bands modulated, magnetic properties including the anisotropy energy and coercivity are changed. While lowering the anisotropy energy is useful for reducing the critical switching current density via STT or SOT effects [228], a full bi-directional switching driven by purely electric field is still not achievable.

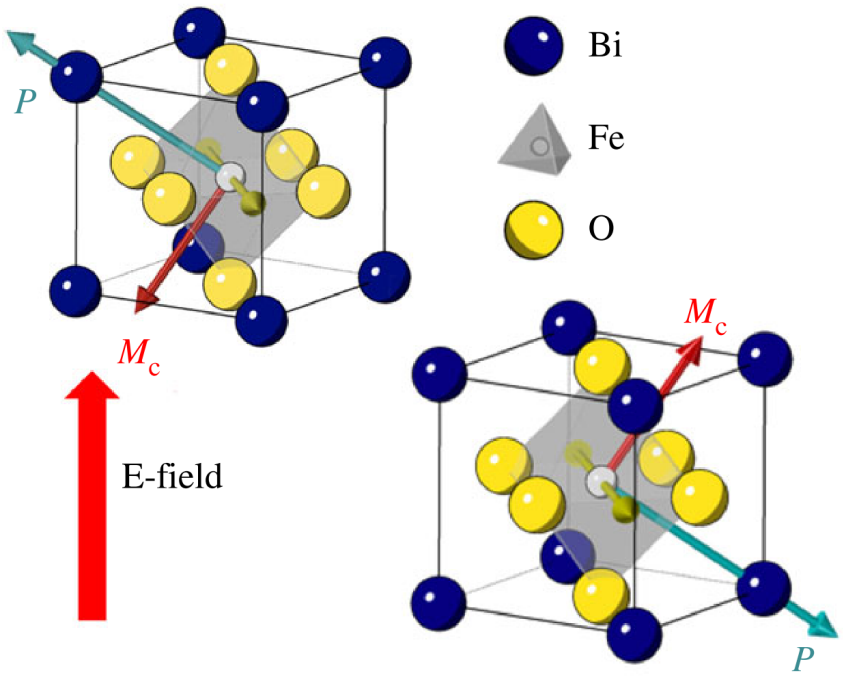

Figure 6.1: Schematic of the rhombohedral bismuth ferrite crystal structure. The directional switching of the ferroelectric polarization coupled with the magnetic moment switching is also drawn. Graph adapted from *Proceedings of the Royal Society A: Mathematical, Physical and Engineering Sciences*. [156]

On the other hand, only two mechanisms in very specific materials have demonstrated the ability to achieve bi-directional magnetic switching without a magnetic field or other spin current contributions. The first one is the multiferroic material system with $BiFeO_3$ as the seminal model material [68, 156]. In $BiFeO_3$, both ferroelectricity and ferromagnetism are present and closely coupled together. In the ground state, $BiFeO_3$ is an antiferromagnet with canted magnetic moments arising from the Dzyalozhinski–Moriya interactions (DMI). One can further engineer for non-zero magnetic moments by strain engineering via epitaxial thin film growth [156]. In Fig. 6.1, we can see that upon the 180° polarization switching, the magnetic moment is also switched in 180° but remains perpendicular to the ferroelectic polarization. The underlying physical interaction and the rise of ferromagnetism is beyond the scope of this chapter but readers are recommended to read selected reviews on multiferrorics such as [48, 179, 156]. Nevertheless, through multiferroric materials, direct magnetization switching via an electric field is possible but is limited to efficienct multiferroic materials with strong coupling between ferroelectric polarization and ferromagnetic magnetization.

The second mechanism is the VCEC mentioned earlier [212]. VCEC is the electric-field modulation of interlayer exchange coupling (IEC) strength and sign between two ferromag-

netic layers separated by a non-magnetic (NM) metallic spacer - synthetic antiferromagnet (SAF). In SAF structures, the adjacent ferromagnetic layers couple either ferromagnetically or antiferromagnetically depending on the (NM) spacer layer thickness. This SAF layer is often used in MTJs to exchange couple to a reference ferromagnetic layers for pinning this layer so it is not easily switched through STT, SOT, or small magnetic fields. Since the exchange coupling sign and strength can be tuned through varying the NM spacer thickness in a SAF structure, previous works [133, 206, 212] have shown that the effective thickness of the spacer layer or ferromagnetic layer can be effectively tuned by an electric field. This is the foundation of VCEC. By tuning the effective thicknesses of the NM spacer and ferromagnetic layer, the exchange coupling sign can be switched from antiferromagnetic to ferromagnetic or vice versa at certain voltages. In Zhang *et al.* [212], bi-directional switching of the magnetization is demonstrated through such mechanism in a free layer magnetization that is strongly coupled to the SAF layer which is modulated by the electric field. This is a very exciting work toward voltage-controlled bi-directional switching and provides immense perspective toward deeper understanding of voltage-controlled magnetism and further lowering of MTJ device power consumption.

In this chapter, I explore the possibility of pure voltage-driven magnetization switching through the combination of interlayer exchange coupling (IEC) and resonant tunneling effect (RTE). This design does not rely on any additional SAF layer to exchange couple to the free layer ferromagnet or electrically modulate the effective thickness of the spacer layer or ferromagnetic layer. The device structure only requires insertion of two additional layers that are no more than 2 nm at most.

Before entering the following section, I would like to point out that majority of effort on the theoretical work was done by Dr. Shehrin Sayed (then postdoc researcher in the group) and the formulation of the idea is led by Professor Sayeef Salahuddin and Dr. Shehrin Sayed. My contribution to this work include partial contribution in the formulation of the idea during the theoretical exploration phase and the main contribution comes in as leading the experimental effort in bringing the idea into reality.

6.2 Interlayer exchange coupling and resonant tunneling effect

Interlayer exchange coupling (IEC)

IEC is explored in a device structure where a non-magnetic metallic spacer is sandwiched between two ferromagnetic layers. The exchange coupling strength and sign (J_{ex}) between the two ferromagnetic layers dictates whether the two ferromagnetic layers are coupled in a ferromagnetic or antiferromagnetic fashion. The exchange coupling strength varies as a function of spacer thickness in a oscillatory manner. In addition, different spacer metals show different exchange coupling strengths and oscillating periodicity in Fig. 6.2.

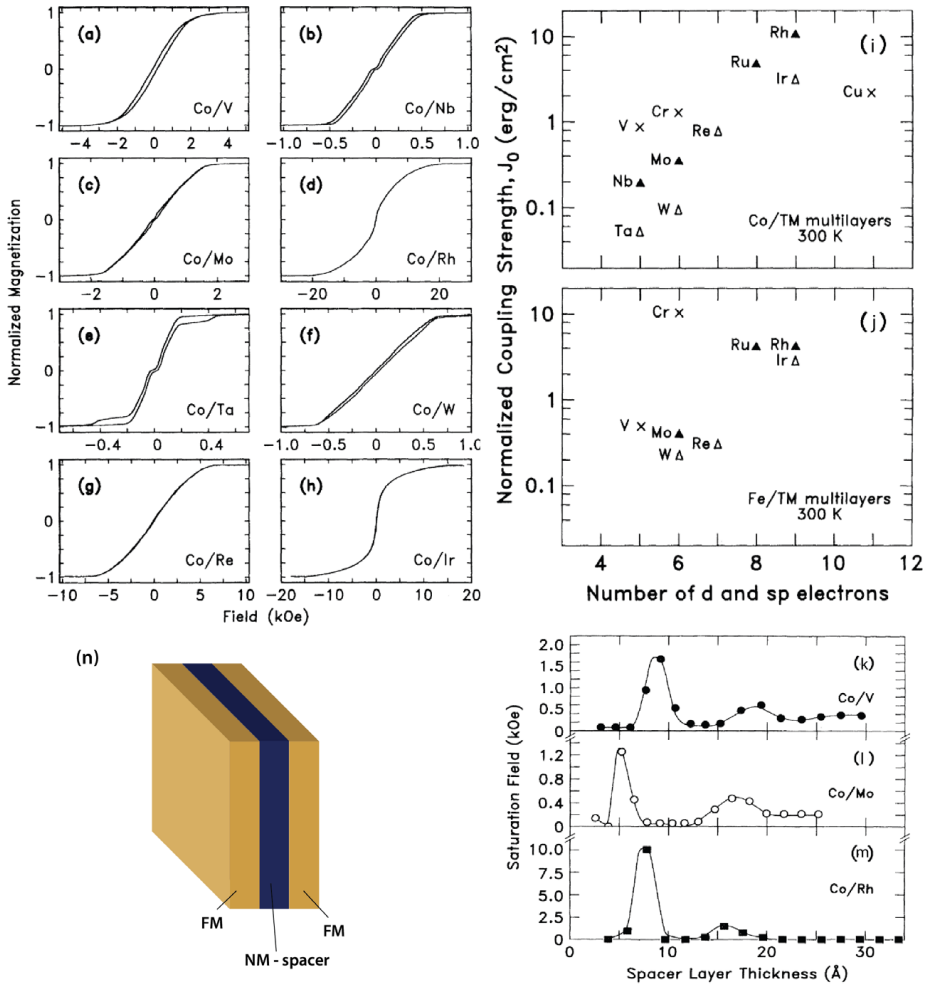

Figure 6.2: Interlayer exchange coupling strength among various 3d, 4d, 5d transition metal non-ferromagnetic spacer layer. a-h, equilibrium magnetometry measured in FM/NM/FM structure with different NM layers. i-j, the coupling strength among the studied transition metals. n, device/material structure undery study. k-m, oscillatory behavior in saturation field as a function of thickness manifesting the oscillatory IEC strength. Graphs except (n) are adapted from *Physical Review Letters* [149].

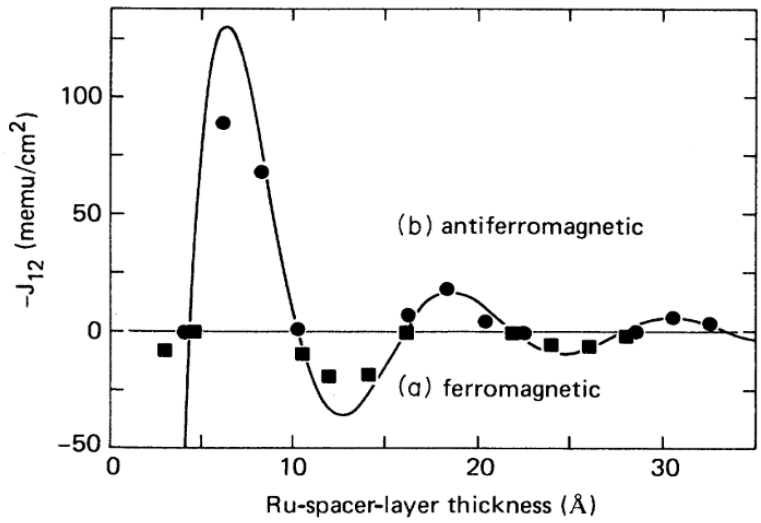

Figure 6.3: Oscillating exchange coupling strength J_{ex} as a function of spacer layer thickness. Graphs adapted from *Physical Review B* [150].

Fundamentally, the spin-dependent wavefunctions from the two ferromagnetic layers interacts and interferes across the spacer layer. Spin-dependent wavefunctions transmit and reflect at the two interfaces and as more reflection take place inside the spacer confinement, interference takes place and induces change in the spin density oscillation. Thickness period is dictated by the spacer material where the strength and phase of the IEC is determined by the spin-asymmetry of the reflection coefficient at the spacer-ferromagnet interfaces. The reflection coefficient at the spacer-ferromagnet interface is determined by the degree of matching of the band structure on both sides of the interface. As a result, different transition metals show a different Fermi surface thus different degree of spin-dependent band matching at the spacer/ferromagnet interface. As the spacer layer thickness varies, the interference of the spin-density inside the spacer layer induces an oscillating behavior similar to optical interference patterns where constructive and destructive interference takes place (Fig. 6.3). Across the different 3d, 4d, 5d transition metals, the exchange coupling strength systematically increases from 5d to 4d and to 3d since the heavier the metal, the stronger the spin-orbit coupling which the spin-dependent wavefunction dephases rapidly [149]. Among the each period of 3d, 4d and 5d, the coupling strength increases as more d-electron is present in Fig. 6.2.

Resonant Tunneling Effect

Resonant tunneling phenomenon has been theoretically explored by Bohm [12] in 1951 which he predicted that in a double barrier well structure, resonance in electron tunneling across the

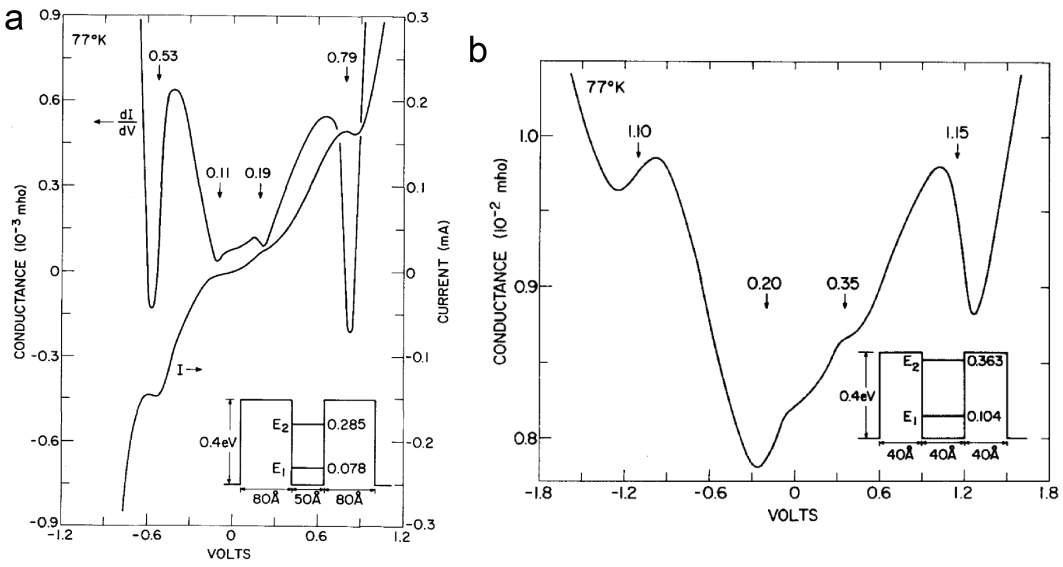

Figure 6.4: Resonant tunneling effect in $Ga_{0.3}Al_{0.7}As/GaAs/Ga_{0.3}Al_{0.7}As$ quantum well structure via negative differential resistance. a, well width of 5 nm. b, well width of 4 nm. Graphs adapted from *Applied Physics Letters* [24].

double barrier well can occur at certain electron injection energies. This leads to transmission coefficients that are near-unity at certain energy values [12]. This is physically intriguing because the transmission coefficient drops significantly as the barrier height or barrier width increases, however, the transmission coefficient can be near-unity with the double barrier well structure. Later in 1974, Chang *et al.* demonstrated that resonant tunneling effect can be manifested through transport I-V characteristics such as the negative differential resistance (NDR) [24] Fig. 6.4.

The fundamental understanding of resonant tunneling in a quantum well structure starts with describing the discrete energy states that are formed inside the well due to quantum confinement. By considering a electrical contact to the left of the quantum well, if the Fermi level inside the well is close to one of the discrete states, electron tunneling across the quantum well can happen near unity. This is because the discrete state in the quantum well serve as available states for electrons to tunnel to from the left side of the well. Once the electron arrives at the descrete state, tunneling can continue to happen across the second barrier to arrive at the electrical contact on the right of the well. By changing the chemical potential of the two contacts creating a chemical potential difference, the Fermi level inside the well will sweep across many discrete energy states.

In the tunneling I-V characteristics, when the applied voltage is swept close to a discrete state, the conductance ($\frac{dI}{dV}$) of the well structure should exhibit a singularity event (Fig. 6.4). In the DC I-V characteristics, the slope of the I-V curve will exhibits a change in the

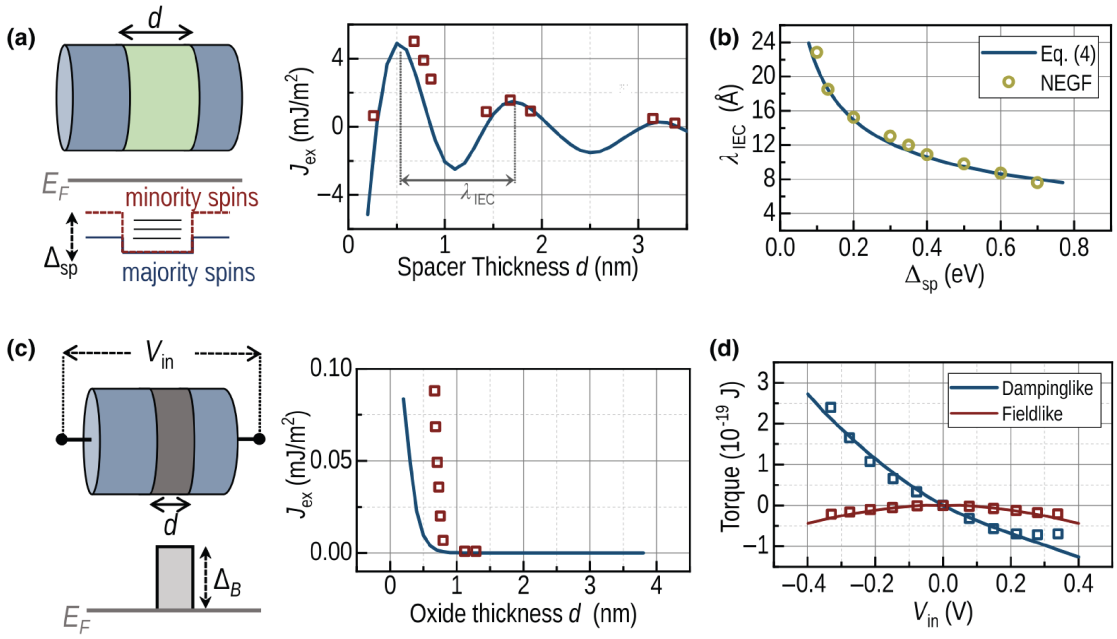

Figure 6.5: Interlayer exchange coupling in FM/NM/FM and FM/oxide/FM structure and the parameter calibration in the theoretical study. Graph adapted from *Physical Review Applied* [164].

slope and even negative slopes - NDR (Fig. 6.4a, V=0.79V). In the conductance versus V curve, when the singularity event is strong, a negative conductance (NDR) can observed. Therefore, NDR is a signature of resonant tunneling effect in a quantum well diode.

6.3 Theory voltage-controlled magnetic switching driven by resonant enhanced interlayer exchange coupling

In this study, IEC and resonant tunneling effect is combined in a device structure that leverages resonant tunneling modulated interlayer exchange coupling. In Fig. 6.5, the exchange coupling strengths J_{ex} between two ferromagnetic layers sandwiching either a metallic spacer or an insulating barrier are calculated. As expected, the J_{ex} exhibits a oscillating behavior that matches well with experimental results from [149] whereas the J_{ex} decreases fast with increasing oxide barrier thickness. These parameters are calibrated with experimental results for the calculation of the proposed two-terminal resonant enhanced IEC device.

The resonant enhanced IEC device is built with a two-terminal structure composed of a quantum well with a spacer layer that possess strong exchange coupling constant sandwiched

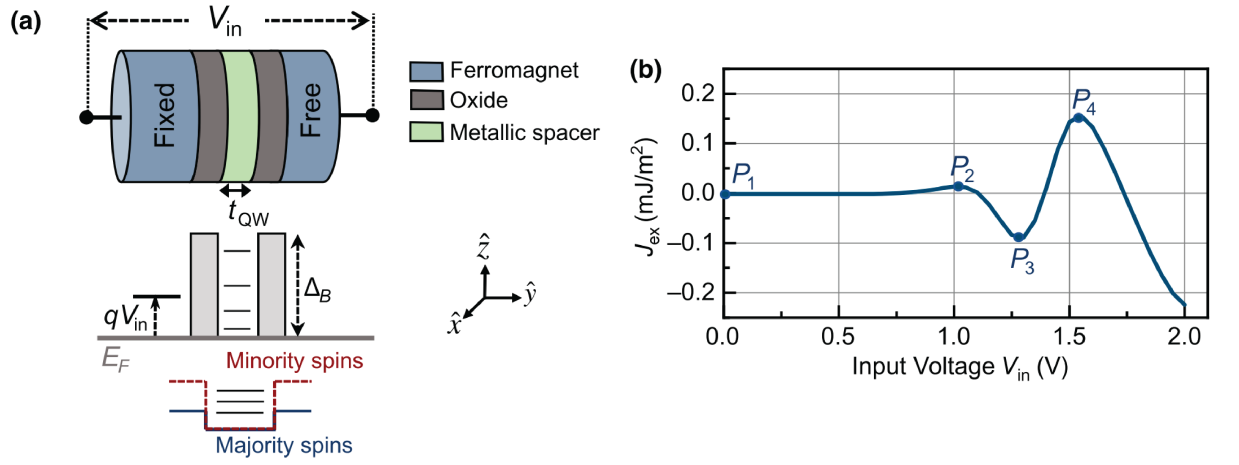

Figure 6.6: Schematics of resonant enhanced IEC device structure, operating principle and exchange coupling strength as a function of voltage. Graph adapted from *Physical Review Applied* [164].

between two ferromagnetic layers (Fig. 6.6a) [164]. The J_{ex} between the two ferromagnetic layer can be modulated by the resonant tunneling effect in the quantum well. As a voltage is applied across the two-terminal device structure, the Fermi level inside the quantum well sweeps through the discrete states with the exchange coupling strength J_{ex} tuned via resonant tunneling (Fig. 6.6b) [164]. As the J_{ex} is tuned as a function of voltage, the exchange coupling switches between antiferromagnetic and ferromagnetic configuration thus the parallel and antiparallel magnetic configuration among the two ferromagnetic layers. The simulation of the resonant enhanced IEC device is done primarily via the non-equilibrium Green's function along with the LLG equation. Details of the simulations results can be found in Sayed *et al.* [164].

Aside from being a purely voltage-driven mechanism to achieve magnetization switching, resonant enhanced IEC device possesses several advantages over the current-driven spin-torque devices. First, the switching speed and switching threshold energy is decoupled in resonant enhanced IEC devices. In a two-terminal STT-MTJ device, the critical switching current density scales proportionally with the damping constant α [181] but the critical switching time (minimal current pulse width) is inversely proportional to the damping constant. As a result, in STT switching, a higher damping constant can result in faster switching but will increase the critical switching current density. In resonant enhanced IEC switching, the switching time is still inversely proportional to the damping constant since switching of magnetic moments are still mainly governed by the balance of damping-related dissipation as the STT [181]. However, the switching threshold is no longer coupled with the damping constant since the mechanism is completely different [164].

Expected device characteristics can be found in Fig. 6.7. The charge current density

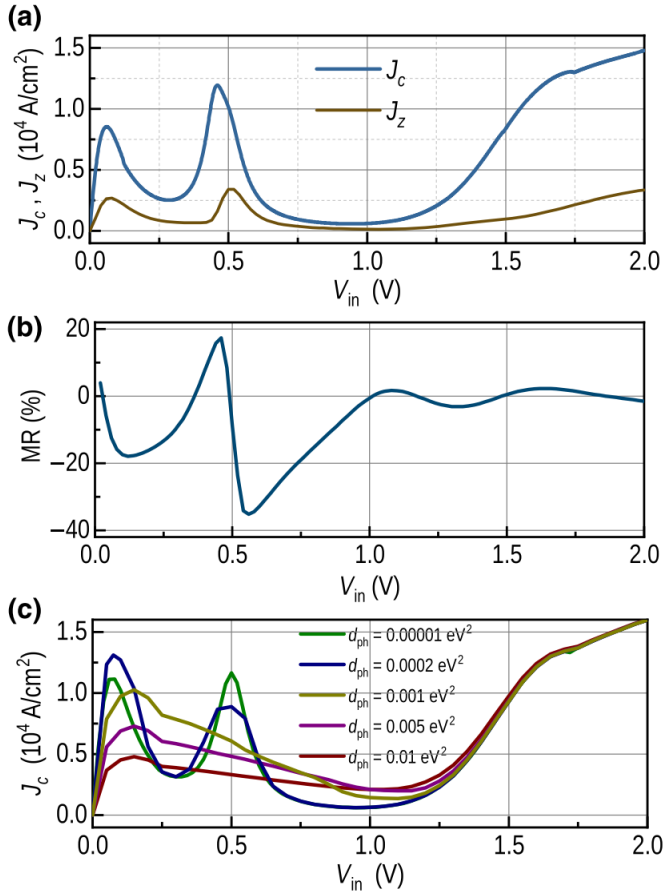

Figure 6.7: (a) J_c (charge current density), J_s(spin current density) as a function of applied voltage. (b) current out-of-plane tunneling magnetoresistance. (c) J_c as a function of applied voltage with different spin dephasing strength. Graph adapted from *Physical Review Applied* [164].

J_c as a function of applied voltage V_{in} shows a highly non-linear relationship and possess the oscillatory behavior. This oscillatory behavior is a signature of the resonant tunneling. The magnetoresistance is also showing a oscillation as a function of applied voltage. This is something to be mindful of when we probe the tunneling I-V characteristics of the resonant enhanced IEC device.

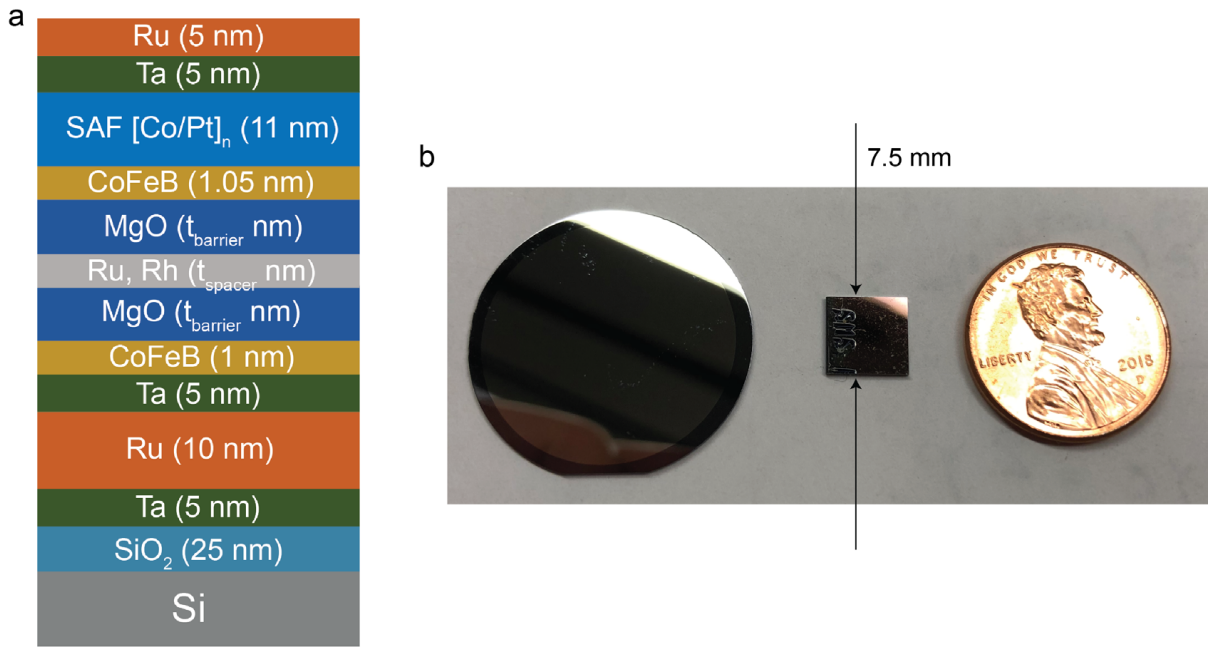

Figure 6.8: a, material stack under study with detail layer thicknesses. b, size comparison of 1 inch wafer deposition.

6.4 Material stack design and fabrication of device under test

Material stack design

It is quite challenging to deposit magnetic tunnel junction based material stacks with high TMR ratio and PMA properties in an academic lab setting, let alone designing a brand new material stack based on this technology. In industry, IBM Research has been a long-time pioneer in spintronics research including the development of GMR, STT, PMA in CoFeB/MgO and IEC. To experimentally study the proposed device, I collaborated with Dr. See-Hun Yang from IBM Research on the material depositions of the resonant enhanced IEC material stack. The stack under study has a general structure of underlayer/FM/oxide barrier/spacer/oxide barrier/FM/SAF layer/capping layer. In my experiments, the free and reference ferromagnetic layers have fixed thicknesses. The spacer layer thickness and oxide barrier thickness are varied. Stacks are grown for Rh and Ru spacer materials since these two elements showed the largest exchange coupling constant [149]. All material stacks have PMA.

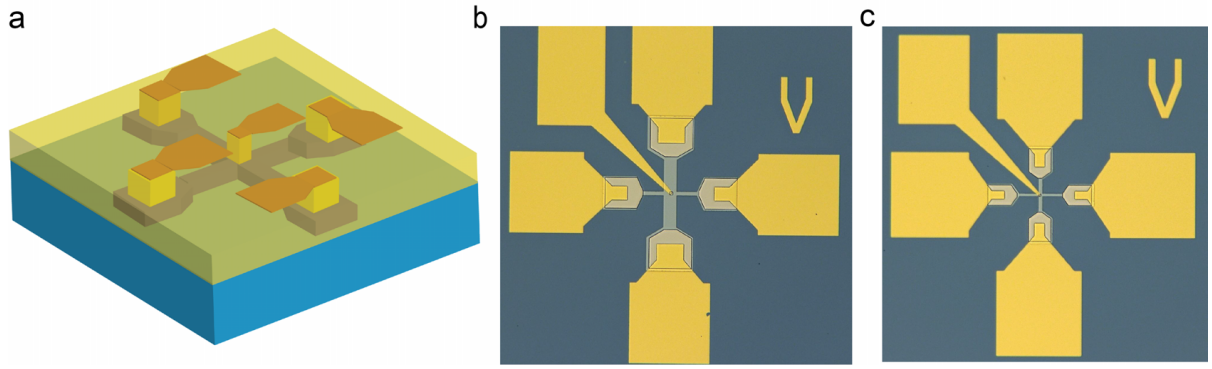

Figure 6.9: a, Schematic of the resonant tunneling IEC device test structure. b, c, optical microscope images of two different device dimensions.

Device Fabrication

With the thin film stack deposited by Dr. Yang from IBM Research, I designed the device fabrication process and fabricated the device in the Berkeley Marvell Nanofabrication Laboratory. Device fabrication is done with standard i-line lithography and ion-milling. Interlayer dielectric filling and contact metal lift-off process are done through electron beam evaporation. The device has a three-terminal structure similar to a SOT-MRAM cell where the center pillar is composed of the MTJ stack sitting on a single Hall bar structure for probing any anomalous Hall signal from the bottom CoFeB ferromagnet free layer (Fig. 6.9). The detail of teh device fabrication process can be found in Appendix 4.

6.5 Equilibrium magnetic property property of material stacks under study

To test whether the as-deposited IEC stacks have varying exchange coupling strength between the two ferromagnetic layers which are separated by a quantum well structure that can be up to 4 nm apart, I conducted magnetometry on a selected set of samples on the 1-inch as-deposited wafers. I first check the varying Rh spacer layer thickness series sample with fixed MgO barrier thickness at 1.5 nm (Fig. 6.10). In Fig. 6.10, it is apparent that by changing the spacer layer thickness, the coercive fields of the two ferromagnetic layers are varied and in a oscillatory manner. At t_{Rh}=0.8 nm, the coercive field is reduced but it quickly returns with t_{Rh}=1.0 nm. From the magnetometry, it is apparent that these material stacks shows clear IEC even with $\sim$ 4 nm of quantum structure separating the two ferromagnetic layer.

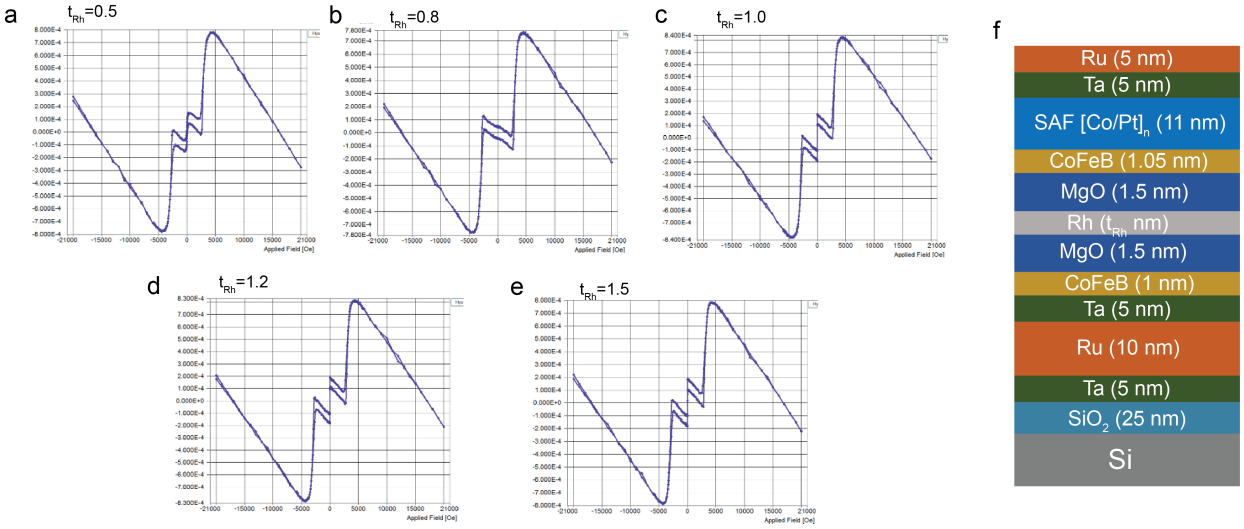

Figure 6.10: a, b, c, d, e, magnetometry done at room temperature on sample stacks with t_{Rh} = 0.5, .8, 1.0, 1.2, 1.5 nm. f, t_{Rh} series sample stack details.

6.6 Tunneling I-V characteristics

Anomalous Hall effect measurement

Before conducting the tunneling I-V measurement, I conducted anomalous Hall effect measurement on the devices to check whether the PMA survived after device fabrication. For all the transport measurement that will show and discuss are done on the stack with MgO thickness of 1.2 nm and Ru spacer thickness of 0.5 nm. In Fig. 6.11, both devices show strong out-of-plane magnetic anisotropy characterized by the strong switching of AHE voltage. For the AHE switching curve in Fig. 6.11, only one pair of switching even is observed. This is most likely due to the fact that current runs through the bottom CoFeB layer which is the free layer where as no current runs through the top CoFeB reference layer due to the pillar on Hall bar structure. On the other hand, two pairs of switching event can be observed because the double Hall bar is fabricated on the full stack instead of a pillar structure. As a result, in the double Hall bar device current is running through both the CoFeB layers showing a pair of switching event. With a simple AHE measurement, we confirm that the small pillar is not damaged and is behaving accordingly after device fabrication.

Tunneling IV: DC measurement

In this subsection, I will show selected DC tunneling IV measurement results. Since this is a very preliminary experimental study on the proposed concept and the study is still ongoing,

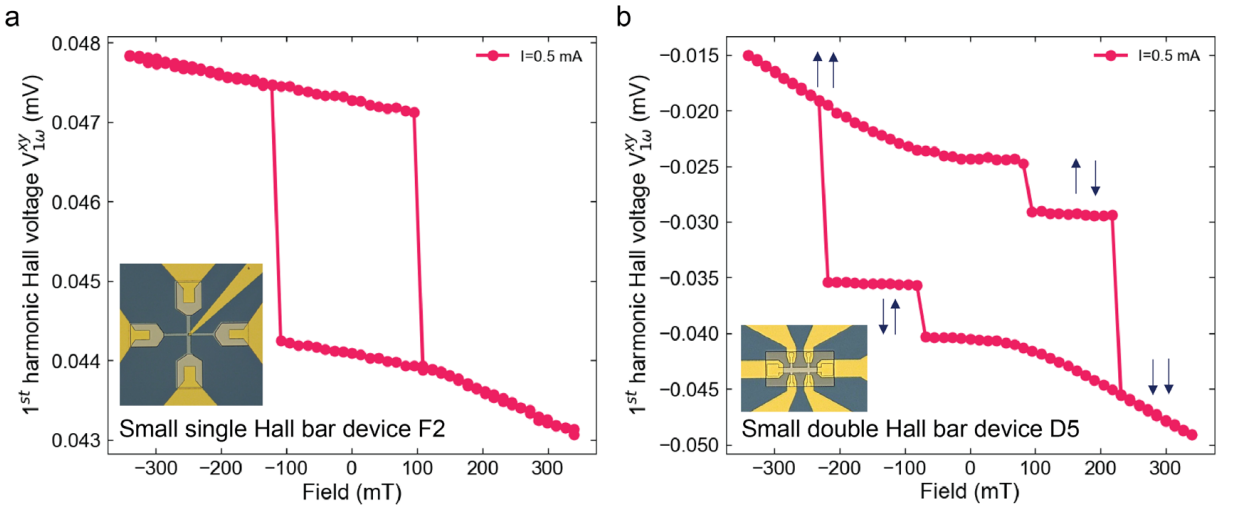

Figure 6.11: a, AHE measurement on a small single Hall bar device with center pillar composed of the full IEC stack. b, AHE measurement on a small double Hall bar device where the entire device is consists of the full IEC stack (no pillar structure).

I will not draw too much conclusions from the results and focus on the observations and hypotheses.

Here DC tunneling IV measurements are done with a very simple IV setup via a Keithley 2400 series sourcemeter unit. The voltage duration is around 1 s thus coined a "DC" measurement. In Fig. 6.12, I show four different measurements with opposite initial set field sign and V_{max}. All measurements shown in Fig. 6.12 are done on the small single Hall bar with the [t_{MgO}= 1.2 nm, t_{Ru}= 0.5 nm]. The left most plot of each row shows the raw tunneling I-V curve, the middle plot shows the DC resistance (from V=IR), the right most plot shows the differential conductance ($\frac{dI}{dV}$. In the first row, it can be observed that a change in the IV slope occurs around 0.9 V, followed by sharp switching at 1V. The resistance switching from a low resistance state to a high resistance state. In this case, resistive switching due to the formation of conductive filaments can be ruled out since in resistive switching the resistance states should go from a high resistance state (no conductive filament) to a low resistance (formation of conductive filament. In the differential conductance dI/dV plot, we can see a singularity event near 1 V is apparent. This is a signature of the resonant tunneling effect. By repeating the DC IV scan with V_{max} of 1.2 V, a similar overall IV shape and direction of switching are observed. However, the sharpness of the switching near 1V is no longer visible. In the DC tunneling resistance, a very similar curve is observed. In the differential conductance, the strong singularity event near 1V is no longer appreciable but with small singularity events happening at similar voltage values as the first row.

In the third and forth rows, the device is reset by a perpendicular field of -60 mT. I

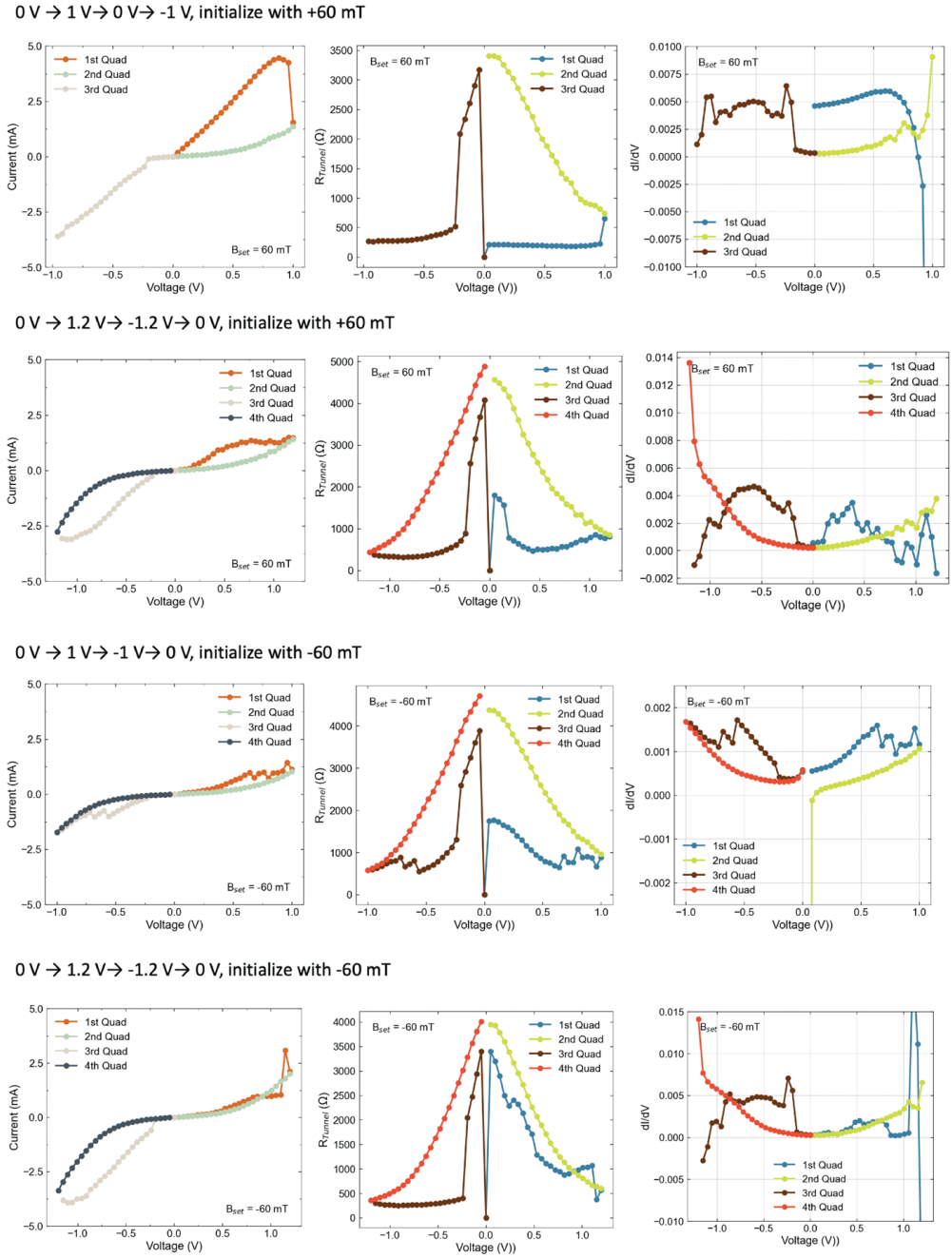

Figure 6.12: DC tunneling I-V measurements. First row, device is reset by +60 mT before IV measurement with voltage up to 0.5 V. Second row, the IV measurement voltage increases to 1.2 V. Third row, device is reset by -60 mT and IV measurement is done up to 0.5V. Forth row, IV measurement up to 1.2V.

repeated the same sets of voltage sweeps and in the same traversing direction. The IV curve exhibits a shape that is more or less similar to the first two cases and switching near 1 V can again be observed in the DC resistance plot of both third and forth rows. Strong singularity event is again observed near 1 V in the forth row where $V_{max} = 1.2V$. A consistent singularity event near -0.25 V is observable across all four cases in their respective differential conductance plot (last column).

At last, I will provide a few comments on these preliminary results. First, it is apparent that signatures of resonant tunneling effect is observable with a collection of both weak and strong singularity events. Second, from the I-V curve, switching of resistance states is also observed and it is highly non-linear which means the device is working in the sense that nothing is shorted or the oxide being damage. In the case of damaged oxide or shorted device, a linear I-V characteristics is expected. The IV result seems to be repeatable to a certain degree. Next step will include more repeatable transport signatures to statistically map out the discrete energy levels in the quantum well. In terms of magnetic dependence, although resistive state has changed, the origin may not be magnetic switching. As a result, finding the signature of magnetic switching in tunneling I-V measurements and also the measurement of TMR is necessary to understand the resonant enhanced IEC device and to provide concrete evidence of resonant enhanced IEC driven magnetic switching. Nevertheless, the signatures of resonant tunneling and switching of resistive states are a promising start.

Chapter 7

Conclusions

7.1 Short summary and implications

This dissertation has successfully addressed a few important spintronics challenges by investigating and engineering new material systems (silicides), developing new processes to tune the existing material systems for new applications (canted GdCo for field-free multi-state switching), and exploring new device operation principles (voltage-controlled resonant enhanced IEC device). Results from this dissertation provide direct or indirect pathways to lowering the energy consumption for future and near-future computing applications at both the materials and device level via spintronic devices.

Silicides as new material system for efficiency spin-orbit torque

This section addresses the challenge of coming up with a scalable material platform that is CMOS compatible and possess efficient SOT generating capability. In chapter 3 and 4, silicide has demonstrated attractive properties for efficient spin-orbit torque generation and full magnetization switching via iron silicide has been achieved with efficiencies higher than topological insulators and heavy metals. In addition, a non-trivial Fe(Co) concentration dependence of spin-orbit torque is found in both amorphous iron silicide and cobalt silicide. This novel concentration dependence has two implications. The first being a potentially new mechanism of understanding and generating spin current in a fully amorphous light element silicide. The novel concentration dependence also shows a functional dependence of energy level with respect to its density of states distribution. This indicates that while the structure is fully amorphous, an intrinsic property which typically requires a well-defined bandstructure may still arise from the density of states. In addition, the effect from the onset of ferromagnetism on spin current generation is amplified in a-Co_xSi_{100-x}, which shows that magnetic interaction or origin plays an equal amount of importance in such magnetic element silicide systems. The second implication is on the technological. In both amorphous iron silicide and cobalt silicide, the scaling trend between resistivity and SOT efficiency is completely opposite than the conventional trend. This scaling trend shows a promising

direction where high SOT efficiency couples to low resistivity. This provides a pathway for SOT technology to scale in the future processing nodes when device design parameters are more stringent without having to switch to a completely new material system. On top of iron silicide, I show that cobalt silicide can extend this scaling trend even further by lowering the resistivity without losing the strong SOT efficiency.

Tunable magnetic anisotropy in canted GdCo for field-free multistate spin-orbit torque switching

This section of the dissertation address the challenge of a fundamental design hurdle - field free SOT switching of perpendicular magnetic anisotropy moments. The ability to induce deterministic SOT switching without a symmetry breaking field is of technological importance. In chapter 5, I present a way to tune the magnetic anisotropy direction by engineering the oxygen content in the ferrimagnetic Gd_xCo_{100-x} alloy. Through this fabrication process, a highly tunable magnetic anisotropy can be obtained which showed a great amount of SOT switching phenomena in addition to field-free SOT switching including multistate switching, SOT ratchet effect, and memristor behavior. These rich SOT transport phenomena can also be easily tuned by the fabrication process developed in this dissertation. These tunable magnetotransport phenomena can serve as fundamental building blocks for non von Neumann computing architectures such as neuromorphic computing.

Resonant enhanced interlayer exchange coupling for voltage-controlled magnetization switching

The last section of this dissertation addresses the long-term challenge of switching magnetization via a purely voltage-driven mechanism. In chapter 6, my colleague (Dr. Shehrin Sayed) and I proposed a new type of spintronic device that leverages both resonant tunneling and interlayer exchange coupling (IEC). In this resonant enhanced IEC device, exchange coupling between two ferromagnetic layers are modulated by a quantum well via the resonant tunneling effect. By applying different voltages, the configuration between the two ferromagnet can be switched between parallel and antiparallel. While the theoretical picture is complete, experimental effort is underway with promising preliminary results. By collaborating with IBM Research for materials deposition, I designed and fabricated the device for transport measurements. The preliminary results showed resonant tunneling signatures, switching of resistance states through tunneling IV which resistive switching mechanisms can be ruled out, and the material stacks shows oscillating IEC at equilibrium. The remaining questions to be experimentally explored are the signature of magnetic switching in the observed resistance state switching and the experimental study of the TMR modulated by resonant enhanced IEC. This work is ongoing but trending in a promising direction experimentally.

7.2 Future directions

This dissertation opens up an abundance of new questions in the realm of spintronics research. I will discuss in three parts addressing them separately regarding to the three different work in this dissertation. First, the underlying physical understanding of strong spin current generation in amorphous light element silicide needs rigorous theoretical effort to support the hypothesis drawn from the experimental results. There exists a wide selection of silicides that are either CMOS compatible or serve as potential candidates for chiral topological semimetals or small gap semiconductors in their crystalline counterpart such as CrSi, MnSi and RhSi. Second, the fabrication process developed in this dissertation to engineer a magnetic canting with almost arbitrary angle is powerful. Future work on utilizing this process to develop spintronics based memory devices that are sophisticated or to leverage this magnetic anisotropy dependence beyond field-free switching in neuromorphic computing devices are all possible and impactful future directions. At last, more experimental efforts need to be put in to fully understand and confirm the working principal of resonant enhanced IEC devices. If succeeded, a new mechanism for achieving pure voltage-driven magnetization switching is invented. This will provide alternative solutions for low-power spintronics memory devices and a converter between voltage and current-driven spin phenomena that can be useful in future spintronics based computing devices such as spin logic.

Bibliography

[1] Taiwan Semiconductor Manufacturing Company (TSMC). *TSMC and OIP Ecosystem Partners Deliver 16FinFET and 3D IC Reference Flows*. 2013. URL: https://pr.tsmc.com/english/news/1787 (visited on 09/17/2013).

[2] Taiwan Semiconductor Manufacturing Company (TSMC). *TSMC FINFLEX™, N2 Process Innovations Debut at 2022 North American Technology Symposium*. 2022. URL: https://pr.tsmc.com/english/news/2939 (visited on 06/17/2022).

[3] Taiwan Semiconductor Manufacturing Company (TSMC). *TSMC's N7+ Technology is First EUV Process Delivering Customer Products to Market in High Volume*. 2019. URL: https://pr.tsmc.com/english/news/2010 (visited on 10/07/2019).

[4] Gary Allen et al. "Experimental demonstration of the coexistence of spin Hall and Rashba effects in β-tantalum/ferromagnet bilayers". In: *Physical Review B - Condensed Matter and Materials Physics* 91.14 (2015), p. 144412. ISSN: 1550235X. DOI: 10.1103/PhysRevB.91.144412.

[5] Hongyu An et al. "Spin–torque generator engineered by natural oxidation of Cu". In: *Nature Communications* 7.1 (Dec. 2016), p. 13069. ISSN: 2041-1723. DOI: 10.1038/ncomms13069.

[6] Kazuya Ando and Eiji Saitoh. "Observation of the inverse spin Hall effect in silicon". In: *Nature Communications* 3.1 (Jan. 2012), p. 629. ISSN: 2041-1723. DOI: 10.1038/ncomms1640.

[7] N. P. Armitage, E. J. Mele, and Ashvin Vishwanath. "Weyl and Dirac semimetals in three-dimensional solids". In: *Reviews of Modern Physics* 90.1 (Jan. 2018), p. 015001. ISSN: 0034-6861. DOI: 10.1103/RevModPhys.90.015001.

[8] ASML. *EUV lithography systems*. 2022. URL: https://www.asml.com/en/products/euv-lithography-systems (visited on 2022).

[9] Can Onur Avci et al. "Interplay of spin-orbit torque and thermoelectric effects in ferromagnet/normal-metal bilayers". In: *Physical Review B* 90.22 (2014), p. 224427. ISSN: 1550235X. DOI: 10.1103/PhysRevB.90.224427.

[10] Behtash Behin-Aein et al. "Proposal for an all-spin logic device with built-in memory". In: *Nature Nanotechnology* 5.4 (2010), pp. 266–270. ISSN: 17483395. DOI: 10.1038/nnano.2010.31.

[11] Andrew J Berger et al. "Determination of the spin Hall effect and the spin diffusion length of Pt from self-consistent fitting of damping enhancement and inverse spin-orbit torque measurements". In: *Physical Review B* 98.2 (2018), p. 24402. ISSN: 24699969. DOI: 10.1103/PhysRevB.98.024402.

[12] David Bohm. *Quantum Theory*. Prentice-Hall, 1951.

[13] Arnab Bose et al. "Effects of Anisotropic Strain on Spin-Orbit Torque Produced by the Dirac Nodal Line Semimetal IrO2". In: *ACS Applied Materials and Interfaces* 12.49 (Dec. 2020), pp. 55411–55416. ISSN: 19448252. DOI: 10.1021/acsami.0c16485.

[14] D S Bouma et al. "Itinerant ferromagnetism and intrinsic anomalous Hall effect in amorphous iron-germanium". In: *Physical Review B* 101.1 (Jan. 2020), p. 014402. ISSN: 2469-9950. DOI: 10.1103/PhysRevB.101.014402.

[15] A. van den Brink et al. "Field-free magnetization reversal by spin-Hall effect and exchange bias". In: *Nature Communications* 7 (1 Apr. 2016), p. 10854. ISSN: 2041-1723. DOI: 10.1038/ncomms10854.

[16] A Brunsch and J Schneider. "Perpendicular magnetic anisotropy in evaporated amorphous GdCo films". In: *Journal of Applied Physics* 48.6 (1977), pp. 2641–2643. ISSN: 00218979. DOI: 10.1063/1.323955.

[17] Yu. A. Bychkov and E. I. Rashba. "Properties of a 2D electron gas with lifted spectral degeneracy". In: *Zh. Eksp. Teor. Fiz.* 39.2 (1984), pp. 78–81. ISSN: 0021-3640.

[18] Lucas Caretta et al. "Fast current-driven domain walls and small skyrmions in a compensated ferrimagnet". In: *Nature Nanotechnology* 13.12 (Dec. 2018), pp. 1154–1160. ISSN: 17483395. DOI: 10.1038/s41565-018-0255-3.

[19] A Ceballos et al. "Coexistence of soft and hard magnetic phases in single layer amorphous Tb-Co thin films". In: *Journal of Applied Physics* 131.3 (2022), p. 33901. ISSN: 10897550. DOI: 10.1063/5.0074314.

[20] Alejandro Ceballos et al. "Role of element-specific damping in ultrafast, helicity-independent, all-optical switching dynamics in amorphous (Gd,Tb)Co thin films". In: *Physical Review B* 103.2 (2021), p. 24438. ISSN: 24699969. DOI: 10.1103/PhysRevB.103.024438.

[21] Alejandro Ceballos-Sanchez. "Characterization and Manipulation of Temperature-Driven Magnetic Phenomena: Magnetic Transition in FeRh Thin Films and Ultrafast Magnetization Reversal in a -Gd 22 -xTbxCo78 Thin Films". PhD thesis. University of California, Berkeley, 2019, p. 106.

[22] C. F. Chang et al. "Dynamic atomic reconstruction: How Fe3O4 thin films evade polar catastrophe for epitaxy". In: *Physical Review X* 6.4 (Oct. 2016), p. 041011. ISSN: 21603308. DOI: 10.1103/PhysRevX.6.041011.

[23] Guoqing Chang et al. "Topological quantum properties of chiral crystals". In: *Nature Materials* 17.11 (2018), pp. 978–985. ISSN: 14764660. DOI: 10.1038/s41563-018-0169-3.

[24] L L Chang, L Esaki, and R Tsu. "Resonant tunneling in semiconductor double barriers". In: *Applied Physics Letters* 24.12 (1974), pp. 593–595. ISSN: 00036951. DOI: 10.1063/1.1655067.

[25] Claude Chappert, Albert Fert, and Frédéric Nguyen Van Dau. "The emergence of spin electronics in data storage". In: *Nature Materials* 6.11 (Nov. 2007), pp. 813–823. ISSN: 14764660. DOI: 10.1038/nmat2024.

[26] P. Chaudhari, J J Cuomo, and R. J. Gambino. "Amorphous Metallic Films for Bubble Domain Applications". In: *IBM Journal of Research and Development* 17.1 (Jan. 1973), pp. 66–68. ISSN: 0018-8646. DOI: 10.1147/rd.171.0066.

[27] Ching-Tzu Chen et al. "Topological Semimetals for Scaled Back-End-Of-Line Interconnect Beyond Cu". In: *2020 IEEE International Electron Devices Meeting (IEDM)*. Vol. 2020-Decem. IEEE, Dec. 2020, pp. 32.4.1–32.4.4. DOI: 10.1109/IEDM13553.2020.9371996.

[28] Guorui Chen et al. "Tunable correlated Chern insulator and ferromagnetism in a moiré superlattice". In: *Nature* 579.7797 (2020), pp. 56–61. ISSN: 14764687. DOI: 10.1038/s41586-020-2049-7.

[29] L. Chen et al. "Robust spin-orbit torque and spin-galvanic effect at the Fe/GaAs (001) interface at room temperature". In: *Nature Communications* 7.1 (Dec. 2016), p. 13802. ISSN: 20411723. DOI: 10.1038/ncomms13802.

[30] Tian Yue Chen et al. "Current-Induced Spin-Orbit Torque and Field-Free Switching in Mo-Based Magnetic Heterostructures". In: *Physical Review Applied* 10.4 (2018), p. 44038. ISSN: 23317019. DOI: 10.1103/PhysRevApplied.10.044038.

[31] Tian-Yue Chen et al. "Efficient Spin–Orbit Torque Switching with Nonepitaxial Chalcogenide Heterostructures". In: *ACS Applied Materials & Interfaces* 12.6 (Feb. 2020), pp. 7788–7794. ISSN: 1944-8244. DOI: 10.1021/acsami.9b20844.

[32] Xianzhe Chen et al. "Electric field control of Néel spin–orbit torque in an antiferromagnet". In: *Nature Materials* 18 (9 2019), pp. 931–935. ISSN: 14764660. DOI: 10.1038/s41563-019-0424-2.

[33] Yan Ting Chen et al. "Theory of spin Hall magnetoresistance". In: *Physical Review B - Condensed Matter and Materials Physics* 87.14 (2013), p. 144411. ISSN: 10980121. DOI: 10.1103/PhysRevB.87.144411.

[34] Young-Gwan Choi et al. "Observation of the orbital Hall effect in a light metal Ti". In: *Nature* 619.7968 (July 2023), pp. 52–56. ISSN: 0028-0836. DOI: 10.1038/s41586-023-06101-9.

[35] T C Chuang, C F Pai, and S Y Huang. "Cr-induced Perpendicular Magnetic Anisotropy and Field-Free Spin-Orbit-Torque Switching". In: *Physical Review Applied* 11.6 (2019), p. 61005. ISSN: 23317019. DOI: 10.1103/PhysRevApplied.11.061005.

[36] Paul Corbae, Frances Hellman, and Sineád M Griffin. "Structural disorder-driven topological phase transition in noncentrosymmetric BiTeI". In: *Physical Review B* 103.21 (2021), p. 214203. ISSN: 24699969. DOI: 10.1103/PhysRevB.103.214203.

[37] Paul Corbae et al. "Observation of spin-momentum locked surface states in amorphous Bi2Se3". In: *Nature Materials* 22.2 (Feb. 2023), pp. 200–206. ISSN: 1476-1122. DOI: 10.1038/s41563-022-01458-0.

[38] DARPA. *Spintronics*. 1993. URL: https://www.darpa.mil/about-us/timeline/spintronics (visited on 07/15/2023).

[39] Mahendra DC et al. "Room-temperature high spin–orbit torque due to quantum confinement in sputtered BixSe(1–x) films". In: *Nature Materials* 17.9 (Sept. 2018), pp. 800–807. ISSN: 1476-1122. DOI: 10.1038/s41563-018-0136-z.

[40] Kai Uwe Demasius et al. "Enhanced spin-orbit torques by oxygen incorporation in tungsten films". In: *Nature Communications* 7.1 (Apr. 2016), p. 10644. ISSN: 20411723. DOI: 10.1038/ncomms10644.

[41] B Dieny et al. "Opportunities and challenges for spintronics in the microelectronics industry". In: *Nature Electronics* 3.8 (2020), pp. 446–459. ISSN: 25201131. DOI: 10.1038/s41928-020-0461-5.

[42] G. Dresselhaus. "Spin-orbit coupling effects in zinc blende structures". In: *Physical Review* 100.2 (1955), pp. 580–586. ISSN: 0031899X. DOI: 10.1103/PhysRev.100.580.

[43] M.I. I. Dyakonov and V.I. I. Perel. "Current-induced spin orientation of electrons in semiconductors". In: *Physics Letters A* 35.6 (July 1971), pp. 459–460. ISSN: 03759601. DOI: 10.1016/0375-9601(71)90196-4.

[44] V. M. Edelstein. "Spin polarization of conduction electrons induced by electric current in two-dimensional asymmetric electron systems". In: *Solid State Communications* 73.3 (Jan. 1990), pp. 233–235. ISSN: 00381098. DOI: 10.1016/0038-1098(90)90963-C.

[45] Satoru Emori et al. "Interfacial spin-orbit torque without bulk spin-orbit coupling". In: *Physical Review B* 93.18 (2016), p. 180402. ISSN: 24699969. DOI: 10.1103/PhysRevB.93.180402.

[46] Arnoud S Everhardt et al. "Tunable charge to spin conversion in strontium iridate thin films". In: *Physical Review Materials* 3.5 (May 2019), p. 051201. ISSN: 2475-9953. DOI: 10.1103/PhysRevMaterials.3.051201.

[47] Yuankan Fang et al. "Evidence for a conducting surface ground state in high-quality single crystalline FeSi". In: *Proceedings of the National Academy of Sciences of the United States of America* 115.34 (2018), pp. 8558–8562. ISSN: 10916490. DOI: 10.1073/pnas.1806910115.

[48] Manfred Fiebig et al. "The evolution of multiferroics". In: *Nature Reviews Materials* 1.8 (July 2016), p. 16046. ISSN: 2058-8437. DOI: 10.1038/natrevmats.2016.46. URL: www.nature.com/natrevmats%20https://www.nature.com/articles/natrevmats201646.

[49] Global Foundries. *GLOBALFOUNDRIES Reshapes Technology Portfolio to Intensify Focus on Growing Demand for Differentiated Offerings*. 2018. URL: https://gf.com/gf-press-release/globalfoundries-reshapes-technology-portfolio-intensify-focus-growing-demand/ (visited on 08/27/2018).

[50] J H Franken, H. J. M. Swagten, and B Koopmans. "Shift registers based on magnetic domain wall ratchets with perpendicular anisotropy". In: *Nature Nanotechnology* 7.8 (Aug. 2012), pp. 499–503. ISSN: 1748-3387. DOI: 10.1038/nnano.2012.111.

[51] K Fritz, L Neumann, and M Meinert. "Ultralow switching-current density in all-amorphous W-Hf/Co-Fe-B/Ta Ox films". In: *Physical Review Applied* 14.3 (2020), p. 34047. ISSN: 23317019. DOI: 10.1103/PhysRevApplied.14.034047.

[52] S Fukami et al. "A spin-orbit torque switching scheme with collinear magnetic easy axis and current configuration". In: *Nature Nanotechnology* 11.7 (2016), pp. 621–625. ISSN: 17483395. DOI: 10.1038/nnano.2016.29.

[53] Shunsuke Fukami et al. "Magnetization switching by spin-orbit torque in an antiferromagnet-ferromagnet bilayer system". In: *Nature Materials* 15.5 (2016), pp. 535–541. ISSN: 14764660. DOI: 10.1038/nmat4566.

[54] K. Garello et al. "SOT-MRAM 300MM Integration for Low Power and Ultrafast Embedded Memories". In: *IEEE Symposium on VLSI Circuits, Digest of Technical Papers*. Vol. 2018-June. IEEE, June 2018, pp. 81–82. DOI: 10.1109/VLSIC.2018.8502269.

[55] Kevin Garello et al. "Symmetry and magnitude of spin-orbit torques in ferromagnetic heterostructures". In: *Nature Nanotechnology* 8.8 (2013), pp. 587–593. ISSN: 17483395. DOI: 10.1038/nnano.2013.145.

[56] Dongwook Go and Hyun-Woo Lee. "Orbital torque: Torque generation by orbital current injection". In: *Physical Review Research* 2.1 (2020), p. 13177. DOI: 10.1103/physrevresearch.2.013177.

[57] Dongwook Go et al. "Intrinsic Spin and Orbital Hall Effects from Orbital Texture". In: *Physical Review Letters* 121.8 (Aug. 2018), p. 086602. ISSN: 0031-9007. DOI: 10.1103/PhysRevLett.121.086602.

[58] O Gomonay, M Kläui, and J Sinova. "Manipulating antiferromagnets with magnetic fields: Ratchet motion of multiple domain walls induced by asymmetric field pulses". In: *Applied Physics Letters* 109 (14 2016), p. 142404. ISSN: 00036951. DOI: 10.1063/1.4964272. URL: https://doi.org/10.1063/1.4964272.

[59] Cheng Gong et al. "Discovery of intrinsic ferromagnetism in two-dimensional van der Waals crystals". In: *Nature* 546.7657 (June 2017), pp. 265–269. ISSN: 0028-0836. DOI: 10.1038/nature22060.

[60] G Y Guo et al. "Intrinsic spin hall effect in platinum: First-principles calculations". In: *Physical Review Letters* 100.9 (2008). ISSN: 10797114. DOI: 10.1103/PhysRevLett.100.096401.

[61] Wei Han, Sadamichi Maekawa, and Xin-Cheng Xie. "Spin current as a probe of quantum materials". In: *Nature Materials* 19.2 (Feb. 2020), pp. 139–152. ISSN: 1476-1122. DOI: 10.1038/s41563-019-0456-7.

[62] Paul M Haney et al. "Current induced torques and interfacial spin-orbit coupling: Semiclassical modeling". In: *Physical Review B - Condensed Matter and Materials Physics* 87.17 (2013), p. 174411. ISSN: 10980121. DOI: 10.1103/PhysRevB.87.174411.

[63] V G Harris et al. "Structural origins of magnetic anisotropy in sputtered amorphous Tb-Fe films". In: *Physical Review Letters* 69.13 (1992), pp. 1939–1942. ISSN: 00319007. DOI: 10.1103/PhysRevLett.69.1939.

[64] Hiroki Hayashi et al. "Observation of long-range orbital transport and giant orbital torque". In: *Communications Physics* 6.1 (Feb. 2023), p. 32. ISSN: 2399-3650. DOI: 10.1038/s42005-023-01139-7.

[65] Masamitsu Hayashi et al. "Quantitative characterization of the spin-orbit torque using harmonic Hall voltage measurements". In: *Physical Review B* 89.14 (2014), p. 144425. ISSN: 1550235X. DOI: 10.1103/PhysRevB.89.144425.

[66] F Hellman and E M Gyorgy. "Growth-induced magnetic anisotropy in amorphous Tb-Fe". In: *Physical Review Letters* 68.9 (1992), pp. 1391–1394. ISSN: 00319007. DOI: 10.1103/PhysRevLett.68.1391.

[67] Frances Hellman et al. "Interface-induced phenomena in magnetism". In: *Reviews of Modern Physics* 89.2 (June 2017), p. 025006. ISSN: 0034-6861. DOI: 10.1103/RevModPhys.89.025006.

[68] J T Heron et al. "Deterministic switching of ferromagnetism at room temperature using an electric field". In: *Nature* 516.7531 (2014), pp. 370–373. ISSN: 14764687. DOI: 10.1038/nature14004.

[69] M. El-Hilo et al. "The sweep rate dependence of coercivity in recording media". In: *Journal of Magnetism and Magnetic Materials* 117.3 (1992), pp. 307–310. ISSN: 03048853. DOI: 10.1016/0304-8853(92)90085-3.

[70] J. E. Hirsch. "Spin Hall Effect". In: *Phys. Rev. Lett.* 83.9 (Aug. 1999), p. 1834. ISSN: 10797114. DOI: 10.1103/PhysRevLett.83.1834.

[71] Axel Hoffmann. "Spin hall effects in metals". In: *IEEE Transactions on Magnetics* 49.10 (2013), pp. 5172–5193. ISSN: 00189464. DOI: 10.1109/TMAG.2013.2262947.

[72] H. Honjo et al. "First demonstration of field-free SOT-MRAM with 0.35 ns write speed and 70 thermal stability under 400°C thermal tolerance by canted SOT structure and its advanced patterning/SOT channel technology". In: *2019 IEEE International Electron Devices Meeting (IEDM)*. Vol. 2019-Decem. IEEE, Dec. 2019, pp. 28.5.1–28.5.4. DOI: 10.1109/IEDM19573.2019.8993443.

[73] D Hsieh et al. "A topological Dirac insulator in a quantum spin Hall phase". In: *Nature* 452.7190 (2008), pp. 970–974. DOI: 10.1038/nature06843.

[74] Chenming Hu. *Modern Semiconductor Devices for Integrated Circuits*. New Jersey: Pearson/Prentice Hall, 2010.

[75] Bevin Huang et al. "Layer-dependent ferromagnetism in a van der Waals crystal down to the monolayer limit". In: *Nature* 546.7657 (2017), pp. 270–273. ISSN: 14764687. DOI: 10.1038/nature22391.

[76] S X Huang, T Y Chen, and C L Chien. "Spin polarization of amorphous CoFeB determined by point-contact Andreev reflection". In: *Applied Physics Letters* 92.24 (2008), p. 242509. ISSN: 00036951. DOI: 10.1063/1.2949740.

[77] Xiaoxi Huang et al. "Novel Spin–Orbit Torque Generation at Room Temperature in an All-Oxide Epitaxial La0.7Sr0.3MnO3/SrIrO3 System". In: *Advanced Materials* 33.24 (May 2021), p. 2008269. ISSN: 15214095. DOI: 10.1002/adma.202008269.

[78] Yu Han Huang et al. "A Spin-Orbit Torque Ratchet at Ferromagnet/Antiferromagnet Interface via Exchange Spring". In: *Advanced Functional Materials* 32 (16 2022), pp. 1–8. ISSN: 16163028. DOI: 10.1002/adfm.202111653.

[79] IBM. *The Application of Spintronics*. URL: https://www.ibm.com/ibm/history/ibm100/us/en/icons/spintronics/ (visited on 07/15/2023).

[80] Hiroshi Idzuchi, Yasuhiro Fukuma, and Yoshichika Otani. "Spin transport in non-magnetic nano-structures induced by non-local spin injection". In: *Physica E: Low-dimensional Systems and Nanostructures* 68 (Apr. 2015), pp. 239–263. ISSN: 13869477. DOI: 10.1016/j.physe.2014.11.023.

[81] Butsurin Jinnai et al. "Scalability and wide temperature range operation of spin-orbit torque switching devices using Co/Pt multilayer nanowires". In: *Applied Physics Letters* 113.21 (2018), p. 212403. ISSN: 00036951. DOI: 10.1063/1.5045814.

[82] Annika Johansson, Jürgen Henk, and Ingrid Mertig. "Edelstein effect in Weyl semimetals". In: *Physical Review B* 97 (2018), p. 85417. ISSN: 24699969. DOI: 10.1103/PhysRevB.97.085417.

[83] Nicola Jones. "The Information Factories". In: *Nature* 561 (2018), pp. 163–167.

[84] Sungjung Joo et al. "Magnetic Anisotropy and Damping Constant of Ferrimagnetic GdCo Alloy near Compensation Point". In: *Materials* 14.10 (May 2021), p. 2604. ISSN: 1996-1944. DOI: 10.3390/ma14102604.

[85] Sangita S Kalarickal et al. "Ferromagnetic resonance linewidth in metallic thin films: Comparison of measurement methods". In: *Journal of Applied Physics* 99.9 (2006), p. 93909. ISSN: 00218979. DOI: 10.1063/1.2197087.

[86] J Karel et al. "Unexpected dependence of the anomalous Hall angle on the Hall conductivity in amorphous transition metal thin films". In: *Physical Review Materials* 4.11 (Nov. 2020), p. 114405. ISSN: 2475-9953. DOI: 10.1103/PhysRevMaterials.4.114405.

[87] J Karel et al. "Using structural disorder to enhance the magnetism and spin-polarization in Fe(x)Si(1-x) thin films for spintronics". In: *Materials Research Express* 1.2 (Apr. 2014), p. 026102. ISSN: 2053-1591. DOI: 10.1088/2053-1591/1/2/026102.

[88] J. Karel et al. "Enhanced spin polarization of amorphous F ex S i1-x thin films revealed by Andreev reflection spectroscopy". In: *Physical Review Materials* 2.6 (2018), pp. 1–6. ISSN: 24759953. DOI: 10.1103/PhysRevMaterials.2.064411.

[89] J. Karel et al. "Scaling of the anomalous Hall effect in lower conductivity regimes". In: *EPL (Europhysics Letters)* 114.5 (June 2016), p. 57004. ISSN: 0295-5075. DOI: 10.1209/0295-5075/114/57004.

[90] Julie E. Karel. "Tuning the Magnetic and Electronic Properties of Iron(x)Silicon(1-x) Thin Films for Spintronics". English. Copyright - Database copyright ProQuest LLC; ProQuest does not claim copyright in the individual underlying works; Last updated - 2021-05-27. PhD thesis. 2012, p. 99. ISBN: 978-1-267-97370-2.

[91] Y. K. Kato et al. "Observation of the Spin Hall Effect in Semiconductors". In: *Science* 306.5703 (Dec. 2004), pp. 1910–1913. ISSN: 0036-8075. DOI: 10.1126/science.1105514.

[92] Nguyen Huynh Duy Khang, Yugo Ueda, and Pham Nam Hai. "A conductive topological insulator with large spin Hall effect for ultralow power spin–orbit torque switching". In: *Nature Materials* 17.9 (2018), pp. 808–813. ISSN: 14764660. DOI: 10.1038/s41563-018-0137-y.

[93] Duck-Ho Kim et al. "Bulk Dzyaloshinskii–Moriya interaction in amorphous ferrimagnetic alloys". In: *Nature Materials* 18.7 (July 2019), pp. 685–690. ISSN: 1476-1122. DOI: 10.1038/s41563-019-0380-x.

[94] Hyun-Joong Kim et al. "Field-Free Switching of Magnetization by Tilting the Perpendicular Magnetic Anisotropy of Gd/Co Multilayers". In: *Advanced Functional Materials* (Mar. 2022), p. 2112561. ISSN: 1616-301X. DOI: 10.1002/adfm.202112561.

[95] Junyeon Kim et al. "Layer thickness dependence of the current-induced effective field vector in Ta—CoFeB—MgO". In: *Nature Materials* 12.3 (2013), pp. 240–245. ISSN: 14761122. DOI: 10.1038/nmat3522.

[96] Junyeon Kim et al. "Nontrivial torque generation by orbital angular momentum injection in ferromagnetic-metal/ Cu/Al2 O3 trilayers". In: *Physical Review B* 103.2 (2021), p. 20407. ISSN: 24699969. DOI: 10.1103/PhysRevB.103.L020407.

[97] Se Kwon Kim et al. "Ferrimagnetic spintronics". In: *Nature Materials* 21.1 (Jan. 2022), pp. 24–34. ISSN: 1476-1122. DOI: 10.1038/s41563-021-01139-4.

[98] Motoi Kimata et al. "Magnetic and magnetic inverse spin Hall effects in a non-collinear antiferromagnet". In: *Nature* 565.7741 (Jan. 2019), pp. 627–630. ISSN: 0028-0836. DOI: 10.1038/s41586-018-0853-0.

[99] H Kontani et al. "Giant intrinsic spin and orbital hall effects in Sr2MO4 (M=Ru, Rh, Mo)". In: *Physical Review Letters* 100.9 (Mar. 2008), p. 096601. ISSN: 00319007. DOI: 10.1103/PhysRevLett.100.096601.

[100] H Kontani et al. "Giant Orbital Hall Effect in Transition Metals: Origin of Large Spin and Anomalous Hall Effects". In: *Physical Review Letters* 102.1 (Jan. 2009), p. 016601. ISSN: 0031-9007. DOI: 10.1103/PhysRevLett.102.016601.

[101] Viola Krizakova et al. "Field-free switching of magnetic tunnel junctions driven by spin–orbit torques at sub-ns timescales". In: *Applied Physics Letters* 116.23 (June 2020), p. 232406. ISSN: 0003-6951. DOI: 10.1063/5.0011433.

[102] Yong Chang Lau et al. "Spin Hall effect from hybridized 3d-4p orbitals". In: *Physical Review B* 99.6 (Feb. 2019), p. 064410. ISSN: 24699969. DOI: 10.1103/PhysRevB.99.064410.

[103] Dongjoon Lee et al. "Orbital torque in magnetic bilayers". In: *Nature Communications* 12.1 (Dec. 2021), p. 6710. ISSN: 2041-1723. DOI: 10.1038/s41467-021-26650-9.

[104] O J Lee et al. "Central role of domain wall depinning for perpendicular magnetization switching driven by spin torque from the spin Hall effect". In: *Physical Review B* 89.2 (Jan. 2014), p. 024418. ISSN: 1098-0121. DOI: 10.1103/PhysRevB.89.024418.

[105] Seo-Won Lee and Kyung-Jin Lee. "Emerging Three-Terminal Magnetic Memory Devices". In: *Proceedings of the IEEE* 104.10 (Oct. 2016), pp. 1831–1843. ISSN: 0018-9219. DOI: 10.1109/JPROC.2016.2543782.

[106] Peng Li et al. "Spin-momentum locking and spin-orbit torques in magnetic nano-heterojunctions composed of Weyl semimetal WTe2". In: *Nature Communications* 9.1 (Dec. 2018), p. 3990. ISSN: 2041-1723. DOI: 10.1038/s41467-018-06518-1.

[107] Xiaona Li et al. "Composition range of semiconducting amorphous Fe-Si thin films interpreted using a cluster-based short-range-order model". In: *Journal of Alloys and Compounds* 706 (June 2017), pp. 495–501. ISSN: 09258388. DOI: 10.1016/j.jallcom.2017.02.255.

[108] Po-Hung Lin et al. "Manipulating exchange bias by spin–orbit torque". In: *Nature Materials* 18 (4 Apr. 2019), pp. 335–341. ISSN: 1476-1122. DOI: 10.1038/s41563-019-0289-4.

[109] Liang Liu et al. "Current-induced magnetization switching in all-oxide heterostructures". In: *Nature Nanotechnology* 14.10 (2019), pp. 939–944. ISSN: 17483395. DOI: 10.1038/s41565-019-0534-7.

[110] Luqiao Liu, R A Buhrman, and D C Ralph. "Review and Analysis of Measurements of the Spin Hall Effect in Platinum". In: (Nov. 2011). arXiv: 1111.3702. URL: https://arxiv.org/pdf/1111.3702.pdf%20http://arxiv.org/abs/1111.3702.

[111] Luqiao Liu et al. "Spin-torque ferromagnetic resonance induced by the spin Hall effect". In: *Physical Review Letters* 106.3 (Jan. 2011), p. 036601. ISSN: 00319007. DOI: 10.1103/PhysRevLett.106.036601.

[112] Luqiao Liu et al. "Spin-torque switching with the giant spin hall effect of tantalum". In: *Science* 336.6081 (May 2012), pp. 555–558. ISSN: 10959203. DOI: 10.1126/science.1218197.

[113] Qianbiao Liu et al. "Giant bulk spin–orbit torque and efficient electrical switching in single ferrimagnetic FeTb layers with strong perpendicular magnetic anisotropy". In: *Applied Physics Reviews* 9.2 (June 2022), p. 021402. ISSN: 1931-9401. DOI: 10.1063/5.0087260.

[114] Zhaochu Luo et al. "Current-driven magnetic domain-wall logic". In: *Nature* 579.7798 (2020), pp. 214–218. ISSN: 14764687. DOI: 10.1038/s41586-020-2061-y.

[115] D MacNeill et al. "Control of spin–orbit torques through crystal symmetry in WTe2/ferromagnet bilayers". In: *Nature Physics* 13.3 (Mar. 2017), pp. 300–305. ISSN: 1745-2473. DOI: 10.1038/nphys3933.

[116] Dowling Magnets. *Who Discovered the Very First Magnet?* 2016. URL: https://www.dowlingmagnets.com/blog/2016/who-discovered-the-very-first-magnet/ (visited on 07/15/2023).

[117] A. Manchon et al. "Current-induced spin-orbit torques in ferromagnetic and antiferromagnetic systems". In: *Reviews of Modern Physics* 91.9 (Sept. 2019), p. 035004. ISSN: 0034-6861. DOI: 10.1103/RevModPhys.91.035004.

[118] A. Manchon et al. "New perspectives for Rashba spin-orbit coupling". In: *Nature Materials* 14.9 (Sept. 2015), pp. 871–882. ISSN: 14764660. DOI: 10.1038/nmat4360.

[119] Sasikanth Manipatruni et al. "Scalable energy-efficient magnetoelectric spin–orbit logic". In: *Nature* 565.7737 (Jan. 2019), pp. 35–42. ISSN: 0028-0836. DOI: 10.1038/s41586-018-0770-2.

[120] R W Mann et al. "Silicides and local interconnections for high-performance VLSI applications". In: *IBM Journal of Research and Development* 39.4 (1995), pp. 403–417. ISSN: 00188646. DOI: 10.1147/rd.394.0403.

[121] T Maruyama et al. "Large voltage-induced magnetic anisotropy change in a few atomic layers of iron". In: *Nature Nanotechnology* 4.3 (Mar. 2009), pp. 158–161. ISSN: 1748-3387. DOI: 10.1038/nnano.2008.406.

[122] V V Mazurenko et al. "Metal-insulator transitions and magnetism in correlated band insulators: FeSi and Fe1-x CoxSi". In: *Physical Review B - Condensed Matter and Materials Physics* 81.12 (Mar. 2010), p. 125131. ISSN: 10980121. DOI: 10.1103/PhysRevB.81.125131.

[123] Andrew T. McCallum and Mark Johnson. "Film edge nonlocal spin valves". In: *Nano Letters* 9.6 (June 2009), pp. 2350–2353. ISSN: 15306984. DOI: 10.1021/nl900816p.

[124] A R Mellnik et al. "Spin-transfer torque generated by a topological insulator". In: *Nature* 511.7510 (July 2014), pp. 449–451. ISSN: 14764687. DOI: 10.1038/nature13534.

[125] G. Mihajlović et al. "Pt thickness dependence of spin Hall effect switching of in-plane magnetized CoFeB free layers studied by differential planar Hall effect". In: *Applied Physics Letters* 109.19 (Nov. 2016), p. 192404. ISSN: 0003-6951. DOI: 10.1063/1.4967318.

[126] Ioan Mihai Miron et al. "Perpendicular switching of a single ferromagnetic layer induced by in-plane current injection". In: *Nature* 476.7359 (Aug. 2011), pp. 189–193. ISSN: 0028-0836. DOI: 10.1038/nature10309.

[127] T Miyazaki and N Tezuka. "Giant magnetic tunneling effect in Fe/Al2O3/Fe junction". In: *Journal of Magnetism and Magnetic Materials* 139.3 (Jan. 1995), pp. L231–L234. ISSN: 03048853. DOI: 10.1016/0304-8853(95)90001-2.

[128] J S Moodera et al. "Large magnetoresistance at room temperature in ferromagnetic thin film tunnel junctions". In: *Physical Review Letters* 74.16 (1995), pp. 3273–3276. ISSN: 00319007. DOI: 10.1103/PhysRevLett.74.3273.

[129] Hiroyuki Moriya et al. "Observation of the crossover between metallic and insulating regimes of the spin Hall effect". In: *Communications Physics* 5.1 (Dec. 2022), p. 12. ISSN: 2399-3650. DOI: 10.1038/s42005-021-00791-1.

[130] T Nan et al. "Anisotropic spin-orbit torque generation in epitaxial SrIrO 3 by symmetry design". In: *Proceedings of the National Academy of Sciences* 116.33 (Aug. 2019), pp. 16186–16191. ISSN: 0027-8424. DOI: 10.1073/pnas.1812822116.

[131] T. Nan et al. "Controlling spin current polarization through non-collinear antiferromagnetism". In: *Nature Communications* 11.1 (Dec. 2020), p. 4671. ISSN: 20411723. DOI: 10.1038/s41467-020-17999-4.

[132] M. Louis Néel. "Propriétés magnétiques des ferrites ; ferrimagnétisme et antiferromagnétisme". In: *Annales de Physique* 12.3 (Apr. 1948), pp. 137–198. ISSN: 0003-4169. DOI: 10.1051/anphys/194812030137.

[133] T Newhouse-Illige et al. "Voltage-controlled interlayer coupling in perpendicularly magnetized magnetic tunnel junctions". In: *Nature Communications* 8.1 (May 2017), p. 15232. ISSN: 2041-1723. DOI: 10.1038/ncomms15232.

[134] Samsung Newrsoom. *Samsung Successfully Completes 5nm EUV Development to Allow Greater Area Scaling and Ultra-low Power Benefits*. 2019. URL: https://semiconductor.samsung.com/news-events/news/samsung-successfully-completes-5nm-euv-development-to-allow-greater-area-scaling-and-ultra-low-power-benefits/ (visited on 04/17/2019).

[135] Intel Newsroom. *First EUV Light Marks Intel 4 Milestone in Ireland*. 2022. URL: https://www.intel.com/content/www/us/en/newsroom/news/first-euv-light-marks-intel-4-milestone-ireland.html#gs.35fk45 (visited on 12/22/2022).

[136] Intel Newsroom. *Intel Reinvents Transistors Using New 3-D Structure*. 2011. URL: https://www.intc.com/news-events/press-releases/detail/655/intel-reinvents-transistors-using-new-3-d-structure (visited on 05/04/2011).

[137] Intel Newsroom. *Intel Unleashed: Engineering the Future*. 2021. URL: https://www.intel.com/content/www/us/en/events/engineering-the-future.html (visited on 03/23/2021).

[138] Samsung Newsroom. *Samsung Announces Mass Production of Industry's First 14nm FinFET Mobile Application Processor*. 2015. URL: https://news.samsung.com/global/samsung-announces-mass-production-of-industrys-first-14nm-finfet-mobile-application-processor (visited on 02/16/2015).

[139] Minh-Hai Nguyen and Chi-Feng Pai. "Spin–orbit torque characterization in a nutshell". In: *APL Materials* 9.3 (Mar. 2021), p. 030902. ISSN: 2166-532X. DOI: 10.1063/5.0041123.

[140] Minh-Hai Nguyen, D. C. Ralph, and R. A. Buhrman. "Spin Torque Study of the Spin Hall Conductivity and Spin Diffusion Length in Platinum Thin Films with Varying Resistivity". In: *Physical Review Letters* 116.12 (Mar. 2016), p. 126601. ISSN: 0031-9007. DOI: 10.1103/PhysRevLett.116.126601.

[141] Young Wan Oh et al. "Field-free switching of perpendicular magnetization through spin-orbit torque in antiferromagnet/ferromagnet/oxide structures". In: *Nature Nanotechnology* 11.10 (2016), pp. 878–884. ISSN: 17483395. DOI: 10.1038/nnano.2016.109.

[142] Yusuke Ohtsuka et al. "Emergence of spin-orbit coupled ferromagnetic surface state derived from Zak phase in a nonmagnetic insulator FeSi". In: *Science Advances* 7.47 (Nov. 2021), eabj0498. ISSN: 23752548. DOI: 10.1126/sciadv.abj0498.

[143] Yongxi Ou, D. C. Ralph, and R. A. Buhrman. "Strong Enhancement of the Spin Hall Effect by Spin Fluctuations near the Curie Point of FexPt1-x Alloys". In: *Physical Review Letters* 120.9 (2018), p. 97203. ISSN: 10797114. DOI: 10.1103/PhysRevLett.120.097203.

[144] Yongxi Ou et al. "Strong spin Hall effect in the antiferromagnet PtMn". In: *Physical Review B* 93.22 (June 2016), p. 220405. ISSN: 2469-9950. DOI: 10.1103/PhysRevB.93.220405.

[145] Chi Feng Pai et al. "Dependence of the efficiency of spin Hall torque on the transparency of Pt/ferromagnetic layer interfaces". In: *Physical Review B - Condensed Matter and Materials Physics* 92.6 (2015), p. 64426. ISSN: 1550235X. DOI: 10.1103/PhysRevB.92.064426.

[146] Chi Feng Pai et al. "Determination of spin torque efficiencies in heterostructures with perpendicular magnetic anisotropy". In: *Physical Review B* 93.14 (2016), p. 144409. ISSN: 24699969. DOI: 10.1103/PhysRevB.93.144409.

[147] Chi Feng Pai et al. "Spin transfer torque devices utilizing the giant spin Hall effect of tungsten". In: *Applied Physics Letters* 101.12 (Sept. 2012), p. 122404. ISSN: 00036951. DOI: 10.1063/1.4753947.

[148] Quanjun Pan et al. "Efficient Spin-Orbit Torque Switching of Perpendicular Magnetization using Topological Insulators with High Thermal Tolerance". In: *Advanced Electronic Materials* 8.9 (2022), pp. 1–10. ISSN: 2199160X. DOI: 10.1002/aelm.202200003.

[149] S. S.P. Parkin. "Systematic variation of the strength and oscillation period of indirect magnetic exchange coupling through the 3d, 4d, and 5d transition metals". In: *Physical Review Letters* 67.25 (1991), pp. 3598–3601. ISSN: 00319007. DOI: 10.1103/PhysRevLett.67.3598.

[150] S. S.P. Parkin and D Mauri. "Spin engineering: Direct determination of the Ruderman-Kittel-Kasuya-Yosida far-field range function in ruthenium". In: *Physical Review B* 44.13 (1991), pp. 7131–7134. ISSN: 01631829. DOI: 10.1103/PhysRevB.44.7131.

[151] Stuart S.P. Parkin et al. "Giant tunnelling magnetoresistance at room temperature with MgO (100) tunnel barriers". In: *Nature Materials* 3.12 (2004), pp. 862–867. ISSN: 14761122. DOI: 10.1038/nmat1256.

[152] Shouzhong Peng et al. "Exchange bias switching in an antiferromagnet/ferromagnet bilayer driven by spin–orbit torque". In: *Nature Electronics* 3 (12 2020), pp. 757–764. ISSN: 25201131. DOI: 10.1038/s41928-020-00504-6.

[153] Nobel Prize. *The Nobel Prize in Physics 2007*. 2007. URL: https://www.nobelprize.org/prizes/physics/2007/summary/ (visited on 07/15/2023).

[154] Rajagopalan Ramaswamy et al. "Extrinsic spin hall effect in Cu1-xPtx". In: *Physical Review Applied* 8.2 (Aug. 2017), p. 024034. ISSN: 23317019. DOI: 10.1103/PhysRevApplied.8.024034.

[155] Rajagopalan Ramaswamy et al. "Hf thickness dependence of spin-orbit torques in Hf/CoFeB/MgO heterostructures". In: *Applied Physics Letters* 108.20 (2016), p. 202406. ISSN: 00036951. DOI: 10.1063/1.4951674.

[156] Ramamoorthy Ramesh and Sasikanth Manipatruni. "Electric field control of magnetism". In: *Proceedings of the Royal Society A: Mathematical, Physical and Engineering Sciences* 477.2251 (July 2021). ISSN: 1364-5021. DOI: 10.1098/rspa.2020.0942.

[157] E. RASHBA. "Properties of semiconductors with an extremum loop. I. Cyclotron and combinational Resonance in a magnetic field perpendicular to the plane of the loop". In: *Sov. Phys.-Solid State* 2 (1960), p. 1109.

[158] Intel Public Relations. *Gordon Moore, Intel Co-Founder, Dies at 94*. 2023. URL: https://www.intel.com/content/www/us/en/newsroom/news/gordon-moore-obituary.html (visited on 03/24/2023).

[159] Xue Ren et al. "Field-free switching of magnetization induced by spin–orbit torque in Pt/CoGd/Pt thin film". In: *Applied Physics Letters* 120 (25 June 2022), p. 252403. ISSN: 0003-6951. DOI: 10.1063/5.0092513.

[160] Neal Reynolds et al. "Spin Hall torques generated by rare-earth thin films". In: *Physical Review B* 95.6 (2017), p. 64412. ISSN: 24699969. DOI: 10.1103/PhysRevB.95.064412.

[161] Niklas Roschewsky, Charles-Henri Lambert, and Sayeef Salahuddin. "Spin-orbit torque switching of ultralarge-thickness ferrimagnetic GdFeCo". In: *Physical Review B* 96.6 (Aug. 2017), p. 064406. ISSN: 2469-9950. DOI: 10.1103/PhysRevB.96.064406.

[162] Niklas Roschewsky et al. "Spin-orbit torque and Nernst effect in Bi-Sb/Co heterostructures". In: *Physical Review B* 99.19 (2019), pp. 195103–195104. ISSN: 24699969. DOI: 10.1103/PhysRevB.99.195103.

[163] Sayeef Salahuddin, Kai Ni, and Suman Datta. "The era of hyper-scaling in electronics". In: *Nature Electronics* 1.8 (Aug. 2018), pp. 442–450. ISSN: 25201131. DOI: 10.1038/s41928-018-0117-x.

[164] Shehrin Sayed et al. "Resonant Enhancement of Exchange Coupling for Voltage-Controlled Magnetic Switching". In: *Physical Review Applied* 14.3 (Sept. 2020), p. 034070. ISSN: 2331-7019. DOI: 10.1103/PhysRevApplied.14.034070.

[165] Niels B. M. Schröter et al. "Observation and control of maximal Chern numbers in a chiral topological semimetal". In: *Science* 369.6500 (July 2020), pp. 179–183. ISSN: 0036-8075. DOI: 10.1126/science.aaz3480.

[166] Samsung Semiconductor. *'GAA structure' transistors: A next-generation process for next-generation semiconductors*. 2019. URL: https://semiconductor.samsung.com/us/support/tools-resources/dictionary/gaa-transistors-a-next-generation-process-for-next-generation-semiconductors/ (visited on 11/20/2019).

[167] Qiming Shao et al. "Room Temperature Highly Efficient Topological Insulator/Mo/CoFeB Spin-Orbit Torque Memory with Perpendicular Magnetic Anisotropy". In: *2018 IEEE International Electron Devices Meeting (IEDM)*. Vol. 2018-Decem. IEEE, Dec. 2018, pp. 36.3.1–36.3.4. ISBN: 978-1-7281-1987-8. DOI: 10.1109/IEDM.2018.8614499.

[168] Qiming Shao et al. "Strong Rashba-Edelstein Effect-Induced Spin-Orbit Torques in Monolayer Transition Metal Dichalcogenide/Ferromagnet Bilayers". In: *Nano Letters* 16.12 (Dec. 2016), pp. 7514–7520. ISSN: 15306992. DOI: 10.1021/acs.nanolett.6b03300.

[169] Shuyuan Shi et al. "All-electric magnetization switching and Dzyaloshinskii–Moriya interaction in WTe2/ferromagnet heterostructures". In: *Nature Nanotechnology* 14.10 (Oct. 2019), pp. 945–949. ISSN: 1748-3387. DOI: 10.1038/s41565-019-0525-8.

[170] Yoichi Shiota et al. "Induction of coherent magnetization switching in a few atomic layers of FeCo using voltage pulses". In: *Nature Materials* 11.1 (2012), pp. 39–43. ISSN: 14764660. DOI: 10.1038/nmat3172.

[171] Pete Singer. *Intel 4 Process Drops Cobalt Interconnect, Goes with Tried and Tested Copper with Cobalt Liner/Cap*. 2022. URL: https://www.semiconductor-digest.com/intel-4-process-drops-cobalt-interconnect-goes-with-tried-and-tested-copper-with-cobalt-liner-cap/ (visited on 07/27/2023).

[172] Jairo Sinova et al. "Spin Hall effects". In: *Reviews of Modern Physics* 87.4 (Oct. 2015), pp. 1213–1260. ISSN: 0034-6861. DOI: 10.1103/RevModPhys.87.1213.

[173] T. D. Skinner et al. "Complementary spin-Hall and inverse spin-galvanic effect torques in a ferromagnet/semiconductor bilayer". In: *Nature Communications* 6.1 (Nov. 2015), p. 6730. ISSN: 20411723. DOI: 10.1038/ncomms7730.

[174] J. C. Slonczewski. "Current-driven excitation of magnetic multilayers". In: *Journal of Magnetism and Magnetic Materials* 159.1-2 (June 1996), pp. L1–L7. ISSN: 03048853. DOI: 10.1016/0304-8853(96)00062-5.

[175] IEEE Magnetics Society. *Magnetics Society Events at IEDM*. 2022. URL: https://www.ieee-iedm.org/mram-events (visited on 07/25/2023).

[176] Cheng Song et al. "Recent progress in voltage control of magnetism: Materials, mechanisms, and performance". In: *Progress in Materials Science* 87 (2017), pp. 33–82. ISSN: 00796425. DOI: 10.1016/j.pmatsci.2017.02.002.

[177] Min Song et al. "Spin-Orbit Torque-Driven Magnetic Switching of Co/Pt-CoFeB Exchange Spring Ferromagnets". In: *IEEE Transactions on Magnetics* 55.8 (Aug. 2019), pp. 1–4. ISSN: 19410069. DOI: 10.1109/TMAG.2019.2911571.

[178] Anjan Soumyanarayanan et al. "Emergent phenomena induced by spin-orbit coupling at surfaces and interfaces". In: *Nature* 539.7630 (Nov. 2016), pp. 509–517. ISSN: 14764687. DOI: 10.1038/nature19820.

[179] N A Spaldin and R Ramesh. "Advances in magnetoelectric multiferroics". In: *Nature Materials* 18.3 (2019), pp. 203–212. ISSN: 14764660. DOI: 10.1038/s41563-018-0275-2.

[180] C D Stanciu et al. "All-Optical Magnetic Recording with Circularly Polarized Light". In: *Physical Review Letters* 99.4 (July 2007), p. 047601. ISSN: 0031-9007. DOI: 10.1103/PhysRevLett.99.047601.

[181] J Z Sun. "Spin-current interaction with a monodomain magnetic body: A model study". In: *Physical Review B* 62.1 (July 2000), pp. 570–578. ISSN: 0163-1829. DOI: 10.1103/PhysRevB.62.570.

[182] Daichi Takane et al. "Observation of Chiral Fermions with a Large Topological Charge and Associated Fermi-Arc Surface States in CoSi". In: *Physical Review Letters* 122.7 (Feb. 2019), p. 076402. ISSN: 0031-9007. DOI: 10.1103/PhysRevLett.122.076402.

[183] T Tanaka et al. "Intrinsic spin Hall effect and orbital Hall effect in 4d and 5d transition metals". In: *Physical Review B* 77.16 (Apr. 2008), p. 165117. ISSN: 10980121. DOI: 10.1103/PhysRevB.77.165117.

[184] Ke Tang et al. "Elemental Doping and Interface Effects on Spin–Orbit Torques in CoSi-Based Topological Semimetal Thin Films". In: *Advanced Materials Interfaces* (Sept. 2022), p. 2201332. ISSN: 2196-7350. DOI: 10.1002/admi.202201332.

[185] Ke Tang et al. "Spin Hall effect in a spin-1 chiral semimetal". In: *Physical Review Research* 3.3 (2021), p. 33101. ISSN: 26431564. DOI: 10.1103/PhysRevResearch.3.033101.

[186] Peizhe Tang, Quan Zhou, and Shou-Cheng Zhang. "Multiple Types of Topological Fermions in Transition Metal Silicides". In: *Physical Review Letters* 119.20 (Nov. 2017), p. 206402. ISSN: 0031-9007. DOI: 10.1103/PhysRevLett.119.206402.

[187] R C Taylor and A Gangulee. "Magnetization and magnetic anisotropy in evaporated GdCo amorphous films". In: *Journal of Applied Physics* 47.10 (1976), pp. 4666–4668. ISSN: 00218979. DOI: 10.1063/1.322397.

[188] Yaroslav Tserkovnyak, Arne Brataas, and Gerrit E.W. Bauer. "Spin pumping and magnetization dynamics in metallic multilayers". In: *Physical Review B - Condensed Matter and Materials Physics* 66.22 (2002), pp. 1–10. ISSN: 1550235X. DOI: 10.1103/PhysRevB.66.224403.

[189] V Tshitoyan et al. "Electrical manipulation of ferromagnetic NiFe by antiferromagnetic IrMn". In: *Physical Review B - Condensed Matter and Materials Physics* 92.21 (2015), p. 214406. ISSN: 1550235X. DOI: 10.1103/PhysRevB.92.214406.

[190] S. O. Valenzuela and M. Tinkham. "Direct electronic measurement of the spin Hall effect". In: *Nature* 442.7099 (July 2006), pp. 176–179. ISSN: 14764687. DOI: 10.1038/nature04937.

[191] P. C. Van Son, H. Van Kempen, and P. Wyder. "Boundary resistance of the ferromagnetic-nonferromagnetic metal interface". In: *Physical Review Letters* 58.21 (1987), pp. 2271–2273. ISSN: 00319007. DOI: 10.1103/PhysRevLett.58.2271.

[192] Saül Vélez et al. "Current-driven dynamics and ratchet effect of skyrmion bubbles in a ferrimagnetic insulator". In: *Nature Nanotechnology, accepted* (July 2022). ISSN: 1748-3387. DOI: 10.1038/s41565-022-01144-x.

[193] Hailong Wang et al. "Large spin-orbit torque observed in epitaxial SrIrO3 thin films". In: *Applied Physics Letters* 114.23 (June 2019), p. 232406. ISSN: 00036951. DOI: 10.1063/1.5097699.

[194] Peng Wang et al. "Giant Spin Hall Effect and Spin–Orbit Torques in 5 d Transition Metal–Aluminum Alloys from Extrinsic Scattering". In: *Advanced Materials* 34.23 (June 2022), p. 2109406. ISSN: 0935-9648. DOI: 10.1002/adma.202109406.

[195] T. Wang et al. "Large spin Hall angle in vanadium film". In: *Scientific Reports* 7.1 (Dec. 2017), p. 1306. ISSN: 2045-2322. DOI: 10.1038/s41598-017-01112-9.

[196] Yi Wang et al. "Determination of intrinsic spin Hall angle in Pt". In: *Applied Physics Letters* 105.15 (2014), p. 103913. ISSN: 00036951. DOI: 10.1063/1.4898593.

[197] Yi Wang et al. "Topological surface states originated spin-orbit torques in Bi2Se3". In: *Physical Review Letters* 114.25 (June 2015), p. 257202. ISSN: 10797114. DOI: 10.1103/PhysRevLett.114.257202.

[198] Martin Weisheit et al. "Electric field-induced modification of magnetism in thin-film ferromagnets". In: *Science* 315.5810 (Jan. 2007), pp. 349–351. ISSN: 10959203. DOI: 10.1126/science.1136629.

[199] Zhenchao Wen et al. "Spin-orbit torque in Cr/CoFeAl/MgO and Ru/CoFeAl/MgO epitaxial magnetic heterostructures". In: *AIP Advances* 6.5 (2016), p. 56307. ISSN: 21583226. DOI: 10.1063/1.4944339.

[200] Hao Wu et al. "Chiral Symmetry Breaking for Deterministic Switching of Perpendicular Magnetization by Spin-Orbit Torque". In: *Nano Letters* 21 (1 2021), pp. 515–521. ISSN: 15306992. DOI: 10.1021/acs.nanolett.0c03972.

[201] Hao Wu et al. "Room-Temperature Spin-Orbit Torque from Topological Surface States". In: *Physical Review Letters* 123.20 (2019), p. 207205. ISSN: 10797114. DOI: 10.1103/PhysRevLett.123.207205.

[202] Di Xiao, Ming Che Chang, and Qian Niu. "Berry phase effects on electronic properties". In: *Reviews of Modern Physics* 82.3 (2010), pp. 1959–2007. ISSN: 00346861. DOI: 10.1103/RevModPhys.82.1959.

[203] Xinkai Xu et al. "Giant Extrinsic Spin Hall Effect in Platinum-Titanium Oxide Nanocomposite Films". In: *Advanced Science* (Apr. 2022), p. 2105726. ISSN: 21983844. DOI: 10.1002/advs.202105726.

[204] Binghai Yan and Claudia Felser. "Topological Materials: Weyl Semimetals". In: *The Annual Review of Condensed Matter Physics is* 8 (2017), pp. 337–54. DOI: 10.1146/annurev-conmatphys.

[205] Huaiwen Yang et al. "Giant Charge-to-Spin Conversion Efficiency in SrTiO 3 -Based Electron Gas Interface". In: *Physical Review Applied* 10.1 (2019), p. 1. ISSN: 2331-7019. DOI: 10.1103/PhysRevApplied.12.034004.

[206] Qu Yang et al. "Ionic liquid gating control of RKKY interaction in FeCoB/Ru/FeCoB and (Pt/Co)2/Ru/(Co/Pt)2 multilayers". In: *Nature Communications* 9.1 (Dec. 2018), p. 991. ISSN: 2041-1723. DOI: 10.1038/s41467-018-03356-z.

[207] Long You et al. "Switching of perpendicularly polarized nanomagnets with spin orbit torque without an external magnetic field by engineering a tilted anisotropy". In: *Proceedings of the National Academy of Sciences of the United States of America* 112.33 (2015), pp. 10310–10315. ISSN: 10916490. DOI: 10.1073/pnas.1507474112.

[208] Guoqiang Yu et al. "Switching of perpendicular magnetization by spin-orbit torques in the absence of external magnetic fields". In: *Nature Nanotechnology* 9.7 (2014), pp. 548–554. ISSN: 17483395. DOI: 10.1038/nnano.2014.94.

[209] Qian-Qian Yuan et al. "Quasiparticle interference evidence of the topological Fermi arc states in chiral fermionic semimetal CoSi". In: *Science Advances* 5.12 (Dec. 2019), eaaw9485. ISSN: 2375-2548. DOI: 10.1126/sciadv.aaw9485.

[210] Shinji Yuasa et al. "Giant room-temperature magnetoresistance in single-crystal Fe/MgO/Fe magnetic tunnel junctions". In: *Nature Materials* 3.12 (2004), pp. 868–871. ISSN: 14761122. DOI: 10.1038/nmat1257.

[211] Jijun Yun et al. "Tailoring Multilevel-Stable Remanence States in Exchange-Biased System through Spin-Orbit Torque". In: *Advanced Functional Materials* 30 (15 Apr. 2020), p. 1909092. ISSN: 16163028. DOI: 10.1002/adfm.201909092.

[212] Delin Zhang et al. "Bipolar Electric-Field Switching of Perpendicular Magnetic Tunnel Junctions through Voltage-Controlled Exchange Coupling". In: *Nano Letters* 22.2 (Jan. 2022), pp. 622–629. ISSN: 15306992. DOI: 10.1021/ACS.NANOLETT.1C03395/SUPPL_FILE/NL1C03395_SI_001.PDF.

[213] Shufeng Zhang. "Spin Hall effect in the presence of spin diffusion". In: *Physical Review Letters* 85.2 (2000), pp. 393–396. ISSN: 00319007. DOI: 10.1103/PhysRevLett.85.393.

[214] Wei Zhang et al. "All-electrical manipulation of magnetization dynamics in a ferromagnet by antiferromagnets with anisotropic spin Hall effects". In: *Physical Review B - Condensed Matter and Materials Physics* 92.14 (2015), p. 144405. ISSN: 1550235X. DOI: 10.1103/PhysRevB.92.144405.

[215] Wei Zhang et al. "Spin Hall Effects in Metallic Antiferromagnets". In: *Physical Review Letters* 113.19 (Nov. 2014), p. 196602. ISSN: 0031-9007. DOI: 10.1103/PhysRevLett.113.196602.

[216] Weifeng Zhang et al. "Giant facet-dependent spin-orbit torque and spin Hall conductivity in the triangular antiferromagnet IrMn3". In: *Science Advances* 2.9 (Sept. 2016). ISSN: 23752548. DOI: 10.1126/sciadv.1600759.

[217] Z C Zheng et al. "Magnetization switching driven by current-induced torque from weakly spin-orbit coupled Zr". In: *Physical Review Research* 2.1 (Feb. 2020), p. 013127. ISSN: 2643-1564. DOI: 10.1103/PhysRevResearch.2.013127.

[218] Zhenyi Zheng et al. "Field-free spin-orbit torque-induced switching of perpendicular magnetization in a ferrimagnetic layer with a vertical composition gradient". In: *Nature Communications* 12 (1 Dec. 2021), p. 4555. ISSN: 2041-1723. DOI: 10.1038/s41467-021-24854-7.

[219] Jing Zhou et al. "Large spin-orbit torque efficiency enhanced by magnetic structure of collinear antiferromagnet IrMn". In: *Science Advances* 5.5 (May 2019), eaau6696. ISSN: 2375-2548. DOI: 10.1126/sciadv.aau6696.

[220] Lijun Zhu, Daniel C Ralph, and Robert A Buhrman. "Effective Spin-Mixing Conductance of Heavy-Metal–Ferromagnet Interfaces". In: *Physical Review Letters* 123.5 (Aug. 2019), p. 057203. ISSN: 0031-9007. DOI: 10.1103/PhysRevLett.123.057203.

[221] Lijun Zhu, Daniel C Ralph, and Robert A Buhrman. "Effective Spin-Mixing Conductance of Heavy-Metal–Ferromagnet Interfaces". In: *Physical Review Letters* 123.5 (2019). ISSN: 0031-9007. DOI: 10.1103/physrevlett.123.057203.

[222] Lijun Zhu, Daniel C Ralph, and Robert A Buhrman. "Enhancement of spin transparency by interfacial alloying". In: *Physical Review B* 99.18 (2019), pp. 180404–180405. ISSN: 24699969. DOI: 10.1103/PhysRevB.99.180404.

[223] Lijun Zhu, Daniel C Ralph, and Robert A Buhrman. "Highly Efficient Spin-Current Generation by the Spin Hall Effect in Au1-xPtx". In: *Physical Review Applied* 10.3 (2018), p. 31001. ISSN: 23317019. DOI: 10.1103/PhysRevApplied.10.031001.

[224] Lijun Zhu, Daniel C. Ralph, and Robert A. Buhrman. "Unveiling the Mechanism of Bulk Spin-Orbit Torques within Chemically Disordered Fe x Pt 1- x Single Layers". In: *Advanced Functional Materials* 31.36 (Sept. 2021), p. 2103898. ISSN: 1616-301X. DOI: 10.1002/adfm.202103898.

[225] Lijun Zhu, Lujun Zhu, and Robert A. Buhrman. "Fully Spin-Transparent Magnetic Interfaces Enabled by the Insertion of a Thin Paramagnetic NiO Layer". In: *Physical Review Letters* 126.10 (Mar. 2021), p. 107204. ISSN: 0031-9007. DOI: 10.1103/PhysRevLett.126.107204.

[226] Lijun Zhu et al. "Origin of strong two-magnon scattering in heavy-metal/ferromagnet/oxide heterostructures". In: *Physical Review Applied* 13.3 (2020), p. 1. ISSN: 23317019. DOI: 10.1103/PhysRevApplied.13.034038.

[227] Lijun Zhu et al. "Variation of the giant intrinsic spin Hall conductivity of Pt with carrier lifetime". In: *Science Advances* 5.7 (July 2019), eaav8025. ISSN: 2375-2548. DOI: 10.1126/sciadv.aav8025.

[228] Brandon R. Zink et al. "Ultralow Current Switching of Synthetic-Antiferromagnetic Magnetic Tunnel Junctions Via Electric-Field Assisted by Spin–Orbit Torque". In: *Advanced Electronic Materials* 8.10 (Oct. 2022), p. 2200382. ISSN: 2199-160X. DOI: 10.1002/aelm.202200382.

Appendix A

Home built experimental setup design and construction

A.1 Resistivity measurement

The resistivity measurement is done in a four terminal resistance measurement configuration on a double Hall bar device. The two outer terminals are for current sourcing and the inner two terminals are for voltage sensing. The measured voltage are converted into resistance by dividing it by the current amplitude. With the thickness (t) of the material under study measured through x-ray reflectivity or cross-sectional TEM imaging and the lateral (w) and longitudinal (L) dimension of the double hall bar device known or confirmed through optical microscope, the resistivity (ρ) of the material under study can be extracted through:

$$R = \rho \frac{L}{wt}. \tag{A.1}$$

The current source used in this dissertation is Keithley 6221A, the nanovoltmeter is Keithle 2182A and the lock-in amplifier is Signal Recovery 7270 by AmTek. Devices are wirebonded onto a chip carrier (44pin leaded chip carrier non-magnetic). The chip carrier is then inserted into a socket with wires connecting the leads on the back of the socket to BNC female connectors. The female connectors are for connecting the voltage and current terminals from the current source, voltmeter or lock-in amplifier.

A.2 Harmonic Hall and magnetoresistance measurement

Harmonic Hall and magnetoresistance measurement setup is built in a similar way as the resistivity measurement in terms of the transport part. On top of the transport part of the setup, additional capabilities such as angle rotation, magnetic field application, magnetic

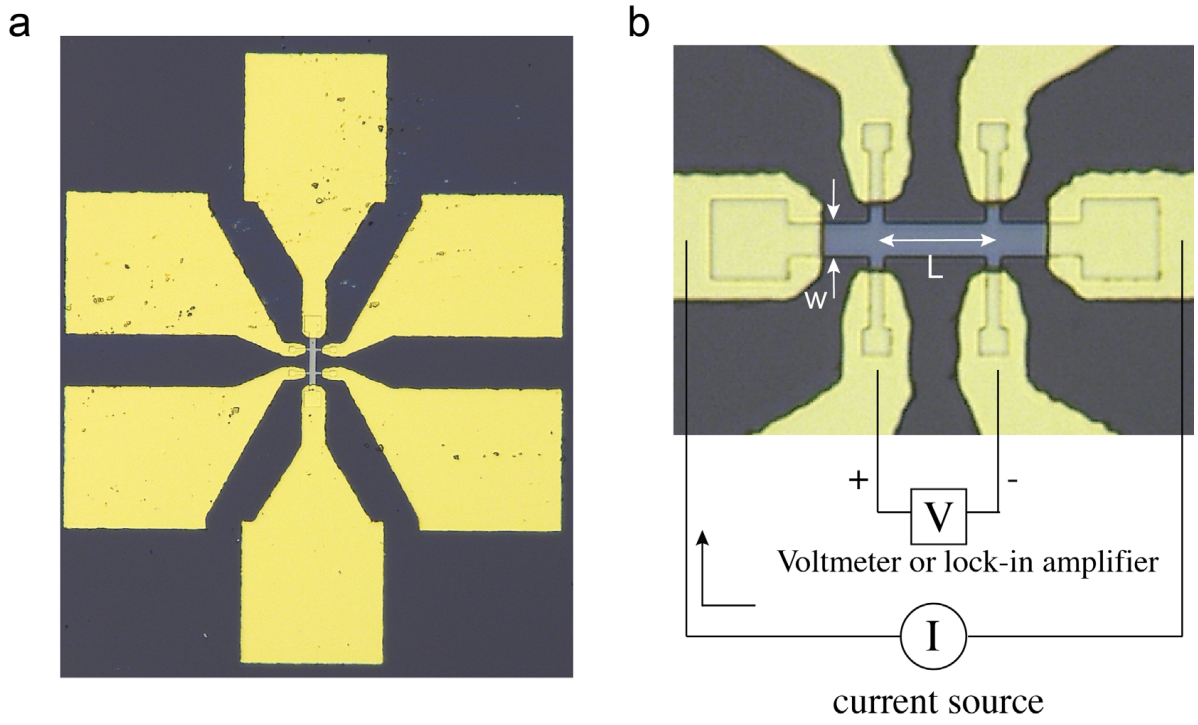

Figure A.1: a, double Hall bar device for resistivity measurement. b, longitudinal resistance measurement.

field sensing, and control of the geometry between magnetic field, current, and rotation axis directions are required.

A.3 Spin-torque ferromagnetic resonance measurement - STFMR

STFMR measurement requires a magnetic field, RF current, lock-in amplifier or nanovoltmeter, bias tee, and electrical network. The STFMR co-planar device is bonded onto a customized RF printed circuit board (PCB). The bonded PCB is then connected to the dipstick through SMA connections. The dipstick is mounted onto the measurement stage with the PCB between the two electromagnet poles. One SMA cable is connected from the RF signal generator output through the bias tee to the current box on the dip stick. The DC signal from the bias tee is connected to a voltage box (not shown in Fig. A.3) and the two terminals of the lock-in amplifier are connected to the voltage box where the DC signal is amplitude modulated. The electromagnet is controlled by the Kepco power supply which is further controlled by the DAQ output analog signal with feedback program doing real-time

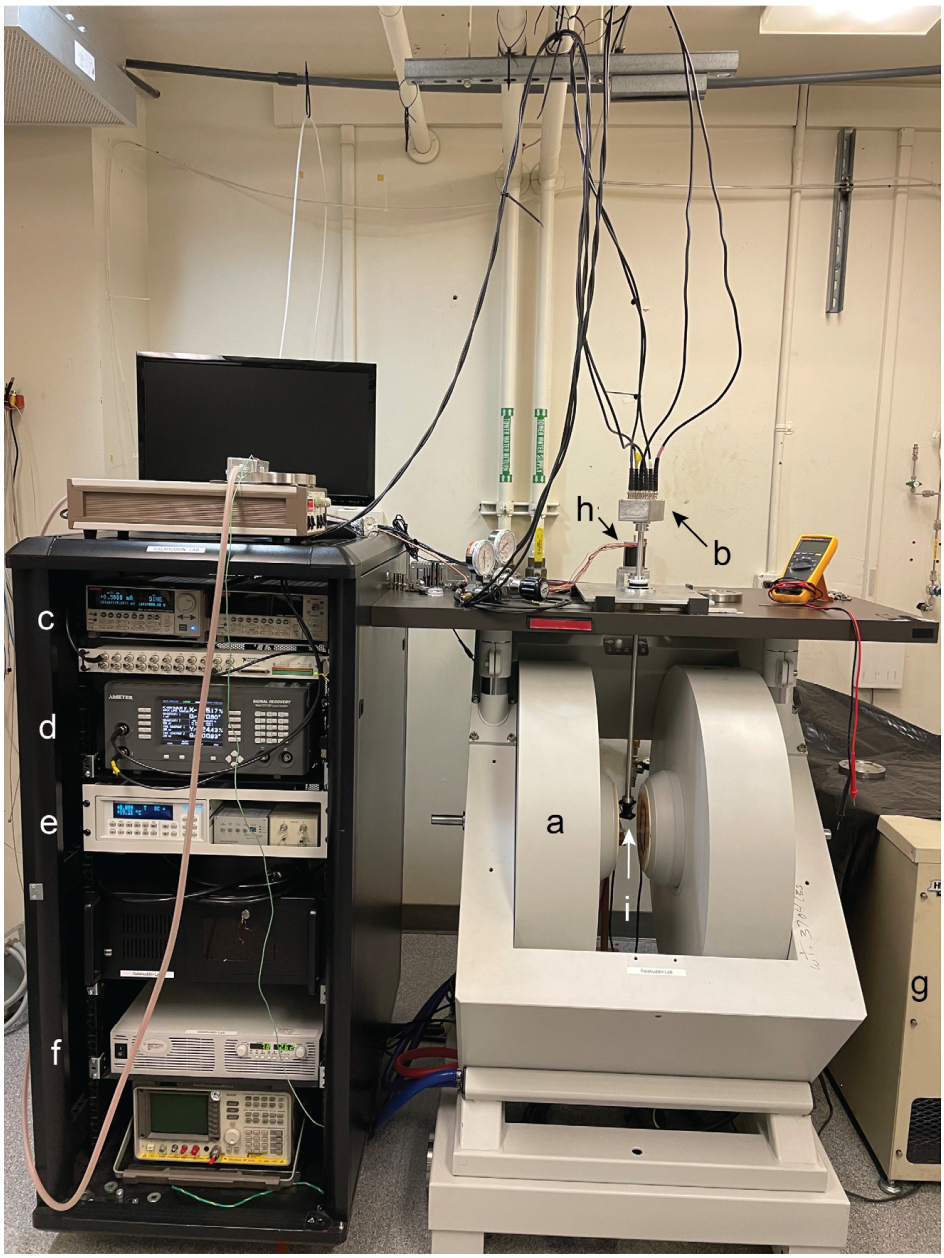

Figure A.2: a, Electromagnet capable of generating up to 1.7 T. b, Current and voltage box for connecting BNC cables to current source and lock-in amplifier. c, Keithley 6221A AC/DC current source. d, Signal Redovery 7270 DSP Lock-in amplifier by AmTek. e, Lakeshore 475 DSP Gaussmeter. f, Keysight N8739A 100V 30A power supply. g, Hakris heat exchanger for chilling the electromagnet. h, Applied motion angle rotation motor assembly. i, sample holder with chip carrier and socket mounted.

Figure A.3: a, Electromagnet capable of generating up to 0.35 T. b, Applied motion angle rotation motor assembly. c, Current box for input RF signal. d, Bias tee. e, Signal Redovery 7270 DSP Lock-in amplifier by AmTek. f, Keithley 6221A AC/DC current source. g, DAQ card. h, Gaussmeter. i, Electromagnet powersupply by Kepco.

feedback control by comparing the measurement field (by the Gaussmeter) with the target field.

A.4 Current and voltage pulse IV switching setup

Current and voltage pulse IV switching setup is very similar to previous setups. Aside from electromagnet control and angle control, the current pulse and voltage measurement are done through combining Keithley 6221A current source as pulse generator and Keithley 2181A as pulse delta voltage amplitude sensing. The two instruments combined to be operated in the pulse-delta mode. For IEC voltage pulse and current sensing, Keithley 2612b is used for voltage pulse sourcing and current sensing. The lock-in amplifier is used for quick out-of-plane anomalous Hall effect measurement to check the perpendicular magnetic anisotropy of the device under study with a small a.c. current.

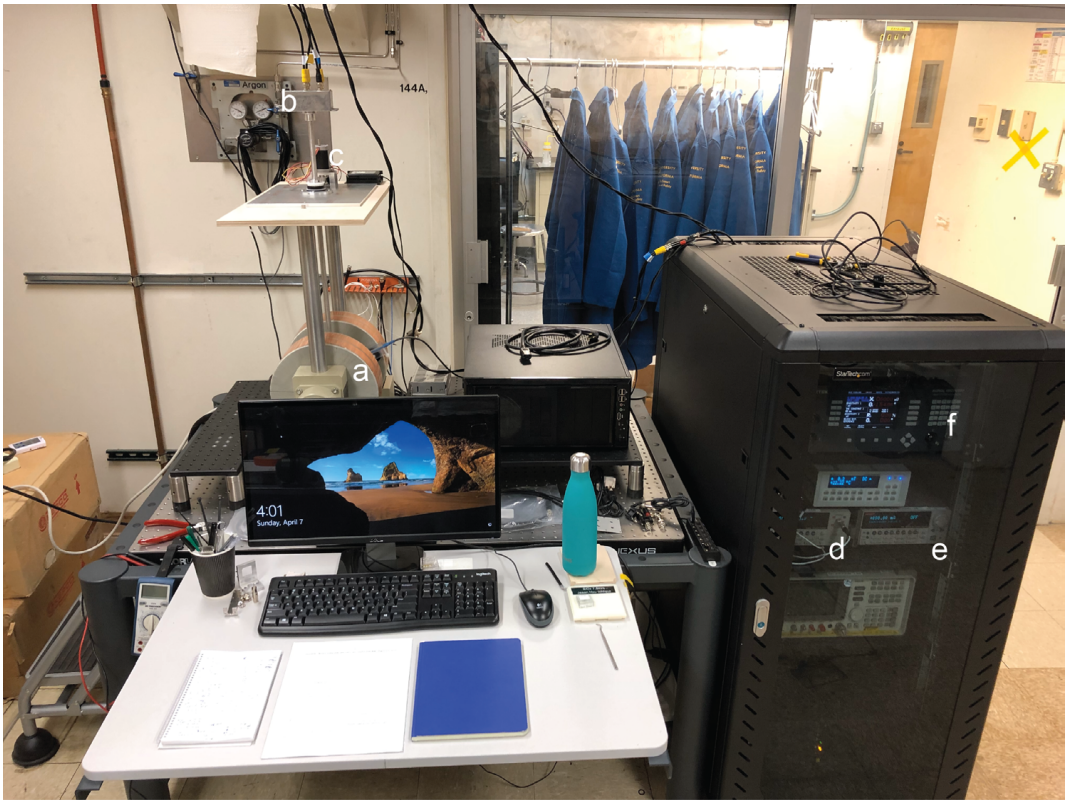

Figure A.4: a, Electromagnet capable of generating up to 0.35 T. b, Current and voltage box for connecting the current source and voltage sense. c, Applied motion angle rotation motor assembly. d, Keithley 2181A nanovoltmeter. e, Keithley 6221A AC/DC current source. f, Signal Recovery 7270 DSP Lock-in amplifier by AmTek.

Appendix B

Device fabrication process flow and recipes

Device fabrication is done in the Berkeley Marvell Nanofabrication Laboratory and Prof. Salahuddin's lab.

B.1 Hall bars, microstrips with CPW and domain wall devices

The different devices in this section are carried out with different photomask layout designs at the device layer but the overall process steps are very similar. Here I will brief the process steps and recipes on the generic process flow and one can insert different photomasks at the device and contact layers for desired device design. Tools for the relevant steps are included in the parentheses.

The full material deposition to device fabrication process begins with preparing the silicon wafer with a thick insulating material. A thick insulating material of thermal oxide or low-stress nitride (LSN) is formed/deposited on the 6" silicon wafer in the furnace tube (Tystar 1 for dry oxidation and Tystar 14 for LSN). Thickness of such insulating layer is between 100 and 250 nm and that should be sufficient. After the insulating layer formation, the 6" wafer is diced into either 5 mm by 5 mm or 7.5 mm by 7.5 mm square chips by Disco DAD3240 Automated Dicing Saw (Disco) and the 6" wafer should be fully coated with at least 1 μm of photoresist for protection during dicing.

At the sputtering chamber in Prof. Salahuddin's lab, take a desired amount of chips and clean off the photoresist with acetone then IPA in the ultrasonicator for at least 5 min on each step. After drying off the residual IPA with N2 gun, the clean substrate chips can be loaded into the sputtering chamber for material stack deposition. After deposition, the sample should be kept safely away from moist. Before device fabrication, clean the sample with acetone and IPA in the ultrasonicator each for 5 min. Immediately dry off the IPA with N2 gun and place the sample on the hotplate at 150°c for 5 min to bakeout the moist.

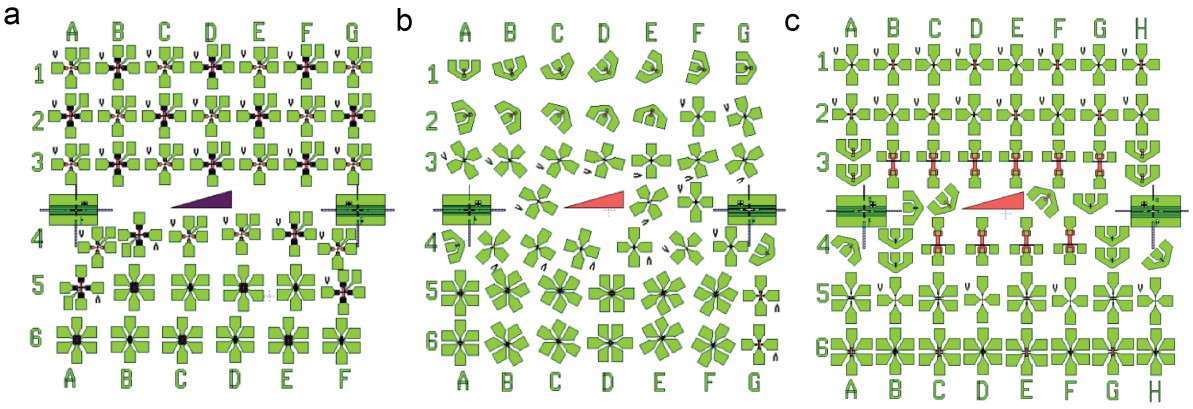

Figure B.1: a, IEC devices and double Hall bar devices. b, STFMR and Hall devices. c, PMA devices and domain wall devices.

After that, spin coat a layer of MCC 80-20 primer, followed by a 1 min 115°c bake (headway spin coater in the Berkeley nanolab). Next, spin coat 1 μm of photoresist (e.g. MiR-701) and softbake at 95°c for 1 min.

With the photoresist coated, one can use either the gcaws6 photolithography stepper or MLA150 maskless aligner to pattern the device layer. For MiR-701 1 μm photoresist, gcaws6 requires an exposure time of 3.6 s and for MLA150 the dose should be 190 mJ/cm^2. Immediately after the exposure, one should develop the photoresist with 60s of MF-26A photoresist developer at room temperature. A post-exposure bake prior to the development is optional. Once the development is complete, inspect the features with optical microscope.

If the pattern of the photoresist looks good, one can proceed with a 1 min oxygen plasma descum at 50W 180mTorr with a chuck at 50°c (technis-c). Next, place the samples in the ion-milling chamber load-lock for pump down in Prof. Salahuddin's lab. Once the pressure in the load-lock is below 5e-6 Torr, one can transfer the samples to the main chamber. Next, turn on Ar gas flow, turn on ion-source controller, setup SIMS detection scan, start the discharge by pressing on the "discharge enable" button and wait for 5 min so that the discharge circuitry can warm up and reach equilibrium. Once the parameters have settled, one can turn on the beam by pressing "beam enable." Proceed with the etching by opening the shutter for 20 s and close the shutter for 40 s so the sample does not get too hot. Repeat this etching cycle until desired end-point is reached. Disable both the discharge and the beam by pressing the "Discharge enable" button and power off the ion-source controller box. Turn off Ar gas, stop the SIMS acquisition and power off the SIMS controller box. Remove the sample and wash off the masking photoresist in acetone followed by IPA rinse and N2 blow dry.

Now the devices have been etched and patterned, the etch depth will be checked by the profilometer (dektak). Typical etch depth is 15 $\sim$ 20 nm over etch into the insulating

layer. If the etch depth looks good, we can proceed with the contact layer definition. Repeat the photoresist coating steps listed earlier with 1 μm thick MiR-701. Once the photoresist is nicely coated, we proceed to the photolithography aligner tool (KSAligner). At the KSAligner, align to the device layer by aligning with the alignment markers or the corner devices. The exposure time is 4.5 s for 1 μm MiR-701. Repeat the photoresist development process and inspect with optical microscope.

Next, bring the sample back to the electron beam evaporator/ion-mill dual chamber, and wait for load-lock to pump down. Once the load-lock is pumped down, transfer the samples into the main chamber and rotate the stage so that it faces the ion-source. We will ion-mill for 2 cycles (20s shutter open, 40s shutter closed) to clean off any residuals and thinning down the insulating capping layer. Once this is done, rotate the stage to vertical configuration where the samples faces the electron beam source. Move the crucible to the material of choice which in this case is Ti. Turn on the electron beam source power supply and turn on the HV. Once the HV reaches 9kV, beam current can be slowly turned on. For Ti, the current where it starts to evaporate is around 33 $\sim$ 36 mA. Open the substrate shutter and zero our the crystal monitor (make sure the crystal monitor has been set to select the correct material to be tracked). Once the crystal monitor reading reaches the desired thick, start to slowly lower the beam current. Once the beam current is completely zero, one can proceed with Au which is the main contact metal. Au begins to evaporate around 57 mA and staying at 69 $\sim$ 72 mA will yield a good rate. Once this is done, turn off the beam current slowly, turn off HV, turn off electron beam source power supply, and unload the samples.

Lastly, soak the samples in acetone for 5 min and then place them in the ultrasonicator for another 5 min for lift-off. Once the lift-off is complete, clean up the lift-off waste and inspect the fabricated device with optical microscope. If device looks good, one can proceed to packaging by placing the device in the 44 pin leaded chip carrier and wirebond the devices to the chip carrier. This sample is ready for measurement.

B.2 Three terminal IEC-Magnetic tunnel junction test devices

The three terminal IEC-Magnetic tunnel junction test device with the top electrode has similar process steps except there is a few additional steps. After the Hall bar device definition, one needs to pattern the MTJ pillar at the cross of the Hall bar by doing an additional lithography step and etch the pillar structure with etch-stop at the Ta/Ru underlayer. Once the pillar etching is done, *in situ* deposition of the interlayer dielectric (ILD) is carried out for about 50 nm of AlO_x. Afterwards, the photoresist masks are washed away with acetone and IPA with ultrasonication. The contact layer and the rest are done in a similar fashion as the previous section.

Appendix C

References to the benchmark plots

C.1 References to the data point in benchmark plot Fig. 2.15, 2.6, 3.17, 4.1, and 4.16.

The benchmark plots are constructed through collecting reported SOT efficiencies in many shown material systems in literature including

1. Heavy metals: Pt/Co [140], Ta/CoFeB [112], W/CoFeB [147], Hf/CoFeB [155], $Au_{0.25}Pt_{0.75}$/Co [223], $W_{0.66}Hf_{0.34}$/CoFeB [51], $Fe_{0.25}Pt_{0.75}$/Hf/CoFeB [143], Pt_xMgO_{1-x}/CoFeB [220], WO_x/CoFeB [40]
2. Topological Insulators: Bi_2Se_3/Py [124], Bi_xSe_{1-x}(6, 8, 16 nm)/CoFeB [39], $(Bi_{0.2}Sb_{0.8})_2Te_3$(6)/Mo(2)/CoFeB(1) [148], $(BiSb)_2Te_3$(6)/Mo(2)/CoFeB(1) [167], $(Bi_{0.07}Sb_{0.93})_2Te_3$(6)/Ti(2)/CoFeB(1.4) [201]
3. Three-dimensional oxide semi-metal: $SrIrO_3$/Py [46], $SrIrO_3$/CoTb [193], $SrIrO_3$/Py [130], [001] IrO_2/Ir/Py [13], $SrIrO_3$/LSMO [77]
4. Antiferromagnets: IrMn/Py [189], PtMn/Co [144], Crystalline IrMn/Py [219], $IrMn_3$[001]/Py, $IrMn_3$[111]/Py, $Ir_{37}Mn_{63}$/Py [216].

C.2 References to the data point in j_c/Δ benchmark plot Fig. 3.20

The benchmark plot (Fig. 3.20) is constructed through collecting reported critical switching current density (J_c) and thermal stability (Δ) in many well-studied systems including: Ta/CoFeB/MgO (PMA) [53], Ta/Pt/$[Co/Pt]_4$ (PMA) [81], Pt/Co/MgO (PMA) [104], Pt/CoFeB/MgO (IMA)[125], Ta/GdFeCo/Pt (PMA) [161], Bi_xTe_{1-x}/Pt/Co/Pt (PMA) [31].